Creative Design and Modelling of Large-Range Translational Compliant Parallel Manipulators

Guangbo Hao

Submitted for the degree of Doctor of Philosophy

Heriot-Watt University

School of Engineering and Physical Sciences

October 2011

Abstract

Compliant parallel mechanisms/manipulators (CPMs) are parallel manipulators that transmit motion/load by deformation of their compliant members. Due to their merits such as the eliminated backlash and friction, no need for lubrication, reduced wear and noise, and monolithic configuration, they have been used in many emerging applications as scanning tables, bio-cell injectors, nano-positioners, and etc.

How to design large-range CPMs is still a challenging issue. To meet the needs for large-range translational CPMs for high-precision motion stages, this thesis focuses on the systematic conceptual design and modelling of large-range translational CPMs with distributed-compliance.

Firstly, several compliant parallel modules with distributed-compliance, such as spatial multi-beam modules, are identified as building blocks of translational CPMs. A normalized, nonlinear and analytical model is then derived for the spatial multi-beam modules to address the non-linearity of load-equilibrium equations. Secondly, a new design methodology for translational CPMs is presented. The main characteristic of the proposed design approach is not only to replace kinematic joints as in the literature, but also to replace kinematic chains with appropriate multiple degrees-of-freedom (DOF) compliant parallel modules. Thirdly, novel large-range translational CPMs are constructed using the proposed design methodology and identified compliant parallel modules. The proposed novel CPMs include, for example, a 1-DOF compliant parallel gripper with auto-adaptive grasping function, a stiffness-enhanced XY CPM with a spatial compliant leg, and an improved modular XYZ CPM using identical spatial double four-beam modules. Especially, the proposed XY CPM and XYZ CPM can achieve a 10mm’s motion range along each axis in the case studies. Finally, kinematostatic modelling of the proposed translational CPMs is presented to enable rapid performance characteristic analysis. The proposed analytical models are also compared with finite element analysis.

.

Acknowledgements

First of all, I would like to thank my thesis's first supervisor: Dr. Xianwen Kong who has give me the opportunity to work in this doctoral project technically and financially, has supervised me throughout my three-year PhD study and research, has encouraged me continuously, and has spent hours and hours with me dealing with problems I encountered in research. I remember clearly that the happiest time in every week is that fixed meeting slot with Dr. Xianwen Kong since the relaxed discussion atmosphere, his constructive suggestions and good knowledge always drive me to produce good inspiration for my research. To Xianwen, I cannot thank you enough for your financial support, excellent supervision, precious time, patience, and tolerance.

I would also like to give my acknowledgement to my thesis's second supervisor: Professor Robert L. Reuben for his invaluable guidance in my research. Thank him for helping me clarify my research objective, and thank him for giving me an opportunity every month in my first year to meet with him. I give my gratitude to Dr. Xichun Luo, who reviewed my first-year report and provided helpful comments. I am greatly grateful to the internal examiner: Dr. Xichun Luo and external examiner: Prof. Jiansheng Dai for reviewing my thesis.

Acknowledgement specially goes to Miss Qiaoling Meng, PhD student in University of Bologna for her kind help in analysing my models. I am indebted to all the staffs and students, who provided help to me, in Heriot-Watt University, and thank Heriot-Watt University, where I started my another dream.

In addition, all individuals and institutions that contributed graphical figures in my thesis are sincerely acknowledged.

Lastly, I would like to deeply acknowledge my parents, my wife, Xiuyun He, and my daughter, Wenying Hao. Especially to my wife, without your accompanying, support, encouragement and understanding, I cannot finish my thesis at all.

Declaration Statement

(Research Thesis Submission Form should be placed here)

Table of Contents

List of Abbreviations

Abbreviation	*Full name*
C	Cylindrical
CBDA	Constraint-Based Design Approach
CPG	Compliant Parallel Gripper
CPM	Compliant Parallel Manipulator/Mechanism
CSOA	Continuum Structure Optimization Approach
DC	Direct Current
DOC	Degree(s) of Constraint
DOF	Degree(s) of Freedom
E	Planar Motion
EDM	Electric Discharge Machine
FCTA	Freedom and Constraint Topology Approach
FEA	Finite Element Analysis
MEMS	Micro-Electro-Mechanical-Systems
N_C	Number of Degree(s) of Constraint
N_F	Number of Degree(s) of Freedom
P	Prismatic
PRBM	Pseudo-Rigid-Body-Model
P^s	Spatial Motion Four-Bar Parallelogram with Four Spherical Lumped-Compliance Joints
PZT	Piezoelectric Ceramics Actuator
R	Revolute
STBA	Screw Theory Based Approach
TPM	Translational Parallel Manipulator/Mechanism
U	Universal

Nomenclature

Symbol	*Explanation of symbol*
E, E'	Young's modulus or plate modules
G	Shear modulus
ν	Poisson's ratio of material
δ	Material property=$2E/G=1/(1+\nu)$
σ_s	Yield stress of material
ρ	Density of material
I, I_z	Second moment of area
I_p	Polar moment of area
r_3', r_3, d_0, r_n, a_0, Δ, r_4', r_4, u, t, w, w_1, w_2, w_3, h_1, h_2, v_1, v_2, s (n=1, 2, 3, 4, …)	Normalized geometrical parameters
L, L_1, L_2, D_0, R_3, R_3', R_4', R_4, U, T, W, W_1, W_2, W_3, H_1, H_2, V_1, V_2, S	Actual geometrical parameters
y, x_s, y_s, z_s, x_{i_0}, y_{i_0}, z_{i_0}, x_i, y_i, z_i, $\bar{x}_s$, $\bar{y}_s$, $\bar{z}_s$, $\hat{y}_s$, $\hat{z}_s$, x_{s1}, y_{s1}, z_{s1}, x_{s2}, y_{s2}, z_{s2}, x_{ax}, y_{ax}, z_{ax}, x_{ay}, y_{ay}, z_{ay}, x_{az}, y_{az}, z_{az}, x_e, y_e, z_e, x_e^e, x_e^k (i_0=1, 2, 3; i=1, 2, 3, …)	Normalized translational displacements
X_1, X_s, Y_s, Z_s, δ_x, δ_y, Δ_I, Δ_{II}, Δ_a, X_e, Y_e, Z_e	Actual translational displacements
θ, θ_x, θ_y, θ_z, θ_{sx}, θ_{sy}, θ_{sz}, θ_{i_0x}, θ_{i_0y}, θ_{i_0z}, θ_{ix}, θ_{iy}, θ_{iz}, $\bar{\theta}_{sy}$, $\bar{\theta}_{sz}$, θ_{sx1}, θ_{sy1}, θ_{sz1}, θ_{sx2}, θ_{sy2}, θ_{sz2}, $\theta_{ax\text{-}x}$, $\theta_{ax\text{-}y}$, $\theta_{ax\text{-}z}$, $\theta_{ay\text{-}x}$, $\theta_{ay\text{-}y}$, $\theta_{ay\text{-}z}$, $\theta_{az\text{-}x}$, $\theta_{az\text{-}y}$, $\theta_{az\text{-}z}$ (i_0=1, 2, 3; i=1, 2, 3, …)	Rotational displacements
m, m_x, m_y, m_z, m_{i_0x}, m_{i_0y}, m_{i_0z}, m_{ix}, m_{iy}, m_{iz}, $m_{ax\text{-}x}$, $m_{ax\text{-}y}$ $m_{ax\text{-}z}$, $m_{ay\text{-}x}$, $m_{ay\text{-}y}$, $m_{ay\text{-}z}$, $m_{az\text{-}x}$, $m_{az\text{-}y}$, $m_{az\text{-}z}$, m_{xe}, m_{ye}, m_{ze}, m_{zmax} (i_0=1, 2, 3; i=1, 2, 3, …)	Normalized moments
M, M_x, M_y, M_z, M_{xe}, M_{ye}, M_{ze}	Actual moments
p, f, f_x, f_y, f_z, p_{i_0}, f_{i_0y}, f_{i_0z}, p_i, f_{iy}, f_{iz}, $f_{ax\text{-}x}$, $f_{ax\text{-}y}$, $f_{ax\text{-}z}$, $f_{ay\text{-}x}$, $f_{ay\text{-}y}$, $f_{ay\text{-}z}$, $f_{az\text{-}x}$, $f_{az\text{-}y}$, $f_{az\text{-}z}$ (i_0=1, 2, 3; i=1, 2, 3, …)	Normalized forces
P, F, F_x, F_y, F_z, $F_{ax\text{-}x}$, $F_{ay\text{-}y}$, $F_{az\text{-}z}$	Actual forces
a, b, c, d, e, g, h, i, j, k, r, s, q	Non-dimensional coefficients: a=12, b=4, c=−6, d=$16/(D_0/L)^2$ or $12/(T/L)^2$, e=1.2, g=2/15, h=−0.1, i=−0.6, j=−1/15, k=1/20, r=1/700, s=11/6300, q=−1/1400.

Symbol	*Explanation of symbol* (Continued)
x''_{i_0}, y''_{i_0}, z''_{i_0}, x'_{i_0}, y'_{i_0}, z''_{i_0}, x_i', y_i', z_i' (i_0=1, 2, 3; i=1, 2, 3, …)	Normalized coordinates
$\mathbf{R}_X$, $\mathbf{R}_Y$, $\mathbf{R}_Z$, $\mathbf{R}_m$, $\mathbf{R}_{dm}$, $\mathbf{R}_{pp}$, $\mathbf{R}_{legi}$ (i=1, 2, 3, …)	Rotational matrices
$\mathbf{K}$, $\mathbf{K}_p$, $\mathbf{K}_i$, $\mathbf{K}_s$, $\mathbf{K}_{ps}$, $\mathbf{K}_{si}$, $\mathbf{K}_{opi}$, $\mathbf{K}_{oi}$, $\mathbf{K}_{leg}$, $\mathbf{K}_m$, $\mathbf{K}_{legi}$, $\mathbf{K}_{spatial}$, $\mathbf{K}_{cpm}$ (i=1, 2, 3, …)	Normalized stiffness matrices
$\mathbf{C}_p$, $\mathbf{C}_s$, $\mathbf{C}_{pi}$, $\mathbf{C}_{ps}$, $\mathbf{C}_{ps}'$, $\mathbf{C}_{opi}$, $\mathbf{C}_{os}$, $\mathbf{C}_{leg}$, $\mathbf{C}_{dm}$, $\mathbf{C}_{mi}$, $\mathbf{C}_{legi}$, $\mathbf{C}_{cpm}$ (i=1, 2, 3, …)	Normalized compliance matrices
$\mathbf{D}_i$, $\mathbf{D}_{pi}$, $\mathbf{D}_{s1}$, $\mathbf{D}_{s2}$, $\mathbf{D}_{op1i}$, $\mathbf{D}_{op2i}$, $\mathbf{D}_{mi}$, $\mathbf{J}$, $\mathbf{J}_p$, $\mathbf{J}_{op}$, $\mathbf{J}_m$, $\mathbf{J}_{dmi}$, $\mathbf{J}_{pai}$, $\mathbf{J}_{pax}$, $\mathbf{J}_{pay}$, $\mathbf{J}_{paz}$ (i=1, 2, 3, …)	Normalized displacement Transformation matrices
$\mathbf{F}$, $\mathbf{F}_2$, $\mathbf{F}_{ax}$, $\mathbf{F}_{ay}$, $\mathbf{F}_{az}$	Normalized load vectors
$\mathbf{X}_s$, $\mathbf{X}_{ax}$, $\mathbf{X}_{ay}$, $\mathbf{X}_{az}$,	Normalized displacement vectors
$\mathbf{s}_i$ (i=1, 2,…, 6)	Screw
p_i (i=1, 2,…, 6)	Pitch of a screw
$\mathbf{r}_i$ (i=1, 2,…, 6)	Position vector of any point on a screw axis
$\mathbf{w}_i$ (i=1, 2,…, 6)	Rotation vector in a screw
$\boldsymbol{v}_i$ (i=1, 2,…, 6)	Translational displacement vector in a screw
k_{m11}, k_{leg11}, $k_{spatial11}$, k', k_x, k_y, k_z, k_{ax}, k_{ay}, k_{az}, k_{px}, k_{py}, k_{pz}	Entries in normalized stiffness matrices or normalized stiffness
c_{cpm22}, c_{leg222}	Entries in normalized compliance matrices
M_{m1} M_{m2}, M_{m3}, M_{s2}, M_s, M_e	Actual mass
K_1, K_2, K_a	Actual stiffness of springs
α, β, α_i (i=1, 2, 3, 4)	Angles in radians
η	Factor of safety
f_{n1}	First natural modal frequency
σ_{max}	Maximal yield stress
α_0	Number of times
x	Normalized axial displacement or normalized position coordinate on a beam
k	Also square roof of the normalized axial force acting at a beam
r_{11}, r_{12}, r_{21}, r_{22}	Parameters associated with the normalized axial force acting at a beam

List of Publications

Journal

[1] **Hao, G.,** and Kong, X., 2011, "A Normalization-Based Approach to the Mobility Analysis of Spatial Compliant Multi-Beam Modules", *Mechanism and Machine Theory*. (Submitted) (**Related to Appendix C**)

[2] **Hao, G.,** and Kong, X., 2011, "Novel XY Compliant Parallel Manipulators for Large Translation with Enhanced Out-of-Plane Stiffness", *Journal of Mechanical Design*. (Revision under Review) (**Related to Chapter 4**)

[3] **Hao, G.,** and Kong, X., 2011, "Design and Modelling of a Large-Range Modular XYZ Compliant Parallel Manipulators Using Identical Spatial Modules", *Journal of Mechanisms and Robotics*. (Revision under Review) (**Related to Chapter 5**)

[4] **Hao, G.,** Kong, X., and Reuben, R.L., 2011, "A Nonlinear Analysis of Spatial Compliant Parallel Modules: Multi-beam Modules", *Mechanism and Machine Theory*, Vol. **46**(5):680–706. (**Related to Chapter 2**)

Conference

[1] **Hao, G.,** and Kong, X., 2011, "A Normalization-Based Approach to the Mobility Analysis of Spatial Compliant Multi-Beam Modules", *13th World Congress in Mechanism and Machine Science*, Guanajuato, México, 19–25 June, 2011. A23-390. (**Related to Appendix C**)

[2] **Hao, G.,** and Kong, X., 2010, "Novel XY Compliant Parallel Manipulators for Large Displacement Translation with Enhanced Stiffness", *Proceedings of the ASME 2010 International Design Engineering Technical Conferences & Computers and Information in Engineering Conference*, August 15–18, 2010, Montreal, Canada. DETC2010-2846 (**Related to Chapter 4)**

[3] **Hao, G.,** and Kong, X., and Meng, Q., 2010, "Design and Modelling of Spatial Compliant Parallel Mechanisms for Large Range of Translation", *Proceedings of the ASME 2010 International Design Engineering Technical Conferences & Computers and Information in Engineering Conference*, August 15–18, 2010, Montreal, Canada. DETC2010-28141 (**Related to Chapter 5**)

[4] **Hao, G.,** and Kong, X., 2009, "A 3-DOF Translational Compliant Parallel Manipulator Based on Flexure Motion", *Proceedings of the ASME 2009 International Design Engineering Technical Conferences & Computers and Information in Engineering Conference*, August 30–September 2, 2009, San Diego, California, USA. DETC2009-86075 (**Related to Chapter 5**)

Chapter 1 – Introduction

In rigid-body robotics, there are three types of mechanisms: serial mechanisms, parallel mechanisms and hybrid mechanisms. Serial mechanisms use one arm/leg to manipulate the object (Figure 1.1a), while parallel mechanisms use two or more arms/legs to manipulate the object (Figure 1.1b). Hybrid mechanisms are an integration of serial mechanisms and parallel mechanisms. Traditional mechanisms move by the motion of traditional joints, and can be used for many applications. However, in some ultra-precision (macro) or micro-electro-mechanical-systems (MEMS) (micro) areas, traditional mechanisms become inapplicable due to friction limitation or small size requirement, and therefore, the alternative mechanisms such as compliant mechanisms are needed increasingly.

1.1 Compliant Parallel Manipulators

Recently, McCarthy [1.1] has identified "*Analysis and Synthesis of Compliant Linkage Systems*" as one of the three research trends of kinematics in the second decade of the 21st century. As novel mechanisms, compliant parallel mechanisms/manipulators (CPMs) (Figure 1.1c) transmit motion/load by deformation of their compliant members (namely jointless), and belong to a class of parallel manipulators. They aim to utilize the compliance to transmit motion/force instead of only analysing the flexibility effects in the initial work in the area of kinematics of mechanisms with elasticity. Unlike the classical mechanisms, the analysis of CPMs is more challenging due to requiring both kinematic analysis and static equilibrium analysis, which is called "kinematostatic analysis" (or "kinetostatic analysis").

(a) PPP Serial Rigid-Body Manipulator (Source: www.directindustry.com)

(b) 3-PRRR Parallel Rigid-Body Manipulator (Gosselin and Kong, U.S. Patent 2004, Courtesy of Gosselin, Uni. Laval)

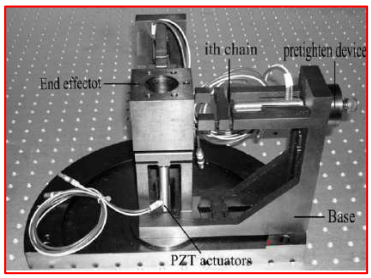

(c) 3-PP^s Compliant Parallel Manipulator (Courtesy of Yue et al, Uni. Shanghai Jiaotong University)

Figure 1.1 Different types of 3-D translational manipulators

In comparison with the traditional rigid-body manipulators and/or serial manipulators, CPMs have the characteristics of both conventional parallel mechanisms [1.2] and compliant mechanisms [1.3, 1.4]. CPMs benefit from many potential merits such as the eliminated backlash and friction (elimination of non-deterministic effects), no need for lubrication, reduced wear and noise, high precision, high payloads, more-compact and monolithic configuration (reduced part count), and having base-mounted/close-to-base actuators. Tables 1.1 and 1.2 show the detailed comparisons between the compliant mechanisms and rigid-body mechanisms, and between the serial mechanisms and parallel mechanisms just from the view point of mechanism design. Due to their merits, CPMs have received much attention over the past two decades.

Types \ *Indices*	Backlash	Lubrication	Wear	Precision	Friction	Noise	Assembly	Motion range
Compliant mechanisms	**Zero**	**No need**	**Reduced**	**High**	**Reduced**	**Reduced**	**No need**	Small
Rigid-body mechanisms	Existing	Needing	Existing	Low	Existing	Existing	Needing	**Large**

Table 1.1 Comparison between compliant mechanisms and rigid-body mechanisms

Types \ *Indices*	Rigidity	Precision	Accumulative errors	Payload	Moving speed	Motion range	Compactness	Actuator mobility	Dynamics
Parallel mechanisms	**High**	**High**	**No**	**High**	**Large**	Small	**Good**	**Base-mounted /close to base**	**Good**
Serial mechanisms	Low	Low	Existing	Low	Small	**Large**	Poor	Mobile	Poor

Table 1.2 Comparison between parallel mechanisms and serial mechanisms

CPMs can be used in a variety of applications including micro and macro scales, especially where high-precision motion are required, such as precision motion positioning stages [1.5-1.7], precision robotics in biomedical applications [1.8], metrology instruments [1.9], MEMS sensors [1.10, 1.11], amplifiers [1.12-1.14], relays [1.15] and actuators [1.16, 1.17], grippers [1.18-1.20], friction force microscopes [1.21], atomic force microscopes [1.22], adaptive mechanisms [1.23], human assistance systems, and design-for-no-assembly [1.24] (see Figure 1.2 for some typical existing applications).

In the design of CPMs for high-precision (nano-positioning) motion stages, good performance characteristics have been specified in Ref. [1.6] along with the nanometric motion quality (<10nm) in terms of motion repeatability, accuracy (lack of error), and resolution (minimum incremental motion) [1.84]. These good characteristics [1.6]

defined in this thesis include: 1) *large range of motion along the desired directions* (>1mm) (also large desired motion[1]), 2) *inherently constrained parasitic error motion* (the minimal undesired motion along the degrees of constraint), 3) *minimal cross-axis coupling* (also output-decoupling [1.25] that is the minimal undesired motion along other degrees of freedom), 4) *maximal actuator isolation* (also input-decoupling [1.26] that is the minimal transverse motion of the actuator), 5) *minimal lost motion* (the minimal displacement difference between the actuator and the motion stage), 6) *maximal drive stiffness* (the maximal overall stiffness between the point of actuation and the motion stage), and 7) *low thermal and manufacturing sensitivities*. In addition, *compactness of the configuration*, *minimal number of the geometrical parameters* (for example using identical modules), *low cost*, *generally desired dynamic performance* (high bandwidth), and *high payloads* may be also design indices.

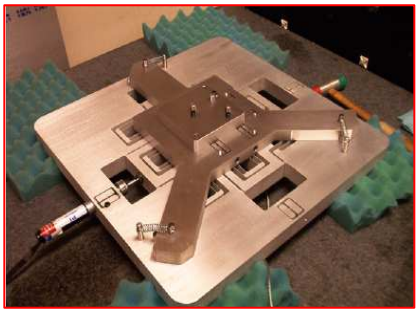

XY Nano-Positioning Motion Stage
(Courtesy of Prof. S., Awtar, University of Michigan)

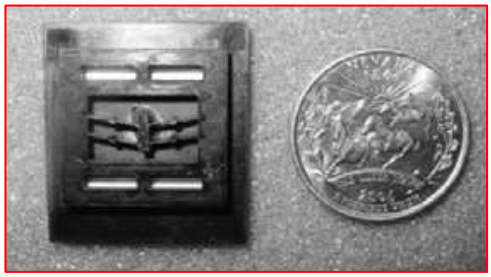

Shock Sensor for Accelerometer
(Courtesy of B. J., Hansen, Brigham Young University)

Compliant Scissors for No Assembly
(Courtesy of the Compliant Mechanisms
Research Group, Brigham Young University)

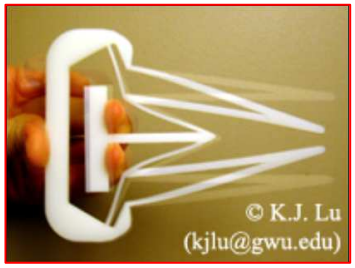

Compliant Gripper for Surgical Tools
(Courtesy of Assistant Prof. K. J. Lu, George
Washington University)

Adaptive Compliant Wing
(Courtesy of Prof. S., Kota, University of Michigan)

Human Assistance System
(Courtesy of Compliant Systems Design Laboratory,
University of Michigan)

Figure 1.2 Typical existing applications for CPMs

[1] The motion in the direction of the applied force is the desired motion, and the other motion is the undesired motion.

It should be noted that to realize the large range of motion is a significant challenge [1.85, 1.86] for the design of CPMs under relatively large primary stiffness since CPMs produce motion by the compliant deformation of the material. Compared with lumped compliant mechanisms (the hinge in lumped-compliance mechanisms is a short-beam considering the shearing deformation [1.49]), distributed-compliance mechanisms provide a good option to produce large range of motion and to reduce stress concentration. They have relatively simpler analytical models (due to negligible shear deformation), and their elastic averaging can permit inexact constraint designs. However, they often result in 1) load-stiffening effect [1.5], 2) relatively low primary stiffness influencing first natural modal frequency, 3) lost motion affecting precision, and 4) loss in drive stiffness influencing the dynamic performance (mostly associated with high-order natural modal frequency) of the motion system. Therefore, if all the above desired performance characteristics cannot be achieved simultaneously, some tradeoffs need to be considered among them.

1.2 Existing Design Methodologies for Compliant Mechanisms

There are several approaches to design compliant mechanisms: a) the Pseudo-Rigid-Body-Model (PRBM) approach (Figure 1.3a) [1.25, 1.27-1.33], b) the continuum structure optimization approach (CSOA) (Figure 1.3b) [1.34-1.37], and c) the other innovative design approaches such as the constraint-based design approach (CBDA) (Figure 1.3c) [1.6, 1.38-1.41, 1.105], the screw theory based approach (STBA) [1.42, 1.43] (Figure 1.3d), the freedom and constraint topology approach (FCTA) [1.44, 1.45] (Figure 1.3e), and the building-block approach [1.46, 1.47] (Figure 1.3f). Compliant mechanisms obtained using different design approaches can be classified into three categories: lumped-compliance mechanisms such as that in Li' work [1.30], distributed-compliance mechanisms such as that in Awtar's work [1.6], and hybrid-compliance mechanisms such as that in Polit's work [1.32].

The PRBM approach is mainly used to design the lumped-compliance mechanisms, while the other approaches are mainly used to deal with the distributed-compliance mechanisms.

Using the PRBM approach, compliant mechanisms are obtained by replacing the traditional kinematic joints with suitable lumped-compliance joints based on type synthesis of rigid-body mechanisms. The performance of CPMs generated by the PRBM approach largely depends on the selected lumped compliance joints (see Ref.

[1.3] for detailed analysis for a variety of flexure hinges).

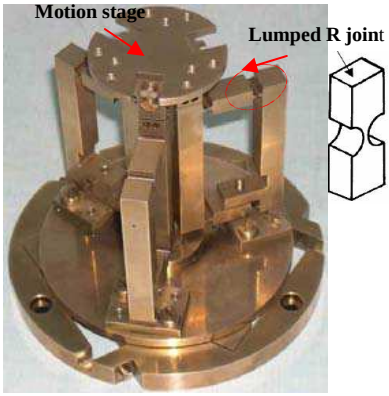

(a) 6-DOF Micro-Manipulator Obtained by the PRBM Approach (Courtesy of D. H., Chao, Beihang University, China)

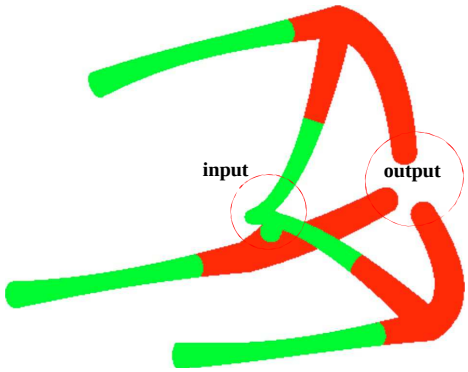

(b) Compliant Gripper Obtained by the CSOA (Courtesy of H., Zhou, Tennessee Technological University)

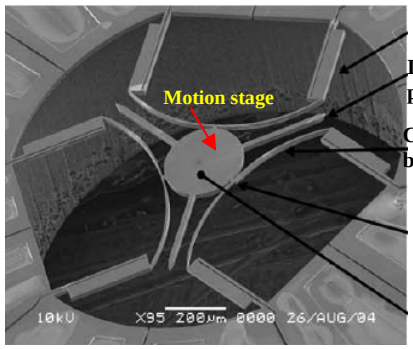

(c) Six-Axis Small-Scale Nanopositioner Obtained by the CBDA (Courtesy of S.-C., Chen and M. L., Culpepper, MIT)

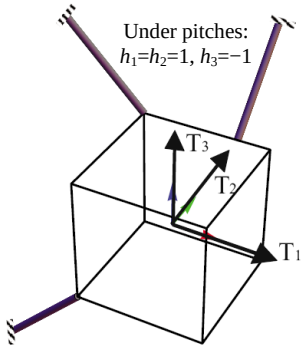

(d) The Mechanism Producing Screw Motion Obtained by the STBA (Courtesy of H.J., Su, University of Maryland)

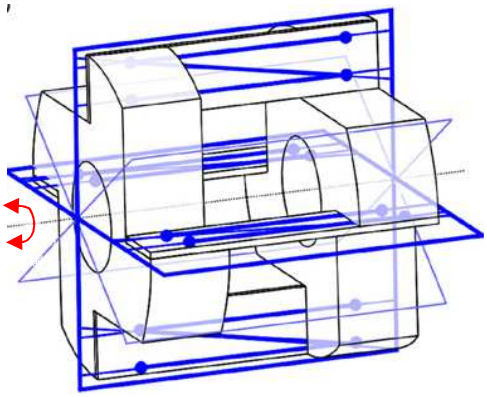

(e) Rotational Joint Obtained by the FCTA (Courtesy of J.B., Hopkins, MIT)

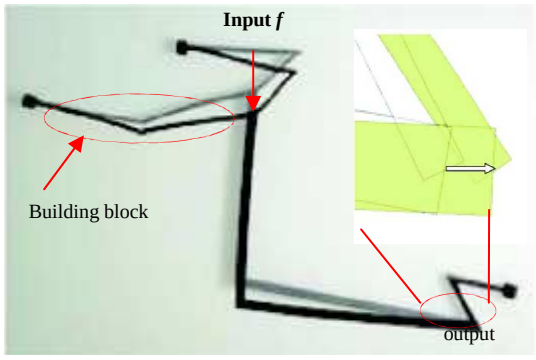

(f) Specified Mechanism Obtained by the Building Block Approach (Courtesy of C., Kim, Bucknell University)

Figure 1.3 Designs produced by different approaches

The CSOA is to re-consider the design problem as an optimal material distribution problem so that the resulting continuum structure can fulfil the requirements of a mechanism [1.37]. The CSOA-based design of a compliant mechanism involves three aspects: (a) topology, i.e. the connectivity of material, (b) size, i.e. the cross-sectional area of each segment, and (c) geometry, i.e. the orientations of the connecting segments

and locations of the junctions [1.8]. However, the CSOA generates mechanisms with the point flexure, and the resulting compliant mechanisms involve many parameters, which are also highly sensitive to manufacture error.

The CBDA uses the fundamental precondition that the motion of a rigid-body is determined by the position and orientation of the constraints, which is well-suited for the conceptual design of compliant mechanisms [1.38, 1.42]. This approach has obtained good outcome in designing precision instruments [1.6, 1.40, 1.41].

Different from the CBDA, the STBA uses the mathematical expressions – screw theory to represent the CBDA and synthesize the constraints under given motion requirement based on reciprocity principle, while the FCTA employs the geometric figures to visualize the CBDA. The STBA and FCTA can also be used to synthesize the mechanisms having screw motion (also helical motion) that cannot be synthesized using the CBDA.

The building block synthesis approach is the method of capturing kinematic behavior using compliance ellipsoids, the mathematical model of which facilitates the characterization of the building blocks, transformation of problem specifications, decomposition into sub-problems, and the ability to search for alternate solutions [1.46]. This approach is also intuitive and provides key insight into how individual building blocks contribute to the overall function [1.46]. However, this approach is currently focusing on dealing with low order and linear problems.

In addtion, one can also obtain compliant mechanisms with good performance characteristics such as kinematic-decoupling[2] and reduced primary stiffness (or double motion stage), respectively, by symmetrical and serial arranging two compliant modules. The kinematic-decoupling is the necessary condition of producing the kinematostatic decoupling[3]. However, the realization of kinematostatic-decoupling for a CPM is not intuitive [1.48] since kinematic-decoupling does not sufficiently lead to kinematostatic-decoupling.

The type synthesis of CPMs is to synthesize the constraint configuration under given design objectives. It is an inverse process of analysis for the degree (s) of freedom (DOF) or degree (s) of constraint (DOC), and is more difficult. As an example, we demonstrate how to use the CBDA to analyse the DOF of a spatial compliant

[2] Kinematic decoupling can be classified into two types: complete decoupling and partial decoupling [1.106–1.108]. This thesis only concerns the complete kinematic decoupling, which refers to that each independent output motion is controlled by only one input motion.

[3] Kinematostatic decoupling means that one primary output translational displacement is only affected by the actuation force along the same direction, which describes the relationship between the input force and output motion. This decoupling is also called the output-decoupling/minimal cross-axis coupling in CPMs. Kinematostatic coupling may lead to complicated motion control.

mechanism composed of multiple beams (wires) following the procedure below.

1) Identify the independent ideal constraints, and draw a DOC line going through the central axis of each beam. Here, a beam is defined as an ideal constraint.

In the case of the spatial non-tilted three-beam module shown in Figure 1.4, which has been proposed before [1.3, 1.5, 1.105], each beam is an ideal constraint that allows five DOF other than the axial motion. Therefore there are three independent constraints in this module, i.e. three independent parallel DOC lines.

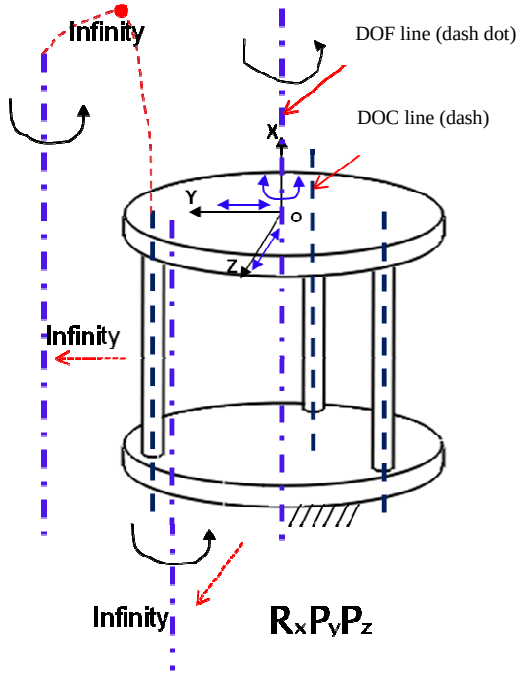

Figure 1.4 A spatial compliant mechanism

2) Calculate the number of the DOF using the equation:

$$N_F=6-N_C$$

where N_F is the number of DOF, and N_C is the number of DOC of independent ideal constraints.

In the case of Figure 1.4, there are three DOF lines, which will be determined in the next step.

3) Determine the orientation and position of each DOF line by making each DOF line intersect all DOC lines and produce independent motion.

In Figure 1.4, each DOF line is parallel to all DOC lines to make each F intersect three DOC lines at the infinity, and therefore one DOF line goes through the symmetrical centre of the spatial compliant mechanism, and the other two DOF lines are at the infinity. Moreover, one infinite DOF line is in the XZ-plane, and another infinite DOF line is in the XY-plane.

4) Determine the DOF of the spatial compliant mechanism by rotating the motion stage of the spatial compliant mechanism about each DOF line.

In the case of Figure 1.4, the DOF line passing through the symmetrical centre of the spatial compliant mechanism produces a pure rotational displacement, and the two DOF lines at the infinity produce two independent translational displacements.

The DOF for the other multi-beam modules can be found in Figures 3–5 in [1.109] and/or Figure 2.21 in [1.105]. In addition, a blade/sheet/leaf flexure module can also be replaced equivalently with three ideal beam constraints. Therefore, we can obtain that a blade/sheet/leaf is able to achieve two rotational displacements and one translational displacement (see Figure 2.22 in [1.105] for details) using the CBDA.

1.3 Nonlinear Analysis of a Basic Cantilever Beam

Force-displacement relationships of a basic cantilever beam are the foundation of design and/or analysis of compliant mechanisms. In order to obtain the accurate mathematical models for compliant mechanisms, traditional linear analysis has a limited application for compliant mechanisms and only provides an initial estimation for displacements as a reference for more accurate nonlinear analysis.

Non-linearities in force-displacement characteristics of a basic cantilever beam (*Euler-Bernoulli beam*) have three sources [1.5]: material non-linearity (Figure 1.5a), geometric non-linearity (Figure 1.5b) and non-linearity of load-equilibrium equations under small deflections. It is noted that the material non-linearity is ignored throughout this thesis in order to make the deformed beams be able to come back to the original undeformed configuration.

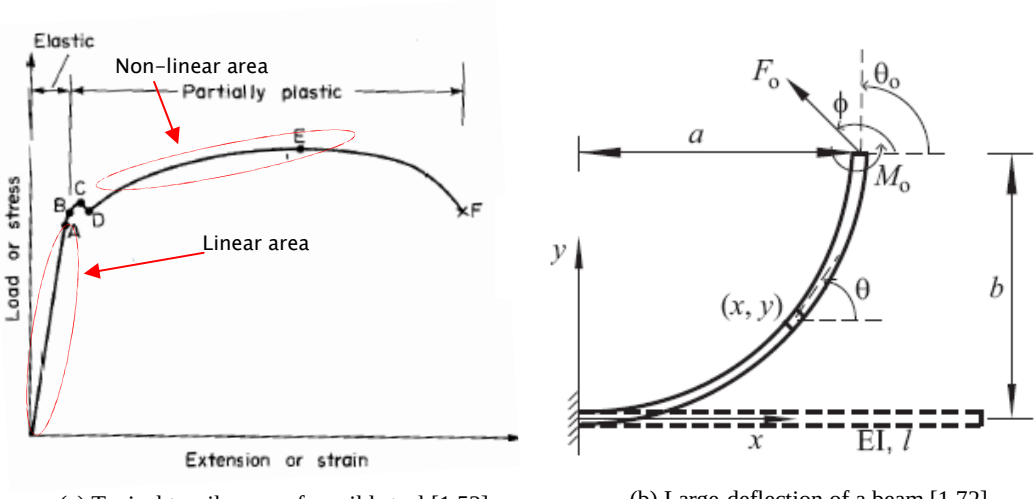

(a) Typical tensile curve for mild steel [1.52]

(b) Large-deflection of a beam [1.72]

Figure 1.5 Illustration for two non-linearities

Currently, most researchers mainly focus on the planar deformation analysis for a basic beam as follows.

To capture the non-linearity of force-displacement equations under small deflections, the load-equilibrium conditions should be applied in the deformed configuration of compliant mechanisms (see *Appendix A* for details) [1.5, 1.49, 1.50], which is different from the configuration before deformation as used in linear load-equilibrium conditions. There are two main methods of solving force-displacement equations: a) differential equation based methods [1.5, 1.51], and b) energy methods, such as Castigliano's theorem [1.52, 1.53] and virtual work principle [1.4, 1.54]. Awtar [1.5] has derived the nonlinear and analytical force-displacement equations of a basic cantilever beam in matrix forms under the small deflection assumption that the transverse displacement is less than 0.1 times of the beam length. These nonlinear equations can be directly used to define the buckling conditions and capture the effects of load-stiffening and elastokinematic nonlinearities, both resulting from axial forces in the beams [1.5, 1.55]. Zelenika *et al* [1.50] also proposed the nonlinear equations of a leaf spring in the cross-spring pivot in the deformed configuration. Nevertheless, these equations are not general due to the limitation of derivation, and the complication of solution using numerical method. Awtar *et al* [1.51] then analysed the characteristics of a double parallelogram flexure module and proposed accurate approximations in simple forms. They further studied the elastic averaging effect in multi-beam parallelogram flexure mechanisms [1.56]. This body of their work revealed that any difference in the axial forces acting on the beams will cause an unequal transverse stiffness change in the beams, and result in rotational yaw.

In addition to considering the non-linearity from force-displacement equations, geometric non-linearity refers to the large deflection of a beam. Therefore, we cannot use the small deflection hypothesis while analysing the beam with large deflection. Due to the complexity, many approaches have been proposed to figure out this open issue. In this subsequent section we will focus on the review of the literatures on large deflection analysis of basic beams. Some selected representative methods for large deflection analysis of a beam are shown in Table 1.3.

In numerical solution obtained using integration, Howell *et al* [1.57] provided an elliptic integral solution, and Saxena *et al* [1.58] solved these equations with numerical integration using Gauss-Chebyshev quadrature formulate. Genetic algorithms for large deflection analysis of beams were also employed in [1.59]. In numerical differential solution, Banerjee *et al* [1.61] proposed the non-linear shooting method where the

boundary value problem is converted to an initial value problem. In other novel numerical methods, Morsch *et al* proposed a direct nonlinear solution [1.62], and Banerjee *et al* also presented an adomian decomposition method [1.61].

Since linear problems are much easier to be solved than nonlinear ones, many linearization solutions have been presented. A pseudo linear equivalent system has been developed by Fertis [1.63] as an attempt to solve for the large-deflected shape of a cantilever beam using a linear approach. Other linearization techniques include the quasilinearization developed by Bellman *et al* [1.64] and generalized quasilinearization by Lakshmikantham *et al* [1.65]. The global coordinate model with an incremental linearization approach was presented to turn the nonlinear problem into a sequence of linear problems in [1.67], which does not require initial guesses to assure convergence in comparison with the numerical approaches.

In the pseudo-rigid-body-model (PRBM), Howell *et al* [1.68] proposed a PRBM 1R model by introducing a linear spring to approximate tip deflection for initially straight cantilever beams subjected to the combined end force and moment, Saxaena and Kramer [1.58] further modified the PRBM 1R model. Saggere and Kota [1.71] proposed a finite element model that evenly decomposes a flexible beam into n (no less than 3) segments joined by n torsion springs with a stiffness EI/L, which is completely load independent and can accommodate a wide range of loads, but approximation accuracy of this model is determined by the number of segments. A load independent pseudo-rigid-body 3R model was further proposed by Su *et al* [1.72] for determining large deflection of beams, of which good accuracy was verified. However, these PRBMs cannot be used to deal with arbitrary loading cases since each loading case demands different characteristic parameters.

Approach family	*Analysis tool*
Numerical approach	Numerical solution solved with integration [1.57-1.60]
	Numerical differential solution [1.61]
	Other novel solutions [1.62, 1.61]
Linearization approach	Linearization solution [1.63-1.67]
Parametric approximation approach	Pseudo-rigid-body-model [1.68-1.72]
Finite element analysis approach	FEA [1.73-1.77]
Experimental approach	Experiment [1.78]

Table 1.3 Classified solutions for large deflection analysis of a beam

In addition, the spatial deformation analysis for a beam can be found in Refs. [1.103, 1.104]. Ref. [1.103] derives the nonlinear analytical constraint model for the three-dimensional symmetrical beams under small deformation assumption, and Ref. [1.104] deals with the spatial-beam large-deflection numerical integration and PRBM for the axisymmetric beams.

Because the beams used in CPMs for high-precision motion stages usually work within small deformation for most applications, the geometry non-linearity will be neglected in this thesis.

1.4 Dynamic Analysis

Dynamic analysis is a foundation of the robot control, structure design and actuator selection. The dynamic analysis of compliant mechanisms includes two aspects: mechanism dynamics and structure dynamics [1.79]. The former aims to achieve the control of compliant mechanisms, and the latter aims to improve the structure design of compliant mechanisms to eliminate the effect of vibration. Therefore, dynamic analysis of the compliant mechanisms is more difficult and complicated than that of the rigid-body mechanisms. Therefore the dynamic analysis of compliant mechanism has received more attention over the past decade [1.80-1.83].

In mechanism dynamics of compliant mechanisms, the dynamics modelling is based on the PRBM [1.80]. Most popular methods to analyse the dynamics of compliant mechanisms such as the Newton-Euler method and the Lagrangian method [1.80, 1.82, 1.84] (energy-based method) are well-known. Compared with the Lagrangian method, the Newton-Euler method needs less calculation and its physical meaning is definite. However, it is difficult to obtain the standard dynamic models. The mechanism dynamics of compliant mechanisms focus on determining the dynamic behavior of compliant mechanisms like velocity and acceleration [1.83].

In structure dynamics of compliant mechanisms, due to the low speed characteristic of most compliant mechanisms, the dynamic model can be simplified, which is a large feature of compliant mechanisms. The structure dynamics of compliant mechanisms focuses on determining the natural characteristic such as the system natural frequency and vibration mode, which is a foundation of transient dynamic analysis and spectrum analysis. The compliant mechanisms can be thought of as structures made up of elastic systems and rigid bodies. The natural characteristics of compliant mechanisms can be obtained by the well-known dynamic equation ($M\ddot{X} + KX = Q$), FEA and/or experiment

[1.40, 1.79, 1.81].

This thesis only deals with the structure dynamics, i.e. considers or calculates the modal frequency for the specified CPMs wherever appropriate, especially the first natural modal frequency.

In practice, the larger the first natural frequency, the better the dynamic performance is. However, if the physical first natural frequency is relatively low, a high-order controller can be used to achieve a high bandwidth greater than this first natural frequency [1.87].

1.5 Objective and Outline of the Thesis

There is an increasing need for high-precision (nanopositioning) motion stages that produce large range of motion (1~10mm) over multi-axes (e.g. XY or XYZ) in a compact (desktop-size) package [1.87]. Such applications, as detailed in [1.87], exist in the scanning probe nanolithography [1.88, 1.89], scanning probe microscopy and metrology [1.90-1.94], memory storage [1.96], hard drive fabrication [1.96], semiconductor fabrication and wafer inspection [1.97], semiconductor packaging [1.98], and imaging for stem cell research [1.86].

Some large-range and high-precision motion stages [1.99-1.102] have been proposed according to magnetic-levitation/aerostatic strategy. However, due to the attractive merits of CPMs as mentioned earlier, *large-range translational CPMs* for high-precision motion stages are selected as the research object for this thesis. It is noted that we limit ourselves to consider a) the fully compliant mechanisms, the motion of which results from the deformation of the compliant members rather than partially compliant mechanisms throughout this thesis, and b) the fully parallel manipulators rather than serial or hybrid ones.

In addition, the existing multi-DOF translational CPMs, using *planar* compliant modules[4] (most lumped-compliance), cannot well fulfil the requirements of the desired performance characteristics mentioned previously. For example, they produce small range of motion only capable of several hundred micros [1.85], involve many geometrical parameters (increase manufacturing cost), have bulky configurations, and/or result in relatively large kinematostatic-coupling (detailed shortcomings for the

[4] Planar compliant joints/modules refer to a class of modules, the size of which in at least one dimension is much smaller than that in the other dimension(s). They can be learnt from Refs. [1.3] and [1.110]. The contrary to a planar compliant joint/module is the spatial compliant joint/module that has compatible size in three dimensions. It should be pointed out that these joints/modules capable of producing only planar motion are called planar motion joints/ modules, and those capable of producing spatial motion are called spatial motion joints/modules.

existing CPMs will be discussed in the next several chapters).

To deal with the above open issues, the objectives of the thesis are:

1) To identify existing or new (especially *spatial*) compliant parallel modules with distributed-compliance, which may be used as building blocks of translational CPMs, and to create nonlinear and analytical model to analyse the load-displacement relationships of spatial modules.

2) To propose a new design methodology for translational CPMs.

3) To propose novel translational CPMs (from 1-DOF up to 3-DOF translational CPMs) with desired performance characteristics, especially *large range of motion*, for high-precision motion stages using the proposed approach and the identified compliant building blocks.

4) To develop kinematostatic modelling of the proposed translational CPMs to enable quick analysis and rapid design synthesis.

The thesis is outlined as follows.

In Chapter 1, the research objectives of this thesis: large-range translational CPMs are firstly introduced, and a general research framework is then provided. Chapter 2 focuses on proposing and analysing compliant parallel modules that can be used as building blocks of large-range translational CPMs. Using the proposed and/or existing compliant parallel modules in Chapter 2, large-range translational CPMs will be proposed and modelled in Chapters 3, 4, and 5. Finally, conclusions are drawn.

Chapter 1: *Introduction*. Firstly, this chapter briefly introduces the research background on CPMs, and then carries out a literature review on design methodology, nonlinear analysis, and dynamics analysis. The objectives and the organization of the thesis are finally stated.

Chapter 2: *Spatial Compliant Parallel Modules: Multi-Beam Modules and Their Nonlinear Analysis*. Firstly, a spatial non-tilted three-beam module is proposed and a nonlinear and analytical model for the spatial three-beam module is obtained using three nonlinear methods: an approximate analytical method, an improved approximate analytical method and a numerical method. The nonlinear model addresses the non-linearity of load-equilibrium equations, applied in the deformed configuration, under small deflection and plane cross-section assumption. The nonlinear solutions, linear solutions and large-deflection FEA solutions are further analysed and compared. FEA verifies that the accuracy of the proposed nonlinear-analytical model is acceptable.

Moreover, a class of spatial multi-beam modules with four or more beams is proposed, and their general nonlinear load-displacement equations are obtained based on the approximate load-displacement equations of the spatial three-beam module. The proposed spatial multi-beam modules and their nonlinear models have potential applications in the CPM design. Especially, the spatial multi-beam modules can be regarded as building blocks of novel CPMs. Finally, other compliant parallel modules with distributed compliance to be used as the building blocks of translational CPMs are listed.

Chapter 3: *Design and Modelling of 1-DOF Translational CPMs: Novel Compliant Parallel Grippers*. A novel auto-adaptive compliant parallel gripper (CPG) for 1-D large-range translation is proposed using a cymbal-type amplifier and two parallelogram modules at first. Then the displacement amplification ratio and the force-displacement equations for the auto-adaptive CPG are derived and compared with FEA. Further, the varied configurations are presented, analysed and discussed. On the one hand, the auto-adaptive grasping function of the proposed CPG is unique in comparison with the existing CPGs driven by only one linear actuator. On the other hand, compared with the closest prior art, the proposed auto-adaptive CPG can achieve good characteristics such as large-stroke, no stress-concentration, well-constrained parasitic rotation of the jaw, actuator isolation, a simple and compact configuration.

Chapter 4: *Design and Modelling of XY CPMs for High-Precision Motion Stages*. A novel planar XY CPM and a spatial double four-beam module both with distributed compliance are first proposed for large range of motion. Then, a large-range stiffness-enhanced XY CPM is proposed by combining the above planar XY CPM and the spatial double four-beam module in an appropriate parallel arrangement. Normalized analytical models for the stiffness-enhanced XY CPM are then presented. As a case study, a stiffness-enhanced XY CPM with large range of motion of 10mm×10mm is presented in detail, covering the geometrical parameter determination, performance characteristic analysis, buckling checking, and actuation force checking. The analytical models are compared with the FEA models. Finally, the dynamic issues, manufacture and out-of-plane stiffness are discussed. It is shown that, in the example case, the stiffness-enhanced XY CPM has the following merits: large range of motion up to 10mm×10mm, well-constrained parasitic motion, approximate cross-axis decoupling, approximate actuation isolation, acceptable lost motion, enhanced out-of-plane stiffness and no friction with ground.

Chapter 5: *Design and Modelling of XYZ CPMs for High-Precision Motion Stages*. Firstly, a design methodology for translational CPMs is proposed. Secondly, applying the presented design methodology, type synthesis is conducted to generate several large-range XYZ CPMs using different modules in a variety of ways: (1) using identical double parallelogram flexure modules, (2) using inverted planar XY CPMs, (3) using identical spatial modules, (4) using embedded spatial modules, (5) using five legs composed of spatial modules, (6) using planar double two-beam modules. Thirdly, the improved modular XYZ CPM using identical spatial double four-beam modules is selected for normalized-modelling. Fourthly, as a case study, an improved modular XYZ CPM with large range of motion of 10mm×10mm×10mm is presented in detail, covering the geometrical parameter determination, performance characteristic analysis, buckling checking, actuation force checking, and manufacture. Fifthly, the first natural frequency for the improved modular XYZ CPM is calculated. Finally, the analytical models are compared with the FEA models. It is shown that, in the example case, the improved modular XYZ CPM has the following unique merits compared with existing designs: (1) large range of motion up to 10mm×10mm×10mm, and (2) reduced number of design parameters by using identical spatial multi-beam modules.

Chapter 6: *Conclusions.* General conclusions and major contributions throughout the thesis are summarized in this chapter. Some future works are identified for further investigation.

1.6 References

[1.1] McCarthy, J.M., 2011, "21st Century Kinematics: Synthesis, Compliance, and Tensegrity", *Journal of Mechanisms and Robotics*, Vol. **3**(2): 020201.

[1.2] Kong, X., and Gosselin, C.M., 2007, *Type Synthesis of Parallel Mechanisms*, Springer, Berlin.

[1.3] Lobontiu, N., 2002, *Compliant Mechanisms: Design of Flexure Hinges*, CRC PRESS, Boca Raton.

[1.4] Howell, L.L., 2001, *Compliant Mechanisms*, Wiley, New York.

[1.5] Awtar, S., 2004, "*Analysis and Synthesis of Planar Kinematic XY Mechanisms*", Sc.D. thesis, Massachusetts Institute of Technology, Cambridge, MA.

[1.6] Awtar, S., Slocum, A. H., 2007, "Constraint-Based Design of Parallel Kinematic XY Flexure Mechanisms", *Journal of Mechanical Design*, Vol. **129**(8): 816–830.

[1.7] Dong, W., Sun, L. N., Du, Z. J., 2007, "Design of a Precision Compliant Parallel

Positioner Driven by Dual Piezoelectric Actuators", *Sensors and Actuators A*, Vol. **135**(1): 250–256.

[1.8] Kota, S., Lu, K. J., Kreiner, Z., et al, 2005, "Design and Application of Compliant Mechanisms for Surgical Tools", *Journal of Biomechanical Engineering*, Vol. **127**(6): 981–989.

[1.9] Qiu, J., Sihler, J., Li, J., et al, 2001, "An Instrument to Measure the Stiffness of MEMS Mechanisms", *Proc. 10th International Conference on Precision Engineering*, July, 2001, Yokohama, Japan, pp. 599–603.

[1.10] Hansen, B. J., Carron, C. J., Jensen, B. D., et al, 2007, "Plastic Latching Accelerometer Based on Bistable Compliant Mechanisms", *Smart Material Structure*, Vol. **16**(5): 1967–1972.

[1.11] Gao, Z., and Zhang, D., 2010, "Design, Analysis and Fabrication of a Multidimensional Acceleration Sensor Based on Fully Decoupled Compliant Parallel Mechanism", *Sensors and Actuators A: Physical*, Vol. **163**(1): 418–427.

[1.12] Krishnan, G., and Ananthasuresh, G. K., 2008, "Evaluation and Design of Displacement-Amplifying Compliant Mechanisms for Sensor Applications", *Journal of Mechanical Design*, Vol. **130**(10): 102304.

[1.13] Xu, Q., and Li, Y., 2010, "Analytical Modeling, Optimization and Testing of a Compound Bridge-Type Compliant Displacement Amplifier", *Mechanism and Machine Theory*, Vol. **46**(2): 183–200.

[1.14] Ouyang, P. R., Zhang, W. J., Gupta M. M., 2008, "A New Compliant Mechanical Amplifier Based on a Symmetric Five-Bar Topology", *Journal of Mechanical Design*, Vol. **130**(10): 104501.

[1.15] Qiu, J., 2003, "*An Electrothermally-Actuated Bistable MEMS Relay for Power Applications*", Sc.D. thesis, Massachusetts Institute of Technology, Cambridge, MA.

[1.16] Li, J., 2004, "*Electrostatic Zipping Actuators and Their Application to MEMS*", Sc.D. thesis, Massachusetts Institute of Technology, Cambridge, MA.

[1.17] Li, J., Sedaghati, R., and et al, 2005, "Design and Development of a New Piezoelectric Linear Inchworm Actuator", *Mechatronics*, Vol. **15**(6): 651–681.

[1.18] Carrozza, M. C., Eisinberg, A., et al, 2000, "Towards a Force-Controlled Microgripper for Assembling Biomedical Microdevices", *Journal of Micromechanics and Microengineering*, Vol. **10**(2): 271–276.

[1.19] Millet, O., Bernardoni, P., 2004, "Electrostatic Actuated Micro Gripper Using an Amplification Mechanism", *Sensors and Actuators A*, Vol. **114**(2–3): 371–378.

[1.20] Nashrul, M., Zubir, M., and et al, 2009, "A New Design of Piezoelectric Driven Compliant-Based Microgripper for Micromanipulation", *Mechanism and Machine Theory*, Vol. **44**(7): 2248–2264.

[1.21] Mahmoodi, S. N., Jalili, N., 2008, "Coupled Flexural-Torsional Nonlinear Vibrations of Piezoelectrically Actuated Microcantilevers with Application to Friction Force Microscopy", *Journal of Vibration and Acoustics*, Vol. **130**(6): 061003.

[1.22] Kim, D., Lee, D. Y., and Gweon, D. G., 2007, "A New Nano-Accuracy AFM System for Minimizing Abbe Errors and the Evaluation of Its Measuring Uncertainty", *Ultramicroscopy*, Vol. **107**(4–5): 322–328.

[1.23] Lu, K. J. and Kota, S., 2003, "Design of Compliant Mechanisms for Morphing Structural Shapes", *Journal of Intelligent Material Systems and Structures*, Vol. **14**(6): 379–391.

[1.24] http://compliantmechanisms.byu.edu/image-gallery/grippers (last accessed on 05/09/2011)

[1.25] Li, Y., and Xu, Q., 2009, "Design and Analysis of a Totally Decoupled Flexure-Based XY Parallel Micromanipulator", *IEEE Transactions on Robotics*, Vol. **25**(3): 645–657.

[1.26] Wang, H., and Zhang, X., 2008, "Input Coupling Analysis and Optimal Design of a 3-DOF Compliant Micro-Positioning Stage", *Mechanism and Machine Theory*, Vol. **43**(4): 400–410.

[1.27] Chao, D. H., Zong, G. H., Liu, R., 2005, "Design of a 6-DOF Compliant Manipulator Based on Serial-Parallel Architecture", *Proceedings of the 2005 IEEE/ASME International Conference on Advanced Intelligent Mechatronics*, July 24–28, 2005, Monterey, California, USA, pp. 765–770.

[1.28] Wang, Y., and Gosselin, C. M., 2004, "On the Design of a 3-PRRR Spatial Parallel Compliant Mechanism", *Proceeding of the ASME 28th Biennial Mechanisms and Robotics Conference*, Sep. 28–Oct. 2, 2004, Salt Lake City, Utah, USA.

[1.29] Pham, H.-H., Yeh, H. C., Chen, I.-M., 2006, "Micromanipulation System Design Based on Selective Actuation Mechanisms", *The International Journal of Robotics Research*, Vol. **25**(2): 171–186.

[1.30] Li, Y., Xu, Q., 2011, "A Totally Decoupled Piezo-Driven XYZ Flexure parallel Micropositioning Stage for Micro/Nanomanipulation", *IEEE Transactions on Automation Science and Engineering*, Vol. **8**(2): 265–279.

[1.31] Li, Y., Xu, Q., 2009, "Design and Optimization of an XYZ Parallel Micromanipulator with Flexure Hinges", *Journal of Intelligent and Robotic Systems*, Vol. **55**(4–5): 377–402.

[1.32] Polit, S., and Dong, J., 2009, "Design of High-Bandwidth High-Precision Flexure-Based Nanopositioning Modules", *Journal of Manufacturing Systems*, Vol. **28**(2–3): 71–77.

[1.33] Yue, Y., Gao, F., Zhao, X., and Ge, Q., 2010, "Relationship among Input-Force, Payload, Stiffness and Displacement of a 3-DOF Perpendicular Parallel Micro-manipulator", *Mechanism and Machine Theory*, Vol. **45**(5): 756–771.

[1.34] Zhou, H., and Ting, K. L., 2009, "Geometric Modeling Synthesis of Spatial Multimaterial Compliant Mechanisms and Structures Using Three-Dimensional Multilayer Wide Curves", *Journal of Mechanical Design*, Vol. **131**(1): 011005.

[1.35] Zhou, H., and Ting, K. L., 2009, "Geometric Modeling and Optimization of Multimaterial Compliant Mechanisms Using Multilayer Wide Curves", *Journal of Mechanical Design*, Vol. **130**(6): 062303.

[1.36] Lu, K.-J., and Kota, S., 2006, "Topology and Dimensional Synthesis of Compliant Mechanisms Using Discrete Optimization", *Journal of Mechanical Design*, Vol. **128**(9): 1080–1090.

[1.37] Wang, M. Y., 2009, "An Analysis of the Compliant Mechanical Models", *ASME/IFToMM International Conference on Reconfigurable Mechanisms and Robots (ReMAR 2009)*, June 22–24, 2009, King's College of London, London, United Kingdom.

[1.38] Maxwell, J. C., 1890, *General Considerations Concerning Scientific Apparatus*, Dover, New York.

[1.39] Blanding, D. K., 1999, *Exact Constraint: Machine Design Using Kinematic Principles*, ASME, New York.

[1.40] Choi, K. B. and Kim D. H., 2006, "Monolithic Parallel Linear Compliant Mechanism for Two Axes Ultra Precision Linear Motion", *Review of Scientific Instruments*, Vol. **77**(6): 065106: 1–7.

[1.41] Chen, S.-C., Culpepper, M. L., 2006, "Design of a Six-axis Micro-Scale Nanopositioner–HexFlex", *Precision Engineering*, Vol. **30**(3): 314–324.

[1.42] Su, H.-J., Dorozhkin, D. V., and Vance, J. M., 2009, "A Screw Theory Approach for the Conceptual Design of Flexible Joints for Compliant Mechanisms", *Journal of Mechanisms and Robotics*, Vol. **1**(4): 041009.

[1.43] Su, H., Tari, H., 2011, "On Line Screw Systems and Their Application to Flexure

Synthesis", *Journal of Mechanisms and Robotics*, Vol. **3**(1): 011009.

[1.44] Hopkins, J. B., and Culpepper, M. L., 2010, "Synthesis of Multi-Degree of Freedom, Parallel Flexure System Concepts via Freedom and Constraint Topology (FACT). Part I: Principles", *Precision Engineering*, Vol. **34**(1): 259–270.

[1.45] Hopkins, J. B., and Culpepper, M. L., 2010, "Synthesis of Multi-Degree of Freedom, Parallel Flexure System Concepts via Freedom and Constraint Topology (FACT). Part II: Practice", *Precision Engineering*, Vol. **34**(1): 271–278.

[1.46] Kim, C. J., Moon, Y. M., Kota, S., 2008, "A Building Block Approach to the Conceptual Synthesis of Compliant Mechanisms Utilizing Compliance and Stiffness Ellipsoids", *Journal of Mechanical Design*, Vol. **130**(2): 022308.

[1.47] Kim, C., 2009, "Design Strategies for the Topology Synthesis of Dual Input-Single Output Compliant Mechanisms", *Journal of Mechanisms and Robotics*, Vol. **1**(4): 041002.

[1.48] Quennouelle, C., and Gosselin, C. M., 2008, "Stiffness Matrix of Compliant Parallel Mechanisms", *Proceeding of the 11th International Symposium on Advances in Robot Kinematics (ARK)*, June 22–26, 2008, Batz-sur-Mer, France, pp. 331–340.

[1.49] Timoshenko, S.P., Gere, J.M., 1961, *Theory of Elastic Stability*, 2nd ed. McGraw-Hill, New York.

[1.50] Zelenika, S., Bona, F. De, 2002, "Analytical and Experimental Characterization of High-Precision Flexural Pivots Subjected to Lateral Loads", *Precision Engineering*, Vol. **26**(4): 381–388.

[1.51] Awtar, S. Slocum, A.H., 2007, "Characteristics of Beam-Based Flexure Modules", *Journal of Mechanical Design*, Vol. **129**(6): 624–639.

[1.52] Hearn, E.J., 1983, *Mechanics of Materials*, Robert Maxwell, M. C. Pergamon Press, Oxford.

[1.53] Nicolae, L. S., Jeffrey, L.P., and et al, 2001, "Corner-Filleted Flexure Hinges", *Journal of Mechanical Design*, Vol. **123**(3): 346–352.

[1.54] Shabana, A.A., 2010, *Computational Dynamics*, Third Edition, John Wiley & Sons, West Sussex.

[1.55] Ryu, J., Kim, S.-S. Kim, S.-S. 1997, "A Criterion on Inclusion of Stress Stiffening Effects in Flexible Multibody Dynamic System Simulation", *Computers & Structures*, Vol. **62**(6): 1035–1048.

[1.56] Awtar, S., Sevincer, E., 2010, "Elastic Averaging in Flexure Mechanisms: a

Three-Beam Parallelogram Flexure Case Study", *Journal of Mechanisms and Robotics*, Vol. **2**(4): 041005.

[1.57] Howell, L. L., and Midha A., 1995, "Parametric Deflection Approximations for End-Loaded, Large-Deflection Beams in Compliant Mechanisms", *Journal of Mechanical Design*, Vol. **117**(1): 156–165.

[1.58] Saxena, A., and Kramer, S. N., 1998, "A Simple and Accurate Method for Determining Large Deflections in Compliant Mechanisms Subjected to End Forces and Moments", *Journal of Mechanical Design*, Vol. **120**(3): 392–400.

[1.59] Kumar, R, 2004. "Techniques Based on Genetic Algorithms for Large Deflection Analysis of Beams", Sadhana, Vol. **29**(6): 589–604.

[1.60] Belendez, T., et al, 2002, "Large and Small Deflections of a Cantilever Beam", *European Journal of Physics*, Vol. **23**(3): 371–379.

[1.61] Banerjee, A, et al., 2007. "Large Deflection of Cantilever Beams with Geometric Non-linearity: Analytical and Numerical Approaches", *International Journal of Non-Linear Mechanics*, Vol. **43**(5): 366–376.

[1.62] Morsch, F. M., Tolou, N., Herder, J. L., 2009, "Comparison of Methods for Large Deflection Analysis of a Cantilever Beam under Free End Point Load", *Proceedings of the ASME 2009 International Design Engineering Technical Conferences &Computers and Information in Engineering Conference*, August 30–September 2, 2009, San Diego, California, US.

[1.63] Fertis, D. G., 1998, *Nonlinear Mechanics*, CRC Press.

[1.64] Bellman, R. E., Kalaba, R. E., 1965, *Quasilinearization and Nonlinear Boundary-Value Problems*, American Elsevier Publishers.

[1.65] Lakshmikantham, V., Vatsala, A. S., 1998, *Generalized Quasilinearization for Nonlinear Problems*, Kluwer Academic Publishers.

[1.66] Bellman, R. E., Roth, R., 1983, *Quasilinearization and the Identification Problem*, World Scientific.

[1.67] Lan, C.-C., 2008, "Analysis of Large-Displacement Compliant Mechanisms Using an Incremental Linearization Approach", *Mechanism and Machine Theory*, Vol. **43**(7): 641–658.

[1.68] Howell, L. L., Midha A., and Norton, T. W., 1996, "Evaluation of Equivalent Spring Stiffness for Use in a Pseudo-Rigid-Body Model of Large-Deflection Compliant Mechanisms", *ASME Journal of Mechanical Design*, Vol. **118**(1): 126–131.

[1.69] Lyon, S. M., Howell, L. L., Roach, G. M., 2000, "Modeling Fixed-Fixed Flexible

Segments via the Pseudo-Rigid-Body Model", *Proceedings of the ASME Dynamics and Control Division at the 2000 ASME International Mechanical Engineering Congress and Exposition*, Nov. 5–10, 2000, Orlando, FL, DSC, Vol. **69**(2): 883–990.

[1.70] Saxena, A., 1997, "*A New Pseudo-Rigid-Body Model for Flexible Members in Compliant Mechanisms*", Masters Thesis, University of Toledo, Toledo, OH, USA.

[1.71] Saggere, L. and Kota, S., 2001, "Synthesis of Planar, Compliant Four-Bar Mechanisms for Compliant-Segment Motion Generation", *Journal of Mechanical Design*, Vol. **123**(4): 535– 541.

[1.72] Su, H.-J. , 2009, "A Pseudo-Rigid-Body 3R Model for Determining Large Deflection of Cantilever Beams Subject to Tip Loads", *Journal of Mechanisms and Robotics* , Vol. **1**(2): 021008.

[1.73] Bathe, K.-J., 1996, *Finite Element Procedures*, Prentice-Hall, NJ.

[1.74] Rankin, C. C., Brogan, F. A., 1986, "An Element Independent Corotational Procedure for the Treatment of Large Rotations", *Journal of Pressure Vessel Technology*, Vol. **108**(2): 165–174.

[1.75] Shabana, A. A., 1998, *Dynamics of Multibody Systems*, Wiley, NY.

[1.76] Coda, H. B., Greco, M., 2004, "A Simple FEM Formulation for Large Deflection 2D Frame Analysis Based on Position Description", *Computer Methods in Applied Mechanics and Engineering*, Vol. **193**(10): 3541–3557.

[1.77] ANSYS Inc., 2008, *Manual of ANSYS 11*, ANSYS Inc.

[1.78] Ye, Z., Yeh, K., 1989, "Exact Solution for Finite Deformation Problems of Cantilever Beam with Variable Section under the Action of Arbitrary Transverse Loads", *Acta Mechanica Sinica*, Vol. **5**(2): 152–158.

[1.79] Yu, J. J., Bi, S. S., and Zong. G. H., 2004, "The Dynamic Characteristic-Based Optimal Design of a Fully Compliant Mechanism", *The 11th World Congress in Mechanism and Machine Science* (IFToMM2004), April 1–4, 2004, Tianjin, China, pp. 1416–1421.

[1.80] Yu, Y.-Q., Howell, L. L., et al, 2005, "Dynamic Modeling of Compliant Mechanisms Based on the Pseudo-Rigid-Body Model", *Journal of Mechanical Design*, Vol. **127**(7): 760–725.

[1.81] Wang, W., Yu, Y., 2008, "Dynamic Analysis of Compliant Mechanisms Using the Finite Element Method", *Proceedings of the 2008 IEEE/ASME International Conference on Advanced Intelligent Mechatronics*, July 2–5, 2008, Xi'an, China.

[1.82] Lee, K. M., Arjunan, S., 1991, "A Three-Degrees-of-Freedom Micromotion in-Parallel Actuated Manipulator", *IEEE Transactions on Robotics and Automation*, Vol. **7**(5): 634–641.

[1.83] Rezaei, M., Tayefeh, M., Bahrami, M., 2006, "Dynamic Behavior Analysis of Compliant Micromechanisms", *Journal of Physics: Conference Series*, Vol. **34**: 583–588.

[1.84] Hicks, T. R., and Atherton, P. D., 1997, *The Nanopositioning Book*, Queensgate Instruments Ltd.

[1.85] Devasia, S., Eleftheriou, E. & Moheimani, S. O. R., 2007, "A Survey of Control Issues in Nanopositioning", *IEEE Transactions on Control Systems Technology*, Vol. **15**(5): 802–823.

[1.86] O'Brien, W., 2005, "Long-Range Motion with Nanometer Precision", *Photonics Spectra*, Laurin Publishing Co. Inc., Pittsfield, MA 01202-4949, United States.

[1.87] Awtar, S., and Parmar, G., 2010, "Design and a Large Range XY Nanopostioning System", *Proceedings of the ASME 2010 International Design Engineering Technical Conferences & Computers and Information in Engineering Conference*, August 15 – 18, 2010, Montreal, Quebec, Canada. DETC2010-28185

[1.88] Salaita, K., Wang, Y. H., and Mirkin, C. A., 2007, "Applications of Dip-Pen Nanolithography", *Nature Nanotechnology*, Vol. **2**(3): 145–155.

[1.89] Mirkin, C. A., 2001, "Dip-Pen Nanolithography: Automated Fabrication of Custom Multicomponent, Sub-100-Nanometer Surface Architectures", *MRS Bulletin*, Vol. **26**(7): 535–538.

[1.90] Dai, G., Pohlenz, F., Danzebrink, H.-U., Xu, M., Hasche, K., and Wilkening, G., 2004, "Metrological Large Range Scanning Probe Microscope", *Review of Scientific Instruments*, Vol. **75**(4): 962–969.

[1.91] Hausotte, T., Jaeger, G., Manske, E., Hofmann, N., and Dorozhovets, N., 2005, "Application of a Positioning and Measuring Machine for Metrological Long-Range Scanning Force Microscopy", *Proceedings of SPIE*, San Diego, CA, Vol. **5878**(2), pp. 1–12.

[1.92] Kramar, J. A., 2005, "Nanometre Resolution Metrology with the Molecular Measuring Machine", *Measurement Science & Technology*, Vol. **16**(11): 2121–2128.

[1.93] Sinno, A., Ruaux, P., Chassagne, L., Topcu, S., and Alayli, Y., 2007, "Enlarged Atomic Force Microscopy Scanning Scope: Novel Sample-Holder Device with Millimeter Range", *Review of Scientific Instruments*, Vol. **78**(9):1–7.

[1.94] Weckenmann, A., and Hoffmann, J., 2007, "Long Range 3D Scanning Tunnelling Microscopy", *CIRP Annals - Manufacturing Technology*, Vol. **56**(1): 525–528.

[1.95] Sebastian, A., Pantazi, A., Pozidis, H., and Eleftheriou, E., 2008, "Nanopositioning for Probe-Based Data Storage [Applications of Control]", *IEEE Control Systems Magazine*, Vol. **28**(4): 26–35.

[1.96] Van De Moosdijk, M., Van Den Brink, E., Simon, K., Friz, A., Phillipps, G., Travers, R., and Raaymakers, E., 2002, "Collinearity and Stitching Performance on an ASML Stepper", *Proceedings of SPIE*, Santa Clara, CA, Vol. **4688**(1–2): 858–866.

[1.97] Liu, H., Liu, B., and et al, 2003, "A Motor-Piezo Actuator for Nano-Scale Positioning Based on Dual Servo Loop and Nonlinearity Compensation", *Journal of Micromechanics and Microengineering*, Vol. **13**(2), 295–299.

[1.98] Han, D., and Zhenhua, X., 2006, "Motion Stages for Electronic Packaging Design and Control", *IEEE Robotics & Automation Magazine*, Vol. **13**(4): 51–61.

[1.99] Kim, W.-J., Verma, S., and Shakir, H., 2007, "Design and Precision Construction of Novel Magnetic-Levitation-Based Multi-Axis Nanoscale Positioning Systems", *Precision Engineering*, Vol. **31**(4): 337–350.

[1.100] Holmes, M., Hocken, R., and Trumper, D., 2000, "The Long-Range Scanning Stage: a Novel Platform for Scanned-Probe Microscopy", *Precision Engineering*, Vol. **24**(3): 191–209.

[1.101] Maeda, G. J., Sato, K., Hashizume, H., and Shinshi, T., 2006, "Control of an XY Nano-Positioning Table for a Compact Nano-Machine Tool", *JSME International Journal, Series C (Mechanical Systems, Machine Elements and Manufacturing)*, Vol. **49**(1): 21–27.

[1.102] Dejima, S., Gao, W., Katakura, K., Kiyono, S., and Tomita, Y., 2005, "Dynamic Modeling, Controller Design and Experimental Validation of a Planar Motion Stage for Precision Positioning", *Precision Engineering*, Vol. **29**(3), pp. 263–271.

[1.103] Sen, S., and Awtar, S., 2010, "Nonlinear Constraint Model for Symmetric Three-Dimensitonal Beams", *Proceedings of the ASME 2010 International Design Engineering Technical Conferences &Computers and Information in Engineering Conference*, August 15–18, 2010, Montreal, Quebec, Cananda. DETC2010-28953

[1.104] Ramirez, I.A., and Lusk, C.P., 2011, "Spatial-Beam Large-Deflection Equations and Pseudo-Rigid-Body Model for Axisymmetric Cantilever Beams",

Proceedings of the ASME 2011 International Design Engineering Technical Conferences &Computers and Information in Engineering Conference, August 29–31, 2011, Washington, DC, US. DETC2011-47389

[1.105] Hale L.C., 1999, "*Principles and Techniques for Designing Precision Machines*", PhD thesis, University of California, Livermore, California.

[1.106] Jin, Y., Chen, I-M., and Yang, G., 2009, "Kinematic Design of a Family of 6-DOF Partially Decoupled Parallel Manipulators", *Mechanism and Machine Theory*, Vol. **44**: 912–922.

[1.107] Jin, Q., and Yang, T., 2004, "Synthesis and Analysis of a Group of 3-Degree-of Freedom Partially Decoupled Parallel Manipulators", *Journal of Mechanical Design*, Vol.**126**: 301–306.

[1.108] Kong, X. and Gosselin, C., 2004, "Type synthesis of input-output decoupled parallel manipulators", *Transactions of the Canadian Society for Mechanical Engineering*, Vol. **28**(2A):185–196.

[1.109] Su, H., and Tari, H., 2010, "Realizing Orthogonal Motions with Wire Flexures Connected in Parallel", *Proceedings of the ASME 2010 International Design Engineering Technical Conferences &Computers and Information in Engineering Conference*, August 15–18, 2010, Montreal, Canada. DETC2010-28517

[1.110] Trease, B.P., Moon, Y.-M., and Kota, S., 2005, "Design of Large-Displacement Compliant Joints", *Journal of Mechanical Design*, Vol. **127**(7): 788–798.

Chapter 2 – Spatial Compliant Parallel Modules: Multi-Beam Modules and Their Nonlinear Analysis

A spatial multi-beam module is composed of a motion stage and a base connected using three or more slender beams (wires) [2.1, 2.2]. In addition to being an independent CPM in its own right, e.g. as a vibratory bowl feeder [2.3, 2.4] and a compliant assembly system device [2.5], spatial multi-beam module can also be used as building blocks of spatial CPMs, which will be discussed in Chapters 4 and 5. This offers an alternative to spatial CPMs composed of a number of planar compliant modules with distributed compliance, which have been proposed elsewhere [2.6–2.8]. Dai *et al* [2.3] analysed the compliance of a three-legged rigidly connected compliant platform using screw theory based on the *linear* compliance matrix for each leg. Ding *et al* [2.4] have carried out a dynamic analysis of a vibratory bowl feeder with three spatial compliant legs based on a characteristic equation. Recently, a spatial tilted three-beam compliant module, producing three pure rotational displacements, is studied to define layouts of actuators using the screw theory [2.9]. However, there has been no analysis of a spatial module with three or more uniform non-tilted slender beams.

This chapter mainly investigates the nonlinear modelling of spatial compliant parallel modules with multiple identical and uniform *Euler-Bernoulli* beams under small deflection and plane cross-section assumption. The nonlinear model addresses the non-linearity of load-equilibrium equations applied in the deformed configuration. By nonlinear analysis, we can identify which spatial module is better suitable for a building block of new spatial CPMs. Accordingly, the research focuses on spatial multi-beam modules with uniform non-tilted beams (Figure 2.1). The reasons for this choice are that the uniform beam is one of the most common flexure elements and the non-tilted arrangement is simple enough to allow for closed-form analysis in terms of constraint-based design. In addition, we will briefly discuss other compliant parallel modules: compliant prismatic joints for applications in new translational CPMs.

This chapter is organized as follows. In Section 2.1, nonlinear load-displacement equations of the tip of a spatial beam, conditions of geometry compatibility and load-equilibrium conditions of the spatial three-beam module are derived. Section 2.2 proposes three methods to solve the nonlinear load-displacement equations for the spatial three-beam module, and also discusses the validity, application, accuracy and advantages/limitations of each method, the error analysis and linear method. In Section

2.3, FEA is conducted to verify the proposed approximate analytical method for the spatial three-beam module. In Section 2.4, a class of spatial multi-beam modules is proposed, and the general load-displacement equations for these modules are summarized. Other compliant parallel modules with distributed compliance to be used as building blocks of new translational CPMs are discussed briefly in Section 2.5. Finally, the summary is performed.

2.1 Spatial Three-Beam Module and Its Nonlinear Analysis

In order to simplify equations and make translational displacements and rotational angles (or forces and moments) comparable, all translational displacements and length parameters are normalized (divided) by the beam length L, forces by EI/L^2, bending moments by EI/L, and torques by GI_p/L (The specific discussions for the normalization strategy can be found in *Appendix C*). Here, E denotes the Young's modulus, I denotes the second moment of the area of a cross-section, G represents the shear modulus, and I_p denotes the polar second moment of the area of the cross-section. In this chapter, non-dimensional quantities are represented by the corresponding lower-case letters, and all beams have round cross-sections with the same diameter D_0 unless indicated otherwise.

A three-beam module, which is the simplest form of the multi-beam modules, is shown in Figure 2.1. It is composed of a base, three identical and uniform beams and a motion stage. The base and the motion stage, which are both assumed to be rigid, are connected by the three compliant beams. Here, the three beams are uniformly spaced around a circle of radius r_3 on the base and on the motion stage, and all external loads, p (axial force), f_y, f_z (transverse forces), m_x (torque), m_y and m_z (bending moments), are acting at the centre, O′, of the motion stage and cause the motion stage to move by deformation of the three beams. p, f_y and f_z are the forces along the X-, Y- and Z-axes, respectively; m_x, m_y and m_z are the moments about the X-, Y- and Z-axes, respectively. For the purpose of simplification, the gravity of the motion stage (including the payloads on it) is integrated into the axial force, and the weights of the compliant beams, which are very small, are neglected.

In the initial configuration, a mobile rigid-body coordinate system O′-X′Y′Z′ and a global fixed coordinate system O-XYZ are coincident and both origins are at the centre (reference point), O′, of the motion stage (Figure 2.2). All translational displacements of the new origin, O′, are denoted by x_s (axial displacement) and y_s and z_s (transverse

displacements) along the X-, Y- and Z-axes, respectively; All rotational displacements (angles) of the motion stage are denoted by θ_{sx} (torsional angle), θ_{sy} and θ_{sz} (bending angles) about the X-, Y- and Z-axes, respectively. The objective is to investigate the translational displacements, x_s, y_s and z_s, and the rotational displacements, θ_{sx}, θ_{sy} and θ_{sz}, of the motion stage as a function of the applied loads: p, f_y, f_z, m_x, m_y and m_z.

It should be pointed out that all loads and displacements shown in Figures 2.1 and 2.2 are represented by the nondimensional quantities with respect to the global fixed coordinate system O-XYZ.

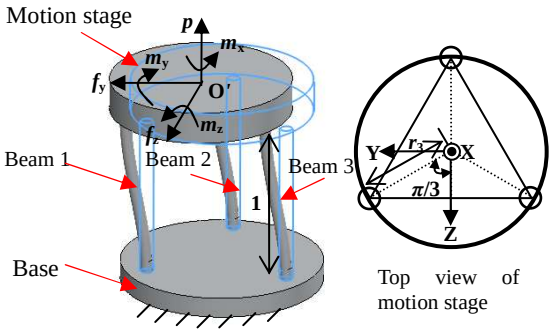

Figure 2.1 A spatial three-beam module

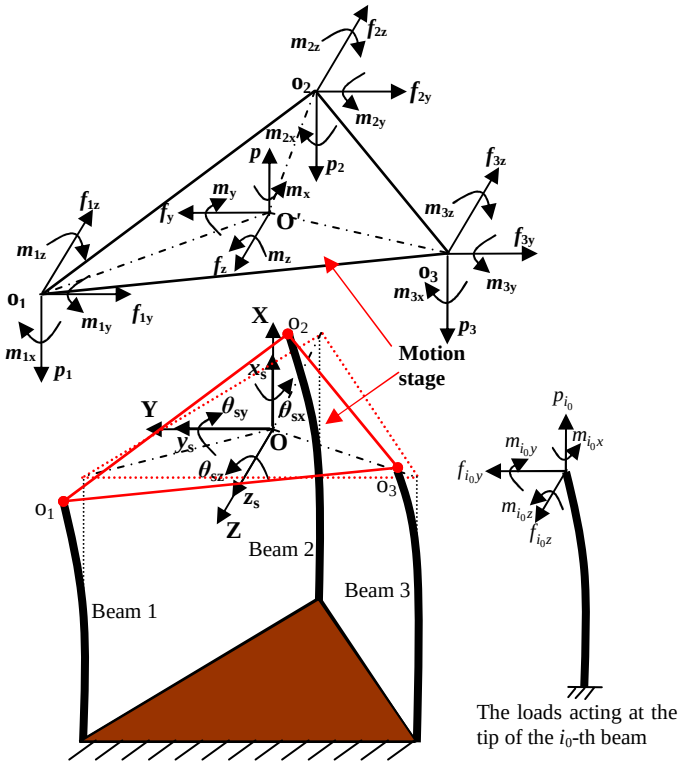

Figure 2.2 Free body diagram of the spatial three-beam module

In terms of the constraint-based design [2.10, 2.16], the three out-of-plane motions, x_s,

θ_{sy} and θ_{sz}, of the spatial three-beam module are suppressed, and its motion stage is constrained to move within the YZ plane, with y_s, z_s and θ_{sx} as the DOF. If the pitch radius r_3 of the beams (hence the motion stage) becomes relatively large, the rotation of the motion stage about the X-axis will be constrained as well.

2.1.1 Nonlinear load-displacement equations of a spatial cantilever beam

The centre of the free-end of the cantilever beam is used as the point (tip) at which the loads and translational displacements are defined. Here, the loads, p_{i_0}, f_{i_0y}, f_{i_0z}, m_{i_0x}, m_{i_0y}, m_{i_0z} (i_0=1, 2, 3), denote internal loads acting at the tip, o_{i_0}, of the i_0-th beam, and are the corresponding reactions at the point i_0 on the motion stage as shown in Figure 2.2. p_{i_0}, f_{i_0y} and f_{i_0z} are the forces along the X-, Y- and Z-axes, respectively; m_{i_0x}, m_{i_0y} and m_{i_0z} are the moments about the X-, Y- and Z-axes, respectively. θ_{i_0x}, θ_{i_0y} and θ_{i_0z} are rotational displacements of the free-end of the i_0-th beam about the X-, Y- and Z-axes, respectively. x_{i_0}, y_{i_0} and z_{i_0} are translational displacements of the tip of the i_0-th beam along the X-, Y- and Z-axes, respectively.

Under the conditions of linear elasticity and small deflections, the principle of superposition [2.11] can be applied straightforwardly to deal with the spatial combined deformation of a beam. The combined deformation can be regarded as the combination of bending deformation in the XY and XZ planes (including the displacement along the X-axis), respectively, and torsional deformation about the X-axis. The bending of a beam in a given plane can be analysed using the nonlinear load-displacement equations derived by Awtar [2.2, 2.6]. An alternative derivation for the nonlinear analysis of planar deflection of a beam can also be found in *Appendix A*.

Equations (A. 12a) and (A. 13a) allow the nonlinear load-displacement equations for the i_0-th beam (i_0 = 1, 2, 3) for bending in the XY and XZ planes to be written as

$$\begin{bmatrix} f_{i_0y} \\ m_{i_0z} \end{bmatrix} = \begin{bmatrix} a & c \\ c & b \end{bmatrix} \begin{bmatrix} y_{i_0} \\ \theta_{i_0z} \end{bmatrix} + p_{i_0} \begin{bmatrix} e & h \\ h & g \end{bmatrix} \begin{bmatrix} y_{i_0} \\ \theta_{i_0z} \end{bmatrix} + p_{i_0}^2 \begin{bmatrix} -1/700 & 1/1400 \\ 1/1400 & -11/6300 \end{bmatrix} \begin{bmatrix} y_{i_0} \\ \theta_{i_0z} \end{bmatrix} + \cdots \quad (2.1)$$

and

$$\begin{bmatrix} f_{i_0z} \\ -m_{i_0y} \end{bmatrix} = \begin{bmatrix} a & c \\ c & b \end{bmatrix} \begin{bmatrix} z_{i_0} \\ -\theta_{i_0y} \end{bmatrix} + p_{i_0} \begin{bmatrix} e & h \\ h & g \end{bmatrix} \begin{bmatrix} z_{i_0} \\ -\theta_{i_0y} \end{bmatrix} + p_{i_0}^2 \begin{bmatrix} -1/700 & 1/1400 \\ 1/1400 & -11/6300 \end{bmatrix} \begin{bmatrix} z_{i_0} \\ -\theta_{i_0y} \end{bmatrix} + \cdots (2.2)$$

where the second term on the right-hand side of Equation (2.1) or (2.2) shows the load-stiffening effect, and the terms after the second can be neglected for most

applications. Equations (2.1) and (2.2) are valid under the assumption that the moment about the Y(Z)-axis acting at any location on the beam does not affect the bending in the XY (XZ) plane, i.e. that the two bending directions are decoupled or are weakly coupled.

The axial displacement of the i_0-th tip can be obtained by adding Equations (A.12b) and (A.13b) (contributions from bending in the XY and XZ planes) and deducting one of the duplicated terms (purely elastic effect):

$$x_{i_0} = \frac{1}{d} p_{i_0} + [y_{i_0}, \theta_{i_0 z}] \begin{bmatrix} i & k \\ k & j \end{bmatrix} \begin{bmatrix} y_{i_0} \\ \theta_{i_0 z} \end{bmatrix} + p_{i_0} [y_{i_0}, \theta_{i_0 z}] \begin{bmatrix} r & q \\ q & s \end{bmatrix} \begin{bmatrix} y_{i_0} \\ \theta_{i_0 z} \end{bmatrix} + [z_{i_0}, -\theta_{i_0 y}] \begin{bmatrix} i & k \\ k & j \end{bmatrix} \begin{bmatrix} z_{i_0} \\ -\theta_{i_0 y} \end{bmatrix} + p_{i_0} [z_{i_0}, -\theta_{i_0 y}] \begin{bmatrix} r & q \\ q & s \end{bmatrix} \begin{bmatrix} z_{i_0} \\ -\theta_{i_0 y} \end{bmatrix}$$
$$+ p_{i_0}^2 \left[y_{i_0}, \theta_{i_0 z} \right] \begin{bmatrix} 1/42000 & -1/84000 \\ -1/84000 & 1/18000 \end{bmatrix} \begin{bmatrix} y_{i_0} \\ \theta_{i_0 z} \end{bmatrix} + \cdots + p_{i_0}^2 \left[z_{i_0}, -\theta_{i_0 y} \right] \begin{bmatrix} 1/42000 & -1/84000 \\ -1/84000 & 1/18000 \end{bmatrix} \begin{bmatrix} z_{i_0} \\ -\theta_{i_0 y} \end{bmatrix} + \cdots \tag{2.3}$$

where the first term on the right-hand side represents the purely elastic effect of the axial force alone, the second and the fourth terms show the purely kinematic effect, and the third and the fifth terms show the elastokinematic effect. For most practical situations the terms after the fifth can be ignored since they are much smaller than the former five terms.

The nonlinear load-displacement equation of the i_0-th beam (i_0=1, 2, 3) for the torsion about the X-axis in deformation can be obtained (see *Appendix B* for detailed derivation):

$$\theta_{i_0 x} = m_{i_0 x} + (f_{i_0 z} y_{i_0} - f_{i_0 y} z_{i_0}) / \delta = m_{i_0 x} - c(\theta_{i_0 z} z_{i_0} + \theta_{i_0 y} y_{i_0}) / \delta - p_{i_0} h(\theta_{i_0 z} z_{i_0} + \theta_{i_0 y} y_{i_0}) / \delta \tag{2.4}$$

where δ=2G/E. The first term shows the purely elastic effect of the torque alone, the second term shows the purely kinematic effect, and the third term shows the elastokinematic effect. Due to the very small bending angles, compared with the transverse displacements and the torsional angle in the spatial three-beam module, we can also omit the purely kinematic and the elastokinematic effects in Equation (2.4).

The coefficients *a*, *b*, *c*, *d*, *e*, *g*, *h*, *i*, *j*, *k*, *q*, *r* and *s* used earlier are all non-dimensional numbers and are the characteristic of the uniform round cross-section beam [2.2]:

a=12, b=4, c=−6, d=16/(D_0/L)^2=16/(d_0)^2;

e=1.2, g=2/15, h=−0.1;

i=−0.6, j=−1/15, k=1/20;

r=1/700, s=11/6300, q=−1/1400.

From Equations (2.1)–(2.4), it can be seen that p_{i_0}, $f_{i_0 y}$, $f_{i_0 z}$, $m_{i_0 y}$ and $m_{i_0 z}$ are all approximately in the order of 1 (one), and $m_{i_0 x}$ is in the order of 0.1 since

$x_{i_0}, y_{i_0}, z_{i_0}, \theta_{i_0x}, \theta_{i_0y}$ and θ_{i_0z} are all in the order of 0.1 under the small deflection assumption [2.2].

Ref. [2.12] also derives a more accurate nonlinear analytical constraint model for the spatial symmetrical beams under small deformation assumption. For a spatial beam in the three-beam module, its nonlinear model proposed in this section can be used to derive the almost same nonlinear model for *the spatial three-beam module* as that obtained using the model in Ref. [2.12].

2.1.2 Conditions of geometric compatibility

For small absolute values of rotational angles (in the order of 0.1), the rotation sequence of three *Euler angles* is insignificant [2.13] and its contribution can be neglected. Due to the rigidity of the motion stage, the geometric compatibility of the rotational angles can be described:

$$\theta_{sx} = \theta_{1x} = \theta_{2x} = \theta_{3x}, \tag{2.5a}$$

$$\theta_{sy} = \theta_{1y} = \theta_{2y} = \theta_{3y}, \tag{2.5b}$$

$$\theta_{sz} = \theta_{1z} = \theta_{2z} = \theta_{3z}. \tag{2.5c}$$

The translational displacement relationships between the tip of the i_0-th beam and the centre of the motion stage can be expressed as

$$\begin{bmatrix} x_{i_0} \\ y_{i_0} \\ z_{i_0} \end{bmatrix} = \begin{bmatrix} x''_{i_0} - x'_{i_0} \\ y''_{i_0} - y'_{i_0} \\ z''_{i_0} - z'_{i_0} \end{bmatrix} + \begin{bmatrix} x_s \\ y_s \\ z_s \end{bmatrix} = \begin{bmatrix} x''_{i_0} \\ y'' \\ z''_{i_0} \end{bmatrix} + \begin{bmatrix} x_s - x'_{i_0} \\ y_s - y'_{i_0} \\ z_s - z'_{i_0} \end{bmatrix} \tag{2.6}$$

where x''_{i_0}, y''_{i_0} and z''_{i_0} are the coordinates of the tip of the i_0-th beam relative to the global fixed coordinate system after only the rotational displacements of the motion stage (no movement at the point O′). x'_{i_0}, y'_{i_0} and z'_{i_0} are the coordinates of the tip the i_0-th beam relative to the global fixed coordinate system in the initial undeformed configuration, which are also the local coordinates of the tip of the i_0-th beam relative to the mobile rigid body coordinate system (x'_1=0, y'_1=$r_3$sin(π/3), and z'_1=$r_3$cos(π/3) for tip 1, x'_2=0, y'_2=0, and z'_2=−r_3 for tip 2, x'_3=0, y'_3=−$r_3$sin(π/3), and z'_3=$r_3$cos(π/3) for tip 3).

The coordinates x''_{i_0}, y''_{i_0} and z''_{i_0} can be further expressed in a rotation matrix form as

$$\begin{bmatrix} x''_{i_0} \\ y'' \\ z''_{i_0} \end{bmatrix} = \mathbf{R}_{\mathrm{Z}}(\theta_{sz})\mathbf{R}_{\mathrm{Y}}(\theta_{sy})\mathbf{R}_{\mathrm{X}}(\theta_{sx}) \begin{bmatrix} x'_{i_0} \\ y'_{i_0} \\ z'_{i_0} \end{bmatrix} \tag{2.7a}$$

where $\mathbf{R}_{\mathrm{X}}$, $\mathbf{R}_{\mathrm{Y}}$ and $\mathbf{R}_{\mathrm{Z}}$ are the sequential rotation matrices [2.13] about the X-, Y- and Z-axes, respectively.

For small rotational angles, their high order terms in the product of three rotation matrices above can be neglected, so:

$$\mathbf{R}_{\mathrm{Z}}(\theta_{sz})\mathbf{R}_{\mathrm{Y}}(\theta_{sy})\mathbf{R}_{\mathrm{X}}(\theta_{sx}) \approx \begin{bmatrix} 1 & -\theta_{sz}+\theta_{sy}\theta_{sx} & \theta_{sz}\theta_{sx}+\theta_{sy} \\ \theta_{sz} & 1 & -\theta_{sx}+\theta_{sz}\theta_{sy} \\ -\theta_{sy} & \theta_{sx} & 1 \end{bmatrix} \approx \begin{bmatrix} 1 & -\theta_{sz} & \theta_{sy} \\ \theta_{sz} & 1 & -\theta_{sx} \\ -\theta_{sy} & \theta_{sx} & 1 \end{bmatrix}. \tag{2.7b}$$

Combining Equations (2.5) to (2.7b), the geometry compatibility conditions can be re-expressed in matrix form as

$$\begin{bmatrix} x_{i_0} \\ y_{i_0} \\ z_{i_0} \\ \theta_{i_0 x} \\ \theta_{i_0 y} \\ \theta_{i_0 z} \end{bmatrix} = \begin{bmatrix} 1 & 0 & 0 & 0 & z'_{i_0} & -y'_{i_0} \\ 0 & 1 & 0 & -z'_{i_0} & 0 & x'_{i_0} \\ 0 & 0 & 1 & y'_{i_0} & -x'_{i_0} & 0 \\ 0 & 0 & 0 & 1 & 0 & 0 \\ 0 & 0 & 0 & 0 & 1 & 0 \\ 0 & 0 & 0 & 0 & 0 & 1 \end{bmatrix} \begin{bmatrix} x_s \\ y_s \\ z_s \\ \theta_{sx} \\ \theta_{sy} \\ \theta_{sz} \end{bmatrix}. \tag{2.8}$$

Substituting the local coordinate values of the tips into Equation (2.8), the translational displacements of the tips can be expressed as follows.

$$x_1 = x_s - \sqrt{3}r_3\theta_{sz}/2 + r_3\theta_{sy}/2, \tag{2.9}$$

$$x_2 = x_s - r_3\theta_{sy}, \tag{2.10}$$

$$x_3 = x_s + \sqrt{3}r_3\theta_{sz}/2 + r_3\theta_{sy}/2, \tag{2.11}$$

$$y_1 = y_s - r_3\theta_{sx}/2 \quad , \tag{2.12}$$

$$y_2 = y_s + r_3\theta_{sx} \quad , \tag{2.13}$$

$$y_3 = y_s - r_3\theta_{sx}/2, \tag{2.14}$$

$$z_1 = z_s + \sqrt{3}r_3\theta_{sx}/2, \tag{2.15}$$

$$z_2 = z_s \quad , \tag{2.16}$$

$$z_3 = z_s - \sqrt{3}r_3\theta_{sx}/2. \tag{2.17}$$

2.1.3 Load-equilibrium conditions

From the free body diagram in Figure 2.2 and similar to the load-equilibrium

relationships used in [2.3], the equilibrium conditions of the motion stage in the deformed configuration can be described:

$$\begin{bmatrix} p \\ f_y \\ f_z \\ m_x \\ m_y \\ m_z \end{bmatrix} = \sum_{i_0=1}^{n=3} \begin{bmatrix} 1 & 0 & 0 & 0 & 0 & 0 \\ 0 & 1 & 0 & 0 & 0 & 0 \\ 0 & 0 & 1 & 0 & 0 & 0 \\ 0 & -z''_{i_0}/\delta & y''_{i_0}/\delta & 1 & 0 & 0 \\ z''_{i_0} & 0 & -x''_{i_0} & 0 & 1 & 0 \\ -y''_{i_0} & x''_{i_0} & 0 & 0 & 0 & 1 \end{bmatrix} \begin{bmatrix} p_{i_0} \\ f_{i_0 y} \\ f_{i_0 z} \\ m_{i_0 x} \\ m_{i_0 y} \\ m_{i_0 z} \end{bmatrix} \tag{2.18}$$

where x''_{i_0}, y''_{i_0} and z''_{i_0} can be obtained from the result of substituting Equation (2.7b) into Equation (2.7a), which can reflect the rotation effects. δ is defined in Equation (2.4).

Neglecting the contribution of small rotational displacements, Equation (2.18) simplifies to:

$$p = p_1 + p_2 + p_3, \tag{2.19}$$

$$f_y = f_{1y} + f_{2y} + f_{3y} \ , \tag{2.20}$$

$$f_z = f_{1z} + f_{2z} + f_{3z}, \tag{2.21}$$

$$m_y \approx m_{1y} + m_{2y} + m_{3y} + (p_1 + p_3 - 2p_2) r_3 / 2, \tag{2.22}$$

$$m_z \approx m_{1z} + m_{2z} + m_{3z} + (p_3 - p_1)\sqrt{3} r_3 / 2 \ , \tag{2.23}$$

$$m_x \approx m_{1x} + m_{2x} + m_{3x} + (f_{1z} - f_{3z})\sqrt{3} r_3 / (2\delta) + [2 f_{2y} - (f_{1y} + f_{3y})] r_3 / (2\delta). \tag{2.24}$$

2.2 Solution to the Nonlinear Load-Displacement Analysis of the Spatial Three-Beam Module

The constitutive, compatibility and equilibrium conditions [Equations (2.1)–(2.4), (2.5), (2.9)–(2.17), and (2.19)–(2.24)] in Section 2.1 permit a solution of the nonlinear load-displacement equations in terms of the geometry of the three-beam module. Three nonlinear methods of increasing accuracy and complexity are presented in this section: an approximate analytical method, an improved approximate analytical method and a numerical method.

2.2.1 Approximate analytical method

An initial FEA showed that, when forces alone are acting, each of the two bending

angles is approximately two orders of magnitude smaller than its corresponding one of two transverse displacements (θ_{sz} to y_s, θ_{sy} to z_s), and the torsional angle is almost zero. Therefore, the rotational angles are dropped out wherever appropriate below.

a) Solution for θ_{sy} and θ_{sz}

Substituting Equation (2.2) into Equation (2.22), combining the result with Equations (2.15) to (2.17), and again neglecting all the rotational displacements:

$$(p_1 + p_3) - 2p_2 \approx \frac{m_y + (3c + ph)z_s}{r_3 / 2} \quad . \tag{2.25}$$

Similarly, the substitution of Equation (2.1) into Equation (2.23) and combining the result with Equations (2.12) to (2.14), yields

$$(p_3 - p_1) \approx \frac{m_z - (3c + ph)y_s}{\sqrt{3}r_3 / 2} \quad . \tag{2.26}$$

From Equations (2.9) to (2.11), one can obtain

$$(x_1 + x_3) - 2x_2 = 3r_3\theta_{sy} . \tag{2.27}$$

Substituting Equations (2.3), and (2.12)–(2.17) into Equation (2.27), and substituting Equation (2.25) into the result give the rotational displacement

$$\theta_{sy} \approx \frac{2}{3r_3^2}(\frac{1}{d} + y_s^2 r + z_s^2 r)[m_y + (3c + ph)z_s] - 2\theta_{sx} y_s i . \tag{2.28}$$

Similarly, the rotational displacement θ_{sz} can also be obtained from Equations (2.9), (2.11), (2.3), (2.12), (2.14), (2.15), (2.17) and (2.26) as

$$\theta_{sz} = \frac{x_3 - x_1}{\sqrt{3}r_3} \approx \frac{2}{3r_3^2}(\frac{1}{d} + y_s^2 r + z_s^2 r)[m_z - (3c + ph)y_s] - 2\theta_{sx} z_s i . \tag{2.29}$$

b) Solution for y_s[1] and z_s

Substituting Equation (2.1) into Equation (2.20) and combining Equations (2.12)–(2.14), we obtain

$$\begin{aligned} f_y &= f_{1y} + f_{2y} + f_{3y} \\ &= ay_1 + c\theta_{sz} + p_1(ey_1 + h\theta_{sz}) + ay2 + c\theta_{sz} + p_2(ey_2 + h\theta_{sz}) + ay_3 + c\theta_{sz} + p_3(ey_1 + h\theta_{sz}) . \\ &= (3a + pe)y_s + (3c + ph)\theta_{sz} + [2p_2 - (p_1 + p_3)]r_3\theta_{sx} e / 2 \end{aligned} \tag{2.30}$$

Rewriting Equation (2.30) and replacing θ_{sz} with $-2\theta_{sx}z_s i$ based on Equation (2.29), we obtain the transverse translational displacement

[1] The bolded symbols are only for the purpose of highlighting rather than vectors if not indicated otherwise.

$$y_s = \frac{f_y - (3c + ph)(-2\theta_{sx} z_s i) + [(p_1 + p_3) - 2p_2] r_3 \theta_{sx} e/2}{3a + pe}. \tag{2.31}$$

The transverse translational displacement z_s can be obtained by substituting Equation (2.2) into Equation (2.21), combining Equations (2.15)–(2.17) and replacing θ_{sy} with $-2\theta_{sx} y_s i$ based on Equation (2.28):

$$z_s = \frac{f_z + (3c + ph)(-2\theta_{sx} y_s i) + (p_3 - p_1)\sqrt{3} r_3 \theta_{sx} e/2}{3a + pe} \quad . \tag{2.32}$$

Finally, substituting Equations (2.25) and (2.26) into Equations (2.31) and (2.32), respectively, we obtain the two transverse displacement equations:

$$y_s \approx \frac{f_y - (3c + ph)(-2\theta_{sx} z_s i) + [m_y + (3c + ph) z_s]\theta_{sx} e}{3a + pe} \approx \frac{f_y + m_y \theta_{sx} e}{3a + pe}, \tag{2.33}$$

$$z_s \approx \frac{f_z + (3c + ph)(-2\theta_{sx} y_s i) + [m_z - (3c + ph) y_s]\theta_{sx} e}{3a + pe} \approx \frac{f_z + m_z \theta_{sx} e}{3a + pe}. \tag{2.34}$$

c) Solution for θ_{sx}

Combining Equations (2.1) and (2.2), and substituting the result along with Equation (2.4) into Equation (2.24), we have

$$m_x \approx 3\theta_{sx} + 3ar_3^2 \theta_{sx}/\delta + per_3^2 \theta_{sx}/\delta + \frac{\sqrt{3}}{2} r_3 (p_1 - p_3) e z_s/\delta + \frac{1}{2} r_3 [2p_2 - (p_1 + p_3)] e y_s/\delta. \tag{2.35}$$

Substituting Equations (2.25) and (2.26) into Equation (2.35), and substituting Equations (2.33) and (2.34) into the result, we obtain the torsional angle (rotational displacement):

$$\theta_{sx} \approx \frac{m_x \delta + (m_z z_s + m_y y_s) e}{3(\delta + ar_3^2 + \frac{p}{3} er_3^2)} \approx \frac{m_x \delta + (m_z f_z + m_y f_y) e/(3a + pe)}{3(\delta + ar_3^2 + \frac{p}{3} er_3^2)}. \tag{2.36}$$

If the torque is normalized by EI/L (rather than by GI_p/L), the torsional angle θ_{sx} becomes

$$\theta_{sx} \approx \frac{m_x + (m_z f_z + m_y f_y) e/(3a + pe)}{3(\delta + ar_3^2 + \frac{p}{3} er_3^2)}. \tag{2.37}$$

d) Solution for x_s

From Equations (2.9) to (2.11), we have

$$x_s = (x_1 + x_2 + x_3)/3. \tag{2.38}$$

Substituting Equations (2.3) and (2.12)–(2.17) into Equation (2.38), substituting Equations (2.25) and (2.26) into the result and omitting some high order terms of

rotational angles, we obtain the axial translational displacement:

$$x_s \approx \frac{p}{3d} + (y_s^2 + z_s^2)i + \frac{p}{3}(y_s^2 + z_s^2)r + r_3^2\theta_{sx}^2 i + \frac{p}{3}r_3^2\theta_{sx}^2 r + 2(y_s\theta_{sz} - z_s\theta_{sy})k - \frac{2}{3}(m_y y_s + m_z z_s)\theta_{sx} r \tag{2.39}$$

where the terms with $r_3^2\theta_{sx}^2$ are retained since θ_{sx} is the DOF, and they are related to the radius r_3.

In summary, the approximate displacements of the motion stage for a given set of loads are obtained as follows:

(1) Calculate the torsional angle θ_{sx} using either Equation (2.36) or Equation (2.37);

(2) Solve for y_s and z_s by substituting the torsional angle into Equations (2.33) and (2.34);

(3) Calculate θ_{sy} and θ_{sz} by substituting θ_{sx}, y_s and z_s into Equations (2.28) and (2.29);

(4) Obtain the axial displacement x_s using Equation (2.39).

If $m_y f_y = -m_z f_z$, Equation (2.36) simplifies to $\theta_{sx}=m_x\delta/[3(\delta+ar_3^2+per_3^2/3)]$. This condition holds when the resultant transverse force is perpendicular to the resultant bending moment. In particular, we focus on five special cases: $m_y=m_z=0$; $f_z=f_y=0$; $m_y=f_z=0$; $f_y=m_z=0$; $m_z=-0.5f_y$ and $m_y=0.5f_z$. In the case: $m_y=m_z=0$, the three DOF equations [Equations (2.33), (2.34) and (2.36)] are independent, and in the case: $m_z=-0.5f_y$ and $m_y=0.5f_z$, the three rotational angles [Equations (2.28), (2.29) and (2.36)] are all equal to zero as long as the axial force $p=0$ and $m_x=0$. Furthermore, according to Equations (2.28), (2.29), (2.33), (2.34), (2.36) and (2.39), when only a torsional moment is imposed on the motion stage, two of the translational displacements, y_s and z_s, and two of the rotational displacements, θ_{sz} and θ_{sy}, are zero while $\theta_{sx}=m_x\delta/[3(\delta+ar_3^2)]$ and $x_s=r_3^2\theta_{sx}^2 i$ (negative), and this reveals how torsion can reduce the axial displacement x_s. If only the two transverse forces are imposed on the motion stage, the spatial three-beam module can be regarded as a good 2-D translation joint.

It can also be observed from Equations (2.28), (2.29), (2.33), (2.34), (2.36) and (2.39) that:

(a) The axial force p affects the transverse displacements (y_s and z_s), which reflects the load-stiffening effect. Either of the two transverse displacement equations shows that the buckling condition $p_{crit1}=-3a/e=-30$ occurs when the transverse stiffness becomes zero. The torsional angle θ_{sx} decreases with the increase of (positive) p, which also shows the load-stiffening effect. The torsional angle equation shows a second buckling condition $p_{crit2}=-3(\delta+ar_3^2)/(er_3^2)=-[30+3\delta/(er_3^2)]$ when the torsional stiffness becomes zero. Therefore, the buckling load for the spatial three-beam module is $p_{crit}=\max(p_{crit1},$

p_{crit2})=−30.

(b) The axial displacement x_s has three components: purely elastic effect from the axial force alone, purely kinematic effect such as $(y_s^2 + z_s^2)i + r_3^2\theta_{sx}^2 i + 2(y_s\theta_{sz} - z_s\theta_{sy})k$ and elastokinematic effect such as $p(y_s^2 + z_s^2)r/3 + pr_3^2\theta_{sx}^2 r/3 - 2(m_y y_s + m_z z_s)\theta_{sx} r/3$. The elastokinematic effect is much smaller that the purely kinematic effect. Similarly, the bending angle, θ_{sy} (θ_{sz}), is also composed of three components.

(c) The torsional angle has a dominant effect on the accuracy of the previously mentioned equations in comparison with θ_{sz} and θ_{sy}. The smaller $|\theta_{sx}|$ is, the more accurate are the previously mentioned force-displacement equations.

(d) All the three rotational angles decrease as r_3 increases. For a typical value 0.6 of r_3 and θ_{sx}=0, θ_{sz} and θ_{sy} can be in the order of 1×10^{-4} if d=40000 (i.e. L/D_0=50). This reveals the fact that the essence of constraint-based design is a combination of the effects of large values of d and small values of r. Furthermore, if θ_{sx} and y_s (or z_s) are all relatively large in absolute value, θ_{sy} (θ_{sz}) is affected by purely kinematic effect: $-2\theta_{sx}y_s i$ (or $-2\theta_{sx}z_s i$) dominantly.

(e) The translational displacement, y_s (or z_s), is weakly dependent on m_x, m_y, m_z, p and f_z (or f_y) (Maxwell Reciprocity [2.2 and 2.14]), and strongly dependent on f_y (or f_z). Here, f_y (or f_z) is a dominant load in determining y_s (or z_s), whereas m_z, m_x, m_y, p and f_z (or f_y) are non-dominant loads. Furthermore, torsional angle θ_{sx} is weakly dependent on m_y, m_z, f_y, f_z and p, and strongly dependent on m_x (m_x is a dominant load in determining θ_{sx}).

2.2.2 Improved approximate analytical method

For relatively large absolute values of θ_{sx}, the dependence of a transverse translational displacement on the relevant non-dominant loads becomes significant, particularly if the absolute values of the relevant dominant load are small relative to the non-dominant ones. Moreover, the purely kinematic effect and the elastokinematic effect in Equation (2.4), the second-order terms in rotational angles neglected in the product of the three rotation matrices in Equation (2.7b), and the rotation contributions in Equation (2.18) need also to be retained wherever appropriate. In addition, we may approximate θ_{sy} and θ_{sz} using Equations (2.28) and (2.29), respectively, in the appropriate derivation below.

Using Equation (2.18), Equations (2.22)–(2.24) for the moment-equilibrium conditions after deformation can be rewritten as

$$\begin{aligned} m_y \approx\ & m_{1y} + m_{2y} + m_{3y} + (p_1 + p_3 - 2p_2)\frac{r_3}{2} \\ & + (p_1 - p_3)\frac{\sqrt{3}}{2} r_3\theta_{sx} + [2f_{2z} - (f_{1z} + f_{3z})]\frac{1}{2} r_3\theta_{sy} + (f_{1z} - f_{3z})\frac{\sqrt{3}}{2} r_3\theta_{sz} \end{aligned}, \quad (2.40a)$$

$$\begin{aligned} m_z \approx\ & m_{1z} + m_{2z} + m_{3z} + (p_3 - p_1)\frac{\sqrt{3}}{2} r_3 \\ & + [(p_1 + p_3) - 2p_2]\frac{r_3}{2}\theta_{sx} + (f_{3y} - f_{1y})\frac{\sqrt{3}}{2} r_3\theta_{sz} + [(f_{1y} + f_{3y}) - 2f_{2y}]\frac{1}{2} r_3\theta_{sy} \end{aligned}, \quad (2.40b)$$

$$\begin{aligned} m_x\delta \approx\ & \delta(m_{1x} + m_{2x} + m_{3x}) + (f_{1z} - f_{3z})\frac{\sqrt{3}}{2} r_3 + [2f_{2y} - (f_{1y} + f_{3y})]\frac{1}{2} r_3 \\ & + (f_{3y} - f_{1y})\frac{\sqrt{3}}{2} r_3\theta_{sx} + [2f_{2z} - (f_{1z} + f_{3z})]\frac{1}{2} r_3\theta_{sx} \end{aligned}. \quad (2.40c)$$

From Equations (2.1), (2.2) and (2.12)–(2.17), one can obtain

$$f_{1z} - f_{3z} = \sqrt{3}ar_3\theta_{sx} + (p_1 - p_3)(ez_s - h\theta_{sy}) + (p_1 + p_3)e\sqrt{3}r_3\theta_{sx}/2, \quad (2.41a)$$

$$2f_{2y} - (f_{1y} + f_{3y}) = 3ar_3\theta_{sx} + [2p_2 - (p_1 + p_3)](ey_s + h\theta_{sz}) + [4p_2 + (p_1 + p_3)]er_3\theta_{sx}/2, \quad (2.41b)$$

$$f_{3y} - f_{1y} = (p_3 - p_1)(ey_s + h\theta_{sz}) + (p_1 - p_3)er_3\theta_{sx}/2, \quad (2.41c)$$

$$2f_{2z} - (f_{1z} + f_{3z}) = [2p_2 - (p_1 + p_3)](ez_s - h\theta_{sy}) + (p_3 - p_1)e\sqrt{3}r_3\theta_{sx}/2 \quad (2.41d)$$

where p_1+p_3 and $4p_2+(p_1+p_3)$ can also be represented by $[2p+(p_1+p_3-2p_2)]/3$ and $2p-(p_1+p_3-2p_2)$, respectively.

Retaining the bending angles in Equations (2.31) and (2.32), the two transverse displacements are obtained as

$$y_s = \frac{f_y - (3c + ph)\theta_{sz} + [(p_1 + p_3) - 2p_2]\frac{1}{2} r_3\theta_{sx}e}{3a + pe}, \quad (2.42)$$

$$z_s = \frac{f_z + (3c + ph)\theta_{sy} + (p_3 - p_1)\frac{\sqrt{3}}{2} r_3\theta_{sx}e}{3a + pe} \quad (2.43)$$

where more accurate solutions for $(p_1+p_3)-2p_2$ and p_3-p_1 can be obtained by substituting Equations (2.41a), (2.41b), (2.41c) and (2.41d) into Equations (2.40a) and (2.40b) and combining the results with Equations (2.1), (2.2) and (2.12)–(2.17):

$$\begin{aligned} (p_1 + p_3) - 2p_2 &= \frac{m_y + [(3c + ph)z_s - (3b + pg)\theta_{sy}] - \{m_z - [(3c + ph)y_s + (3b + pg)\theta_{sz}]\}\theta_{sx}(h-1) - (3a + pe)r_3^2\theta_{sz}\theta_{sx}/2}{(r_3/2)(\theta_{sx}^2(h-1)^2 + 1)}, \\ &\approx \frac{m_y + [(3c + ph)z_s - (3b + pg)\theta_{sy}] - [m_z - (3c + ph)y_s]\theta_{sx}(h-1)}{(r_3/2)} \end{aligned} \quad (2.44)$$

$$p_3 - p_1 = \frac{m_z - [(3c+ph)y_s + (3b+pg)\theta_{sz}] + \{m_y + [(3c+ph)z_s - (3b+pg)\theta_{sy}]\}\theta_{sx}(h-1) + (3a+pe)r_3^2\theta_{sy}\theta_{sx}/2}{(\sqrt{3}r_3/2)(\theta_{sx}^2(h-1)^2+1)}$$
$$\approx \frac{m_z - [(3c+ph)y_s + (3b+pg)\theta_{sz}] + [m_y + (3c+ph)z_s]\theta_{sx}(h-1)}{(\sqrt{3}r_3/2)} \quad (2.45)$$

For relatively large absolute values of θ_{sx}, Equation (2.28) is re-written as

$$\begin{aligned}
3r_3\theta_{sy} &= (x_1+x_3) - 2x_2 - 3r_3\theta_{sx}\theta_{sz} \\
&\approx \frac{(p_3+p_1)-2p_2}{d} + [(y_1^2+y_3^2)-2y_2^2]i + [(z_1^2+z_3^2)-2z_2^2]i + 2k\theta_{sz}(y_1+y_3-2y_2) - 2k\theta_{sy}(z_1+z_3-2z_2) \\
&\quad + [(p_1y_1^2+p_3y_3^2)-2p_2y_2^2]r + [(p_1z_1^2+p_3z_3^2)-2p_2z_2^2]r + 2[(p_1+p_3)-2p_2](y_s\theta_{sz}-z_s\theta_{sy})q - 3r_3\theta_{sx}\theta_{sz} \\
&\approx \frac{(p_3+p_1)-2p_2}{d} - 6r_3\theta_{sx}y_s i - 6r_3\theta_{sx}\theta_{sz}(k+0.5) + [(p_1+p_3)-2p_2](y_s^2+z_s^2)r - [(p_1+p_3)+4p_2]r_3\theta_{sx}y_s r \\
&\quad + (p_1-p_3)\sqrt{3}r_3\theta_{sx}z_s r + [(p_1+p_3)-2p_2]r_3^2\theta_{sx}^2 r - 4[(p_1+p_3)-2p_2](y_s z_s - z_s y_s)\theta_{sx} iq \\
&\approx \frac{(p_3+p_1)-2p_2}{d} - 6r_3\theta_{sx}y_s i - 3r_3\theta_{sx}\theta_{sz} + [(p_1+p_3)-2p_2](y_s^2+z_s^2)r + [((p_1+p_3)-2p_2)-2p]r_3\theta_{sx}y_s r \\
&\quad + (p_1-p_3)\sqrt{3}r_3\theta_{sx}z_s r + [(p_1+p_3)-2p_2]r_3^2\theta_{sx}^2 r
\end{aligned} \quad (2.46)$$

The substitution of Equations (2.29), (2.44) and (2.45) into Equation (2.46) produces

$$\begin{aligned}
\theta_{sy} &\approx \frac{2}{3r_3^2}[\frac{1}{d} + (y_s^2+z_s^2+r_3^2\theta_{sx}^2)r][m_y + (3c+ph)z_s - m_z\theta_{sx}(h-1)] \\
&\quad - \frac{2}{3r_3^2}[\frac{1}{d} + (y_s^2+z_s^2+r_3z_s)r][m_z + m_y\theta_{sx}(h-1)]\theta_{sx} - 2\theta_{sx}y_s(i+\frac{p}{3}r) + 2\theta_{sx}^2 z_s i
\end{aligned} \quad (2.47)$$

Similarly, Equation (2.29) is re-written as

$$\begin{aligned}
\sqrt{3}r_3\theta_{sz} &= x_3 - x_1 + \sqrt{3}r_3\theta_{sx}\theta_{sy} \\
&\approx \frac{(p_3-p_1)}{d} + (y_3^2-y_1^2)i + (z_3^2-z_1^2)i + 2k\theta_{sz}(y_3-y_1) - 2k\theta_{sy}(z_3-z_1) + (p_3y_3^2 - p_1y_1^2)r \\
&\quad + (p_3z_3^2 - p_1z_1^2)r + 2(p_3-p_1)(y_s\theta_{sz} - z_s\theta_{sy})q + \sqrt{3}r_3\theta_{sx}\theta_{sy} \\
&\approx \frac{(p_3-p_1)}{d} - 2\sqrt{3}r_3\theta_{sx}z_s i + 2\sqrt{3}r_3\theta_{sx}\theta_{sy}(k+0.5) + (p_3-p_1)(y_s^2+z_s^2)r + (p_1-p_3)r_3\theta_{sx}y_s r \\
&\quad - (p_1+p_3)\sqrt{3}r_3\theta_{sx}z_s r + (p_3-p_1)r_3^2\theta_{sx}^2 r - 4(p_3-p_1)(y_s z_s - z_s y_s)\theta_{sx} iq \\
&\approx \frac{(p_3-p_1)}{d} - 2\sqrt{3}r_3\theta_{sx}z_s i + \sqrt{3}r_3\theta_{sx}\theta_{sy} + (p_3-p_1)(y_s^2+z_s^2)r + (p_1-p_3)r_3\theta_{sx}y_s r \\
&\quad - \frac{2p + [(p_1+p_3)-2p_2]}{3}\sqrt{3}r_3\theta_{sx}z_s r + (p_3-p_1)r_3^2\theta_{sx}^2 r
\end{aligned} \quad (2.48)$$

Substituting Equations (2.28), (2.44) and (2.45) into Equation (2.48), we have

$$\begin{aligned}
\theta_{sz} &\approx \frac{2}{3r_3^2}[\frac{1}{d} + (y_s^2+z_s^2+r_3^2\theta_{sx}^2 - r_3\theta_{sx}y_s)r][m_z - (3c+ph)y_s + m_y\theta_{sx}(h-1)] \\
&\quad + \frac{2}{3r_3^2}[\frac{1}{d} + (y_s^2+z_s^2)r][m_y + m_z\theta_{sx}(h-1)]\theta_{sx} - 2\theta_{sx}z_s(i+\frac{p}{3}r) - 2\theta_{sx}^2 y_s i
\end{aligned} \quad (2.49)$$

Then, substituting Equations (2.44) and (2.45) into Equations (2.42) and (2.43), respectively, the two transverse displacements can be obtained as

$$y_s \approx \frac{f_y-(3c+ph)\theta_{sz}+\{m_y+[(3c+ph)z_s-(3b+pg)\theta_{sy}]-[m_z-(3c+ph)y_s]\theta_{sx}(h-1)\}\theta_{sx}e}{3a+pe}, \tag{2.50}$$

$$z_s \approx \frac{f_z+(3c+ph)\theta_{sy}+\{m_z-[(3c+ph)y_s+(3b+pg)\theta_{sz}]+[m_y+(3c+ph)z_s]\theta_{sx}(h-1)\}\theta_{sx}e}{3a+pe}. \tag{2.51}$$

Equations (2.50) and (2.51) can be further simplified as

$$\begin{aligned} y_s &\approx \frac{f_y-(3c+ph)(\bar{\theta}_{sz}-2\theta_{sx}z_s i)+[m_y+(3c+ph)z_s]\theta_{sx}e-m_z\theta_{sx}^2(h-1)e}{3a+pe} \\ &\approx \bar{y}_s-\frac{(3c+ph)\bar{\theta}_{sz}+m_z\theta_{sx}^2(h-1)e}{3a+pe} \end{aligned}, \tag{2.52}$$

$$\begin{aligned} z_s &\approx \frac{f_z+(3c+ph)(\bar{\theta}_{sy}-2\theta_{sx}y_s i)+[m_z-(3c+ph)y_s]\theta_{sx}e+m_y\theta_{sx}^2(h-1)e}{3a+pe} \\ &\approx \bar{z}_s+\frac{(3c+ph)\bar{\theta}_{sy}+m_y\theta_{sx}^2(h-1)e}{3a+pe} \end{aligned} \tag{2.53}$$

where $\bar{y}_s=\frac{f_y+m_y\theta_{sx}e}{3a+pe}$, $\bar{z}_s=\frac{f_z+m_z\theta_{sx}e}{3a+pe}$, $\bar{\theta}_{sz}=\frac{2}{3r_3^2}[\frac{1}{d}+(\bar{y}_s^2+\bar{z}_s^2)r][m_z-(3c+ph)\bar{y}_s]$, and $\bar{\theta}_{sy}=\frac{2}{3r_3^2}[\frac{1}{d}+(\bar{y}_s^2+\bar{z}_s^2)r][m_y+(3c+ph)\bar{z}_s]$.

Substituting Equation (2.41) into Equation (2.40c) and combining with Equation (2.4), we have

$$\begin{aligned} m_x\delta \approx\ & 3\delta\theta_{sx}+3c(\theta_{sz}z_s+\theta_{sy}y_s)+ph(\theta_{sz}z_s+\theta_{sy}y_s)+3ar_3^2\theta_{sx}+per_3^2\theta_{sx} \\ & +\frac{\sqrt{3}}{2}r_3(p_1-p_3)[(ez_s-h\theta_{sy})-(ey_s+h\theta_{sz})\theta_{sx}] \\ & +\frac{1}{2}r_3[2p_2-(p_1+p_3)][(ey_s+h\theta_{sz})+(ez_s-h\theta_{sy})\theta_{sx}] \end{aligned}. \tag{2.54}$$

We can further substitute Equations (2.44), (2.45), (2.47), (2.49), (2.52) and (2.53) into Equation (2.54) and omit some high order terms of rotational angles. Then we obtain the torsional angle as follows:

$$\begin{aligned} \theta_{sx} \approx\ & \{m_x\delta+[m_z-(3c+ph)\hat{y}_s-(3b+pg)(\bar{\theta}_{sz}-2\theta_{sx}\hat{z}_s i) \\ & +[m_y+(3c+ph)\hat{z}_s]\theta_{sx}(h-1)][(e\hat{z}_s-h\bar{\theta}_{sy}+2h\theta_{sx}\hat{y}_s i)-e\hat{y}_s\theta_{sx}] \\ & +[m_y+(3c+ph)\hat{z}_s-(3b+pg)(\bar{\theta}_{sy}-2\theta_{sx}\hat{y}_s i) \\ & -[m_z-(3c+ph)\hat{y}_s]\theta_{sx}(h-1)][(e\hat{y}_s+h\bar{\theta}_{sz}-2h\theta_{sx}\hat{z}_s i)+e\hat{z}_s\theta_{sx}] \\ & -(3c+ph)(\bar{\theta}_{sz}\hat{z}_s+\bar{\theta}_{sy}\hat{y}_s)\}/\{3[\delta+ar_3^2+\frac{p}{3}er_3^2-2ci(\hat{z}_s^2+\hat{y}_s^2)-\frac{2phi}{3}(\hat{z}_s^2+\hat{y}_s^2)]\} \end{aligned} \tag{2.55}$$

where $\hat{y}_s = \dfrac{f_y + m_y\theta_{sx}e - (3c+ph)\bar{\theta}_{sz}}{3a+pe}$, and $\hat{z}_s = \dfrac{f_z + m_z\theta_{sx}e + (3c+ph)\bar{\theta}_{sy}}{3a+pe}$. Only one real solution is the desired solution for the polynomial equation of degree 8 with one unknown θ_{sx}. Equation (2.55) can be shown to reduce to Equation (2.36) for relatively small $|\theta_{sx}|$.

In addition, substituting the torsional angle θ_{sx} obtained from Equation (2.55) into Equations (2.52) and (2.53), the two transverse displacements, y_s and z_s, can be found.

Once θ_{sx}, y_s and z_s have been obtained, the other two rotational angles, θ_{sy} and θ_{sz}, can be obtained using Equations (2.47) and (2.49), and the axial displacement x_s can then be obtained using Equations (2.3) and (2.9)–(2.17) as

$$\begin{aligned} x_s &= \frac{1}{3}(x_1+x_2+x_3) \approx \frac{p}{3d} + (y_s^2+z_s^2)i + \frac{p}{3}(y_s^2+z_s^2)r + r_3^2\theta_{sx}^2 i + \frac{p}{3}r_3^2\theta_{sx}^2 r \\ &+ \frac{1}{3}[(2p_2-(p_1+p_3))r_3y_s + (p_1-p_3)\sqrt{3}r_3z_s]\theta_{sx}r \\ &+ 2(y_s\theta_{sz} - z_s\theta_{sy})k + (\theta_{sz}^2+\theta_{sy}^2)j + \frac{2}{3}p(y_s\theta_{sz} - z_s\theta_{sy})q \\ &+ \frac{1}{3}[(2p_2-(p_1+p_3))r_3\theta_{sz} - (p_1-p_3)\sqrt{3}r_3\theta_{sy}]\theta_{sx}q + \frac{p}{3}(\theta_{sz}^2+\theta_{sy}^2)s \end{aligned} \quad . \qquad (2.56)$$

Substituting Equations (2.44) and (2.45) into Equation (2.56) and making further simplification, we have

$$\begin{aligned} x_s &\approx \frac{p}{3d} + (y_s^2+z_s^2)i + \frac{p}{3}(y_s^2+z_s^2)r + r_3^2\theta_{sx}^2 i + \frac{p}{3}r_3^2\theta_{sx}^2 r + 2(y_s\theta_{sz} - z_s\theta_{sy})k \\ &- \frac{2}{3}(m_y y_s + m_z z_s)\theta_{sx}r - \frac{2}{3}[(m_y + (3c+ph)z_s)\theta_{sz} - (m_z - (3c+ph)y_s)\theta_{sy}]\theta_{sx}q \end{aligned} \quad . (2.57)$$

Equations (2.47), (2.49), (2.52), (2.53), (2.55) and (2.57) are the improved approximate analytical load-displacement equations for large $|\theta_{sx}|$, which can capture more nonlinear effects. It can be shown that $\theta_{sx}\approx 0$ for the five special loading cases: $m_x=m_y=m_z=0$; $m_x=f_z=f_y=0$; $m_x=m_y=f_z=0$; $m_x=f_y=m_z=0$; $m_x=0$, $m_z=-0.5f_y$ and $m_y=0.5f_z$.

If m_y or m_z in Equations (2.52) and (2.53) and all of the dominant transverse forces are very small in absolute value, we can obtain more accurate solutions to the load-displacement equations. Starting from the θ_{sx}, θ_{sy} and θ_{sz} obtained above, the two accurate transverse displacements (y_s and z_s) can be obtained from Equations (2.50) and (2.51). Then, we can obtain more accurate values of θ_{sx}, θ_{sy}, θ_{sz} and x_s step-by-step by substituting the above y_s and z_s into Equations (2.55), (2.47), (2.49) and (2.57).

2.2.3 Numerical method

Exact solutions for the nonlinear load-displacement equations can be obtained numerically without the need for approximation, although this has the disadvantage that the qualitative behavior of the spatial modules is more difficult to explore.

The numerical scheme involves seven unknown terms: $(p_1+p_3)-2p_2$, p_3-p_1, θ_{sx}, θ_{sy}, θ_{sz}, y_s and z_s that are obtained by solving the seven following equations, obtained from Equations (2.42)–(2.46), (2.48) and (2.54):

$$y_s = \{ f_y - (3c + ph)\theta_{sz} + [(p_1 + p_3) - 2p_2]\frac{1}{2} r_3 \theta_{sx} e\} / (3a + pe), \tag{2.58}$$

$$z_s = \{ f_z + (3c + ph)\theta_{sy} + (p_3 - p_1)\frac{\sqrt{3}}{2} r_3 \theta_{sx} e\} / (3a + pe), \tag{2.59}$$

$$\begin{aligned}[(p_1 + p_3) - 2p_2]r_3/2 = m_y + [(3c + ph)z_s - (3b + pg)\theta_{sy}] \\ - \{m_z - [(3c + ph)y_s + (3b + pg)\theta_{sz}]\}\theta_{sx}(h-1) - (3a + pe)r_3^2 \theta_{sz}\theta_{sx}/2\end{aligned}, \tag{2.60}$$

$$\begin{aligned}(p_3 - p_1)\sqrt{3}r_3/2 = m_z - [(3c + ph)y_s + (3b + pg)\theta_{sz}] \\ + \{m_y + [(3c + ph)z_s - (3b + pg)\theta_{sy}]\}\theta_{sx}(h-1) + (3a + pe)r_3^2 \theta_{sy}\theta_{sx}/2\end{aligned}, \tag{2.61}$$

$$\begin{aligned}3r_3\theta_{sy} = \frac{(p_3 + p_1) - 2p_2}{d} - 6r_3\theta_{sx}y_s i - 6r_3\theta_{sx}\theta_{sz}(k + 0.5) + [(p_1 + p_3) - 2p_2](y_s^2 + z_s^2)r \\ + [((p_1 + p_3) - 2p_2) - 2p]r_3\theta_{sx}y_s r + (p_1 - p_3)\sqrt{3}r_3\theta_{sx}z_s r + [(p_1 + p_3) - 2p_2]r_3^2\theta_{sx}^2 r \\ + 2[(p_1 + p_3) - 2p_2](y_s\theta_{sz} - z_s\theta_{sy})q\end{aligned}, \tag{2.62}$$

$$\begin{aligned}\sqrt{3}r_3\theta_{sz} = \frac{(p_3 - p_1)}{d} - 2\sqrt{3}r_3\theta_{sx}z_s i + 2\sqrt{3}r_3\theta_{sx}\theta_{sy}(k + 0.5) + (p_3 - p_1)(y_s^2 + z_s^2)r \\ + (p_1 - p_3)r_3\theta_{sx}y_s r - \frac{2p + [(p_1 + p_3) - 2p_2]}{3}\sqrt{3}r_3\theta_{sx}z_s r + (p_3 - p_1)r_3^2\theta_{sx}^2 r \\ + 2(p_3 - p_1)(y_s\theta_{sz} - z_s\theta_{sy})q\end{aligned}, \tag{2.63}$$

$$\begin{aligned}m_x\delta = 3\delta\theta_{sx} + (3c + ph)(\theta_{sz}z_s + \theta_{sy}y_s) + (3a + pe)r_3^2\theta_{sx} \\ + \frac{\sqrt{3}}{2}r_3(p_1 - p_3)[(ez_s - h\theta_{sy}) - (ey_s + h\theta_{sz})\theta_{sx}] \\ + \frac{1}{2}r_3[2p_2 - (p_1 + p_3)][(ey_s + h\theta_{sz}) + (ez_s - h\theta_{sy})\theta_{sx}]\end{aligned}. \tag{2.64}$$

Once $(p_1+p_3)-2p_2$, p_3-p_1, θ_{sx}, θ_{sy}, θ_{sz}, y_s and z_s have been obtained using Maple *fsolve* function with initial set values of all zeros, they can be substituted into Equation (2.56) to obtain the axial displacement x_s. We can also obtain p_1 and p_2 and p_3 by combining Equations (2.60), (2.61) and (2.19), which is useful for further stress analysis.

2.2.4 Discussions

a) Validity condition of the proposed nonlinear methods

The nonlinear methods proposed in Sections 2.2.1 to 2.2.3 are valid only for small deflections (usually all normalized displacements less than 0.1 [2.2]) and large ratios of length to diameter, i.e. slenderness ratios (usually L/D_0 more than 10 [2.15] for slender beams ignoring shear deformation). If the proposed nonlinear methods are applied to the analysis of spatial three-beam modules under the conditions of large deflections or small slenderness ratios (for Timoshenko beams), errors between the analytical results and real results will be unacceptable, but these nonlinear methods can still capture certain nonlinear constraint characteristics of the spatial modules.

Now discuss the range of r_3 under given conditions. If we make a rotational angle (such as θ_{sz}) smaller than α_0 times (usually $\geq$ 50) a corresponding transverse displacement (such as y_s) in absolute value under only one transverse force acting (such as f_y), we have the following relationship based on Equation (2.29):

$$\frac{2}{3r_3^2}(1/d + y_s^2 r)(-3cy_s) \leq y_s/\alpha_0 .$$

The above equation is simplified to determine the range of r_3:

$$r_3^2 \geq 12\alpha_0/d .$$

It should be emphasized that the analytical method has an apparant advantage in quantitatively determining certain geometrical parameters such as the radius of the pitch circle of the spatial three-beam module demonstrated above.

b) Application of the proposed methods to spatial three-beam modules with regular polygon cross-section beams and generalized beams

It should be noted that the normalized and nonlinear methods proposed above are also applicable for the spatial three-beam modules with regular polygon cross-section beams (ignoring warping effect under torsion), but the non-dimensional coefficient d should be modified accordingly. For example, for the square cross-section multi-beam module, $d=12/(T/L)^2$ (T is the thickness of the beam). Here, this modified nonlinear method suits the layouts of the square cross-section as shown in Figure 2.3 due to its inherent symmetry.

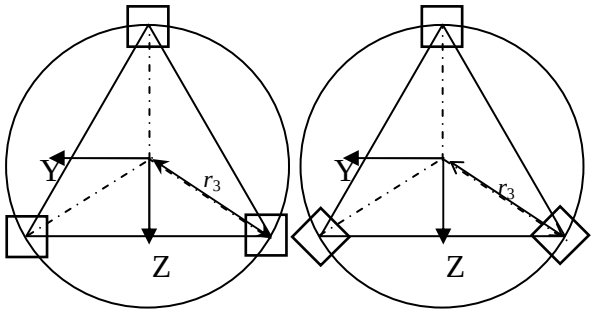

a) Layout 1 b) Layout 2

Figure 2.3 Top view illustrations for the square cross-section layouts in the spatial three-beam module with same pitch circle radius

In addition, these nonlinear methods can be used to deal with generalized beam modules by modifying the coefficients *a*, *b*, *c*, *d*, *e*, *g*, *h*, *i*, *j*, *k*, *q*, *r* and *s* based on Ref. [2.6], and using $\delta=G/(Ea_0)$ and then replacing $m_x\delta$ with $2a_0m_x\delta$ in Equations (2.36), (2.55) and (2.64). Here, a generalized beam of length L is composed of two uniform compliant segments and one rigid segment [2.6], and a_0 denotes the normalized length of each compliant segment.

c) Characteristics of three nonlinear methods

In order to illustrate the applicability of the various solutions, an example spatial three-beam module is analysed below. The spatial three-beam module is taken to be made from an aluminium alloy for which Young's modulus, E, is 69,000Nmm^{-2} and Poisson's ratio, v, is 0.33. The dimensions are D_0=4mm (d=2500), R_3=30mm (r_3=0.6) and L=50 mm. All the normalized external transverse forces need to be approximately over [−3.6, 3.6] yielding normalized transverse displacements over [−0.1, 0.1]. The normalized external torque needs to be approximately in the order of 1.8 to limit the torsional angle to the order of 0.1. Other normalized external loads may be all in the order of 1.8 or greater compared with the pre-determined loads.

In practice, the simpler and more analytical the method is, the more useful the analysis for the design of CPMs is. If each of the dominate forces for transverse displacements, such as f_y for y_s, is relatively large (for example, 2 times larger than all the relevant non-dominant moments in absolute value) or two bending moments are both zero (m_y=m_z=0), the approximate analytical method should be acceptable for design purposes (the case under the latter condition is shown in Figure 2.4). When the above condition does not hold, a balance needs to be made between accuracy and complexity.

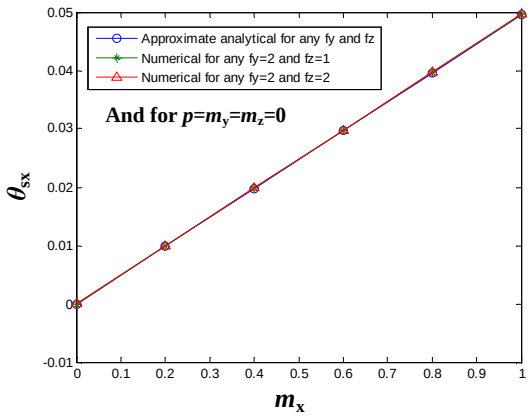

Figure 2.4 Comparison of results obtained using nonlinear methods for m_y=m_z=0

Table 2.1 shows the calculated displacements of the motion stage of the spatial three-beam module using the approximate and improved approximate analytical methods and the numerical method under loads: f_z=2, m_z=10 ($m_z f_z$ =20) and p=m_x=m_y=m_z=0, i.e. where the torsional angle is relatively large.

Displacements / *Methods*	y_s	z_s	x_s	θ_{sz}	θ_{sy}	θ_{sx}
Approximate analytical method	0.00	0.0702	−0.00390	0.0112	-9.518×10^{-4}	0.0438
Improved approximate analytical method	0.00513	0.0755	−0.00424	0.0131	-1.106×10^{-3}	0.0607
Numerical method	0.00514	0.0764	−0.00436	0.0131	-1.111×10^{-3}	0.0609
Error between improved and approximate analytical methods	100%	7.02 %	7.80%	14.50%	13.94%	28.08%

Table 2.1 Comparison of three nonlinear methods under the large torsion

We can observe from Table 2.1 that, for relatively large θ_{sx}, the error (|(improved approximate analytical result − approximate analytical result)/improved approximate analytical result|×100%) is relatively large and is unacceptably high for y_s since the dominant load f_y for y_s is zero. Table 2.1 also shows that the approximations for the improved approximate analytical method are reasonable, leading to very small differences between the analytical and numerical solutions. If the loading is changed to f_z=2, m_z=5 ($m_z f_z$=10), and p=m_x=m_y =m_z =0, the error in the torsional angle reduces from the 28.08% in Table 2.1 to 6.40%.

Figure 2.5 shows that the torsional angle error between the numerical, improved approximate analytical, and approximate analytical results increases at an accelerating rate as the ratio of f_z to m_z decreases starting at around 1.6, and also verifies the accuracy of the improved approximate analytical method. It is concluded that the difference between the solutions obtained using the improved and approximate analytical methods

decreases with the increase of the transverse loads.

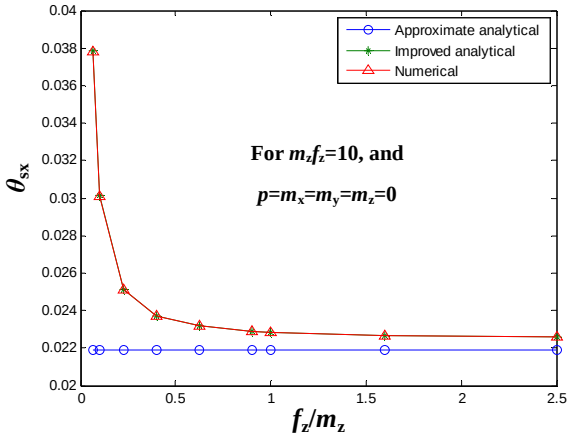

Figure 2.5 Comparison of torsional angles obtained using three nonlinear methods for fixed product of $m_z f_z$

d) Error analysis of the spatial three-beam module

In this section, error analysis will be implemented to analyse how the beam length error affects the DOF equations. In turn, the derived DOF equations can be used to diagnose the length error.

We only deal with the case that two beams (beams 1 and 3) are of length L_1, and one beam (beam 2) is of length L_2 (see Figure 2.6).

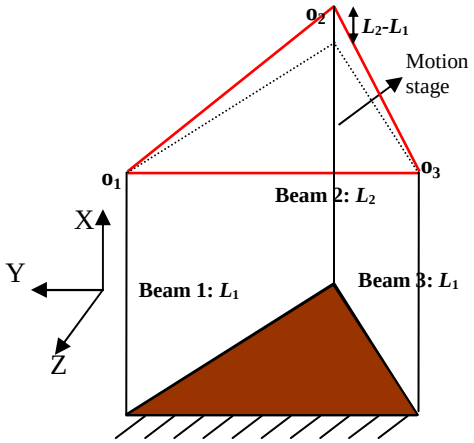

Figure 2.6 Variation of the spatial three-beam module

Let L_1 is the characteristic length. Then force-displacement equations for beam 1 or beam 3 remain unchanged, while those for beam 2 change as follows based on Equations (2.1)–(2.4).

$$\begin{bmatrix} f_{2z} \\ -m_{2y} \end{bmatrix} = \begin{bmatrix} (L_1/L_2)^3 a & (L_1/L_2)^2 c \\ (L_1/L_2)^2 c & (L_1/L_2) b \end{bmatrix} \begin{bmatrix} z_2 \\ -\theta_{2y} \end{bmatrix} + p_2 \begin{bmatrix} (L_1/L_2) e & h \\ h & (L_2/L_1) g \end{bmatrix} \begin{bmatrix} z_2 \\ -\theta_{2y} \end{bmatrix}, \quad (2.65)$$

$$\begin{bmatrix} f_{2y} \\ m_{2z} \end{bmatrix} = \begin{bmatrix} (L_1/L_2)^3 a & (L_1/L_2)^2 c \\ (L_1/L_2)^2 c & (L_1/L_2) b \end{bmatrix} \begin{bmatrix} y_2 \\ \theta_{2z} \end{bmatrix} + p_2 \begin{bmatrix} (L_1/L_2) e & h \\ h & (L_2/L_1) g \end{bmatrix} \begin{bmatrix} y_2 \\ \theta_{2z} \end{bmatrix}, \tag{2.66}$$

$$\begin{aligned} x_2 = \frac{L_2}{L_1}\frac{p_2}{d} &+ [y_2, \theta_{2z}] \begin{bmatrix} (L_1/L_2) i & k \\ k & (L_2/L_1) j \end{bmatrix} \begin{bmatrix} y_2 \\ \theta_{2z} \end{bmatrix} + p_2 [y_2, \theta_{2z}] \begin{bmatrix} (L_2/L_1) r & (L_2/L_1)^2 q \\ \left(\frac{L_2}{L_1}\right)^2 q & (L_2/L_1)^3 s \end{bmatrix} \begin{bmatrix} y_2 \\ \theta_{2z} \end{bmatrix} \\ &+ [z_2, -\theta_{2y}] \begin{bmatrix} (L_1/L_2) i & k \\ k & (L_2/L_1) j \end{bmatrix} \begin{bmatrix} z_2 \\ -\theta_{2y} \end{bmatrix} + p_2 [z_2, -\theta_{2y}] \begin{bmatrix} (L_2/L_1) r & (L_2/L_1)^2 q \\ (L_2/L_1)^2 q & (L_2/L_1)^3 s \end{bmatrix} \begin{bmatrix} z_2 \\ -\theta_{2y} \end{bmatrix} \end{aligned}, \tag{2.67}$$

$$\theta_{2x} L_1 / L_2 = m_{2x} - c(\theta_{2z} z_2 + \theta_{2y} y_2)/\delta - p_2 h(\theta_{2z} z_2 + \theta_{2y} y_2)/\delta . \tag{2.68}$$

Let $\Delta = 1 - L_2/L_1$ and be very small, we have

$$\frac{1}{1-\Delta} = \frac{1+\Delta}{1-\Delta^2} \approx 1 + \Delta . \tag{2.69}$$

Further, based on Taylor series expansion, we obtain

$$(1 \pm \Delta)^n \approx 1 \pm n\Delta . \tag{2.70}$$

Therefore, we can re-write the above equations [Equations (65)–(68)] as

$$\begin{aligned} \begin{bmatrix} f_{2z} \\ -m_{2y} \end{bmatrix} &= \begin{bmatrix} (1+\Delta)^3 a & (1+\Delta)^2 c \\ (1+\Delta)^2 c & (1+\Delta) b \end{bmatrix} \begin{bmatrix} z_2 \\ -\theta_{2y} \end{bmatrix} + p_2 \begin{bmatrix} (1+\Delta) e & h \\ h & (1-\Delta) g \end{bmatrix} \begin{bmatrix} z_2 \\ -\theta_{2y} \end{bmatrix}, \\ &= \begin{bmatrix} (1+3\Delta) a & (1+2\Delta) c \\ (1+2\Delta) c & (1+\Delta) b \end{bmatrix} \begin{bmatrix} z_2 \\ -\theta_{2y} \end{bmatrix} + p_2 \begin{bmatrix} (1+\Delta) e & h \\ h & (1-\Delta) g \end{bmatrix} \begin{bmatrix} z_2 \\ -\theta_{2y} \end{bmatrix} \end{aligned} \tag{2.71}$$

$$\begin{aligned} \begin{bmatrix} f_{2y} \\ m_{2z} \end{bmatrix} &= \begin{bmatrix} (1+\Delta)^3 a & (1+\Delta)^2 c \\ (1+\Delta)^2 c & (1+\Delta) b \end{bmatrix} \begin{bmatrix} y_2 \\ \theta_{2z} \end{bmatrix} + p_2 \begin{bmatrix} (1+\Delta) e & h \\ h & (1-\Delta) g \end{bmatrix} \begin{bmatrix} y_2 \\ \theta_{2z} \end{bmatrix}, \\ &= \begin{bmatrix} (1+3\Delta) a & (1+2\Delta) c \\ (1+2\Delta) c & (1+\Delta) b \end{bmatrix} \begin{bmatrix} y_2 \\ \theta_{2z} \end{bmatrix} + p_2 \begin{bmatrix} (1+\Delta) e & h \\ h & (1-\Delta) g \end{bmatrix} \begin{bmatrix} y_2 \\ \theta_{2z} \end{bmatrix} \end{aligned} \tag{2.72}$$

$$\begin{aligned} x_2 = (1-\Delta)\frac{p_2}{d} &+ [y_2, \theta_{2z}] \begin{bmatrix} (1+\Delta) i & k \\ k & (1-\Delta) j \end{bmatrix} \begin{bmatrix} y_2 \\ \theta_{2z} \end{bmatrix} + p_2 [y_2, \theta_{2z}] \begin{bmatrix} (1-\Delta) r & (1-\Delta)^2 q \\ (1-\Delta)^2 q & (1-\Delta)^3 s \end{bmatrix} \begin{bmatrix} y_2 \\ \theta_{2z} \end{bmatrix} \\ &+ [z_2, -\theta_{2y}] \begin{bmatrix} (1+\Delta) i & k \\ k & (1-\Delta) j \end{bmatrix} \begin{bmatrix} z_2 \\ -\theta_{2y} \end{bmatrix} + p_2 [z_2, -\theta_{2y}] \begin{bmatrix} (1-\Delta) r & (1-\Delta)^2 q \\ (1-\Delta)^2 q & (1-\Delta)^3 s \end{bmatrix} \begin{bmatrix} z_2 \\ -\theta_{2y} \end{bmatrix} \\ = (1-\Delta)\frac{p_2}{d} &+ [y_2, \theta_{2z}] \begin{bmatrix} (1+\Delta) i & k \\ k & (1-\Delta) j \end{bmatrix} \begin{bmatrix} y_2 \\ \theta_{2z} \end{bmatrix} + p_2 [y_2, \theta_{2z}] \begin{bmatrix} (1-\Delta) r & (1-2\Delta) q \\ (1-2\Delta) q & (1-3\Delta) s \end{bmatrix} \begin{bmatrix} y_2 \\ \theta_{2z} \end{bmatrix} \\ &+ [z_2, -\theta_{2y}] \begin{bmatrix} (1+\Delta) i & k \\ k & (1-\Delta) j \end{bmatrix} \begin{bmatrix} z_2 \\ -\theta_{2y} \end{bmatrix} + p_2 [z_2, -\theta_{2y}] \begin{bmatrix} (1-\Delta) r & (1-2\Delta) q \\ (1-2\Delta) q & (1-3\Delta) s \end{bmatrix} \begin{bmatrix} z_2 \\ -\theta_{2y} \end{bmatrix} \end{aligned}, \tag{2.73}$$

$$\theta_{2x}(1+\Delta) = m_{2x} - c(\theta_{2z} z_2 + \theta_{2y} y_2)/\delta - p_2 h(\theta_{2z} z_2 + \theta_{2y} y_2)/\delta . \tag{2.74}$$

It is noted that the conditions of geometric compatibility (neglecting the effect of high order term: $\theta_{sy}\Delta$ or $\theta_{sz}\Delta$) and force equilibrium remain the same.

Retaining the significant terms associated with error Δ, similarly, we obtain the three approximate analytical DOF equations as follows.

$$\theta_{sx} \approx \frac{m_x\delta + (m_z f_z + m_y f_y)e/(3a+pe) - 6a\Delta r_3 \bar{y}_s - [pr_3 - 2(m_y + (3c+ph)\bar{z}_s)]e\Delta\bar{y}_s}{3\{(1+\Delta/3)\delta + a(1+\Delta)r_3^2 + \frac{p}{3}(1+\Delta)er_3^2 + a\Delta r_3^2 - \frac{4}{3}\Delta ci\bar{z}_s r_3 - 2[m_y + (3c+ph)\bar{z}_s]\Delta e r_3/3\}} \quad (2.75)$$

where $\bar{y}_s = \dfrac{f_y}{3a+pe}$, and $\bar{z}_s = \dfrac{f_z}{3a+pe}$.

$$y_s \approx \frac{f_y - (3c+ph+2\Delta c)\bar{\theta}_{sz} + m_y\theta_{sx}e + 3\Delta(a+\frac{p}{9})r_3\theta_{sx}}{3(1+\Delta)a + p(1+\Delta/3)e - 2[m_y + (3c+ph)z_s]\Delta e/(3r_3)} \quad (2.76)$$

where $\bar{\theta}_{sz} = \dfrac{2}{3r_3^2}[\dfrac{1}{d} + (\bar{y}_s^2 + \bar{z}_s^2)r][m_z - (3c+ph)\bar{y}_s]$.

$$z_s \approx \frac{f_z + (3c+ph+2\Delta c)\bar{\theta}_{sy} + m_z\theta_{sx}e}{3(1+\Delta)a + p(1+\Delta/3)e - 2[m_y + (3c+ph)z_s]\Delta e/(3r_3)} \quad (2.77)$$

where $\bar{\theta}_{sy} = \dfrac{2}{3r_3^2}[\dfrac{1}{d} + (\bar{y}_s^2 + \bar{z}_s^2)r][m_y + (3c+ph)\bar{z}_s]$.

Equations (2.75) and (2.76) show that the transverse translational displacement along the Y-axis, y_s, can cause the torsion about the X-axis when $\Delta \neq 0$, vice versa. These conclusions can help us recognise which beam's length is different from that of the other two beams by the following steps:

a) Applying a transverse force, parallel to a side of the triangular formed by the three tips of the three-beam modules, on the centre of the motion stage;

b) If the transverse force causes a transverse translational displacement and also brings coupled torsion without any other transverse translation, then the one beam, separated at one side by the caused translation, has length error.

e) Linear analytical method

If the effects of load-stiffening and elastokinematic non-linearities in Equations (2.1)–(2.4) are all neglected, the linear load-displacement equations of the tip of the i_0-th beam are:

$$\begin{cases} \begin{bmatrix} f_{i_0 y} \\ m_{i_0 z} \end{bmatrix} = \begin{bmatrix} a & c \\ c & b \end{bmatrix} \begin{bmatrix} y_{i_0} \\ \theta_{i_0 z} \end{bmatrix} \\ \begin{bmatrix} f_{i_0 z} \\ -m_{i_0 y} \end{bmatrix} = \begin{bmatrix} a & c \\ c & b \end{bmatrix} \begin{bmatrix} z_{i_0} \\ -\theta_{i_0 y} \end{bmatrix} \\ x_{i_0} = \dfrac{1}{d} p_{i_0} + [y_{i_0}, \theta_{i_0 z}] \begin{bmatrix} i & k \\ k & j \end{bmatrix} \begin{bmatrix} y_{i_0} \\ \theta_{i_0 z} \end{bmatrix} + [z_{i_0}, -\theta_{i_0 y}] \begin{bmatrix} i & k \\ k & j \end{bmatrix} \begin{bmatrix} z_{i_0} \\ -\theta_{i_0 y} \end{bmatrix} \\ \theta_{i_0 x} = m_{i_0 x} - c(\theta_{i_0 z} z_{i_0} + \theta_{i_0 y} y_{i_0})/\delta \end{cases} . \quad (2.78)$$

Using Equation (2.65), and following the solution process in Section 2.2.1, one can

obtain the linear load-displacement equations of the motion stage as

$$\begin{cases} \theta_{sx} \approx \dfrac{m_x \delta}{3(\delta + ar_3^2)}; \quad \theta_{sy} \approx \dfrac{2}{3r_3^2 d}(m_y + 3c\bar{z}_s) - 2\theta_{sx}\bar{y}_s i; \quad \theta_{sz} \approx \dfrac{2}{3r_3^2 d}(m_z - 3c\bar{y}_s) - 2\theta_{sx}\bar{z}_s i \\ y_s \approx \dfrac{f_y - (3c + ph)\theta_{sz}}{3a}; \quad z_s \approx \dfrac{f_z + (3c + ph)\theta_{sy}}{3a} \\ x_s \approx \dfrac{p}{3d} + y_s^2 i + z_s^2 i + r_3^2 \theta_{sx}^2 i + 2(y_s\theta_{sz} - z_s\theta_{sy})k \end{cases} \tag{2.79}$$

where $\bar{y}_s = f_y / 3a$, and $\bar{z}_s = f_z / 3a$.

Figures 2.7–2.9 show a comparison of results using linear and nonlinear approximate analytical methods for $m_x = m_y = m_z = 0$ (in which case, θ_{sx}=0). Figure 2.9 also shows that Equation (2.79) only captures the effects of dominant loads (such as m_z, f_y) upon the rotational displacements (like θ_{sz}) while the nonlinear equation [Equation (2.29)] captures the effects of all loads upon the rotational displacements. Thus, the linear equations may be applicable under a very small range of deflection, such as that indicated by the rectangular area in Figure 2.9 drawn for 1.65% error compared with the nonlinear analysis.

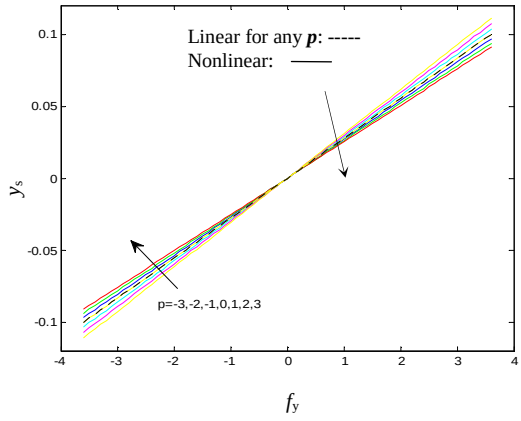

Figure 2.7 Primary motion in the Y direction

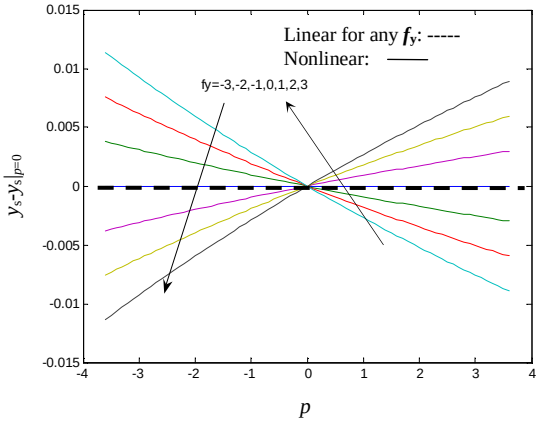

Figure 2.8 Load-stiffening effect

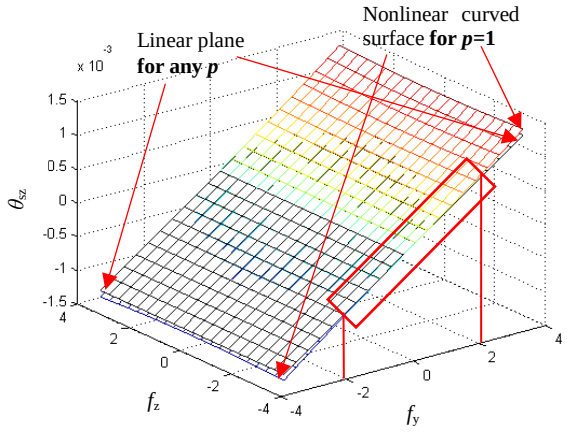

Figure 2.9 Rotational angle about the Z-axis

If the purely kinematic component in Equation (2.3) is also neglected, the single beam load-displacement equations are simplified and the approximate linear load-displacement equations of the motion stage, similar to the ones used in [2.3–2.4] will be discussed in detail in *Appendix C* that mainly deals with the mobility analysis of spatial compliant parallel multi-beam modules.

2.3 FEA Verification for the Spatial Three-Beam Module

The displacements obtained for the example spatial three-beam module using FEA method are compared with the three nonlinear methods in Table 2.2. Here, we choose *Comsol large-displacement module* for FEA using tetrahedron element with fine mesh, which has been frequently adopted for verification by other researchers. The translational displacements obtained using FEA method were given directly by the software, and the rotational angles were calculated from the displacements of points: o_1, o_2, and o_3 using Equations (2.9), (2.10) and (2.12). The other nonlinear results were obtained by first normalizing the loads then substituting these into the analytical equations correspondingly to obtain the normalized translational displacements and the actual rotational angles (radians). The actual translational displacements (mm) were then obtained through multiplying the normalized translational displacements by L.

Table 2.2 shows that the displacement errors (|(analytical result − FEA result)/analytical result|×100%) between FEA method and anyone of the three nonlinear methods are within 3.5% and considerably less for θ_{sx} (|analytical result − FEA result|). As mentioned earlier, it can be observed from Table 2.2 that the two bending angles, θ_{sz} and θ_{sy}, are approximately two orders smaller than the normalized transverse

translational displacements, y_s and z_s, respectively, and the torsional angle, θ_{sx}, is 3.33×10^{-6} small.

Displacements / *Methods*	Y_s (mm)	y_s	Z_s (mm)	z_s	X_s (mm)	x_s	θ_{sz} (radian)	θ_{sy} (radian)	θ_{sx} (radian)
FEA method	1.0050	**0.02010**	0.0403	**8.0534×10^{-4}**	−0.0120	**-2.3958×10^{-4}**	2.5980×10^{-4}	-1.0802×10^{-5}	3.3333×10^{-6}
Approximate analytical method	0.9985	**0.01998**	0.0400	**8.0000×10^{-4}**	−0.0120	**-2.3958×10^{-4}**	2.6690×10^{-4}	-1.0682×10^{-5}	0
Improved approximate analytical method	1.0050	**0.02012**	0.0403	**8.0534×10^{-4}**	−0.0121	**-2.4279×10^{-4}**	2.6869×10^{-4}	-1.0753×10^{-5}	6.5715×10^{-15}
Numerical method	1.0050	**0.02012**	0.0403	**8.0533×10^{-4}**	−0.0121	**-2.4280×10^{-4}**	2.6631×10^{-4}	-1.0658×10^{-5}	-2.8988×10^{-15}
Error between approximate analytical and FEA methods	0.65 %		0.74 %		0.00 %		2.66%	1.10 %	3.3333×10−6
Error between improved approximate analytical and FEA methods	0.00%		0.00 %		0.82 %		3.30%	0.65 %	3.3333×10−6
Error between numerical and FEA methods	0.00 %		0.00 %		0.82 %		2.44%	2.87 %	3.3333×10−6

Table 2.2 Comparisons of results between FEA and nonlinear methods for P=10N, F_z=10N, F_y=249.59N, M_x=M_y=M_z=0

Figures 2.10–2.13 show more results obtained using both the FEA and the approximate analytical equations [Equations (2.28), (2.29), (2.33), (2.34), (2.36) and (2.39)] without moments acting. It can be learnt from these figures that the average errors between the analytical results and FEA results for a given force are acceptable. This verifies the accuracy of the proposed nonlinear equations for the spatial three-beam module.

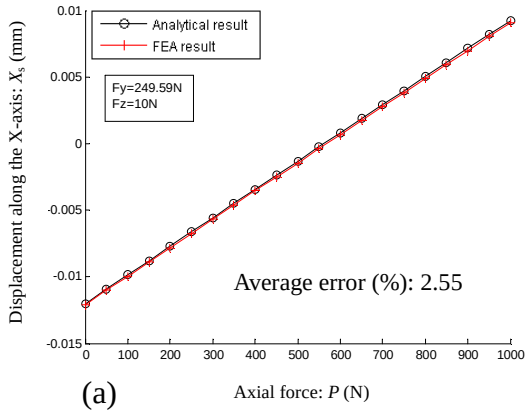

(a)

Figure 2.10 Axial displacement (a) against axial force P, and (b) against transverse force F_y

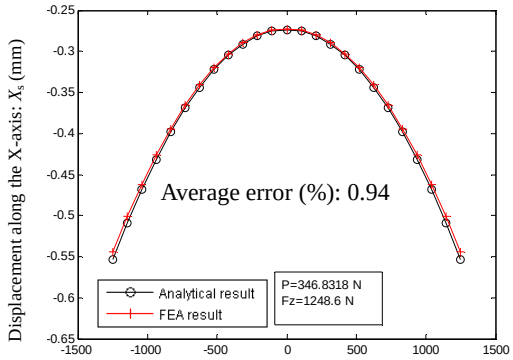

(b)

Figure 2.10 Axial displacement (a) against axial force P, and (b) against transverse force F_y ((continued))

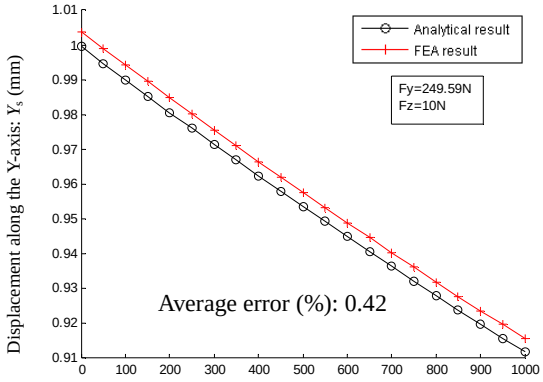

(a)

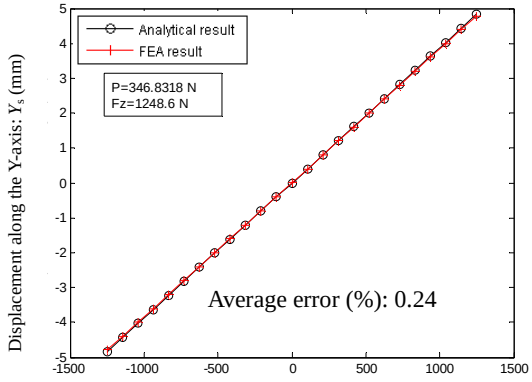

(b)

Figure 2.11 Y-displacement: (a) load-stiffening effect, and (b) primary motion

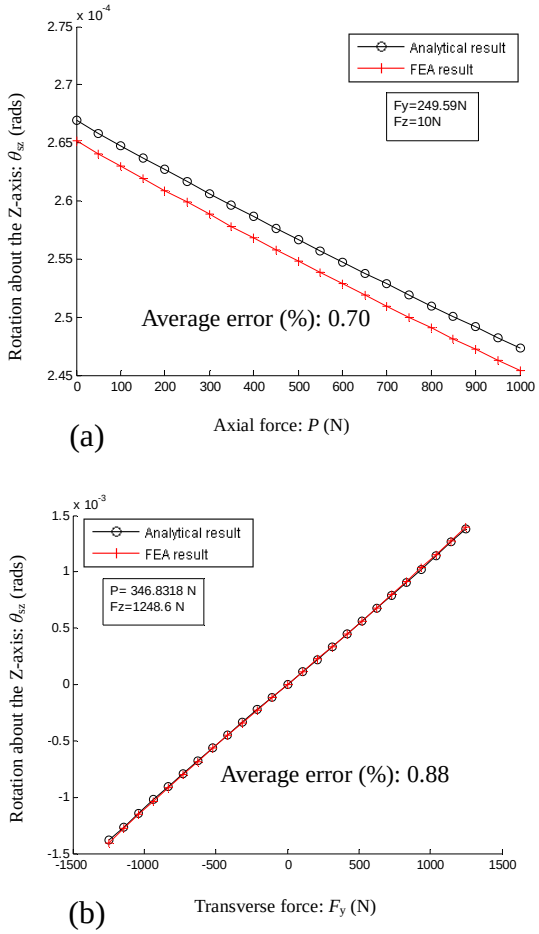

Figure 2.12 Bending angle about the Z-axis (a) against axial force P, and (b) against transverse force F_y

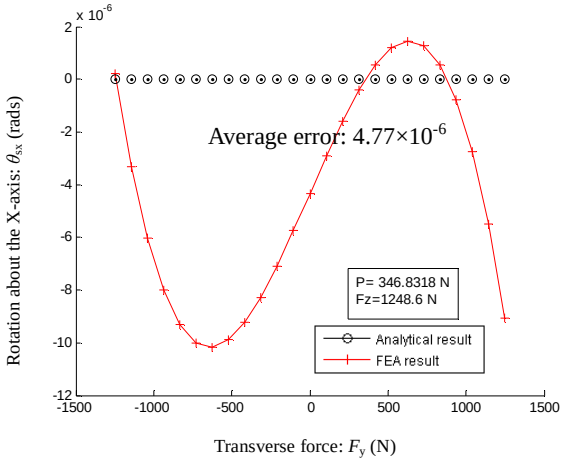

Figure 2.13 Torsional angle against transverse force F_y

If only the torsional moment, $M_x=GI_p/L=1.3069\times10^4$ Nmm, is imposed on the motion stage, the analytical result using Equation (2.36) and the FEA result of the rotational angle θ_{sx} are respectively 0.0495 rad and 0.0494 rad, an error of about 0.2%.

A prototype of a three-beam module, made of engineering plastic, has been fabricated using a 3-D printer for initial qualitative analysis (see *Appendix D* for details). The preliminary test results with the prototype comply with the modelling presented in this chapter.

It should be pointed out that we did not conduct experiment verification for the derived nonlinear methods due to our current financial limitation considering the costly manufacture or experimental measurement (relate to sensors etc) accuracy required although experiment is a better choice.

2.4 Analysis of Spatial Multi-Beam Modules

2.4.1 Approximate analytical method

In this section, we will deal briefly with spatial multi-beam modules, proposed using the constraint-based design approach, with more than three beams only having three in-plane DOF, in particular five classes of multi-beam module with different layouts of beams. As in the case of the spatial three-beam module, the loads are taken to be acting at the centre of the motion stage, and the coordinate system, displacements and loads are defined in the same way. Figure 2.14 shows spatial six-beam modules with a variety of layouts.

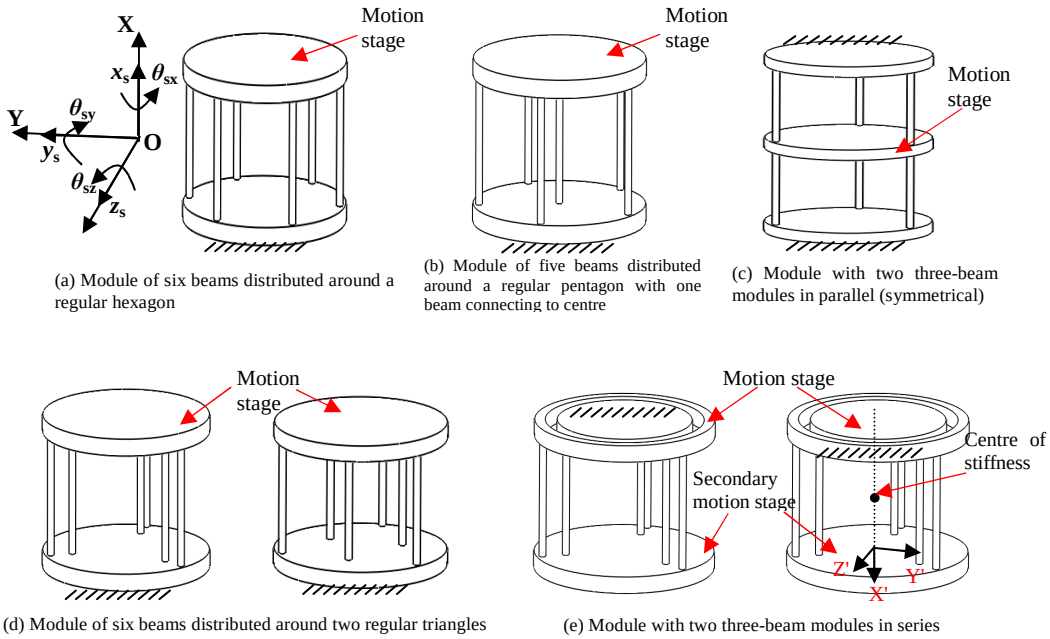

(a) Module of six beams distributed around a regular hexagon

(b) Module of five beams distributed around a regular pentagon with one beam connecting to centre

(c) Module with two three-beam modules in parallel (symmetrical)

(d) Module of six beams distributed around two regular triangles

(e) Module with two three-beam modules in series

Figure 2.14 Spatial six-beam modules with round cross-section beams

In the following, we limit ourselves to spatial multi-beam modules, which have an even number of beams, *n*, and in which all identical and uniform beams are uniformly distributed around a circle [Figure 2.14a].

The approximate analytical load-displacement equations for the motion stages of the spatial four-beam and six-beam modules can be obtained in a similar way to the approximate analytical method for the spatial three-beam module as detailed in Sections 2.1 and 2.2:

$$\begin{cases} \theta_{sx} \approx \dfrac{m_x\delta+(m_z f_z+m_y f_y)e/(4a+pe)}{4(\delta+ar_4^2+\dfrac{p}{4}er_4^2)} \\ y_s \approx \dfrac{f_y+m_y\theta_{sx}e}{4a+pe} \\ z_s \approx \dfrac{f_z+m_z\theta_{sx}e}{4a+pe} \\ \theta_{sy} \approx \dfrac{1}{2r_4^2}(\dfrac{1}{d}+y_s^2r+z_s^2r)[m_y+(4c+ph)z_s]-2\theta_{sx}y_s i \\ \theta_{sz} \approx \dfrac{1}{2r_4^2}(\dfrac{1}{d}+y_s^2r+z_s^2r)[m_z-(4c+ph)y_s]-2\theta_{sx}z_s i \\ x_s \approx \dfrac{p}{4d}+(y_s^2+z_s^2)i+\dfrac{p}{4}(y_s^2+z_s^2)r+r_4^2\theta_{sx}^2 i+\dfrac{p}{4}r_4^2\theta_{sx}^2 r+2(y_s\theta_{sz}-z_s\theta_{sy})k-\dfrac{1}{2}(m_y y_s+m_z z_s)\theta_{sx}r \end{cases},$$

(2.80)

$$\begin{cases} \theta_{sx} \approx \dfrac{m_x\delta+(m_z f_z+m_y f_y)e/(6a+pe)}{6(\delta+ar_6^2+\dfrac{p}{6}er_6^2)} \\ y_s \approx \dfrac{f_y+m_y\theta_{sx}e}{6a+pe} \\ z_s \approx \dfrac{f_z+m_z\theta_{sx}e}{6a+pe} \\ \theta_{sy} \approx \dfrac{1}{3r_6^2}(\dfrac{1}{d}+y_s^2r+z_s^2r)[m_y+(6c+ph)z_s]-2\theta_{sx}y_s i \\ \theta_{sz} \approx \dfrac{1}{3r_6^2}(\dfrac{1}{d}+y_s^2r+z_s^2r)[m_z-(6c+ph)y_s]-2\theta_{sx}z_s i \\ x_s \approx \dfrac{p}{6d}+(y_s^2+z_s^2)i+\dfrac{p}{6}(y_s^2+z_s^2)r+r_6^2\theta_{sx}^2 i+\dfrac{p}{6}r_6^2\theta_{sx}^2 r+2(y_s\theta_{sz}-z_s\theta_{sy})k-\dfrac{1}{3}(m_y y_s+m_z z_s)\theta_{sx}r \end{cases}.$$

(2.81)

It is noted that Equation (2.80) can be used to deal with the spatial four-beam module with square cross-section in the following layouts (Figure 2.15).

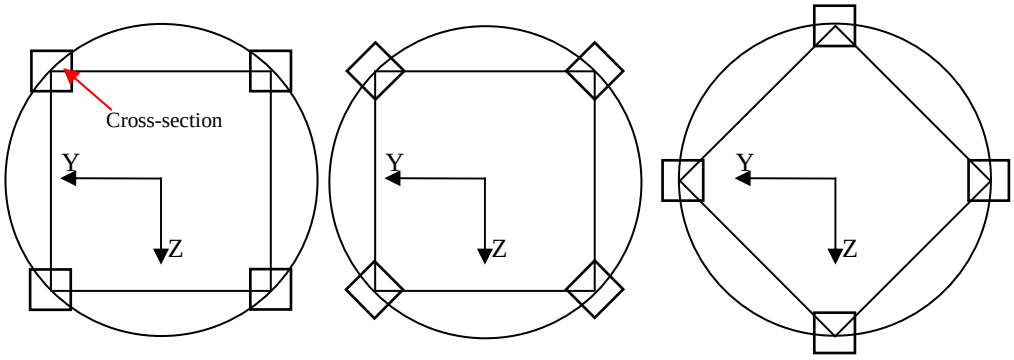

a) Layout 1 b) Layout 2 c) Layout 3

Figure 2.15 Top view illustrations for the square cross-section layouts in the four-beam modules with same pitch circle radius

The general load-displacement equations for spatial multi-beam modules can be summarized as follows:

$$
\begin{cases}
\theta_{sx} \approx \dfrac{m_x\delta + (m_z f_z + m_y f_y)e/(na+pe)}{n(\delta + ar_n^2 + \dfrac{p}{n}er_n^2)} \\
y_s \approx \dfrac{f_y + m_y\theta_{sx}e}{na+pe} \\
z_s \approx \dfrac{f_z + m_z\theta_{sx}e}{na+pe} \\
\theta_{sy} \approx \dfrac{1}{4r_n^2\sum\limits_{i_0=1(odd)}^{n/2}[\cos\dfrac{i_0\pi}{n}]^2}(\dfrac{1}{d}+y_s^2r+z_s^2r)[m_y+(nc+ph)z_s]-2\theta_{sx}y_s i \\
\quad = \dfrac{2}{nr_n^2}(\dfrac{1}{d}+y_s^2r+z_s^2r)[m_y+(nc+ph)z_s]-2\theta_{sx}y_s i \\
\theta_{sz} \approx \dfrac{1}{4r_n^2\sum\limits_{i_0=1(odd)}^{n/2}[\sin\dfrac{i_0\pi}{n}]^2 - j_0 2r_n^2}(\dfrac{1}{d}+y_s^2r+z_s^2r)[m_z-(nc+ph)y_s]-2\theta_{sx}z_s i \\
\quad = \dfrac{2}{nr_n^2}(\dfrac{1}{d}+y_s^2r+z_s^2r)[m_z-(nc+ph)y_s]-2\theta_{sx}z_s i \\
x_s \approx \dfrac{p}{nd}+(y_s^2+z_s^2)i+\dfrac{p}{n}(y_s^2+z_s^2)r+r_n^2\theta_{sx}^2 i+\dfrac{p}{n}r_n^2\theta_{sx}^2 r+2(y_s\theta_{sz}-z_s\theta_{sy})k-\dfrac{2}{n}(m_y y_s+m_z z_s)\theta_{sx}r
\end{cases}
\tag{2.82}
$$

where, $j_0 = \begin{cases} 0 & \text{for } n/4 = \text{int} \\ 1 & \text{for } n/4 \neq \text{int} \end{cases}$, the beam number n is even and $n < \dfrac{2\pi r_n}{D_0/L}$, r_n denotes the nondimensional pitch circle radius of the beam tips. Equation (2.82) reveals that the buckling load is p=10n for the spatial multi-beam module composed of n beams. If the torque is normalized by EI/L, the torsional angle becomes

$$\theta_{sx} \approx [m_x + (m_z f_z + m_y f_y)e/(na + pe)]/[n(\delta + ar_n^2 + \frac{p}{n} er_n^2)].$$

Apparently, the multi-beam module has better dynamic performance of high band-width and larger buckling load without affecting the maximal allowable motion range with the increase of the number of beams, but in turn results in large primary motion stiffness. In addition, with the increase of the beam number, the bending angle (such as θ_{sy}) does not change if only the transverse force (such as f_z) is applied.

2.4.2 Discussions

In practice, in order to apply the proposed nonlinear methods of the multi-beam modules to the analysis of CPMs, *all moments should be unified to be normalized by EI/L***.** Therefore, in the derivation for other spatial multi-beam modules with different layouts and the later chapters, we all assume that all moments are normalized by *EI*/*L*.

The system shown in Figure 2.14c is obtained by symmetrically arranging two three-beam modules as building blocks in parallel. This system is kinematically decoupled if only transverse forces are applied, but has larger load-stiffening effect if there is a large transverse motion. The larger load-stiffening effect results from the augmentation of transverse stiffness in the presence of gradually increased axial tension-force in the configuration of two symmetrical three-beam modules, as shown in the transverse displacement equations of the spatial three-beam module [Equations (2.33) and (2.34)].

The spatial six-beam module shown in Figure 2.14e (also spatial double three-beam module) is obtained by connecting two three-beam modules as two building blocks in series. As it will be shown in the following approximate analytical load-displacement equations, this system has approximately half the primary stiffness and doubles the motion range of the single three-beam module, and can especially alleviate the load-stiffening effect compared with the system shown in Figure 2.14c. In addition, the spatial double three-beam module can approximately eliminate the purely kinematic effect upon its axial displacement as the transverse forces and torque imposed on the secondary motion stage produce positive axial displacement, while the transverse forces and torque imposed on the motion stage produce negative axial displacement. Therefore, compared with the spatial three-beam module, this spatial double three-beam module is a better option acting as the building block of new CPMs, and is suitable for the symmetrical design.

We take the one on the right-hand side in Figure 2.14e for detailed consideration. Let θ_{sx1}, θ_{sy1}, θ_{sz1}, x_{s1}, y_{s1}, z_{s1} be the displacement components of the motion stage with respect to the global coordinate system O-XYZ, which results from the inner three-beam module deformation alone, θ_{sx2}, θ_{sy2}, θ_{sz2}, x_{s2}, y_{s2}, z_{s2} be the displacements of the secondary stage with respect to the local coordinate system O'-X'Y'Z', which results from the outer three-beam module deformation alone, and the applied torque is normalized by EI/L.

Equations (2.28), (2.29), (2.33), (2.34), (2.37) and (2.39) give

$$\theta_{sx1} = \frac{1}{3(\delta + ar_3^2 + \frac{p}{3}er_3^2)}[m_x + \frac{e}{3a+pe}(m_z f_z + m_y f_y)], \tag{2.83a}$$

$$y_{s1} \approx \frac{f_y + m_y\theta_{sx1}e}{3a+pe}, \tag{2.83b}$$

$$z_{s1} \approx \frac{f_z + m_z\theta_{sx1}e}{3a+pe}, \tag{2.83c}$$

$$\theta_{sy1} \approx \frac{1}{3r_3^2}(\frac{1}{d} + y_{s1}^2 r + z_{s1}^2 r)(m_y + (3c+ph)z_{s1}) - 2i\theta_{sx1}y_{s1}, \tag{2.83d}$$

$$\theta_{sz1} \approx \frac{1}{3r_3^2}(\frac{1}{d} + y_{s1}^2 r + z_{s1}^2 r)(m_z - (3c+ph)y_{s1}) - 2i\theta_{sx1}z_{s1}, \tag{2.83e}$$

$$\begin{aligned} x_{s1} \approx{}& \frac{p}{3d} + (y_{s1}^2 + z_{s1}^2)i + \frac{p}{3}(y_{s1}^2 + z_{s1}^2)r + r_3^2\theta_{sx1}^2 i + \frac{p}{3}r_3^2\theta_{sx1}^2 r \\ &+ 2(y_{s1}\theta_{sz1} - z_{s1}\theta_{sy1})k - \frac{2}{3}(m_y y_{s1} + m_z z_{s1})\theta_{sx1}r \end{aligned} \tag{2.83f}$$

where r_3 is the radius of the pitch circle around which the inner three beam are uniformly spaced.

We use the applied moments acting in the secondary stage in the deformed configuration to further obtain

$$\begin{aligned} \theta_{sx2} &= \frac{1}{3(\delta + ar_3'^2 - \frac{p}{3}er_3'^2)}\{-m_x + \frac{e}{3a-pe}[(m_z + f_y - py_{s1})f_z + (-m_y + f_z - pz_{s1})(-f_y)]\} \\ &= -\frac{1}{3(\delta + ar_3'^2 - \frac{p}{3}er_3'^2)}[m_x - \frac{e}{3a-pe}(m_z f_z + m_y f_y + f_y m_z\theta_{sx1}e - f_z m_y\theta_{sx1}e)] \end{aligned}, \tag{2.83g}$$

$$y_{s2} \approx \frac{-f_y + [-m_y + f_z - pz_{s1}]\theta_{sx2}e}{3a-pe}, \tag{2.83h}$$

$$z_{s2} \approx \frac{f_z + [m_z + f_y - py_{s1}]\theta_{sx2}e}{3a-pe}, \tag{2.83i}$$

$$\theta_{sy2} \approx (\frac{1}{3r_3^{'2}}(\frac{1}{d} + y_{s2}^2 r + z_{s2}^2 r)[-m_y + f_z - pz_{s1}) + (3c - ph)z_{s2}] - 2i\theta_{sx2}y_{s2}, \quad (2.83j)$$

$$\theta_{sz2} \approx (\frac{1}{3r_3^{'2}}(\frac{1}{d} + y_{s2}^2 r + z_{s2}^2 r)[(m_z + f_y - py_{s1}) - (3c - ph)y_{s2}] - 2i\theta_{sx2}z_{s2}, \quad (2.83k)$$

$$\begin{aligned} x_{s2} \approx & \frac{-p}{3d} + (y_{s2}^2 + z_{s2}^2)i + \frac{-p}{3}(y_{s2}^2 + z_{s2}^2)r + r_3^{'2}\theta_{sx2}^2 2i + \frac{-p}{3}r_3^{'2}\theta_{sx2}^2 r + 2(y_{s2}\theta_{sz2} - z_{s2}\theta_{sy2})k \\ & -\frac{2}{3}[(-m_y + f_z - pz_{s1})y_{s2} + (m_z + f_y - py_{s1})z_{s2}]\theta_{sx2}r \end{aligned} \quad (2.83l)$$

where r_3' is the radius of the pitch circle around which the outer three beams are uniformly spaced.

Then, we have the displacements of the motion stage of the spatial double three-beam module as

$$\theta_{sx} = \theta_{sx1} - \theta_{sx2}, \quad (2.84a)$$

$$y_s \approx y_{s1} - y_{s2} + \theta_{sz2}, \quad (2.84b)$$

$$z_s \approx z_{s1} + z_{s2} + \theta_{sy2}, \quad (2.84c)$$

$$\theta_{sy} \approx \theta_{sy1} - \theta_{sy2}, \quad (2.84d)$$

$$\theta_{sz} \approx \theta_{sz1} + \theta_{sz2}, \quad (2.84e)$$

$$x_s \approx x_{s1} - x_{s2}. \quad (2.84f)$$

Substituting Equations (2.83a) to (2.83l) into Equation (2.84), we obtain the displacements of the motion stage under applied loads.

If the tosional angle is constrained to be as small as the two bending angles, for example, the spatial module is used as the building block of the translational CPMs, Equation (2.84) can be simplified as

$$y_s \approx \frac{f_y}{3a + pe} + \frac{f_y}{3a - pe} = \frac{6af_y}{(3a)^2 - (pe)^2}, \quad (2.85a)$$

$$z_s \approx \frac{f_z}{3a + pe} + \frac{f_z}{3a - pe} = \frac{6af_z}{(3a)^2 - (pe)^2}, \quad (2.85b)$$

$$\begin{aligned} x_s \approx & \frac{p}{3d} + \frac{(f_y^2 + f_z^2)}{(3a + ep)^2}i + \frac{p}{3}\frac{(f_y^2 + f_z^2)}{(3a + ep)^2}r - (-\frac{p}{3d} + \frac{(f_y^2 + f_z^2)}{(3a - ep)^2}i - \frac{p}{3}\frac{(f_y^2 + f_z^2)}{(3a - ep)^2}r) \\ = & \frac{2p}{3d} - 12p\frac{(f_y^2 + f_z^2)}{((3a)^2 - (ep)^2)^2}aei + \frac{2p}{3}\frac{(f_y^2 + f_z^2)}{((3a)^2 - (ep)^2)^2}((3a)^2 + (ep)^2)r \\ \approx & \frac{2p}{3d} - \frac{p}{3a}(y_s^2 + z_s^2)ei + \frac{p}{6}(y_s^2 + z_s^2)r \end{aligned}, \quad (2.85c)$$

$$\theta_{sy} \approx \frac{1}{3r_3^2}\left(\frac{1}{d}+\frac{(f_y^2+f_z^2)}{(3a+ep)^2}r\right)\left(m_y+(3c+ph)\frac{f_z}{3a+pe}\right) + \frac{1}{3r_3'^2}\left(\frac{1}{d}+\frac{(f_y^2+f_z^2)}{(3a-ep)^2}\right)\left(m_y-f_z\cdot 1+p\frac{f_z}{3a+pe}+(3c-ph)\frac{-f_z}{3a-pe}\right), \quad (2.85d)$$

$$\theta_{sz} \approx \frac{1}{3r_3^2}\left(\frac{1}{d}+\frac{(f_y^2+f_z^2)}{(3a+ep)^2}r\right)\left(m_z-(3c+ph)\frac{f_y}{3a+pe}\right) - \frac{1}{3r_3'^2}\left(\frac{1}{d}+\frac{(f_y^2+f_z^2)}{(3a-ep)^2}\right)\left(-(m_z+f_y\cdot 1-p\frac{f_y}{3a+pe})-(3c-ph)\frac{f_y}{3a-pe}\right), \quad (2.85e)$$

$$\begin{aligned}\theta_{sx} &= \frac{1}{3(\delta+ar_3^2+\frac{p}{3}er_3^2)}[m_x+(m_z\frac{f_z}{3a+pe}+m_y\frac{f_y}{3a+pe})\cdot e] \\ &\quad -\frac{1}{3(\delta+ar_3'^2-\frac{p}{3}er_3'^2)}[-m_x+(-(m_z+f_y-p\frac{f_y}{3a+pe})(\frac{-f_z}{3a-pe}) \\ &\quad +(m_y-f_z+p\frac{f_z}{3a+pe})\frac{f_y}{3a-pe})\cdot e] \\ &= \frac{1}{3(\delta+ar_3^2+\frac{p}{3}er_3^2)}[m_x+\frac{e}{3a+pe}(m_z f_z+m_y f_y)] \\ &\quad -\frac{1}{3(\delta+ar_3'^2-\frac{p}{3}er_3'^2)}[-m_x+\frac{e}{3a-pe}(m_z f_z+m_y f_y)]\end{aligned} \quad . \quad (2.85f)$$

From Equations (2.85d) and (2.85e), we can conclude that when we only exert two transverse forces at the symmetric centre of all beams on the motion stage, all parasitic rotational displacements are eliminated. This action position refers to the *centre of stiffness* [2.16] (see Figure 2.14e). In addition, Equation (2.85c) reveals that the axial displacement is equal to zero if no axial force is exerted.

Similarly, the approximate analytical load-displacement equations for a spatial double four-beam module (i.e. spatial eight-beam module) under very small torsional angle can be given as follows.

$$y_s \approx \frac{f_y}{4a+pe}+\frac{f_y}{4a-pe}=\frac{8af_y}{(4a)^2-(pe)^2}, \quad (2.86a)$$

$$z_s \approx \frac{f_z}{4a+pe}+\frac{f_z}{4a-pe}=\frac{8af_z}{(4a)^2-(pe)^2}, \quad (2.86b)$$

$$\begin{aligned}x_s &\approx \frac{p}{4d}+\frac{(f_y^2+f_z^2)}{(4a+ep)^2}i+\frac{p}{4}\frac{(f_y^2+f_z^2)}{(4a+ep)^2}r-(-\frac{p}{4d}+\frac{(f_y^2+f_z^2)}{(4a-ep)^2}i-\frac{p}{4}\frac{(f_y^2+f_z^2)}{(4a-ep)^2}r) \\ &= \frac{p}{2d}-16p\frac{(f_y^2+f_z^2)}{[(4a)^2-(ep)^2]^2}aei+\frac{p}{2}\frac{(f_y^2+f_z^2)}{[(4a)^2-(ep)^2]^2}[(4a)^2+(ep)^2]r \\ &\approx \frac{p}{2d}-\frac{p}{4a}(y_s^2+z_s^2)ei+\frac{p}{8}(y_s^2+z_s^2)r\end{aligned} \quad , \quad (2.86c)$$

$$\theta_{sy} \approx \frac{1}{2r_4^2}\left(\frac{1}{d}+\frac{(f_y^2+f_z^2)}{(4a+ep)^2}r\right)\left(m_y+(4c+ph)\frac{f_z}{4a+pe}\right) + \frac{1}{2r_4'^2}\left(\frac{1}{d}+\frac{(f_y^2+f_z^2)}{(4a-ep)^2}\right)\left(m_y-f_z\cdot 1+p\frac{f_z}{4a+pe}+(4c-ph)\frac{-f_z}{4a-pe}\right), \quad (2.86d)$$

$$\theta_{sz} \approx \frac{1}{2r_4^2}\left(\frac{1}{d}+\frac{(f_y^2+f_z^2)}{(4a+ep)^2}r\right)\left(m_z-(4c+ph)\frac{f_y}{4a+pe}\right) - \frac{1}{2r_4'^2}\left(\frac{1}{d}+\frac{(f_y^2+f_z^2)}{(4a-ep)^2}\right)\left(-\left(m_z+f_y\cdot 1-p\frac{f_y}{4a+pe}\right)-(4c-ph)\frac{f_y}{4a-pe}\right), \quad (2.86e)$$

$$\begin{aligned}\theta_{sx} &= \frac{1}{4\left(\delta+ar_4^2+\frac{p}{4}er_4^2\right)}\left[m_x+\left(m_z\frac{f_z}{4a+pe}+m_y\frac{f_y}{4a+pe}\right)\cdot e\right] \\ &\quad -\frac{1}{4\left(\delta+ar_4'^2-\frac{p}{4}er_4'^2\right)}\left[-m_x+\left(-\left(m_z+f_y-p\frac{f_y}{4a+pe}\right)\left(\frac{-f_z}{4a-pe}\right)\right.\right. \\ &\quad \left.\left.+\left(m_y-f_z+p\frac{f_z}{4a+pe}\right)\frac{f_y}{4a-pe}\right)\cdot e\right] \\ &= \frac{1}{4\left(\delta+ar_4^2+\frac{p}{4}er_4^2\right)}\left[m_x+\frac{e}{4a+pe}(m_z f_z+m_y f_y)\right] \\ &\quad -\frac{1}{4\left(\delta+ar_4'^2-\frac{p}{4}er_4'^2\right)}\left[-m_x+\frac{e}{4a-pe}(m_z f_z+m_y f_y)\right]\end{aligned} \quad (2.86f)$$

where r_4' (or r_4) is the radius of the pitch circle around which the outer (inner) four beams are uniformly spaced. The motion stage is supported by the inner four-beam.

Note that if the spatial double multi-beam modules are used independently as a planar motion stage, the large torsional moment acting at motion stage doesn't cause the axial displacement under the condition of two equal pitch circle radii such as $r_4'=r_4$. A CAD prototype of spatial double four-beam module in this case is shown in Figure 2.16.

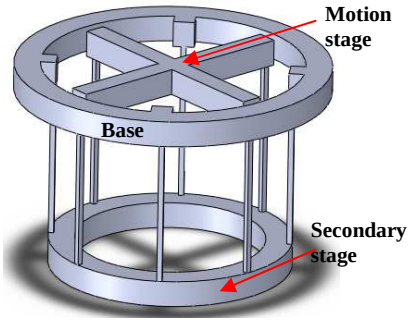

Figure 2.16 A CAD prototype of spatial double four-beam module with two equal pitch circle radii

In addition, the analysis of several other multi-beam modules with different layouts is also performed in *Appendix E*.

2.5 Other Compliant Parallel Modules: Compliant Prismatic Joints

In addition to the spatial multi-beam modules proposed and analysed in Sections 2.1 to 2.4, there are other compliant parallel modules that can be used as building blocks of large-range translational CPMs.

Figure 2.17 shows several other compliant parallel modules: compliant prismatic joints proposed and studied in detail in [2.6, 2.17 and 2.18]. These modules have distributed compliance to produce large range of motion compared with their counterparts with lumped-compliance. It is noted that these modules in Figures 2.17a, 2.17b and 2.17c are planar modules and that in Figure 2.17d is a spatial module having planar motion. Here, the module in Figure 2.17c is also a displacement amplifier.

In the following chapters, we will demonstrate how to use these modules or their variations to construct new translational CPMs.

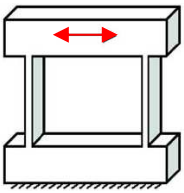

a) Basic parallelogram module [2.6]

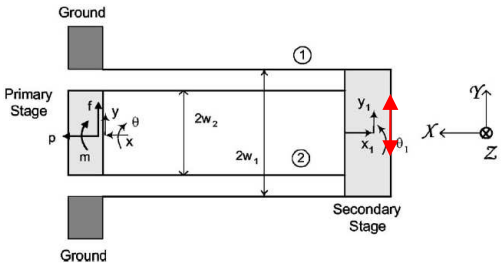

b) Double parallelogram module [2.6]

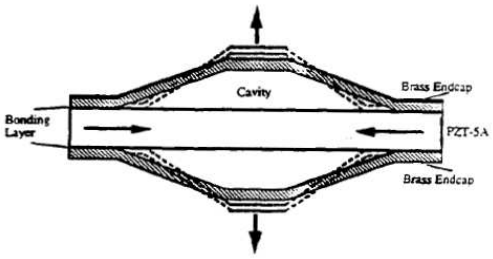

c) Cymbal displacement amplifier

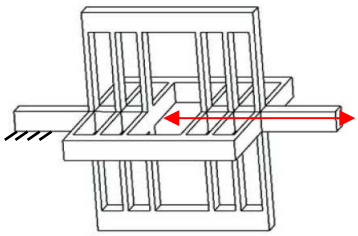

d) Large-range prismatic joint [2.17]

Figure 2.17 Compliant prismatic joints

2.6 Summary

The nonlinear and analytical load-displacement equations of a class of spatial multi-beam modules, with round or regular polygon cross-section beams, have been formulated and analysed by mathematical transformation and substitution. A method has also been presented to analyse the spatial combined deformation of compliant beams or mechanisms.

For a set of given payloads exerted on the motion stage of the spatial three-beam

module, one can obtain quickly the displacements using the proposed nonlinear methods as compared with FEA or other numerical methods. In particular, the proposed nonlinear analytical methods can capture the accurate constraint characteristics, which can guide the design for the new CPMs, of the spatial three-beam module fast, and enables rapid design synthesis. The larger the pitch circle radius of beam tips, the smaller the absolute value of the torsional angle and therefore the more accurate the proposed approximate analytical method. It has been verified using the large-deflection FEA that the accuracy of the proposed approximate analytical method is acceptable.

For the spatial multi-beam modules including spatial double layer modules (double three-beam/double four-beam module), the comparisons of some characteristics among them are performed to identify the better building blocks. We can conclude that the spatial double layer modules, such as the spatial double three-beam and spatial double four-beam modules, are preferred as building blocks of new translational CPMs.

2.7 References

[2.1] Lobontiu, N., 2002, *Compliant Mechanisms: Design of Flexure Hinges*, CRC PRESS.

[2.2] Awtar, S., 2004, "*Analysis and Synthesis of Planar Kinematic XY Mechanisms*", Sc.D. thesis, Massachusetts Institute of Technology, Cambridge, MA.

[2.3] Dai, J.S., Ding, X.L., 2006, "Compliance Analysis of a Three-Legged Rigidly-Connected Platform Device", *Journal of Mechanical Design*, Vol. **128** (6): 755–764.

[2.4] Ding, X.L., Dai, J.S., 2006, "Characteristic Equation-Based Dynamics Analysis of Vibratory Bowl Feeders with Three Spatial Compliant Legs", *IEEE Transactions on Robotics and Automation*, Vol. **5**(1): 164–175.

[2.5] Samuel, H.D., and Sergio, N.S., 1979, *Compliant Assembly System*, United States Patent, No.: 4155169.

[2.6] Awtar, S., Slocum, A.H., 2007, "Characteristics of Beam-Based Flexure Modules", *Journal of Mechanical Design*, Vol. **129**(6): 624–639.

[2.7] Awtar, S., Sevincer, E., 2010, "Elastic Averaging in Flexure Mechanisms: a Three-Beam Parallelogram Flexure Case Study", *Journal of Mechanisms and Robotics*, Vol. **2**(4): 041004.

[2.8] Pei, X., Yu, J., Zong, G., et al., 2009, "A Novel Family of Leaf-Type Compliant Joints: Combination of Two Isosceles-Trapezoidal Flexural Pivots", *Journal of*

Mechanism and Robotics, Vol. **1**(2): 1–6.

[2.9] Hopkins, J.B., Culpepper, M.L., 2010, "A Screw Theory Basis for Quantitative and Graphical Design Tools That Define Layout of Actuators to Minimize Parasitic Errors in Parallel Flexure Systems", *Precision Engineering*, Vol. **34**(4): 767–776.

[2.10] Blanding, D. K., 1999, *Exact Constraint: Machine Design Using Kinematic Principles*, ASME, New York.

[2.11] Hearn, E.J., 1983, *Mechanics of Materials*, Robert Maxwell, M. C. Pergamon Press, Oxford.

[2.12] Sen, S., and Awtar, S., 2010, "Nonlinear Constraint Model for Symmetric Three-Dimensitonal Beams", *Proceedings of the ASME 2010 International Design Engineering Technical Conferences &Computers and Information in Engineering Conference*, August 15–18, 2010, Montreal, Quebec, Cananda. DETC2010-28953

[2.13] Kuipers, J.B., 2002, *Quaternions and Rotation Sequences*, Princeton University Press, US.

[2.14] Maxwell, J. C., 1890, *General Considerations Concerning Scientific Apparatus*, Dover, New York.

[2.15] Salisbury, S.P., Mrad, R. Ben, 2006, "Analytical Stiffness Estimation for Short Flexures", *Mechatronics*, Vol. **16**(7): 399–403.

[2.16] Awtar, S., Slocum, A. H., 2007, "Constraint-Based Design of Parallel Kinematic XY Flexure Mechanisms", *Journal of Mechanical Design*, Vol. **129**(8): 816 – 830.

[2.17] Trease, B.P., Moon,Y.-M., Kota, S., 2005, "Design of Large-Displacement Compliant Joints", *Journal of Mechanical Design*, Vol. **127**(7): 788–798.

[2.18] Dogan, A., Fernandez, J.F., Uchino, K., 1996, "The 'CYMBAL' Electromechanical Actuator", *Proceedings of the 10-th IEEE International Symposium on Applications of Ferroelectrics*, 18–26, August, 1996, East Brunswick, NJ, USA, Vol. **1**: 213–216.

Chapter 3 – Design and Modelling of 1-DOF Translational CPMs: Novel Compliant Parallel Grippers

One specific form of 1-DOF translational CPMs is the compliant parallel gripper (CPG), which is composed of a base, compliant members and two or more jaws. The jaws are indirectly driven by a linear actuator to grasp the objects. The CPG can be used in precision engineering/MEMS areas.

In order to grasp the objects firmly, the two jaws of the compliant gripper should ideally be parallel all the time. However, in compliant mechanisms, some parasitic motion such as undesired rotation of the jaw will always accompany the primary motion if no suitable measure is taken. Figure 3.1 shows two cases for the reaction forces acting at the jaws. One shows that when the parasitic rotation of the jaws exists, a component of the reaction force will cause the circular object unstable during grasping. Another case shows that when there is no parasitic rotation of the jaws, no component of reaction force exists to make the circular object unstable.

In the design of single-DOF CPGs, some desired characteristics: large stroke, no stress-concentration, actuator isolation, and a simple and compact configuration should be pursued.

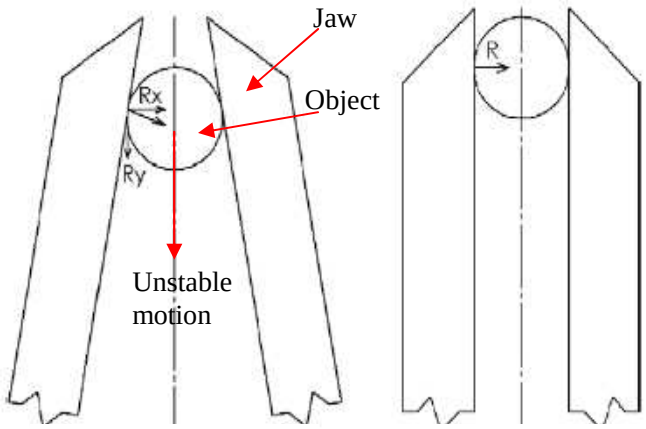

a) Unstable grasping b) Stable grasping

Figure 3.1 Reaction force on the jaws [3.1]

Several typical existing designs of CPGs are shown in Figures 3.2–3.6. Despite their characteristics, these CPGs have shortcomings are as follows. The designs in Figures 3.2 and 3.3 can cause the stress-concentration, due to the use of lumped compliance, and parasitic rotation. The design in Figure 3.4 uses the hybrid-compliance (integrating

lumped and distributed compliance) to alleviate the effect of parasitic rotation and improve the dynamics, but there is still the stress-concentration and non-negligible parasitic rotation. The model 2 in Figure 3.4 also causes the slight actuation non-isolation of piezoelectric ceramics actuator (PZT) due to the use of lever amplifier. Figure 3.5 shows a design using distributed-compliance without stress-concentration, but it is obtained using continuum optimization method, which involves many design parameters and results in slight actuation non-isolation. In addition, all these existing designs (Figures 3.2–3.5) cannot achieve the auto-adaptive and large stroke grasping.

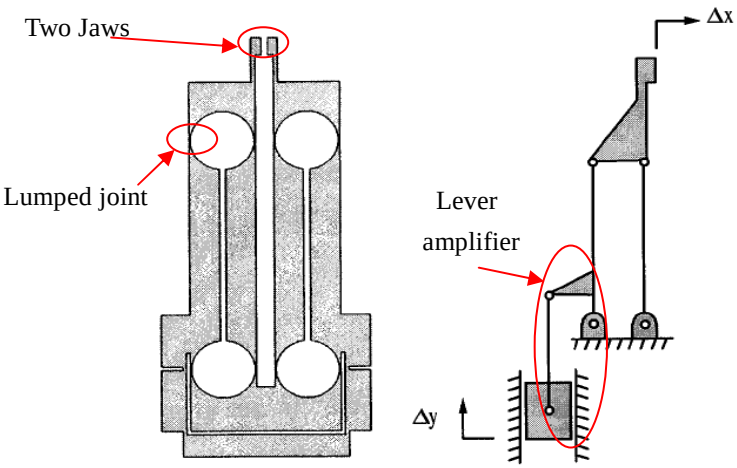

Figure 3.2 CPG designed by M. Goldfarb *et al* (1999) [3.2]

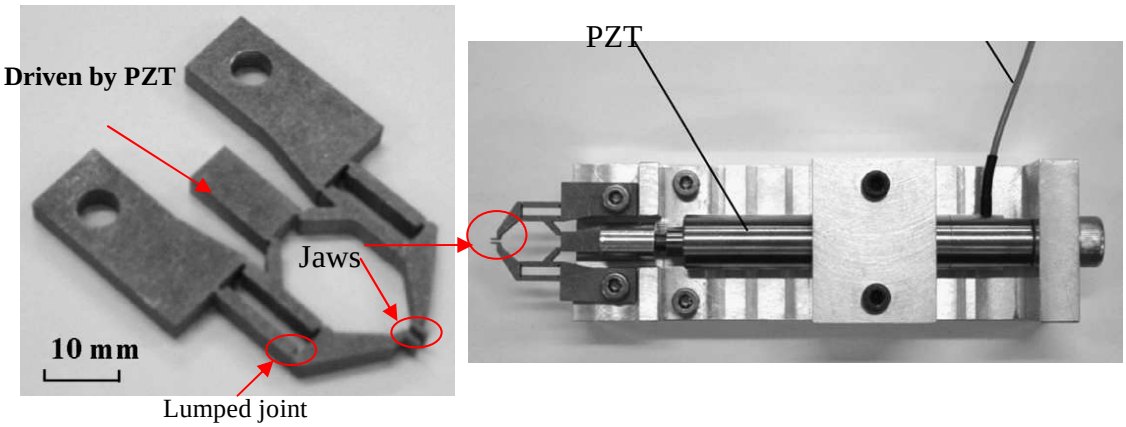

Figure 3.3 CPG designed by S.K. Nah and Z.W. Zhong (2007) [3.3]

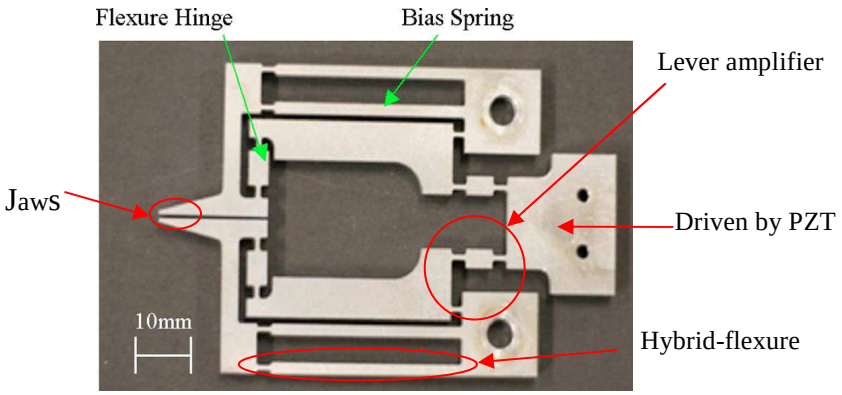

(a) Model 1

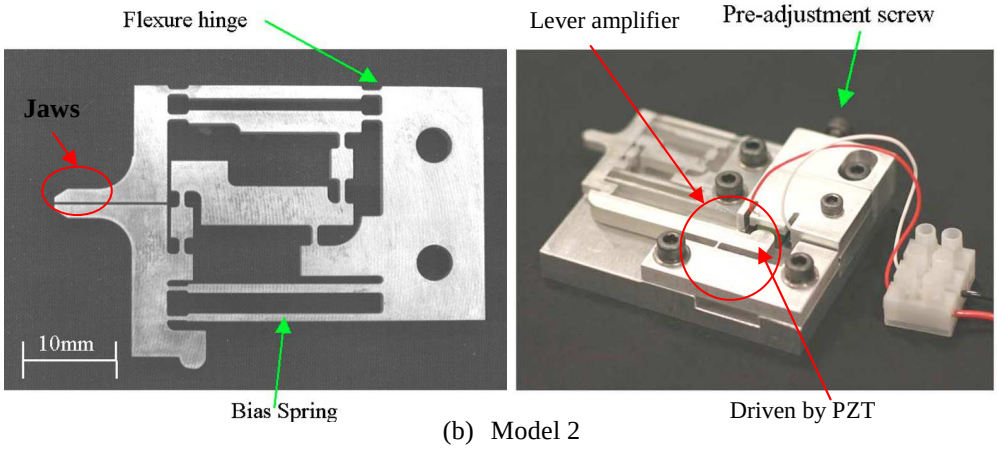

(b) Model 2

Figure 3.4 CPGs designed by M.N.M. Zubir *et al* (2009) [3.1]

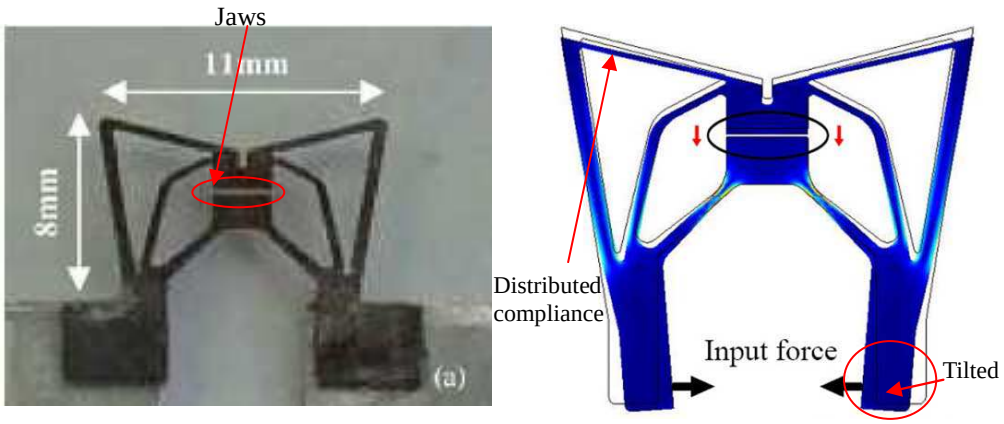

Figure 3.5 CPG designed by A.N. Reddy *et al* (2010) [3.4]

Inspired by the above advances, this chapter aims to propose a CPG that can produce *large-stroke and auto-adaptive* grasping without causing parasitic rotation of its jaws and actuator non-isolation for macro-/micro-applications.

This chapter is organised as follows: In Section 3.1, the conceptual design of a novel auto-adaptive CPG is presented. Section 3.2 derives the analytical model and analyses

its performances both using analytical and FEA models. Varied configurations for CPGs are first proposed in Section 3.3, and the manufacture and potential applications for the proposed CPGs are further discussed. Finally, the summary is conducted.

3.1 Conceptual Design of an Auto-Adaptive CPG

In order to construct a large-stoke auto-adaptive CPG, we will start with discussing compliant building blocks in the following sections.

3.1.1 Displacement amplifier

The cymbal-type displacement amplifier with distributed compliance proposed in [3.5–3.7] is shown in Figure 3.6. In this amplifier, two equal forces with opposite direction are exerted at two input ports to cause two output ports to move, and all rigid-body parts only have translational motion. Due to the intrinsic symmetry and limitations in the gripper configuration, the two output ports only have the translation along the X-axis, and the two input ports only have the translation along the Y-axis (Figure 3.6b). Especially in the case that one output port is held fixed, the other output port can still achieve the translation along the X-axis, and two input ports have the translation along the Y-axis and an additional simultaneous translation along the X-axis.

The above statement provides an argument that one can use the cymbal-type amplifier to construct a large-stoke and auto-adaptive grasping CPG by connecting the two output ports of the amplifier to other parts of the CPG.

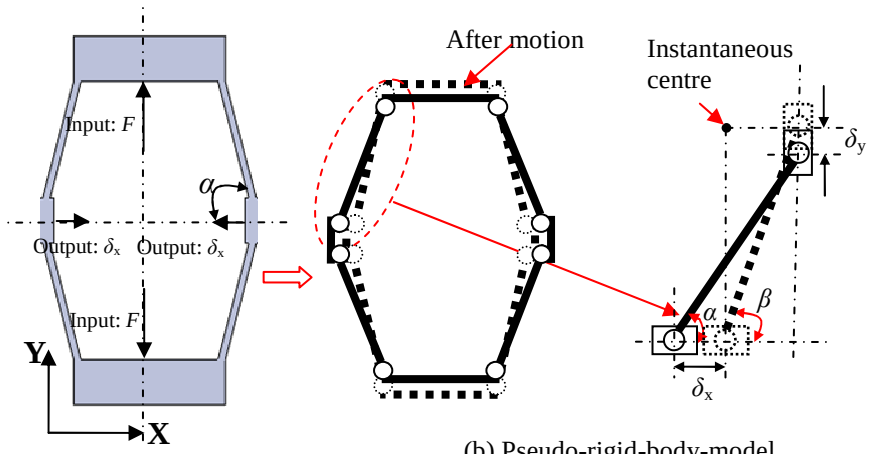

(a) Compliant displacement amplifier

(b) Pseudo-rigid-body-model of the amplifier

Figure 3.6 Cymbal-type displacement amplifier

3.1.2 Parallelogram flexure module

We can also use the parallelogram flexure module (Figure 3.7) as the building block of a CPG as in [3.1–3.3] (Figures 3.1–3.4). This module can achieve large translation along the Y-axis, and has large stiffness along the X-axis and about the Z-axis.

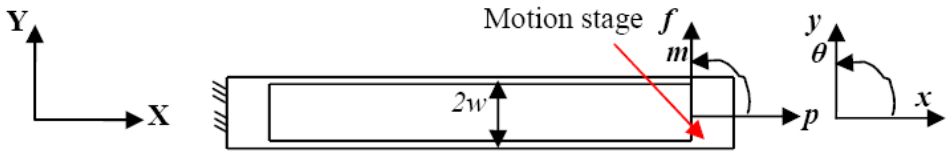

Figure 3.7 Parallelogram flexure module

The normalized nonlinear load-displacement equations, as discussed in Section 2.2, for the parallelogram module are shown below [3.8]:

$$y = \frac{f}{2a + pe} \quad , \tag{3.1}$$

$$\theta = \frac{1}{2w^2}\left(\frac{1}{d} + y^2 r\right)[m - y(2c + pe)], \tag{3.2}$$

$$x = \frac{p}{2d} + y^2 i + \frac{p}{2} y^2 r \tag{3.3}$$

where a=12, c=−6, d=12/$(T/L_2)^2$, e=1.2, i=−0.6, r=1/700. p, f and m are normalized the loads acting at the motion stage of the parallelogram module. x, y and θ are the normalized displacements of the motion stage. All the loads and displacements are relative to the coordinate system in Figure 3.7.

Equation (3.2) shows that, when p=0 and m=−f/2, the parasitic angle is zero. This reveals that θ=0 if we exert only transverse load f on the motion stage and at the half position of the beam length (*centre of stiffness*).

3.1.3 An auto-adaptive CPG

From the above discussion, we can obtain an auto-adaptive CPG with eliminated parasitic rotation of each jaw (Figure 3.8) by connecting the centre of the stiffness of one parallelogram module (Figure 3.7) to each output port of the amplifier (Figure 3.6). Here, the auto-adaptive CPG can be driven by a PZT embedded inside the amplifier. It possesses desired performance characteristics, especially auto-adaptive function, the summarized comparisons of which are shown in Table 3.1.

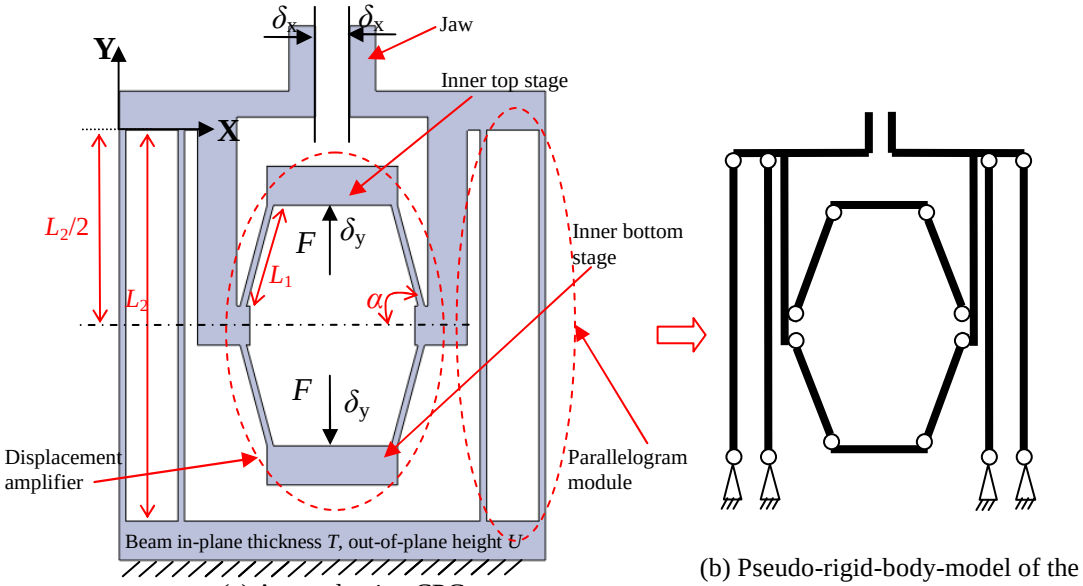

(a) Auto-adaptive CPG

(b) Pseudo-rigid-body-model of the CPG with ideal pivots

Figure 3.8 An auto-adaptive CPG

CPGs / *Characteristics*	Goldfard's design [3.2]	Nah's design [3.3]	Zubir's design [3.1]	Reddy's design [3.4]	Proposed CPG
Auto-adaptive grasping	−	−	−	−	+
Parasitic rotation	0	0	0	0	+
Large-stroke	0	0	0	−	+
Maximal actuator isolation	0	0	0	−	+
Stress-concentration	0	0	0	+	+

Table 3.1 Characteristic comparisons of CPGs (Good: +, Normal: 0, Poor: −)

3.2 Analysis for the Auto-Adaptive CPG

This section will derive the relationships between the input force and the output displacement of the jaw and investigate the analytical displacement amplification ratio.

3.2.1 Modelling of the auto-adaptive CPG

Using PRBM in Figure 3.6b, we can derive the following approximate relationships:

$$\cos\beta = \frac{L_1\cos\alpha - \delta_x}{L_1} = \cos\alpha - \frac{\delta_x}{L_1}, \tag{3.4}$$

$$\delta_y = L_1(\sin\beta - \sin\alpha) = L_1(\sqrt{1-\cos^2\beta} - \sin\alpha) = L_1(\sqrt{1-(\cos\alpha - \delta_x/L_1)^2} - \sin\alpha), \tag{3.5}$$

$$\delta_x / \delta_y = \delta_x / [L_1(\sqrt{1-(\cos\alpha - \delta_x / L_1)^2} - \sin\alpha)] \tag{3.6}$$

where δ_x (output displacement) and δ_y (input displacement) are the actual (not normalized) translational displacements of the centres of the left jaw and the inner top stage, respectively. L_1, L_2, and α are the geometrical parameters as indicated in Figure 3.8a. Equation (3.6) defines the displacement amplification ratio.

Using energy conversation principle, we can obtain the following force-displacement equation:

$$F\delta_y / 2 = K_1(\delta_x^2 + \delta_y^2) + K_2\delta_x^2 / 2 \tag{3.7}$$

where the term on the left-hand side is the work caused by one input force, and the terms on the right-hand side are a half of the elastic energy stored in the amplifier and parallelogram flexure modules. $K_1 = EUT^3 / L_1^3$ and $K_2 = 2EUT^3 / L_2^3$ (T is beam in-plane thickness, and U is out-plane-of height as indicated in Figure 3.8a), which are the primary translational stiffness of the single beam in the amplifier and that of the parallelogram flexure module, respectively. δ_y is obtained based on Equation (3.5). E is the Young's modules for plane stress or plate modules for plane strain. F is the actual input force acting at each inner stage.

It is noted that Equation (3.7) is obtained under the assumption of material linear elasticity and small deformation, and therefore it is accurate enough to deal with small displacement cases.

3.2.2 FEA comparisons

As an example, the material can be chosen as AL6061-T6 for which Young's modulus, E, is 69000Nmm, Possion ratio, v, is 0.33, and let T=1mm, U=5mm, L_1=15mm, L_2=50mm and α=5π/12. Based on these given parameters and Equation (F.6) in *Appendix F*, we can determine that the each jaw'motion range for the example auto-adaptive CPG is approximately 0.3mm.

The simulation results obtained using FEA for the proposed CPG (Figure 3.8) is shown in Figures 3.9–3.11. Here, *Comsol large-displacement module* for FEA using tetrahedron element with fine mesh (maximum element size 0.8mm) are chosen. The reference points are chosen to be the centres of the left jaw and the inner top stage.

Figure 3.9 shows that, if one of the two jaws is fixed or held fixed, the auto-adaptive grasping function can be also achieved by the proposed design (see Figure 3.11b for example). It is noted that when a fixed object needs to be manipulated we need not to

place the object at the right middle of the two jaws. In the case of one jaw being fixed, another jaw's displacement is $2\delta_x$.

Figure 3.10 shows the relationship between the input displacement and output displacement obtained both from FEA and the analytical model [Equation (3.5)]. It is shown that the slope at any point of the relationship curve stands for the velocity amplification ratio of the auto-adaptive CPG.

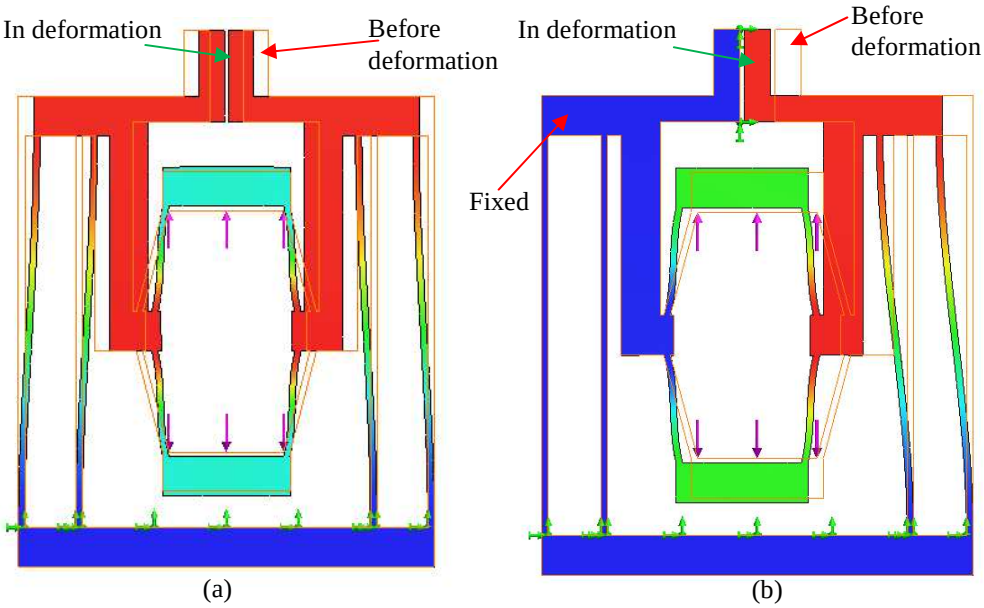

Figure 3.9 FEA models: (a) free-grasping;
(b) auto-adaptive grasping in the case that one jaw is fixed

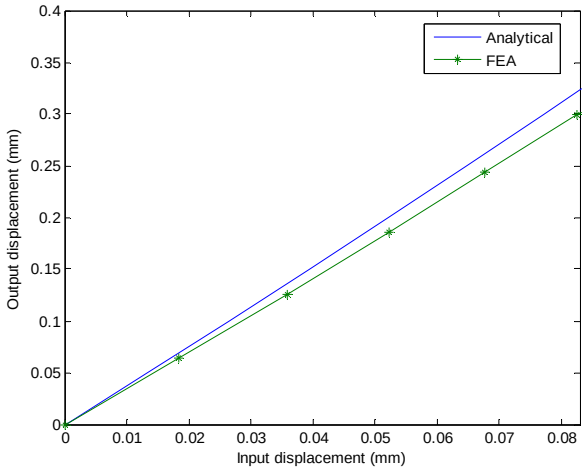

Figure 3.10 Relationship between the input displacement and output displacement for the auto-adaptive CPG

Figure 3.11 shows that the varied displacement amplification ratio obtained using FEA is smaller than that obtained using the analytical model [Equation (3.6)]. The

difference of displacement amplification ratio between two models is between 6.7% and 7.7%.

From FEA or analytical model in Figure 3.11, the relationship between the amplication ratio and output displacment is approximately a tilted straight line as shown in Figure 3.11 because the relationship between the input displacement and output displacement is curved. Figure 3.11 also shows that two approximate straight lines are parallel.

Figure 3.12 shows that the output displacement obtained using FEA is larger than that obtained using the analytical model [Equation (3.7)] under a given input force. The difference of output displacement between two models is about 13%.

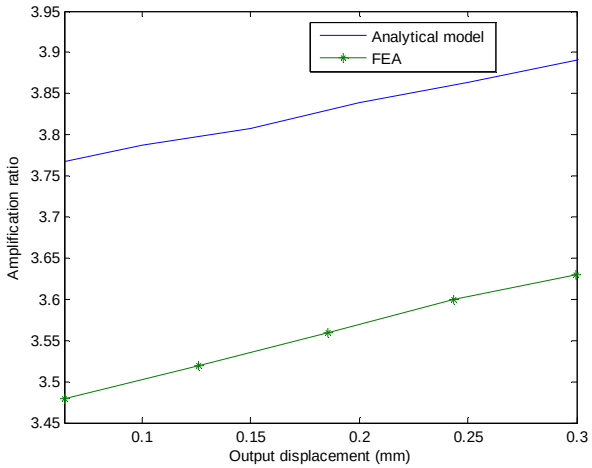

Figure 3.11 Displacement amplification ratio versus output displacement for the auto-adaptive CPG

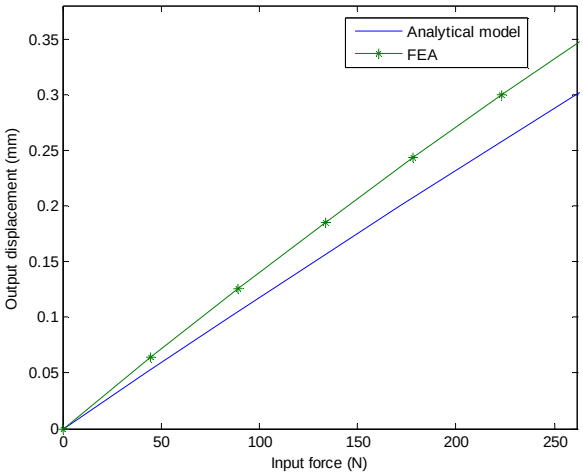

Figure 3.12 Force-displacement relationship of the auto-adaptive CPG

In addtion, FEA resutls show that the parasitic rotation about the Z-axis, and the parasitic translation along the Y-axis, of the left jaw are less than 9×10^{-5} mm and 8×10^{-5}

rads, respectively.

The above comparisons show that there are certain difference between the FEA and the analytical results. This is due to inaccuracy of either analytical model or FEA model, and the difference (%) between the analytical model and FEA decreases with the increase of output displacement. Here, the accuracy of analytical model is mainly affected by the assumptions, and FEA model is mainly influenced by the element type and size. Therefore, experiment verification is further needed to determine which model is more accurate.

3.3 Variations and Discussions

3.3.1 Variations

In order to further eliminate the parasitic translational displacement of the jaw along the Y-axis for the auto-adaptive CPG, we can introduce a double parallelogram module to replace the above parallelogram module in the compliant gripper. Also, we can replace the single beam in the above amplifier with a tilted parallelogram module, i.e. using multi-beam strategy, to guarantee relatively large stiffness affecting the dynamic performance. Thus, we obtained a varied configuration for CPGs as shown in Figure 3.13.

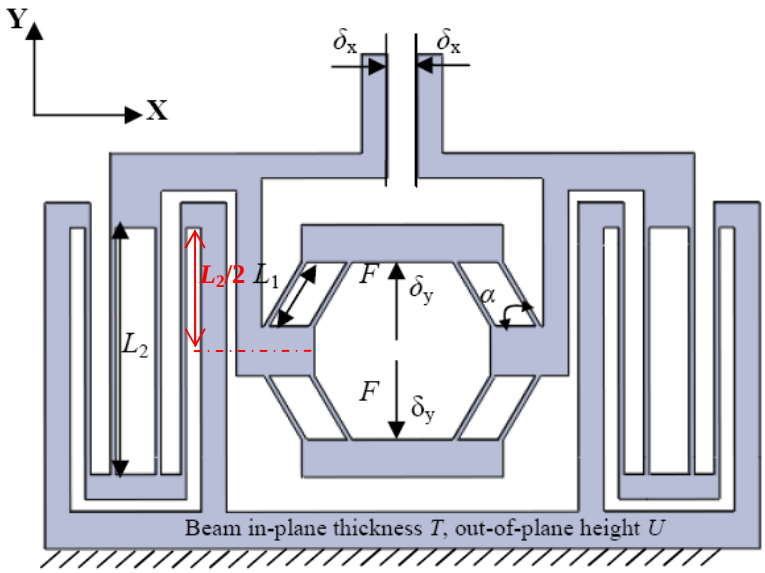

Figure 3.13 A varied configuration

We first discuss the double parallelogram module as shown in Figure 3.14. The normalized nonlinear load-displacement equations for the double parallelogram module

are shown as follows [3.8]:

$$y = \frac{4af}{(2a)^2 - (pe)^2}, \tag{3.8}$$

$$\begin{aligned}\theta &= \frac{1}{2w_1^2}\left(\frac{1}{d} + \frac{f^2}{(2a+pe)^2}r\right)\left[m - \frac{f}{(2a+pe)}(2c+ph)\right] \\ &= \frac{1}{2w_2^2}\left(\frac{1}{d} + \frac{f^2}{(2a-pe)^2}r\right)\left\{m + f\left[1 - \frac{p}{(2a+pe)} + \frac{(2c-ph)}{(2a-pe)}\right]\right\}\end{aligned}, \tag{3.9}$$

$$x = \frac{p}{d} + py^2\frac{r[(2a)^2 + (pe)^2] - 8aei}{(4a)^2} \tag{3.10}$$

where a=12, c=−6, d=12/$(T/L_2)^2$, e=1.2, h=−0.1, i=−0.6, r=1/700. p, f and m are the normalized loads acting at the motion stage of the parallelogram module. x, y and θ are the normalized displacements of the motion stage. All the loads and displacements are relative to the coordinate system in Figure 3.14.

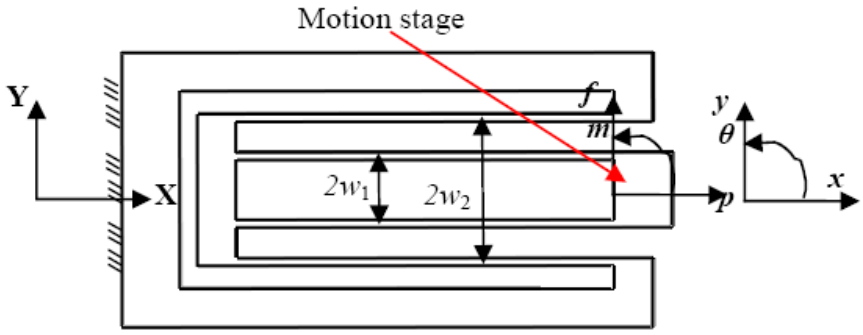

Figure 3.14 Double parallelogram flexure module

Equations (3.9) and (3.10) show that, when p=0 and m=−f/2, the parasitic angle θ and parasitic translational displacement x are all zero. This verifies that the varied CPG can eliminate all the parasitic motions of the jaw including the parasitic translational displacement along the Y-axis (Figure 3.13).

Similar to Equation (3.7), we can then obtain the following load-displacement equation for the varied CPG (Figure 3.13):

$$F\delta_y / 2 = K_1(\delta_x^2 + \delta_y^2) + K_2\delta_x^2 / 2 \tag{3.11}$$

where $K_1 = 2EUT^3 / L_1^3$ and $K_2 = EUT^3 / L_2^3$, which are the primary translational stiffness of the tilted parallelogram module in the amplifier and that of the double parallelogram module, respectively. δ_y is obtained based on Equation (3.5).

In addition, two auto-adaptive planar CPGs (Figure 3.8) can be further used to construct a spatial CPG (Figure 3.15) with four jaws. This new spatial CPG doesn't have the auto-adaptive grasping function but still can be employed for most

applications. We may also obtain a CPG without auto-adaptive grasping as shown in Figure 3.16. Here, two additional parallelogram modules are introduced to decouple the transverse motion of the amplifier.

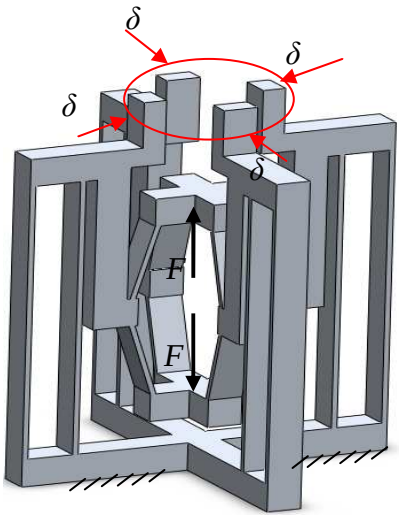

Figure 3.15 Spatial CPG with four jaws

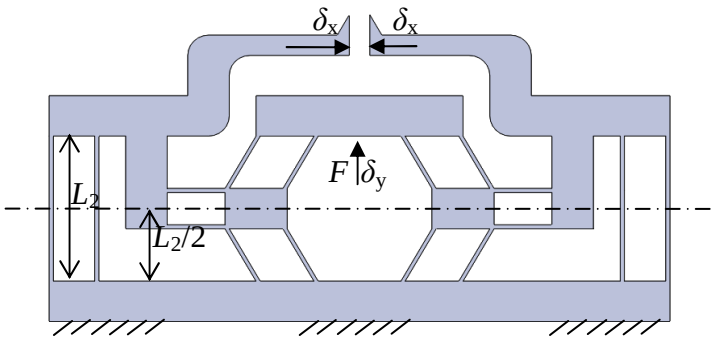

Figure 3.16 Planar CPG without auto-adaptive grasping

3.3.2 Discussions

The proposed auto-adaptive CPG (Figure 3.8) may be used in both in macro- (precision engineering) or micro-area (MEMS) for precision manipulation, and can be easily fabricated by micro-wire electric discharge machine (EDM). Here, PZT is employed to produce input force due to its major advantages of the large blocking force, high stiffness, fast response, compact size and up to nano-positioning. Also, *CEDRAT TECHNOLOGIES* company [3.9] has fabricated many cymbal-type amplifier integrating PZT together from small size to large size (Figure 3.17), which provides us with an option that we only need to fabricate two parallelogram modules and then

assembly all parts together.

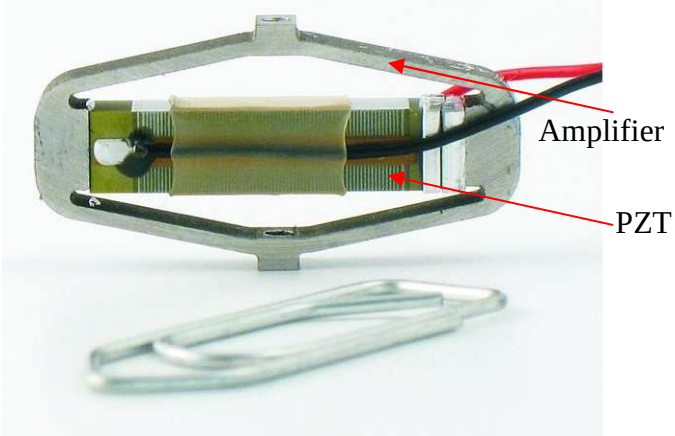

Figure 3.17 An integrated amplifier product with PZT [3.9]

In order to further improve the dynamic performance of the proposed auto-adaptive CPG (Figure 3.8) without affecting its allowable maximal motion range, one can choose the multi-beam strategy, which has been demonstrated in Figure 3.13.

In addition to be applied in precision engineering and MEMS areas, these above proposed CPGs (Figures 3.8, 3.13, 3.15 and 3.16) can also be used in the areas in which the precision required is not high such as food industry. For example, the CPG (jointless) can be used to grasp the chicken drumsticks due to the hygiene requirement.

3.4 Summary

An auto-adaptive CPG has been proposed. Using a cymbal-type displacement amplifier, it not only magnifies the small input displacement resulting from PZT to produce accurate motion, but also can produce auto-adaptive grasping for applications in complex environment.

The proposed auto-adaptive CPG (Figure 3.8) can ensure actuator isolation due to no transverse force acting at the actuator, and firmly grasp the objects due to well-constrained parasitic rotation of its two jaws. The auto-adaptive CPG can also perform large range of motion and has no stress-concentration effect due to the use of distributed-compliance.

3.5 References

[3.1] Zubir, M.N.M., Shirinzadeh, B. and et al, 2009, “Development of Novel Hybrid Flexure-Based Microgrippers for Precision Micro-Object Manipulation”, *Review*

of Scientific Instruments, Vol. **80**: 065106.

[3.2] Nah, S.K., Zhong, Z.W., 2007, "A Microgripper Using Piezoelectric Actuation for Micro-Object Manipulation", *Sensors and Actuators A*, Vol. **133**: 218–223.

[3.3] Goldfarb, M., and Celanovic, N., 1999, "A Flexure-Based Gripper for Small-scale Manipulation", *Robotica*, Vol**. 17**: 181–187.

[3.4] Reddy, A.N., Maheshwari, N., and et al, 2010, "Miniature Compliant Grippers with Vision-Based Force Sensing", *IEEE Transactions on Robotics*, Vol. **26**(5): 867–877.

[3.5] Dogan, A., Uchino, K., 1997, "Composite Piezoelectric Transducer with Truncated Conical End Caps 'Cymbal'", *IEEE Transactions on Ultrasonics Ferroelectrics and Frequency Control*, Vol. **44**(3): 597–605.

[3.6] Dogan, A., Fernandez, J.F., Uchino, K., 1996, "The 'CYMBAL' Electromechanical Actuator", *Proceedings of the 10-th IEEE International Symposium on Applications of Ferroelectrics*, 18–26, August, 1996, East Brunswick, NJ, USA, Vol. **1**: 213–216.

[3.7] Newnham, R.E., Zhang, J., Meyer, R.J., 2000, "Cymbal Transducers: a Review", *Proceedings of the 12-th IEEE International Symposium on Applications of Ferroelectrics*, 21 July–02 August, 2000, Honolulu, HI , USA, Vol. **1**: 29–32

[3.8] Awtar, S., and Slocum, A. H., 2007, "Characteristics of Beam-Based Flexure Modules", *Journal of Mechanical Design*, Vol. **129**(6): 624–639.

[3.9] http://www.cedrat.com/en/mechatronic-products/actuators/apa.html (last accessed on 05/09/2011)

Chapter 4 – Design and Modelling of XY CPMs for High-Precision Motion Stages

An XY compliant parallel manipulator (CPM) for high-precision motion stage is a mechatronic motion system, which is an integration of compliant mechanism (composed of a base and a motion stage connected by compliant members), linear actuators, sensors and controller. Its motion stage, indirectly driven by actuators, is capable of moving along the X-and Y-axes, respectively. XY CPMs for high-precision motion stages can be used in a variety of applications such as the atomic force microscope [4.1, 4.2], micro-assembly [4.3], data storage [4.4] and potential mechanical in-plane loading device. Their merits and desired performance characteristics (design indices) have been discussed in Chapter 1.

Many researchers [4.2, 4.5–4.12] have conducted the creative design of XY CPMs using the basic parallelogram or double parallelogram modules with lumped-compliance, distributed-compliance or hybrid-compliance. Three of them are shown in Figure 4.1. Awtar *et al* [4.5, 4.6] made a pioneering contribution on XY CPMs (Figure 4.1a) for large-range translation using the identical distributed-compliance double parallelogram modules as compliant prismatic (P) joints. In order to make the whole configuration more compact and reduce the in-plane parasitic rotational angle of the motion stage, the compliant P joints connected to the base are arranged in rotation-symmetry about the centre of the motion stage, and the compliant P joints connected the motion stage are arranged in mirror-symmetry with respect to the X- or Y-axis. Choi *et al* [4.7] also proposed a 4-PP monolithic parallel linear compliant mechanism with distributed-compliance (Figure 4.1b). They used two mirror-symmetric double-parallelogram modules as the compliant P joint connected to the base in each leg in order to reduce the input-coupling and the in-plane parasitic angle. Li *et al* [4.8] further proposed a totally decoupled flexure-based XY CPM with displacement amplifiers (Figure 4.1c) using lumped-compliance. This design is more compact than Choi's design, and its in-plane parasitic angle and cross-axis coupling can be well-constrained.

Despite their characteristics, these existing designs can still be improved as articulated below. In Awtar's design, the rotation-symmetry is not the ideal constraint strategy, and the resulting XY CPM may have a very small in-plane parasitic angle and slight actuator non-isolation (input-coupling). Choi's design is not compact

enough due to the simple serial connection of two P joints. In addition, it has relatively small motion range and larger cross-axis coupling due to the use of the basic parallelogram module (having larger load-stiffening effect). Li's design has limited motion range and relatively low transverse stiffness of the amplifier. The amplifier also augments the minimum incremental motion from the actuators. The other existing designs are also subjected to their own limitations, which produce small range of motion [4.9–4.12], relatively large in-plane parasitic angle [4.9–4.11], relatively large cross-axis coupling [4.2, 4.12], and/or relatively large input-coupling [4.9].

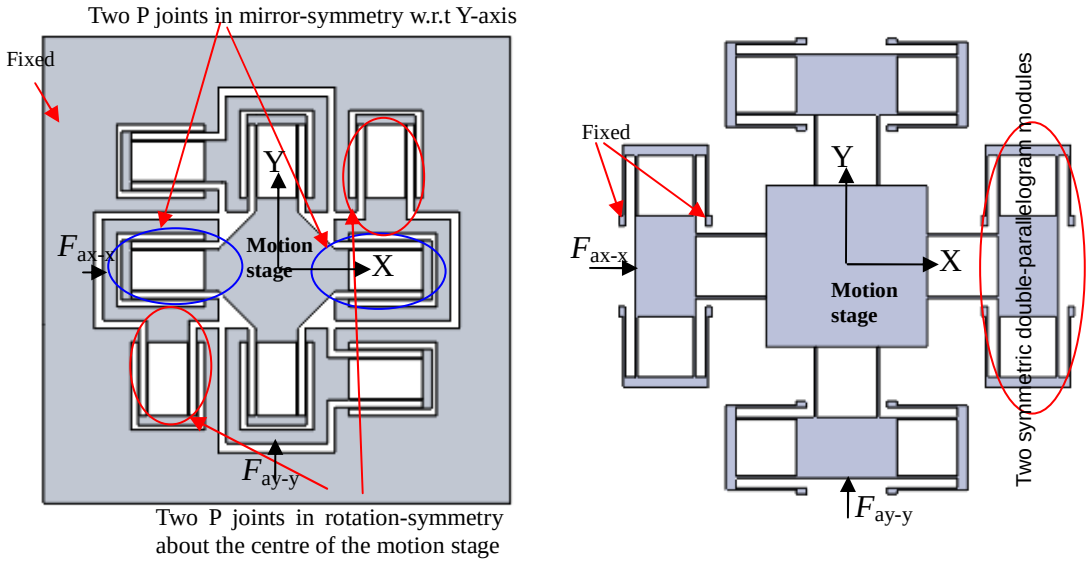

(a) Awtar's Design

(b) Choi's design

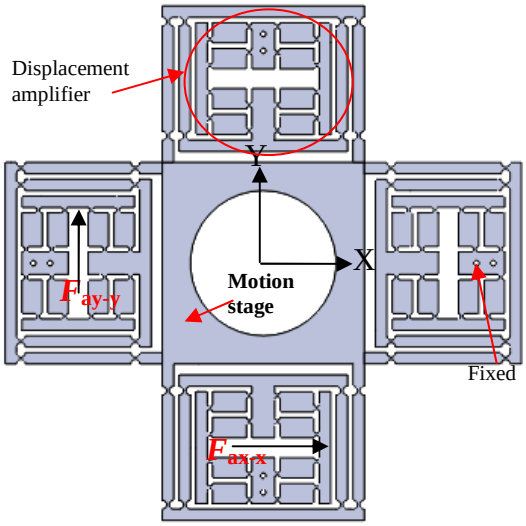

(c) Li's design

Figure 4.1 Three existing XY CPMs using kinematically decoupled configuration

Another open issue in XY high-precision motion stages is the friction between the motion stage and ground/base. A magnetic-levitation or aerostatic strategy [4.13–4.16]

has been proposed to deal with this issue in the past because of their non–contact operation. While in the current XY CPMs, an option to overcome this problem is to separate the motion stage and the ground. However, for the motion stage under a high payload or out-of-plane vibration, one needs to increase the out-of-plane height of beams to enhance the out-of-plane stiffness. This strategy will cause manufacture/machining complexity/difficulty. Therefore, how to improve the out-of-plane stiffness without increasing the out-of-plane height of beams becomes a key issue. An approach to address this issue was proposed in Ref. [4.9] for a multiple DOF compliant robot using lumped flexure joint but subjected to its own disadvantages such as small range of motion and relatively large in-plane parasitic angle .

To deal with the above unsolved issues, especially to increase out-of-plane stiffness in the existing designs, this chapter focuses on the design and modelling of XY CPMs for *large range of motion and enhanced out-of-plane stiffness*. While other desirable performance characteristics are also taken into consideration. Our strategy for enhancing out-of-plane stiffness is to use a spatial multi-beam module to constrain the out-of-plane motion.

This chapter is organized as follows. Section 4.1 proposes a planar XY CPM, a spatial double four-beam module, and a stiffness-enhanced XY CPM. In Section 4.2, the proposed stiffness-enhanced XY CPM using a linear analytical approach is modelled using a normalized and linear analytical approach. Section 4.3 analyses the material, actuator and geometrical parameter selection, performance characteristics, and buckling checking and actuation checking for a case stiffness-enhanced XY CPM with large motion range of 10mm×10mm. Section 4.4 compares the proposed analytical model with FEA. In Section 4.5, the dynamics issues, manufacture and out-of-plane stiffness are discussed. Finally, the summary is stated in Section 4.6.

4.1 Conceptual Design of Large-Range XY CPMs

The totally decoupled XY CPMs, with input-decoupling and out-decoupling, can be constructed starting from a rigid-body 2-PP decoupled parallel mechanism (Figure 4.2). The 2-PP parallel mechanism is composed of two PP legs in parallel. Each leg consists of two P joints in a serial arrangement. Two P joints connected to the based are actuated, denoted by P. Here, the axes of two passive P joints are perpendicular to achieve kinematic decoupling, which is the necessary condition for cross-axis decoupling (kinematostatic decoupling).

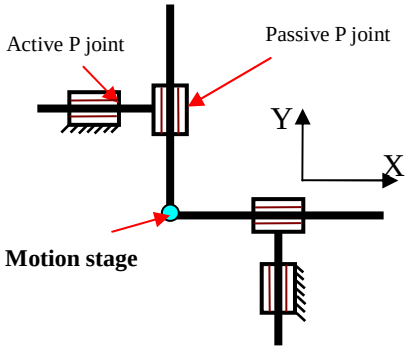

Figure 4.2 Schematic diagram of a 2-PP decoupled parallel mechanism

4.1.1 Compliant prismatic joints

The basic parallelogram flexure modules (Figure 2.16a) have been chosen as compliant P joints frequently in the design of XY CPMs. In order to achieve large range of motion, distributed-compliance mechanisms are employed in this chapter. However, the basic distributed-compliance parallelogram module can result in the relatively large load-stiffening effect [4.6, 4.17], affecting cross-axis decoupling, and relatively low primary motion stiffness, influencing the dynamic performance.

One can obtain a double parallelogram flexure module by connecting two parallelograms in series in order to double the primary motion range of a single parallelogram module.

Based on the nonlinear analysis in Refs. [4.6, 4.17] (also see Equation (3.3) in Chapter 3), we learn that the axial displacement for a basic parallelogram flexure module depends on three components: purely elastic effect of the axial force, purely kinematic effect and the elastokinematic effect (the elastokinematic effect is much smaller than the purely kinematic effect). Nevertheless, for the double parallelogram module, the purely kinematic effect of axial displacement can be largely attenuated as the transverse forces imposed on the secondary stage produce positive axial displacement, whereas the transverse forces imposed on the primary stage produce negative axial displacement (see Equation (3.10) in Chapter 3). In addition, this double parallelogram module can alleviate the load-stiffening effect from the axial force (see Equations (3.1) and (3.8) in Chapter 3). Therefore, when two mirror-symmetric basic parallelogram modules act as the active P joint, the resulting XY CPM has very large load-stiffening effect resulting from the augmentation of transverse stiffness in the presence of (a) large proportion of axial tension-force compared to double parallelogram module, and (b) gradually increased axial tension-force in the

configuration of two mirror-symmetry parallelogram modules. This load-stiffening effect limits the motion range of the resulting XY CPM.

One can further increase the number of beams [4.18], i.e. using multi-beam strategy (i.e. the number of beams >2), in each parallelogram module to improve the primary motion stiffness without affecting the allowable maximal motion range.

Therefore, we use two mirror-symmetric double three-beam parallelogram modules (Figure 4.3a) as the compliant P joint I, and use a double four-beam parallelogram modules as the compliant P joint II (Figure 4.3b). Here, the length of each beam in the compliant P joint II is set to be larger (for example 2.2 times larger) than that in the compliant P joint I, and the in-plane thickness of each beam in the compliant P joint II is accordingly set to be larger than that in the compliant P joint I. We may fix the ratio of length to in-plane thickness to make all beams have same transverse motion stiffness.

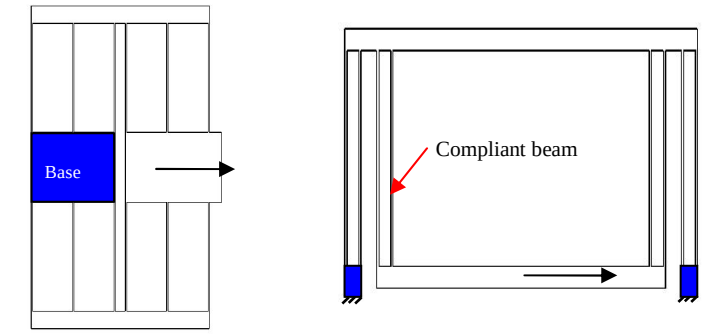

a) Compliant P joint I b) Compliant P joint II

Figure 4.3 Proposed compliant P joints

Alternatively, we may further increase the beam in-plane thickness and choose more-layer (for example quadruple) strategy for the multi-beam parallelogram modules to produce a same allowable maximal motion range.

4.1.2 A planar XY CPM

In order to obtain a stiffness-enhanced XY CPM, we start with proposing a planar large-range XY CPM. One can first replace the active/passive P joint in each leg in Figure 4.2 with the proposed compliant P joint I/II in Figure 4.3 to obtain a 2-PP XY CPM, and then add two same auxiliary compliant legs to the motion stage to further constrain the in-plane parasitic rotation to obtain a planar XY CPM (Figure 4.4). Here, each compliant P joint I is placed inside its adjacent compliant P joint II to make the configuration compact.

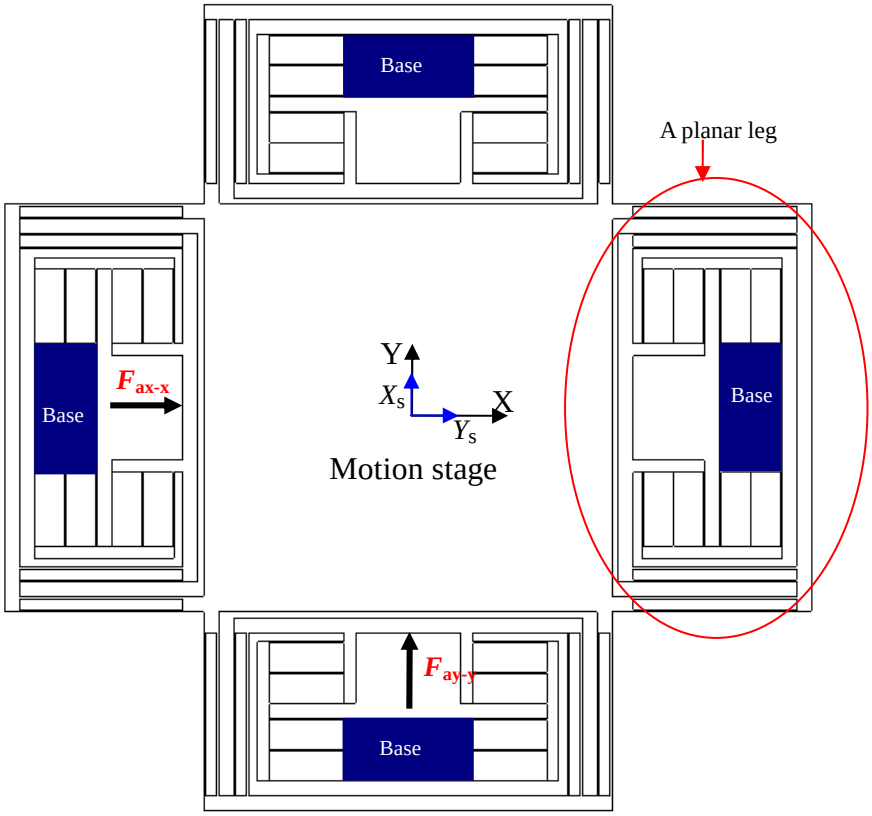

Figure 4.4 A planar XY CPM

In addition to using the above all-symmetry strategy (4-leg) for well constraining in-plane parasitic rotation, alternatively, we can employ both symmetry and centre of stiffness based approach to constrain the parasitic rotation well, and thus obtain a 3-legged XY CPM (see *Appendix L* for an example).

This proposed planar XY CPM (Figure 4.4) has desirable performance characteristics, such as large range of motion, well-constrained in-plane parasitic rotation (θ_{sz}), approximate actuator-isolation, approximate cross-axis decoupling, excluding enhanced out-of-plane stiffness. It should be noted that the out-of-plane thickness may be relatively small. In this case, the motion stage of the proposed planar XY CPM can not only move along the X- and Y-axes, but also may move out of plane. This means that its out-of-plane motion, Z_s, θ_{sx} and θ_{sy}, should be constrained by further strategy.

In order to reach only pure translational displacements along the X- and Y-axes for an XY CPM, we can further add an auxiliary spatial leg, only having planar motion, to its motion stage to constrain its out-of-plane motion. Therefore, the DOF of the spatial leg to be proposed should follow the set intersection equation below.

$$[X_s, Y_s\ (Z_s, \theta_{sx}, \theta_{sy})] \cap [\text{DOF of the spatial leg}] = [X_s, Y_s]. \quad (4.1)$$

One of the solutions to Equation (4.1) is that the DOF of the spatial leg are X_s, Y_s, and

θ_{sz}. Therefore, we can know that the spatial leg is an E (planar motion) joint.

4.1.3 A spatial compliant leg

In Chapter 2, spatial multi-beam modules have been proposed and analysed in detail. It has been shown that all the out-of-plane motions of the spatial multi-beam module are suppressed, which leaves the planar motions as the DOF. This provides a good argument to choose the spatial multi-beam modules as the needed E leg (also spatial leg) as mentioned in Section 4.1.2. It is noted that if the spatial multi-beam module is used as a spatial compliant leg of a new XY CPM, its torsional angle is constrained as well by the compliant P joints I and II.

In order to a) increase the motion range, b) alleviate the load-stiffening effect, c) approximately eliminate the purely kinematic effect of the axial displacement, d) have a simple enough configuration and e) improve the dynamic performance, a spatial double four-beam module (Figure 4.5), obtained by connecting two spatial four-beam modules in series, is used as the spatial compliant leg. Here, the beam has a square cross-section, the thickness and length of which are the same as those in the compliant P joint I of the planar XY CPM.

From Equations (2.86d) and (2.86e), we learn that if only two transverse forces are exerted at the *centre of stiffness* of the spatial compliant leg (Figure 4.5b), all parasitic rotations, θ_{sx} and θ_{sy}, are eliminated. Also, the parasitic translation, Z_s, is equal to zero if no axial force is applied.

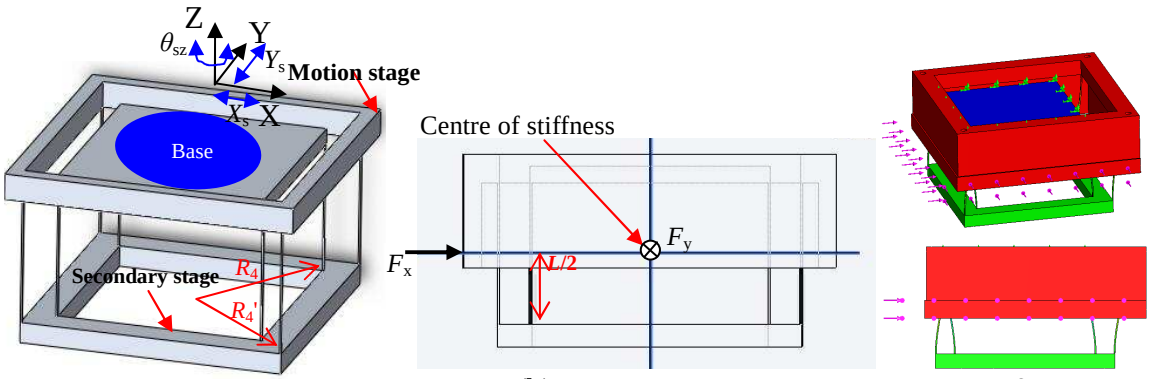

(a) 3-D view (b) Front view (c) Deformation

Figure 4.5 Spatial double four-beam module

4.1.4 A stiffness-enhanced XY CPM

Combining the proposed planar XY CPM (Figure 4.4) and the proposed spatial

compliant leg (Figure 4.5) in parallel, and making the centre of the motion stage of the planar XY CPM and the stiffness centre of the spatial compliant leg overlap, we may obtain a stiffness-enhanced XY CPM (Figure 4.6).

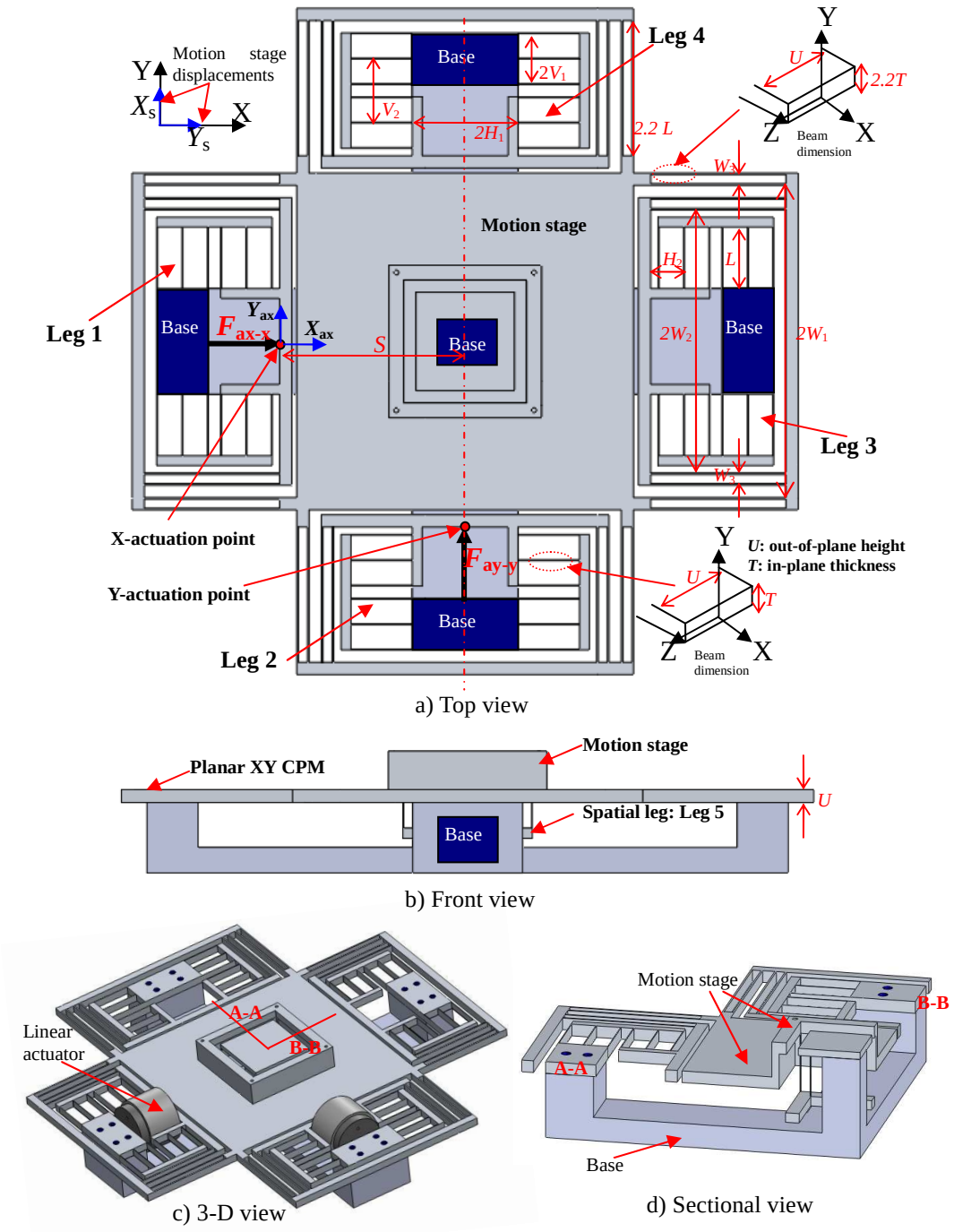

a) Top view

b) Front view

c) 3-D view

d) Sectional view

Figure 4.6 A stiffness-enhanced XY CPM

As it will be shown in the following sections, the stiffness-enhanced XY CPM has large out-of-plane stiffness in addition to the desired characteristics such as large range of motion, well-constrained parasitic motion, approximate actuator-isolation, and approximate cross-axis decoupling.

The summarized comparisons among the existing XY CPMs and the stiffness-enhanced XY CPM are shown in Table 4.1.

XY CPMs / *Characteristics*	Awtar's design [4.5]	Choi's design [4.7]	Li's design [4.8]	Tam's design [4.9]	Stiffness-enhanced XY CPM
Large range of motion	+	0	−	−	+
Constrained in-plane parasitic angle	0	+	+	−	+
Large out-of-plane stiffness	0	0	0	+	+
Minimal cross-axis coupling	+	0	+	0	+
Maximal actuator isolation	0	+	+	−	+
Compactness	+	0	0	0	−

Table 4.1 Characteristic comparisons of XY CPMs (Good: +, Normal: 0, Poor: −)

4.2 Kinematostatic Modelling of the Stiffness-Enhanced XY CPM

Similar to Chapter 2, all translational displacements and length parameters are normalized by length L of the beam in the compliant P joint I (Figure 4.5a) of the planar XY CPM, forces by $E'I_z/L^2$, and moments by $E'I_z/L$ in order to simplify the representation and derivation of equations unless indicated otherwise. Here, $E'=E/(1-\nu^2)$ denotes plate modulus (usually for out-of-plane thickness U/in-plane thickness T>10), and I_z denotes the second moment of the area of a rectangle cross-section in the beam of the compliant P joint I about the Z-axis. All normalized non-dimensional quantities in the following sections are represented using the corresponding lower-case letters.

4.2.1 Modelling of the three-beam parallelogram module

The three-beam parallelogram module in the compliant P joint I of the planar XY CPM is shown in Figure 4.7. It is assumed that u/t>10. Based on the linear modelling approaches for CPMs in *Appendix C*, we can obtain its stiffness matrix that reflects the relationships between the loads and displacements both defined at the same point, C_p, as shown in Figure 4.7 as follows:

$$\mathbf{K}_{\mathrm{p}} = \sum_{i=1}^{3} \mathbf{D}_{\mathrm{p}i}^{\mathrm{T}} \mathbf{K}_i \mathbf{D}_{\mathrm{p}i} \tag{4.2}$$

where $\mathbf{K}_i$ (i=1, 2, 3) is the stiffness matrix of the i-th beam for the mobile-end, and $\mathbf{D}_{\mathrm{p}i}$ (i=1, 2, 3) is the transformation matrix of the displacements of the centre of the primary

stage (neglecting its thickness). We have

$$\mathbf{K}_i = \begin{bmatrix} d & 0 & 0 \\ 0 & a & c \\ 0 & c & b \end{bmatrix}, \tag{4.3a}$$

$$\mathbf{D}_{pi} = \begin{bmatrix} 1 & 0 & -y_i' \\ 0 & 1 & x_i' \\ 0 & 0 & 1 \end{bmatrix} \tag{4.3b}$$

where non-dimensional numbers are a=12, b=4, c=−6, d=12(1−v^2)/t^2. The relative coordinates of the tips of the beams with respect to the centre of the primary stage are x_1'=0, y_1'=v_1, x_2'=0, y_2'=0, x_3'=0, and y_3'=−v_1.

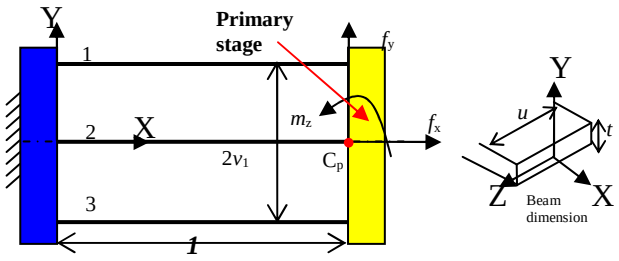

Figure 4.7 Three-beam parallelogram module

Then we obtain the corresponding compliance matrix:

$$\mathbf{C}_p = \mathbf{K}_p^{-1}. \tag{4.4}$$

It is noted that the above stiffness and compliance matrices are all symmetrical matrices, which are affected by the spanning parameter v_1. The larger v_1 is, the better the translational performance of this module is.

4.2.2 Modelling of the double three-beam parallelogram module

The double three-beam parallelogram flexure module (Figure 4.8) is a typical serial system composed of two parallelogram three-beam modules. The compliance matrix of the double parallelogram module, for the loads and displacements defined at the centre, C_{p1}, of the primary stage, can be expressed based on the approaches in *Appendix C* as

$$\mathbf{C}_s = \mathbf{C}_{p1} + \mathbf{J}_p \mathbf{C}_{p2} \mathbf{J}_p^T \tag{4.5}$$

where $\mathbf{C}_{p1}$ and $\mathbf{C}_{p2}$ are the local compliance matrices of the first and second three-beam parallelogram modules, respectively, obtained using Equation (4.4). $\mathbf{J}_p$ is the transformation matrix, obtained based on $\mathbf{D}_{pi}$ in Equation (4.3b) using the relative

location (0, v_2) of the centre, C_{p1}, of primary stage with respect to the indicated point, C_{s2}, on the secondary stage. We have

$$\mathbf{C}_{p1}=\mathbf{C}_p,\mathbf{C}_{p2}=\begin{vmatrix}\cos\pi & -\sin\pi & 0\\ \sin\pi & \cos\pi & 0\\ 0 & 0 & 1\end{vmatrix}\mathbf{C}_p\begin{vmatrix}\cos\pi & -\sin\pi & 0\\ \sin\pi & \cos\pi & 0\\ 0 & 0 & 1\end{vmatrix}^{-1}, \text{ and } \mathbf{J}_p=\begin{bmatrix}1 & 0 & -v_2\\ 0 & 1 & 1\\ 0 & 0 & 1\end{bmatrix}.$$

Then, we obtain the corresponding stiffness matrix

$$\mathbf{K}_s=\mathbf{C}_s^{-1}. \tag{4.6}$$

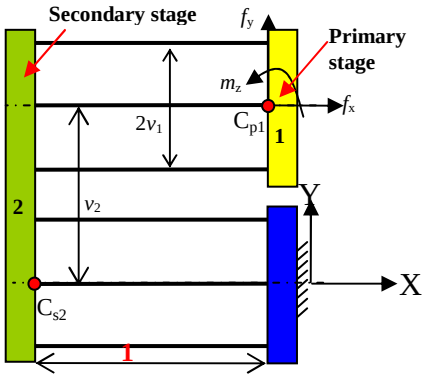

Figure 4.8 Double three-beam parallelogram module

4.2.3 Modelling of the compliant P joint I

The compliant P joint I (Figure 4.9) consists of two double three-beam parallelogram modules in parallel. Let α_i represent the rotation angle between two coordinate systems. We can derive its stiffness matrix for the loads and displacements defined at the actuation point, C_a, as

$$\mathbf{K}_{ps}=\mathbf{D}_{s1}^{T}\mathbf{K}_{s1}\mathbf{D}_{s1}+\mathbf{D}_{s2}^{T}\mathbf{K}_{s2}\mathbf{D}_{s2} \tag{4.7}$$

where $\mathbf{K}_{s1}$ and $\mathbf{K}_{s2}$ are obtained based on Equation (4.6), and $\mathbf{D}_{s1}$ and $\mathbf{D}_{s2}$ are obtained based on $\mathbf{D}_{pi}$ in Equation (4.3b). We have

$$\mathbf{K}_{si}=\begin{bmatrix}\cos\alpha_i & 0 & \sin\alpha_i\\ 0 & 1 & 0\\ -\sin\alpha_i & 0 & \cos\alpha_i\end{bmatrix}\mathbf{K}_s\begin{bmatrix}\cos\alpha_i & 0 & \sin\alpha_i\\ 0 & 1 & 0\\ -\sin\alpha_i & 0 & \cos\alpha_i\end{bmatrix}^{-1} \quad (i=1, 2),$$

$$\mathbf{D}_{s1}=\begin{bmatrix}1 & 0 & h_2\\ 0 & 1 & -h_1\\ 0 & 0 & 1\end{bmatrix}, \text{ and } \mathbf{D}_{s2}=\begin{bmatrix}1 & 0 & h_2\\ 0 & 1 & h_1\\ 0 & 0 & 1\end{bmatrix}.$$

Here α_1=0 and α_2=π.

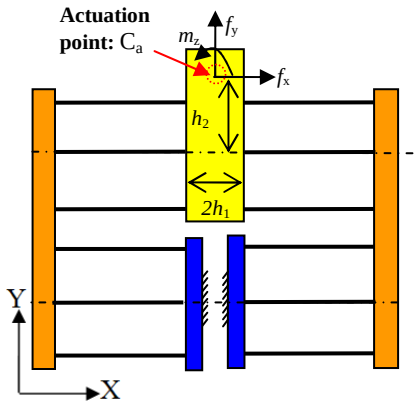

Figure 4.9 Compliant P joint I with geometrical parameters and loading representation

Then we obtain the corresponding compliance matrix

$$\mathbf{C}_{ps} = \mathbf{K}_{ps}^{-1}. \tag{4.8}$$

4.2.4 Modelling of the compliant P joint II

The compliant P joint II (Figure 4.10 is composed of two four-beam parallelogram modules in series.

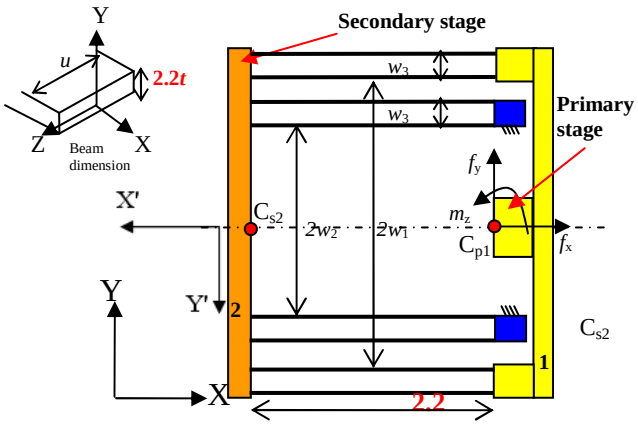

Figure 4.10 Compliant P joint II with geometrical parameters and loading representation

For the first four-beam parallelogram module (outer one) with displacements and loads defined at the point, C_{p1}, its own stiffness matrix with respect the global coordinate system XYZ can be obtained as

$$\mathbf{K}_{op1} = \sum_{i=1}^{4} \mathbf{D}_{op1i}^{T} \mathbf{K}_{oi} \mathbf{D}_{op1i} \tag{4.9}$$

where $\mathbf{K}_{oi}$ (i=1, 2, 3, 4) is the stiffness matrix of each beam, with 2.2 times of the above

length and thickness, in the compliant P joint II, and $\mathbf{D}_{\text{op1}i}$ (i=1, 2, 3, 4) is the transformation matrix of displacements, which are shown as

$$\mathbf{K}_{oi}=\begin{bmatrix} d & 0 & 0 \\ 0 & a & 2.2c \\ 0 & 2.2c & 2.2^2 b \end{bmatrix} \text{ if } u/(2.2t)>10,$$

$$\mathbf{K}_{oi}=\begin{bmatrix} d & 0 & 0 \\ 0 & a(1-v^2) & 2.2c(1-v^2) \\ 0 & 2.2c(1-v^2) & 2.2^2 b(1-v^2) \end{bmatrix} \text{ if } u/(2.2t)<10, \text{ and}$$

$$\mathbf{D}_{\text{op1}i}=\begin{bmatrix} 1 & 0 & -y_i' \\ 0 & 1 & 0 \\ 0 & 0 & 1 \end{bmatrix}.$$

Here $y_1'= w_1+w_3$, $y_2'= w_1$, $y_3'=-w_1$ and $y_4'=-(w_1+w_3)$.

The compliance matrix for the first four-beam parallelogram module is then obtained as

$$\mathbf{C}_{\text{op1}}=\mathbf{K}_{\text{op1}}^{-1}. \tag{4.10}$$

Similarly, the stiffness matrix for the second four-beam parallelogram module (inner one) with displacements and loads defined at the point, C_{s2}, with respect to its own local coordinate system X'Y'Z', is

$$\mathbf{K}_{\text{op2}}=\sum_{i=1}^{4}\mathbf{D}_{\text{op2}i}^{\text{T}}\mathbf{K}_{oi}\mathbf{D}_{\text{op2}i} \tag{4.11}$$

where

$$\mathbf{D}_{\text{op2}i}=\begin{bmatrix} 1 & 0 & -y_i' \\ 0 & 1 & 0 \\ 0 & 0 & 1 \end{bmatrix}.$$

Here $y_1'= w_2+w_3$, $y_2'= w_2$. $y_3'=-w_2$ and $y_4'=-(w_2+w_3)$.

Thus, the compliance matrix for the second four-beam parallelogram module, with respect to the global coordinate system XYZ, is given as

$$\mathbf{C}_{\text{op2}}=\begin{bmatrix} \cos\pi & -\sin\pi & 0 \\ \sin\pi & \cos\pi & 0 \\ 0 & 0 & 1 \end{bmatrix}\mathbf{K}_{\text{op2}}^{-1}\begin{bmatrix} \cos\pi & -\sin\pi & 0 \\ \sin\pi & \cos\pi & 0 \\ 0 & 0 & 1 \end{bmatrix}^{-1}. \tag{4.12}$$

Once $\mathbf{C}_{\text{op1}}$ and $\mathbf{C}_{\text{op2}}$ are obtained based on Equations (4.10) and (4.12), we obtain the compliance matrix of the compliant joint II following the derivation of Equation (4.5) as

$$\mathbf{C}_{\text{os}}=\mathbf{C}_{\text{op1}}+\mathbf{J}_{\text{op}}\mathbf{C}_{\text{op2}}\mathbf{J}_{\text{op}}^{\text{T}} \tag{4.13}$$

where $\mathbf{J}_{\text{op}}$ is obtained based on Equation (4.3b) using the relative location (2.2, 0) of the

centre of primary stage with respect to that of the secondary motion stage, which is shown below:

$$\mathbf{J}_{\text{op}} = \begin{bmatrix} 1 & 0 & 0 \\ 0 & 1 & 2.2 \\ 0 & 0 & 1 \end{bmatrix}.$$

4.2.5 Modelling of a planar leg

Base on the above compliant matrices of compliant P joints, we can further derive the compliance matrix of a planar leg, for the loads and displacements defined at the virtual action point of the primary stage (Figure 4.11), as

$$\mathbf{C}_{\text{leg}} = \mathbf{C}_{\text{ps}}' + \mathbf{C}_{\text{os}} \tag{4.14}$$

where $\mathbf{C}_{\text{ps}}' = \begin{bmatrix} \cos\pi/2 & \sin\pi/2 & 0 \\ -\sin\pi/2 & \cos\pi/2 & 0 \\ 0 & 0 & 1 \end{bmatrix} \mathbf{C}_{\text{ps}} \begin{bmatrix} \cos\pi/2 & \sin\pi/2 & 0 \\ -\sin\pi/2 & \cos\pi/2 & 0 \\ 0 & 0 & 1 \end{bmatrix}^{-1}$.

Then, the corresponding stiffness matrix for the planar leg is

$$\mathbf{K}_{\text{leg}} = \mathbf{C}_{\text{leg}}^{-1}. \tag{4.15}$$

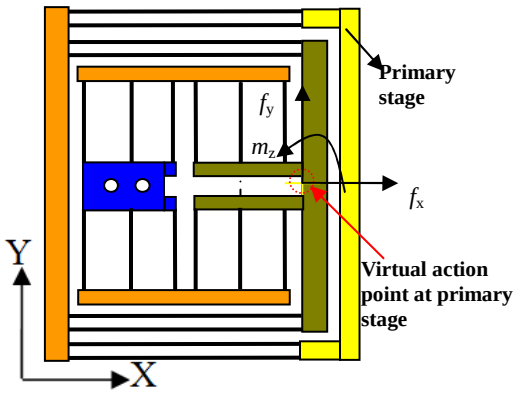

Figure 4.11 A planar leg

4.2.6 Modelling of the stiffness-enhanced XY CPM

Using Equation (4.15), the stiffness matrices of all planar PP legs in the local coordinate system are obtained by appropriate coordinate transformation. The stiffness matrix, $\mathbf{K}_{\text{spatial}}$, of the spatial compliant leg (Figure 4.5a) under the planar loads can be obtained based on the results of subtracting the effects of the out-of-plane loads from Equations (2.86a), (2.86b) and (2.86f), and the normalization conditions mentioned earlier, which is given below:

$$\mathbf{K}_{\text{spatial}}=\begin{bmatrix} 2at(1-v^2)/u & 0 & 0 \\ 0 & 2at(1-v^2)/u & 0 \\ 0 & 0 & t(1-v^2)/[\dfrac{u}{4(\delta+ar_4^2)}+\dfrac{u}{4(\delta+ar_4'^2)}] \end{bmatrix}$$

where v is the Possion's ratio, and δ = 1/(1+v). r_4' and r_4' are the two pitch circle radii, around which inner and outer four beams in the spatial compliant leg are spaced.

Then the stiffness matrix of the stiffness-enhanced XY CPM (Figure 4.6), for the loads and displacements defined at the centre of the motion stage of the planar XY CPM, can be obtained accordingly as

$$\mathbf{K}_{\text{m}}=\sum_{i=1}^{4}\mathbf{D}_{\text{m}i}^{\text{T}}\mathbf{K}_{\text{leg}i}\mathbf{D}_{\text{m}i}+\mathbf{K}_{\text{spatial}} \tag{4.16}$$

where $\mathbf{K}_{\text{leg}i}$ is the stiffness matrix for each leg, which is shown below

$$\mathbf{K}_{\text{leg}i}=\begin{bmatrix} \cos\alpha_i & -\sin\alpha_i & 0 \\ \sin\alpha_i & \cos\alpha_i & 0 \\ 0 & 0 & 1 \end{bmatrix}\mathbf{K}_{\text{leg}}\begin{bmatrix} \cos\alpha_i & -\sin\alpha_i & 0 \\ \sin\alpha_i & \cos\alpha_i & 0 \\ 0 & 0 & 1 \end{bmatrix}^{-1}.$$

Here α_1=0, α_2=π/2, α_3=π, and α_4=3π/2. $\mathbf{D}_{\text{m}i}$ is the displacement transformation matrix, which is defined as

$$\mathbf{D}_{\text{m}i}=\begin{bmatrix} 1 & 0 & -y_i' \\ 0 & 1 & x_i' \\ 0 & 0 & 1 \end{bmatrix}.$$

Let s denote the normalized distance between the centre of the motion stage and the actuation point. We have x_1'=−s, y_1'=*0*, x_2'=0, y_2'=−s, x_3'=s, y_3'=0, x_4'=0, and y_4'=s.

It is noted that all the above modelling builds on small deformation assumptions, and the material non-linearity has been ignored. The much smaller the motion range is, the more accurate the liner model is due to small deformation assumptions. All these equations can be programmed using *Maple*.

Then, we have the load-displacement equations

$$\mathbf{F}=\mathbf{K}_{\text{m}}\mathbf{X}_{\text{s}} \tag{4.17}$$

where $\mathbf{F}=[f_x, f_y, m_z]^{\text{T}}$ and $\mathbf{X}_{\text{s}}=[x_s, y_s, \theta_{sz}]^{\text{T}}$, which are the load and displacement vectors at the center of the motion stage of the planar XY CPM, respectively.

In practice, two actuation forces should be exerted at the actuation points (Figure 4.6a) rather than the centre of the motion stage of the planar XY CPM. The difference between the two actuation ways is due to the axial compression deformation of the beams in the compliant P joint II (for details, see *Appendix G*).

Similar to the derivation of Equation (4.17), the load-displacement equations capturing the effects for loads acting at both the actuation points and the centre of the motion stage are

$$\mathbf{F} = \mathbf{K}_{\mathrm{m}}\mathbf{X}_{\mathrm{s}} - \mathbf{D}_{\mathrm{m1}}^{\mathrm{T}}\mathbf{K}_{\mathrm{leg1}}\mathbf{C}_{\mathrm{ps}}'\mathbf{F}_{\mathrm{ax}} - \mathbf{D}_{\mathrm{m2}}^{\mathrm{T}}\mathbf{K}_{\mathrm{leg2}}\mathbf{C}_{\mathrm{ps}}\mathbf{F}_{\mathrm{ay}} \tag{4.18}$$

where $\mathbf{F}_{\mathrm{ax}} = [f_{ax-x}, f_{ax-y}, m_{ax-z}]^{\mathrm{T}}$ and $\mathbf{F}_{\mathrm{ay}} = [f_{ay-x}, f_{ay-y}, m_{ay-z}]^{\mathrm{T}}$, which denote the actuation load vectors at the X- and Y-actuation points, respectively. $f_{\mathrm{ax\text{-}x}}$ and $f_{\mathrm{ax\text{-}y}}$ denote the forces acting at the X-actuation point along the X- and Y-axes, respectively.

It is noted that when $\mathbf{F}_{\mathrm{ax}}$ and $\mathbf{F}_{\mathrm{ay}}$ are all zero vectors, Equation (4.18) can be reduced to Equation (4.17).

When $\mathbf{F}$ is equal to a zero vector, Equation (4.18) can be further simplified to obtain the displacement vector as

$$\mathbf{X}_{\mathrm{s}} = \mathbf{K}_{\mathrm{m}}^{-1}(\mathbf{D}_{\mathrm{m1}}^{\mathrm{T}}\mathbf{K}_{\mathrm{leg1}}\mathbf{C}_{\mathrm{ps}}'\mathbf{F}_{\mathrm{ax}} + \mathbf{D}_{\mathrm{m2}}^{\mathrm{T}}\mathbf{K}_{\mathrm{leg2}}\mathbf{C}_{\mathrm{ps}}\mathbf{F}_{\mathrm{ay}}). \tag{4.19}$$

Using the result of Equation (4.19), we can derive the displacements at the X-actuation point (the connecting centre between the X-actuator and the XY CPM) as

$$\mathbf{X}_{\mathrm{ax}} = \mathbf{C}_{\mathrm{ps}}'[\mathbf{K}_{\mathrm{leg1}}(\mathbf{D}_{\mathrm{m1}}\mathbf{X}_{\mathrm{s}} - \mathbf{C}_{\mathrm{ps}}'\mathbf{F}_{\mathrm{ax}}) + \mathbf{F}_{\mathrm{ax}}] \tag{4.20}$$

where $\mathbf{X}_{\mathrm{ax}} = [x_{ax}, y_{ax}, \theta_{ax-z}]^{\mathrm{T}}$, which is the displacement vector at the X-actuation point. x_{ax} and y_{ax} denote the translational displacements of the X-actuation point along the X- and Y-axes, respectively.

4.3 Case Study of a Stiffness-Enhanced XY CPM

4.3.1 Material, actuator and geometrical parameter determination

As an example, the material for the stiffness-enhanced XY CPM is chosen to be an aluminium alloy, AL6061-T651, for which Young's modulus, E, is 69,000 Nmm^{-2} and Poisson's ratio, v, is 0.33, due to the material's low internal stresses, good strength and phase stability [4.6] suitable for precision engineering application.

The objective of 10mm×10mm's motion range requires a large-range linear actuator. Because of the merits such as large-range nanopositioning (the large range of motion and high nanometric resolution), *linear model*, and *force-control* along with hysteresis-free, frictionless and cog-free motion, one can choose the linear voice coil actuator from BEI Kimco Magnetics (*LA28-22-000A*), which provides a total stroke of 11.43mm and a relatively large peak force of 266.89N, with dimension: Φ 69.85 mm×55.88 mm, for the stiffness-enhanced XY CPM.

Based on maximal shear stress theory, the actual (non-normalized) transverse motion range for the beams both in the compliant P joints I and II should meet the following conditions based on *Appendix F*:

$$\Delta_{\mathrm{I}} \le \frac{1}{3\eta}\frac{\sigma_s}{E}\frac{L^2}{T} \quad , \tag{4.21}$$

$$\Delta_{\mathrm{II}} \le \frac{1}{3\eta}\frac{\sigma_s}{E}\frac{(2.2L)^2}{2.2T} = \frac{2.2}{3\eta}\frac{\sigma_s}{E}\frac{L^2}{T} \tag{4.22}$$

where Δ_{I} and Δ_{II} are the actual transverse motion range of the beams in the compliant P joints I and II, respectively. σ_{s} =276Mpa, which is the yield strength of the chosen material, and η is the safety coefficient.

Equations (4.21) and (4.22) show that the allowable maximal motion range of the compliant P joint II is larger than that of the compliant P joint I. Therefore, we may further increase the in-plane thickness of the beam in the compliant P joint II to let it produce the same allowable maximal motion range as the compliant P joint I. But this will enlarge its primary stiffness, which leads to worse actuator isolation performance.

To achieve a 10mm's motion range along each axis, i.e. twice of the beam's transverse motion range, for the stiffness-enhanced XY CPM, we obtain from Equation (4.21)

$$\frac{2}{3\eta}\frac{\sigma_s}{E}\frac{L^2}{T} \ge 10\mathrm{mm}\,. \tag{4.23}$$

According to Equation (4.23), the actuator mounting size and minimum manufacture requirements, the dimension for a beam in the compliant P joint I is L=50mm, T=0.66mm (t=0.0132), and U=10mm (u=0.2), and the other geometric parameters in the planar XY CPM (Figure 4.6a) are V_1=20.66mm (v_1=0.4132), V_2=52mm (v_2=1.04), W_1=127.726mm (w_1=2.5545), W_2=107.726mm (w_2=2.1545), W_3=8.548mm (w_3=0.1510), H_1=43mm (h_1=0.86), H_2=27.01mm (h_2=0.5402), and S=149 mm (s=2.98).

In order to make the spatial compliant leg (Figure 4.5a) produce the same motion range as that of the compliant P joint I, the thickness and length of the beam in the spatial compliant leg are 0.66mm and 50 mm, respectively. Two pitch circle radiues in the spatial leg, are, respectively, set up to be R_4=56.1069mm (r_4=1.1220) and R_4'=71.1774mm (r_4'=1.4235), accordingly. Here, R_4 is set to be comparable with the beam length in order to reduce the parasitic motion and R_4' is obtained based on the motion range requirement and the predetermined R_4.

The overall dimension for the above stiffness-enhanced XY CPM with base frame is 540 mm×540mm×75mm.

4.3.2 Input load-output displacement equations

Substituting the above geometrical dimensions into Equation (4.19), we obtain the displacements for the motion stage under only two actuation forces, $f_{\text{ax-x}}$ and $f_{\text{ay-y}}$:

$$[x_s, y_s, \theta_{sz}]^{\mathrm{T}} = \left[0.0086078 f_{ax-x}, \quad 0.0086078 f_{ay-y}, \quad 0\right]^{\mathrm{T}}. \tag{4.24}$$

Equation (4.24) shows that the stiffness-enhanced XY CPM has no cross-axis coupling. It also reveals that if no moment acts at two actuation points, no in-plane parasitic rotation exists.

4.3.3 Lost motion

Substituting the geometrical dimensions of the stiffness-enhanced XY CPM into Equation (4.20) under only two actuation forces, $f_{\text{ax-x}}$ and $f_{\text{ay-y}}$, we have

$$[x_{ax}, y_{ax}, \theta_{ax-z}]^{\mathrm{T}} = [8.6134\times10^{-3} f_{ax-x}, \quad 2.995\times10^{-6} f_{ay-y}, \quad -9.8927\times10^{-9} f_{ay-y}]^{\mathrm{T}}. \tag{4.25}$$

The linear lost motion percentage can be obtained based on Equations (4.24) and (4.25):

$$\frac{x_{ax} - x_s}{x_s}\times100\% = \frac{(0.0086134 - 0.0086078)}{0.0086078} = 0.065\%. \tag{4.26}$$

4.3.4 Actuation isolation performance

From Equation (4.25), we can obtain the input coupling for the X-actuator, which is reflected by the transverse motion of the X-actuation point, as follows

$$y_{ax} = 2.995\times10^{-6} f_{ay-y}. \tag{4.27}$$

4.3.5 Buckling checking

The conditions for no buckling to occur in the beams in both the compliant P joint II and compliant P joint I are

$$10\times(\mathrm{k}_{\mathrm{m11}} - \mathrm{k}_{\mathrm{leg11}})\frac{EUT^3}{12(1-v^2)L^3} = 10\times(116.14 - 35.9854)\frac{EUT^3}{12(1-v^2)L^3} \le 40\frac{EU(2.2T)^3}{12(2.2L)^2}, \tag{4.28}$$

$$10\times\frac{(\mathrm{k_{m11}}-2\mathrm{k_{leg11}}-\mathrm{k_{spatial11}})}{2}\frac{EUT^3}{12(1-v^2)L^3}=5(116.14-2\times35.9854-1.4115)\frac{EUT^3}{12(1-v^2)L^3}\le 60\frac{EUT^3}{12(1-v^2)L^2} \tag{4.29}$$

where $\mathrm{k_{m11}}$, $\mathrm{k_{leg11}}$ and $\mathrm{k_{spatial11}}$ denote the elements (entries) in the first row and first column of the matrices: $\mathbf{K}_{\mathrm{m}}$ [Equation (4.16)], $\mathbf{K}_{\mathrm{leg}}$ [Equation (4.15)], and $\mathbf{K}_{\mathrm{spatial}}$ [Equation (4.16)], respectively. The term on the left-hand side in Equation (4.28), $10\times(\mathrm{k_{m11}}-\mathrm{k_{leg11}})\frac{EUT^3}{12(1-v^2)L^3}$, denotes the actual axial load acting at the compliant P joint II when producing 10 mm's motion range. The term on the right-hand side in Equation (28), $40\frac{EU(2.2T)^3}{12(2.2L)^2}$, denotes the actual buckling load for the compliant P joint II in the leg 1 or 2 obtained from [4.6]. The term on the left-hand side in Equation (4.29), $10\times\frac{(\mathrm{k_{m11}}-2\mathrm{k_{leg11}}-\mathrm{k_{spatial11}})}{2}\frac{EUT^3}{12(1-v^2)L^3}$, denotes the actual axial load acting at the compliant P joint I in any leg when producing 10 mm's motion range. The term on the right-hand side in Equation (4.29), $60\frac{EUT^3}{12(1-v^2)L^2}$, denotes the actual buckling load for the compliant P joint I obtained from [4.6].

It is verified that the above inequalities [Equations (4.28) and (4.29)] are satisfied under the given conditions. Therefore, no buckling occurs in the compliant P joints.

4.3.6 Actuation force checking

In order to ensure the voice coil actuator to works normally, the actual actuation force must be not greater than the peak force of the selected voice coil actuator. In the case studied above, we have

$$10\times\frac{1}{0.0086078}\times\frac{EUT^3}{12(1-v^2)L^3}=172.4\mathrm{N}\le 266.9\mathrm{N} \tag{4.30}$$

where the term on the left-hand side is the actual actuation force to produce 10mm's primary motion obtained using Equation (4.24), and the term on the right-hand side is the peak force of the selected voice coil actuator (*LA28-22-000A*).

4.4 FEA Comparisons

Figures 4.12–4.16 show the performance characteristics, such as primary compliance, lost motion, and actuation isolation, of the stiffness-enhanced XY CPM (Figure 4.6)

based on FEA and the proposed analytical models. Here, we choose *Comsol large-displacement module* for FEA using tetrahedron element with fine mesh (maximum element size 0.2mm). The reference point is the centre of the top surface of the motion stage of the stiffness-enhanced XY CPM for translational displacements.

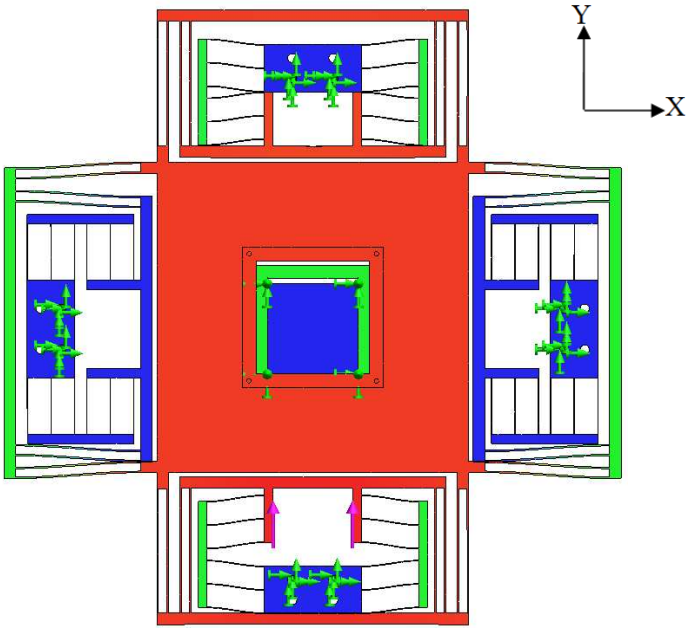

a) 10mm's translational displacement along the Y-axis

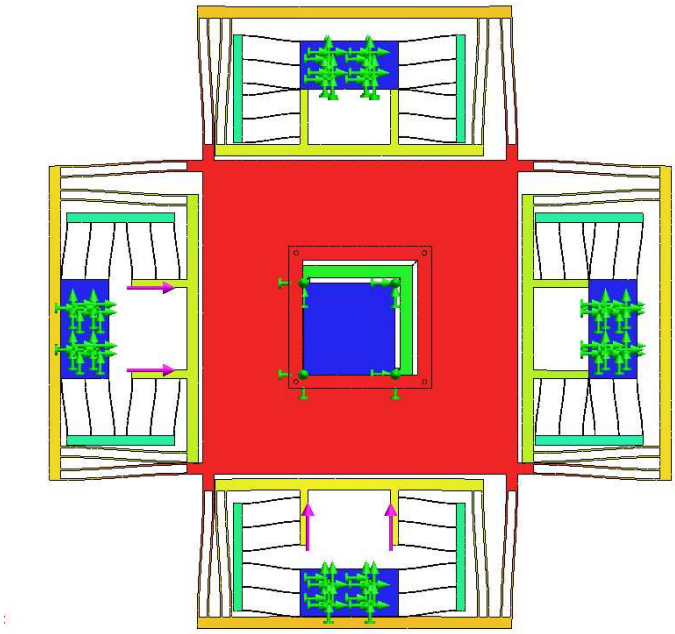

b) 10mm's translational displacements along both the X- and Y-axes

Figure 4.12 FEA illustrations in deformation for the large range of motion

Figure 4.12 illustrates the large range of motion for two cases obtained using FEA under static elastic domain: a) 10mm's translation along the Y-axis, and b) 10mm's

translations along both the X- and Y-axes.

a) Primary motion comparison

Figure 4.13 shows that the nominal X-axis compliance ($\partial X_s / \partial F_{ax-x}$ for zero Y-actuation) obtained using the linear analytical model [Equation (4.24)] is slightly lower than that obtained using FEA, with an acceptable difference of 4.8%.

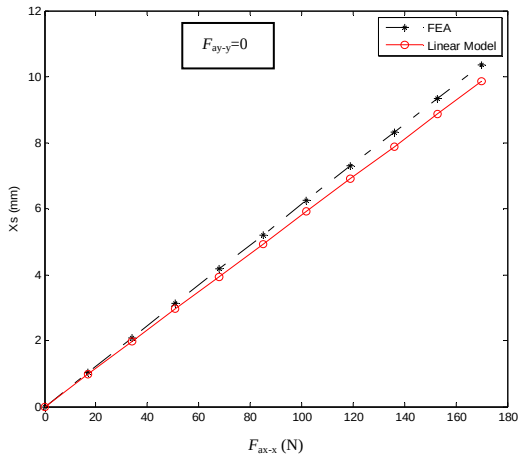

Figure 4.13 Primary motion in the X-direction

b) Cross-axis coupling comparison

It is noted that FEA (Figure 4.14) can capture the negligible cross-axis coupling effect (for instance the effect of F_{ay-y} upon X_s) that the linear analytical model [Equation (4.24)] cannot. This input coupling effect results in a slight reduction of the primary stiffness. FEA results reveal that the maximal cross-axis coupling error in the X-direction is 1.56% of the primary motion, X_s, under F_{ay-y}=0.

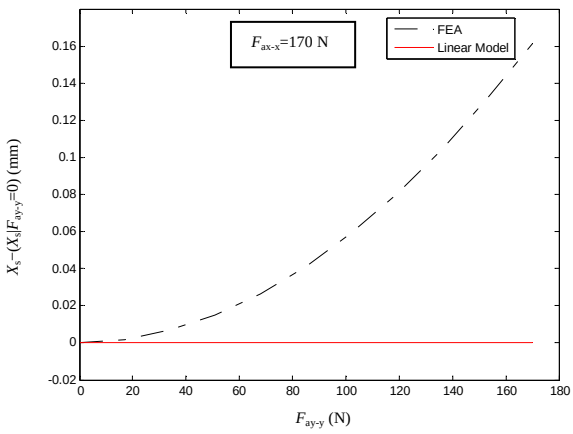

Figure 4.14 Cross-axis coupling error: X-displacement error affected by F_{ay-y}

c) Input-coupling comparison

Figure 4.15 shows that the input coupling obtained using the linear analytical model [Equation (4.27)] is much smaller than that obtained using FEA. FEA also reveals that the input-coupling takes on a nonlinear relationship rather than a linear one, and that Y_{ax} is less than 1.52% of the primary motion, Y_s, which may be acceptable for most applications.

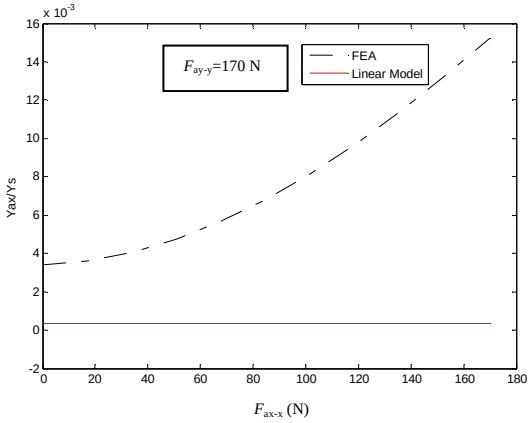

Figure 4.15 Input coupling percentage of the actuation point producing X-axis primary motion caused by $F_{ax\text{-}x}$

d) Lost motion comparison

Figure 4.16 shows that the comparison of the lost motion in the X-direction. It shows that the ratio of the lost motion to the primary motion obtained using FEA is less than 4.45%, which can be also tolerated for most applications, but much larger than 0.065%, obtained using the linear analytical model [Equation (4.26)]. In addition, FEA shows that the lost motion has a nonlinear relationship rather than a linear one.

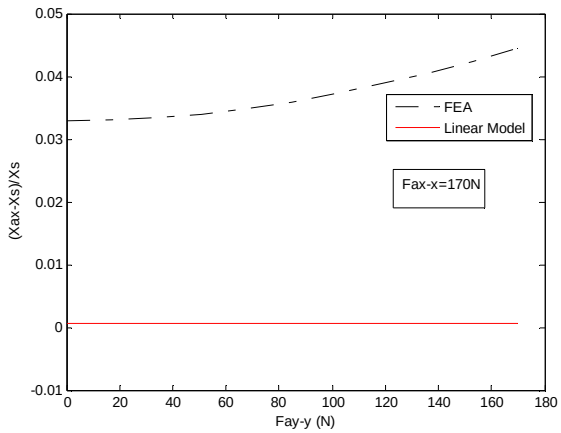

Figure 4.16 Lost motion percentage in the X-direction

e) Parasitic rotation comparison

FEA results also show that, over the motion range of 10mm×10mm, the parasitic translational displacement along the Z-axis is below 2×10^{-4} mm (4×10^{-6} for normalize value), the parasitic rotation about the X-/Y-axis is below 2×10^{-6}, and the parasitic rotation about the Z-axis is below 1×10^{-6}, while all the corresponding analytical results are equal to zero. All these parasitic rotational displacements can be tolerated in this paper considering the accuracy of FEA.

f) Remarks

The above comparisons show that there are certain differences between the FEA and the analytical results. These differences are due to inaccuracy of either linear analytical model or FEA. The results obtained from FEA are larger than that obtained from the analytical model since all elements are considered as elastic bodies in FEA. It is also noted that the lost motion and input coupling effects differ the most. This is probably because these characteristics are very small and FEA has relatively large inaccuracy in dealing with very small deformation/displacements.

Although FEA can be used to analyse the proposed design and even capture more accurate nonlinear characteristics than the analytical model, it cannot enable rapid analysis and quick design synthesis as compared with the proposed linear analytical models.

In addition, it is noted that the large-range translation of the stiffness-enhanced XY CPM can be achieved through using distributed-compliance modules. The smaller the translational displacement is, the more accurate the linear model is.

4.5 Discussions

4.5.1 Dynamics issues

To improve the dynamic performance of an XY CPM, we may reduce the mass or increase the stiffness to raise the modal frequencies. Therefore, we can further increase the beam number in the double multi-beam parallelogram modules (Figure 4.3) to raise the primary stiffness (therefore the first natural frequency) of the stiffness-enhanced XY CPM without affecting the maximal motion range. We may also increase the beam

number in the spatial double four-beam module (Figure 4.5) to improve its primary stiffness and out-of-plane stiffness along with the buckling load.

If the primary stiffness needs to be increased, a higher-performance linear voice coil actuator with large range of motion and a *higher-peak force* (therefore bulkier) is accordingly required.

In addition to the above measures, one may also improve dynamic performance by using a high-order controller to achieve a high bandwidth greater than the first natural frequency [4.19].

4.5.2 Manufacture

The stiffness-enhanced XY CPM can be fabricated in the following ways. Firstly, fabricate monolithically the XY CPM without the spatial leg from an AL6061-T651 plate of 10 mm thickness using the electric discharge machining (EDM). Then, fabricate the spatial leg (spatial double four-beam module) from an AL6061-T651 block using the EDM (which will be discussed in Chapter 5 in detail). Here, the spatial double four-beam module is composed of several parts fabricated separately. By assembling the spatial leg and the XY CPM without the spatial leg, one can get the stiffness-enhanced XY CPM.

However, the above manufacturing process induces assembly error, and results in increased number of parts. Advances in manufacturing technologies, such as rapid prototyping, may provide an appropriate method for fabricating monolithic spatial compliant mechanisms in the future.

4.5.3 Out-of-plane stiffness

It should be pointed out that FEA results shows that a planar XY CPM without the spatial compliant leg should have approximately 2.2 times higher beams than the associated stiffness-enhanced XY CPM of the case study in order to have the same normal stiffness in the Z-direction. In other words, the stiffness-enhanced XY CPM has approximately 7.1 times larger normal stiffness than its planar XY CPM without the spatial compliant leg.

Compared with the planar XY CPM having 2.2 times higher beams, the stiffness-enhanced XY CPM benefits from reduced linear actuator cost due to smaller primary stiffness.

4.6 Summary

A stiffness-enhanced XY CPM for large translation has been proposed. The analytical modelling has been derived. The analytical and FEA results have shown that, in the example case, the stiffness-enhanced XY CPM has large range of motion up to 10mm×10mm, well-constrained parasitic motion, approximate actuator-isolation, approximate cross-axis decoupling, acceptable lost motion, and especially enhanced out-of-plane stiffness.

Nonlinear modelling of the stiffness-enhanced XY CPM deserves further investigation in order to capture accurate constraint characteristics. Experiment verification is also needed to compare with the analytical models and/or FEA results.

It is emphasized that the stiffness-enhanced XY CPM can be used as a building block of new spatial translational CPMs which will be studied in the next chapter.

4.7 References

[4.1] Kim, D., Lee, D.Y., and Gweon, D.G., 2007, "A New Nano-Accuracy AFM System for Minimizing Abbe Errors and the Evaluation of Its Measuring Uncertainty", *Ultramicroscopy*, Vol. **107**(4–5): 322–328.

[4.2] Schitter, G., Thurner, P.J, and et al, 2008, "Design and Input-Shaping Control of a Novel Scanner for High-Speed Atomic Force Microscopy", *Mechatronics*, Vol. **18**: 282–288.

[4.3] Gorman, J. J., and Dagalakis, N. G., 2003, "Force Control of Linear Motor Stages for Microassembly", *ASME International Mechanical Engineering Conference and Exposition*, November 15–21, 2003, Washington, DC, USA.

[4.4] Vettiger, P., Despont, M., Drechsler, U., Durig, U., Haberle, W., Lutwyche, M. I., Rothuizen, H. E., Stutz, R., Widmer, R., and Binnig, G. K., 2000, "The Millipede—More Than One Thousand Tips for Future AFM Data Storage", *IBM Journal of Research and Development*, Vol. **44**(3): 323–340.

[4.5]Awtar, S., and Slocum, A. H., 2007, "Constraint-Based Design of Parallel Kinematic XY Flexure Mechanisms", *Journal of Mechanical Design*, Vol. **129**(8): 816–830.

[4.6] Awtar, S., 2004, "*Analysis and Synthesis of Planar Kinematic XY Mechanisms*", Sc.D. thesis, Massachusetts Institute of Technology, Cambridge, MA.

[4.7] Choi, K. B. and Kim D. H., 2006, "Monolithic Parallel Linear Compliant

Mechanism for Two Axes Ultra Precision Linear Motion", *Review of Scientific Instruments*, Vol. **77**(6): 065106: 1–7.

[4.8] Li, Y., and Xu, Q., 2009, "Design and Analysis of a Totally Decoupled Flexure-Based XY Parallel Micromanipulator", *IEEE Transactions on Robotics*, Vol. **25**(3): 645–657.

[4.9] Tam, M., Payandeh, S., and Parmaswaran, A.M., 2005, "Design and Development of a Multiple DOF Compliant Robot", *Proceedings of 12th IEEE International Conference on Advanced Robotics*, 18–20 July 2005, Washington, USA, pp. 876–882.

[4.10] Polit, S., Dong, J., 2009, "Design of High-Bandwidth High-Precision Flexure-Based Nanopositioning Modules", *Journal of Manufacturing System*, Vol. **28**: 71–77.

[4.11] Dong, J., Ferreira, P.M., 2009, "Electrostatically Actuated Cantilever with SOI-MEMS Parallel Kinematic XY Stage", *Journal of Microeletromechanical Systems*, Vol. **18**(3): 641–651.

[4.12] Sun, L., Wang, J., and et al, 2008, "A Silicon Integrated Micro Nano-Positioning XY-Stage for Nano-Manipulation", *Journal of Micromechanics and Microeng*ineering, Vol.**18**: 125004.

[4.13] Kim, W.-J., Verma, S., and Shakir, H., 2007, "Design and Precision Construction of Novel Magnetic-Levitation-Based Multi-Axis Nanoscale Positioning Systems", *Precision Engineering*, Vol. **31**(4): 337–350.

[4.14] Holmes, M., Hocken, R., and Trumper, D., 2000, "The Long-Range Scanning Stage: a Novel Platform for Scanned-Probe Microscopy", *Precision Engineering*, Vol. **24**(3):191–209.

[4.15] Maeda, G. J., Sato, K., Hashizume, H., and Shinshi, T., 2006, "Control of an XY Nano-Positioning Table for a Vompact Nano-Machine Tool", *JSME International Journal, Series C (Mechanical Systems, Machine Elements and Manufacturing)*, Vol. **49**(1), pp. 21–27.

[4.16] Dejima, S., Gao, W., Katakura, K., Kiyono, S., and Tomita, Y., 2005, "Dynamic Modeling, Controller Design and Experimental Validation of a Planar Motion Stage for Precision Positioning", *Precision Engineering*, Vol. **29**(3): 263–271.

[4.17] Awtar, S. Slocum, A.H., 2007, "Characteristics of Beam-Based Flexure Modules", *Journal of Mechanical Design*, Vol. **129** (6): 624–639.

[4.18] Awtar, S., Sevincer, E., 2010, "Elastic Averaging in Flexure Mechanisms: a Three-Beam Parallelogram Flexure Case Study", *Journal of Mechanisms and*

Robotics, Vol. **2**(4): 041004.

[4.19] Awtar, S., and Parmar, G., 2010, "Design and a Large Range XY Nanopostioning System", *Proceedings of the ASME 2010 International Design Engineering Technical Conferences & Computers and Information in Engineering Conference*, August 15 – 18, 2010, Montreal, Quebec, Canada. DETC2010-28185

Chapter 5 – Design and Modelling of XYZ CPMs for High-Precision Motion Stages

In addition to XY CPMs studied in Chapter 4, an XYZ CPM for high-precision motion stage is a mechatronic motion system, which is an integration of compliant mechanism (composed of a base and a motion stage connected by compliant members), actuators, sensors and controllers. Its motion stage is capable of translating along the X-, Y- and Z-axes actuated by three actuators indirectly, respectively. XYZ CPMs can be used in various applications such as the scanning table, bio-cell injector, nano-positioner, adjustable mounting [5.1–5.4], and potential 3-D mechanical loading device. Their merits and desired performance characteristics (design indices) have mentioned in the Chapter 1. One of popular stable 3-DOF translational stages on the market is the Elliot Gold^{TM} *series* XYZ flexure stage invented by Martock Design [5.4]. But this serial XYZ flexure stage has some shortcomings such as having accumulation of errors compared with CPMs.

XYZ CPMs belong to a class of spatial mechanisms, and their synthesis and modelling are more complicated than planar CPMs. Recent research advances on the type synthesis of (rigid-body) translational parallel manipulators (TPMs) provide a starting point for the conceptual design of XYZ CPMs – 3-DOF translational CPMs. A number of XYZ CPMs using lumped compliance, such as the 3-PRRR [5.5, 5.6], 3-PPPR [5.7], 3-PRC [5.8, 5.9], 3-PUU [5.10], 3-PP^{s} [5.11] and 3-PPP [5.12] CPMs, have been proposed on the basis of the PRBM approach. Here, R, C, U and P^{s} denote revolute, cylindrical, revolute, universal joints and spatial motion four-bar parallelogram with four spherical lumped-compliance joints, respectively. In addition, hybrid motion CPMs (partially CPMs) combining macro motion (driven by DC motor) and micro motion (driven by PZT actuator) have been developed in order to achieve large range of motion and high resolution [5.13, 5.14]. Typical existing designs for XYZ CPMs are shown in Figure 5.1.

Despite their characteristics, these existing XYZ CPMs have several drawbacks. Firstly, planar (no spatial currently) and lumped-compliance joints/modules [5.5–5.12] are used in the CPMs. This may result in stress-concentration and especially small range of motion (100μm~1mm). Secondly, the CPMs are input-output coupled [5.8], which causes complicated control. Thirdly, the CPMs may have the *bulky configuration* [5.12], 3. In addition, the resolution of hybrid motion CPMs [5.13. 5.14] depends on the resolution of macro motion and the motion range of micro motion. If the macro motion

resolution is larger than the motion range of micro motion, high resolution cannot be reached by the compensation of micro motion control. Also, hybrid motion CPMs may have more bulkier systems including the mechanism, actuator, driver and controller.

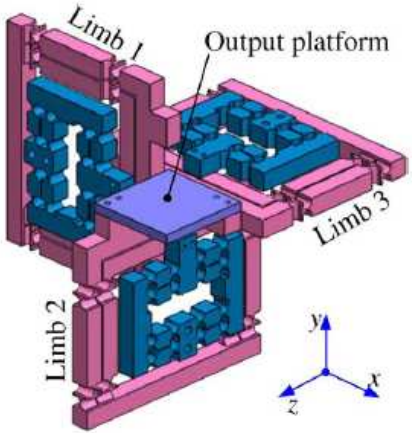

(a) 3-PPPR CPM [5.7]

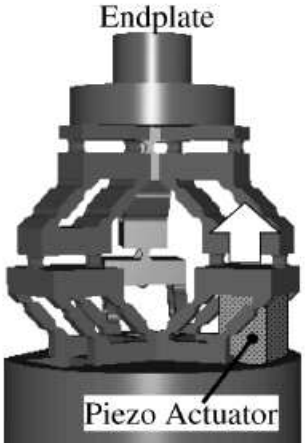

(b) 3-PRC CPM [5.8]

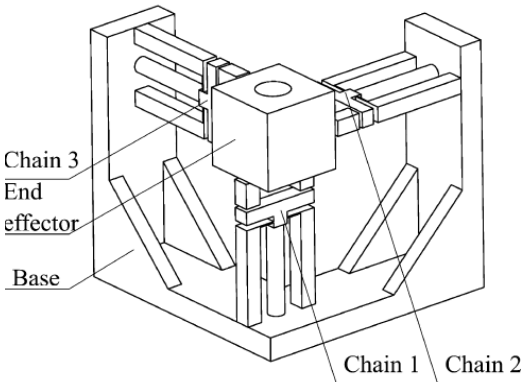

(c) 3-PP^{s} CPM [5.11]

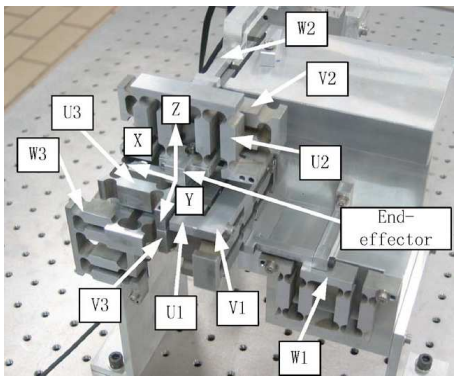

(d) 3-PPP CPM [5.12]

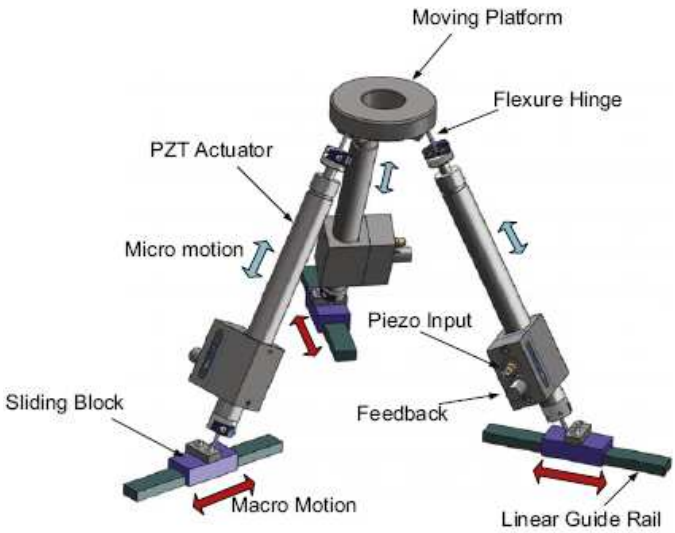

e) 3-PUPU partially CPM [5.13]

Figure 5.1 Typical existing designs for the XYZ CPMs

To overcome the small-range-of-motion drawback for the existing designs, this

chapter focuses on design and modelling of XYZ CPMs for *large range of motion* using (*spatial*) *distributed-compliance* modules, and also deals with other desired performance characteristics such as well-constrained parasitic motion, minimal cross-axis coupling and maximal actuator isolation.

This chapter is organized as follows. In Section 5.1, a general design methodology for translational CPMs is introduced. In Section 5.2, type synthesis of XYZ CPMs is then conducted to generate several large-range XYZ CPMs using the proposed approach through the use of: 1) identical double parallelogram flexure modules, 2) inverted planar XY CPMs, 3) identical spatial modules, 4) embedded spatial modules, 5) five legs composed of spatial modules, and 6) planar double two-beam modules. In Section 5.3, the kinematostatic modelling of the improved modular XYZ CPM using identical spatial double four-beam modules is implemented. In Section 5.4, the material, actuator and geometrical parameter determination, performance characteristic analysis, buckling and actuation force checking, and manufacture discussion are performed for a case improved modular XYZ CPM with a motion range of 10mm×10mm×10mm. In Section 5.5, the first natural frequency is calculated. In Section 5.6, the analytical models are compared with FEA. Finally, the summary is conducted.

5.1 Design Methodology for Translational CPMs

In Chapters 3 and 4, we have studied 1-DOF and 2-DOF CPMs. For 1-DOF translational CPMs, the design approach is institutive or brainstormed due to the very straightforward configuration (see Figure 3.8 for instance). For 2-DOF translational CPMs, the design approach has been observed that we can replace the traditional P joints with lumped or distributed compliance P joints based on the type synthesis of rigid-body parallel mechanisms (see Figure 4.4 for instance).

XYZ CPMs are more complicated than 1-DOF and 2-DOF CPMs, a new design methodology is therefore to be presented in order to obtain the desired XYZ CPMs.

XYZ CPMs can be designed following the procedure below:

(1) Determine the design objective for CPMs such as an XYZ CPM.

(2) Identify proper rigid-body parallel mechanisms, such as the 3-PPPR TPM, based on the type synthesis of rigid-body parallel mechanisms in a way similar to the PRBM approach [5.5–5.12].

(3) Replace the traditional kinematic joints or kinematic sub-chains (such as the passive PPR kinematic chain in the 3-PPPR TPM) with suitable lumped joints or

distributed-compliance building-block modules (such as the spatial double four-beam parallel module). Here, the building-block modules may be existing ones or those to be proposed based on the actual requirement.

(4) Check if the resulting CPMs meet the design objective, if not, go back to the first step.

(5) Take further measures to constrain the parasitic motion, make whole configuration compact, and/or address certain specific requirement.

It should be noted that the proposed design approach is also suitable for designing 1-DOF and 2-DOF translational CPMs. Unlike the traditional PRBM approach in which the traditional joints are replaced with lumped compliance joints, the proposed approach to synthesize translational CPMs involves both replacing kinematic chains with appropriate multi-DOF compliant parallel modules and replacing traditional joints with lumped compliance joints. Therefore, this approach can produce more and better CPMs and make the configuration more compact.

In the next section, the proposed design methodology will be illustrated by designing several XYZ CPMs.

5.2 Type Synthesis of Large-Range XYZ CPMs

The works on 3-DOF rigid-body TPMs [5.15–5.17] provide a basis to construct the XYZ CPMs. Based on these works, we can obtain three classes of kinematically decoupled 3-DOF TPMs (Figure 5.2) as follows:

(1) 3-$\underline{P}$PP TPMs;

(2) 3-$\underline{P}$PPR TPMs (equivalent to 3-$\underline{P}$RRR, 3-$\underline{P}$PRR, and 3-$\underline{P}$RC TPMs in some cases);

(3) 3-$\underline{P}$PPRR TPMs (equivalent to 3-$\underline{P}$PCR, 3-$\underline{P}$UU and 3-$\underline{P}P^s$ TPMs in some cases).

Here, as pointed out in [5.15], the three planes associated with the passive PP/PPR/PPRR kinematic chains are orthogonal to produce the kinematic decoupling, and all the R joints in the second or third class are inactive. Each active P joint is arranged to be perpendicular to the passive PP/PPR/PPRR plane in each leg so that the configuration of the resulting 3-DOF TPMs can be used to construct *kinematostatically* decoupled XYZ CPMs. This is because the motion of CPMs depends on the acting of loads which is completely different from that of the rigid-body parallel manipulators.

In the subsequent sections, we will rest on the above identified three classes of 3-DOF TPMs to design *large-range* XYZ CPMs with *distributed compliance* using the design approach proposed in Section 5.1, and identify existing or new spatial compliant

modules, which can be used as building blocks of XYZ CPMs.

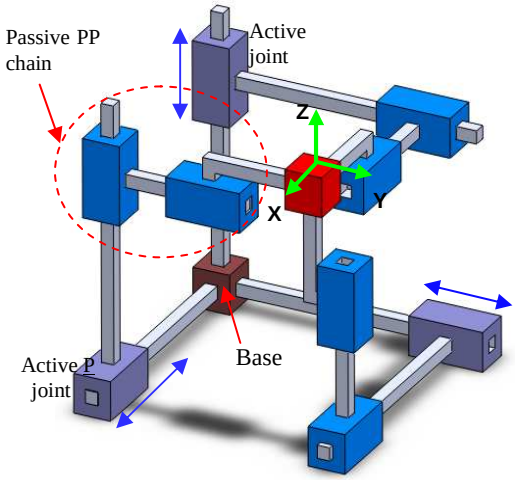

(a) 3-PPP TPM

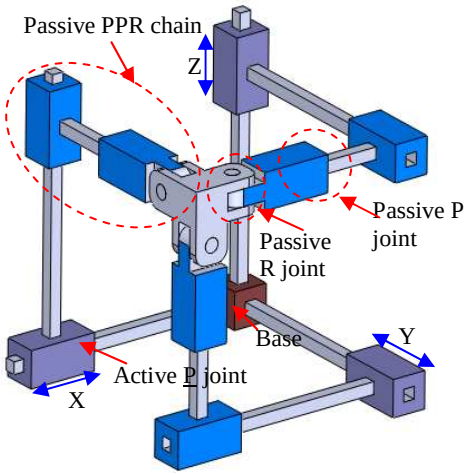

(b) 3-PPPR TPM

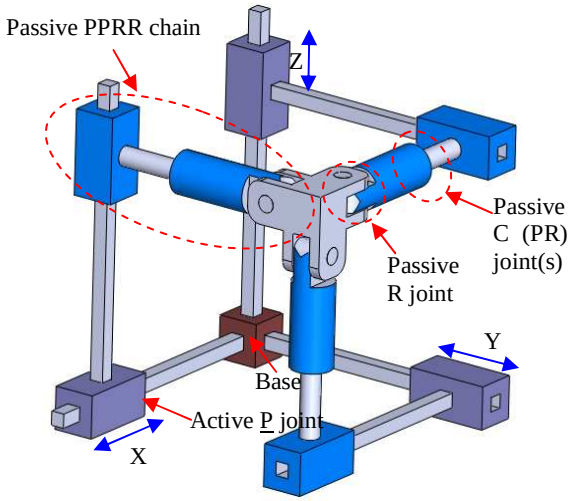

(c) 3-PPPRR (3-PPCR) TPM

Figure 5.2 Three classes of kinematically decoupled 3-DOF TPMs

5.2.1 XYZ CPMs based on 3-PPP TPMs

(1) XYZ CPMs using identical double parallelogram flexure modules

It is well known that a double parallelogram flexure module (Figure 5.3a) is a compliant P joint when its out-of-plane height is large enough. Therefore, we can obtain an XYZ CPM (Figure 5.3b) by replacing the active P joint in each leg in the 3-PPP TPM (Figure 5.2a) with two mirror-symmetry double parallelogram flexure modules, and replacing each passive P joint in each leg in the 3-PPP TPM (Figure 5.2a) with a double parallelogram flexure module.

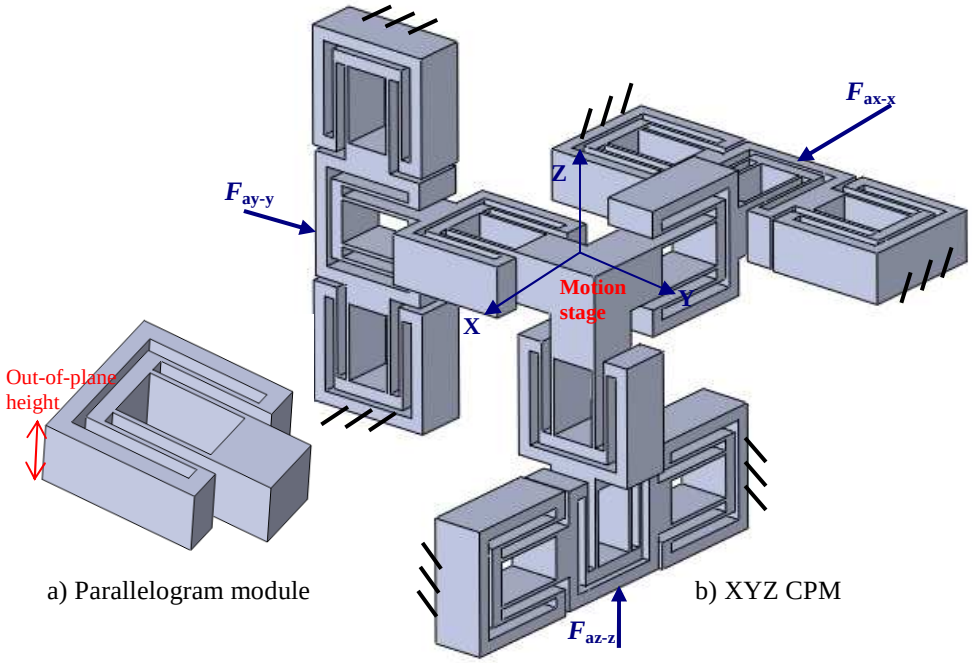

a) Parallelogram module b) XYZ CPM

Figure 5.3 XYZ CPM with three legs using identical parallelogram modules

In order to further reduce the parasitic rotational displacements, we can use symmetrical design approach to obtain an XYZ CPM with six legs using identical parallelogram modules (Figure 5.4a) by adding three auxiliary legs to the above proposed XYZ CPM (Figure 5.3b).

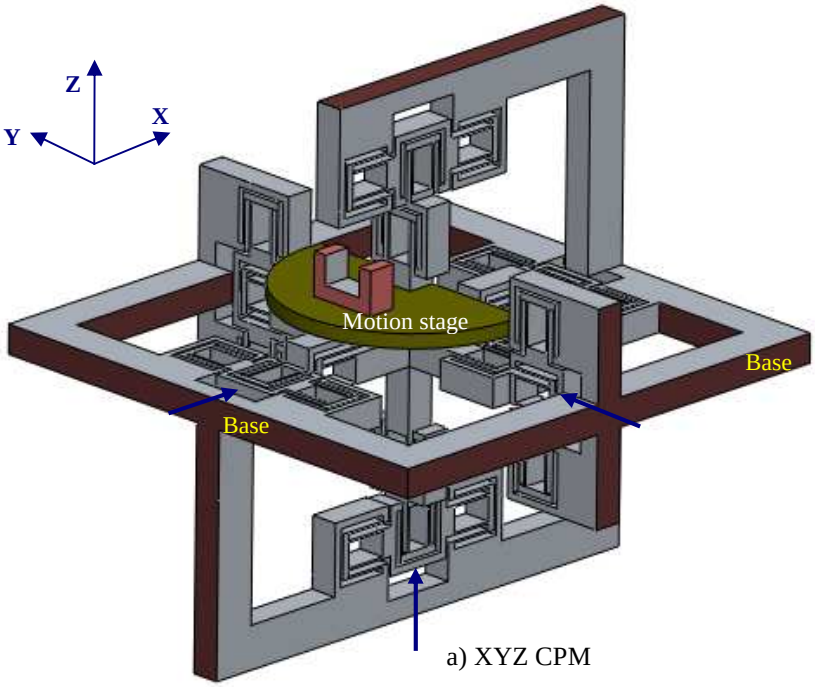

a) XYZ CPM

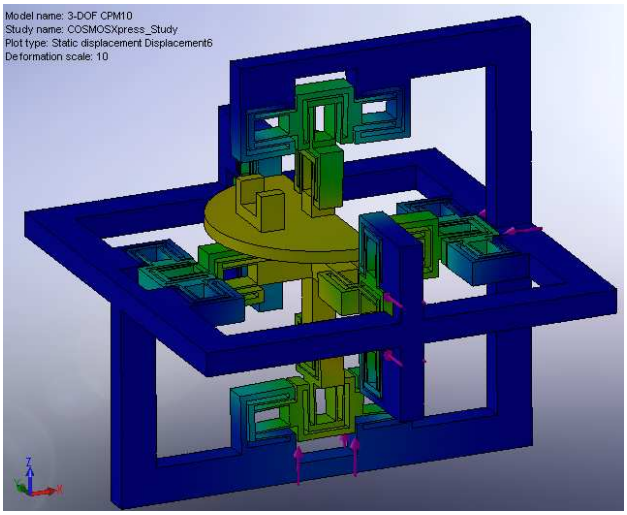

b) FEA illustration under three-axis loading

Figure 5.4 XYZ CPM with six legs using identical parallelogram modules

However, these designs (Figures 5.3 and 5.4) can only be applicable under the precondition of relatively small range of motion or large out-of-plane height of parallelogram module, which may result in manufacturing complexity/difficulty. Also, the design in Figure 5.4 has a bulky configuration.

(2) XYZ CPMs using inverted planar XY CPMs

Awtar [5.18] proposed an interesting planar XY CPM for nanopositioning application with desired performance characteristics such as kinematostatic-decoupling.

By replacing the two passive P joints (PP chain) in each leg of the 3-PPP TPM (Figure 5.2a) with an inverted Awtar's planar mechanism (Figure 5.5a), and replacing the active P joint in each leg in the 3-PPP TPM (Figure 5.2a) with a large-range compliant P joint (Figure 5.5b), similar to Trease's design [5.19], we obtain an XYZ CPM (Figure 5.5c).

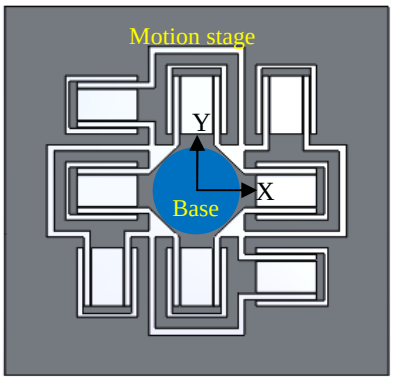

a) Inverted Awtar's XY CPM

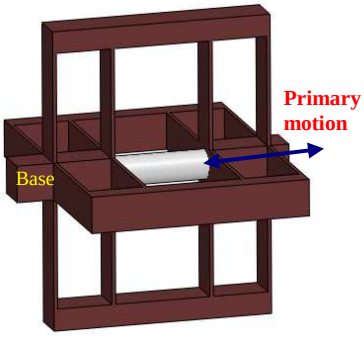

b) Large-range compliant P joint

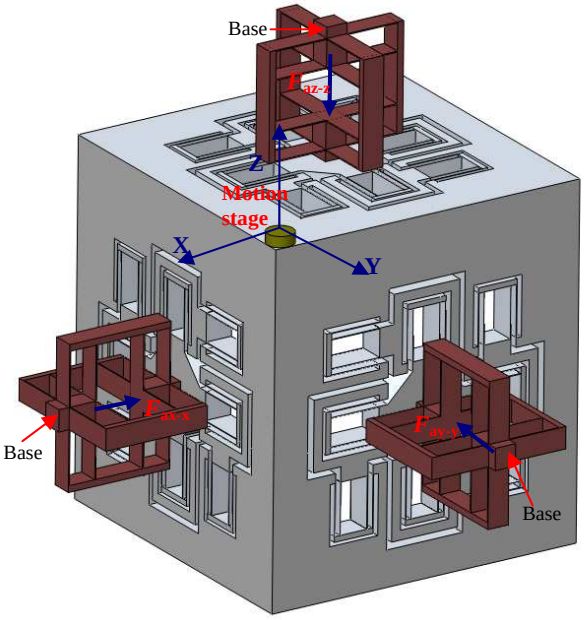

c) XYZ CPM

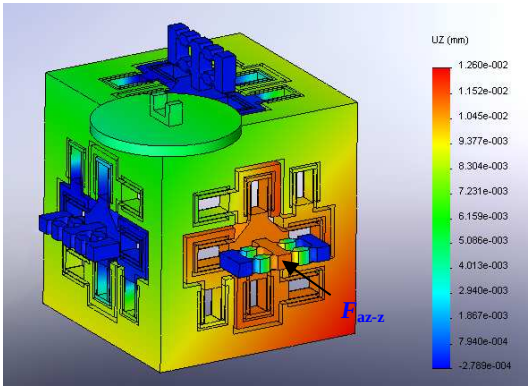

d) FEA illustration under the action of single axis force along the Z-axis

Figure 5.5 XYZ CPM using inverted Awtar's XY CPM

Due to the relatively low out-of-plane stiffness of the planar XY CPM (inverted Awtar's XY CPM) used in the XYZ CPM, which leads to undesired out-of-plane deformation (see Figure 5.5d), so we can further choose the XY CPM (Figure 5.6a) with enhanced out-of-plane stiffness, similar to the design in Chapter 4, to replace the passive PP chain in each leg in the 3-PPP TPM (Figure 5.2a). Accordingly, we obtain a new XYZ CPM (Figure 5.6b) using inverted stiffness-enhanced XY CPM.

However, these designs (Figures 5.5 and 5.6) induce manufacturing complexity/difficulty and bulky configurations.

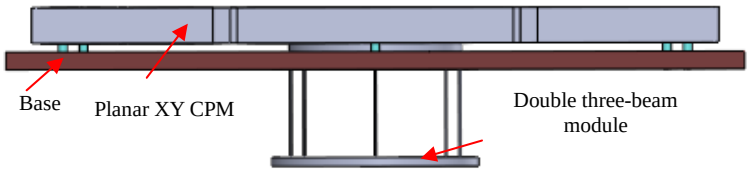

a) Planar XY CPM with enhanced stiffness

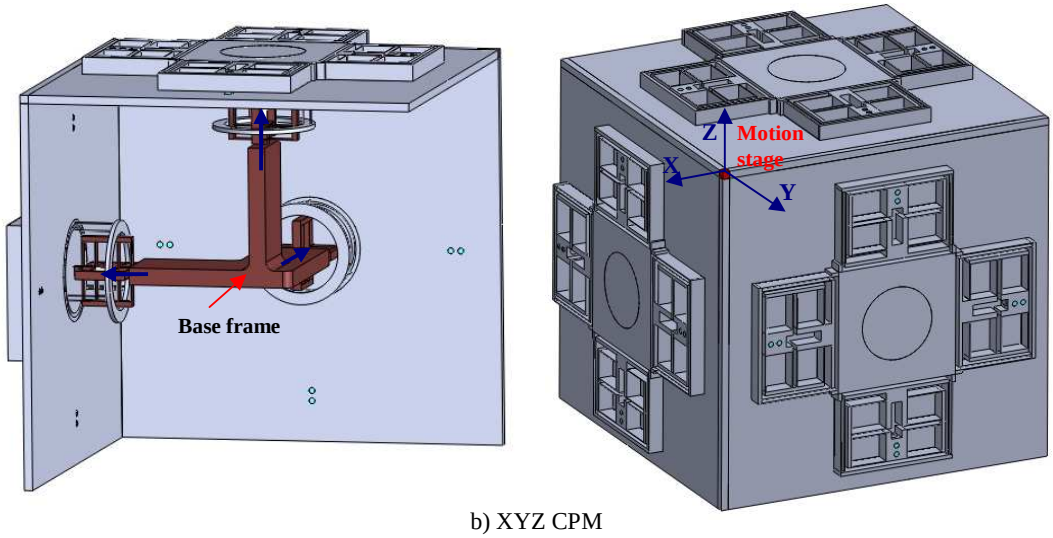

b) XYZ CPM

Figure 5.6 XYZ CPM using inverted stiffness-enhanced XY CPM

5.2.2 XYZ CPMs based on 3-PPPR TPMs

(1) Building blocks: spatial multi-beam modules and their combinations

In this chapter, we use the spatial four-beam module and the spatial double four-beam module (Figures 5.7a and 5.8a) as the building blocks of new spatial translational CPMs since they have relatively high modal frequency (relative to the spatial three-beam module and spatial double three-beam module, respectively) and simple enough configuration. From the analysis in Chapter 2, we learn that we can decrease the cross-section size of the beam and increase the radius of the circle, which the beams are spaced around, to constrain the parasitic rotational displacements under constant beam length.

In terms of the constraint-based design [5.20], two spatial four-beam modules (Figure 5.7a) connected in parallel and having two orthogonal planes, each plane of which is associated with two translational displacements and one torsional angle of each spatial

four-beam module, can construct a compliant P joint (Figure 5.7b).

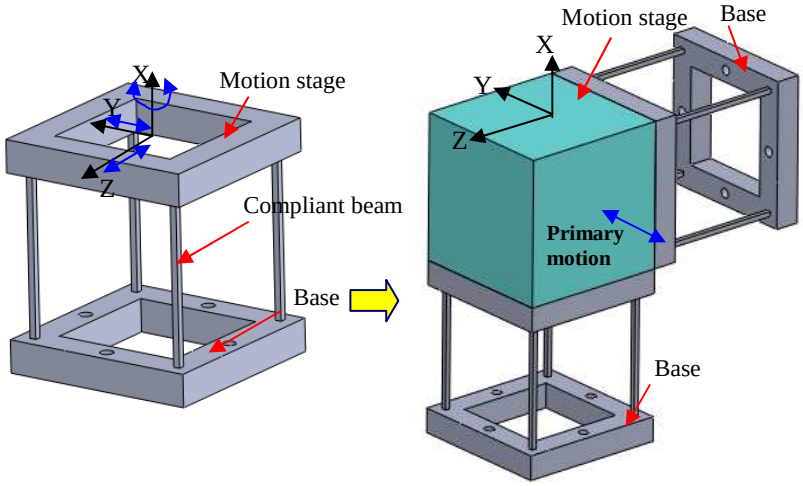

(a) Spatial four-beam module (b) Compliant P joint

Figure 5.7 A compliant P joint

Similarly, two spatial double four-beam modules (Figure 5.8a) can also construct an improved compliant P joint (Figure 5.8b).

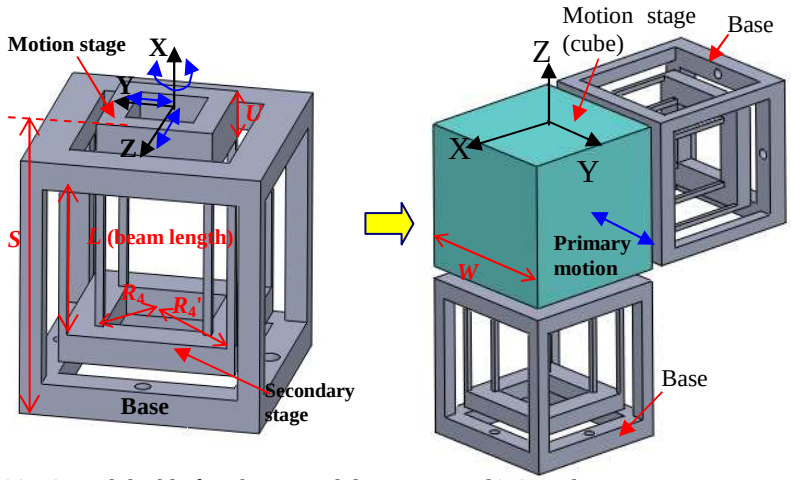

(a) Spatial double four-beam module (b) Compliant P joint

Figure 5.8 An improved compliant P joint

The above compliant P joint or improved compliant P joint can also be obtained by replacing each planar RRR kinematic chain in the well-known *Sarrus* linkage with the proposed spatial compliant module having planar motion (Figure 5.7a or 5.8a).

(2) XYZ CPMs using identical spatial modules

A modular and compact XYZ CPM (Figure 5.9), *using identical spatial modules*, can

be obtained by replacing the active P joint and the passive PPR chain in each leg of the 3-PPPR TPM (Figure 5.2b) with a compliant P joint (Figure 5.7b) and a spatial four-beam module (Figure 5.7a), respectively, and making an appropriate arrangement for the configuration. Here, the R joint of the passive spatial four-beam module in each leg is constrained by the other two adjacent legs simultaneously.

In order to further increase the range of motion along the desired direction, minimize cross-axis coupling, and maximize actuator isolation (i.e. reduce input-coupling), an improved modular XYZ CPM (Figure 5.10) can also be obtained by replacing the active P joint and the PPR chain in each leg of the 3-PPPR TPM (Figure 5.2b) with the improved compliant P joint (Figure 5.8b) and a spatial double four-beam module (Figure 5.8a), respectively.

It should be noted that the parasitic rotational displacements of motion stage of the designs of Figure 5.9 and 5.10 can be reduced by increasing the size of the pitch circle(s), which all beams are spaced around, under constant beam length.

In addition, the XYZ CPM composed of identical spatial modules can be turned into an XY CPM by removing the compliant active P joint in the Z-direction. An example can be found in *Appendix H*.

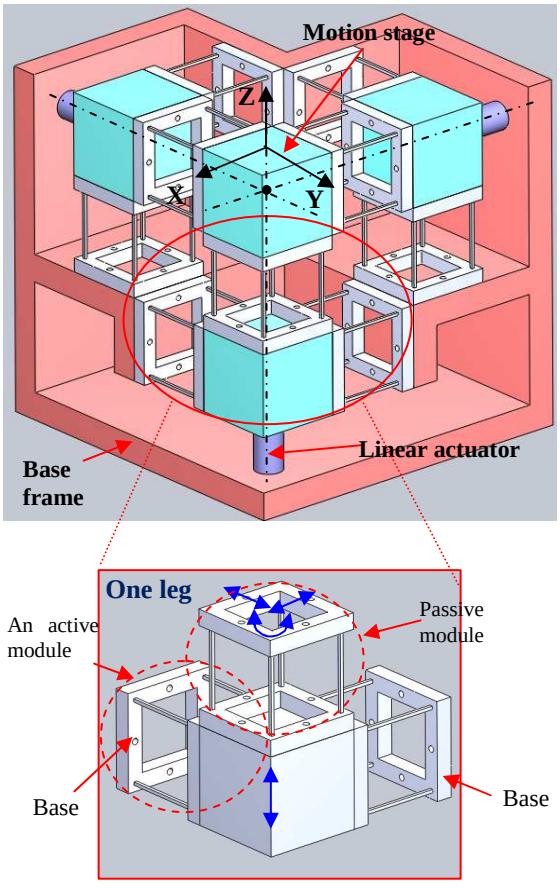

Figure 5.9 A modular XYZ CPM with three legs using identical spatial modules

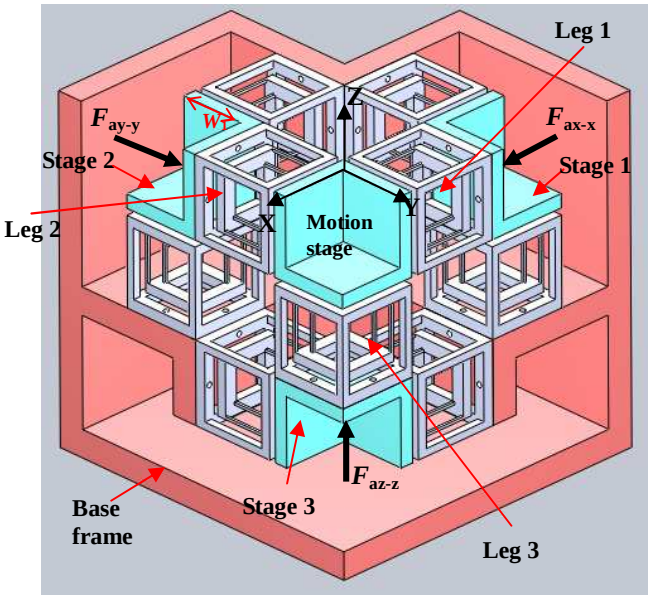

Figure 5.10 An improved modular XYZ CPM with three legs using identical spatial modules

(3) XYZ CPMs using embedded spatial modules

In order to alleviate the parasitic rotational displacements of the motion stage and input-coupling effect, we can use the *center-of-stiffness-based* approach to re-arrange the spatial modules in Figures 5.9 and 5.10, i.e. we need make centres of stiffness, associated with the spatial modules, overlap at a point that applied input force(s) can go through. Also we must make *embedded arrangement* to integrate the spatial modules.

For example, two centres of stiffness of two spatial modules in each compliant P joint in Figure 5.9, are set up to overlap at a same centre to yield a new embedded compliant P joint (Figure 5.11a) at first. Then three centres of stiffness of three spatial modules, passive modules that are directly connected to the motion stage, in Figure 5.9, are set up to overlap at a same centre to produce a new embedded integrated block (Figure 5.11b). Here, the new centre of stiffness is the intersected point of three symmetrical planes. Ultimately, we connect three new embedded compliant P joints to the new embedded integrated block to obtain an embedded (more compact) XYZ CPM (Figure 5.11c) with well-constrained parasitic rotational displacements and reduced input-coupling effect based on the design in Figure 5.9.

Based on the characteristics of spatial double four-beam modules, the design in Figure 10 can also be transformed into an improved embedded XYZ CPM (Figure 5.12c)

with well-constrained parasitic rotational displacements and reduced input-coupling, which has better characteristics than that embedded one as shown in Figure 5.11c.

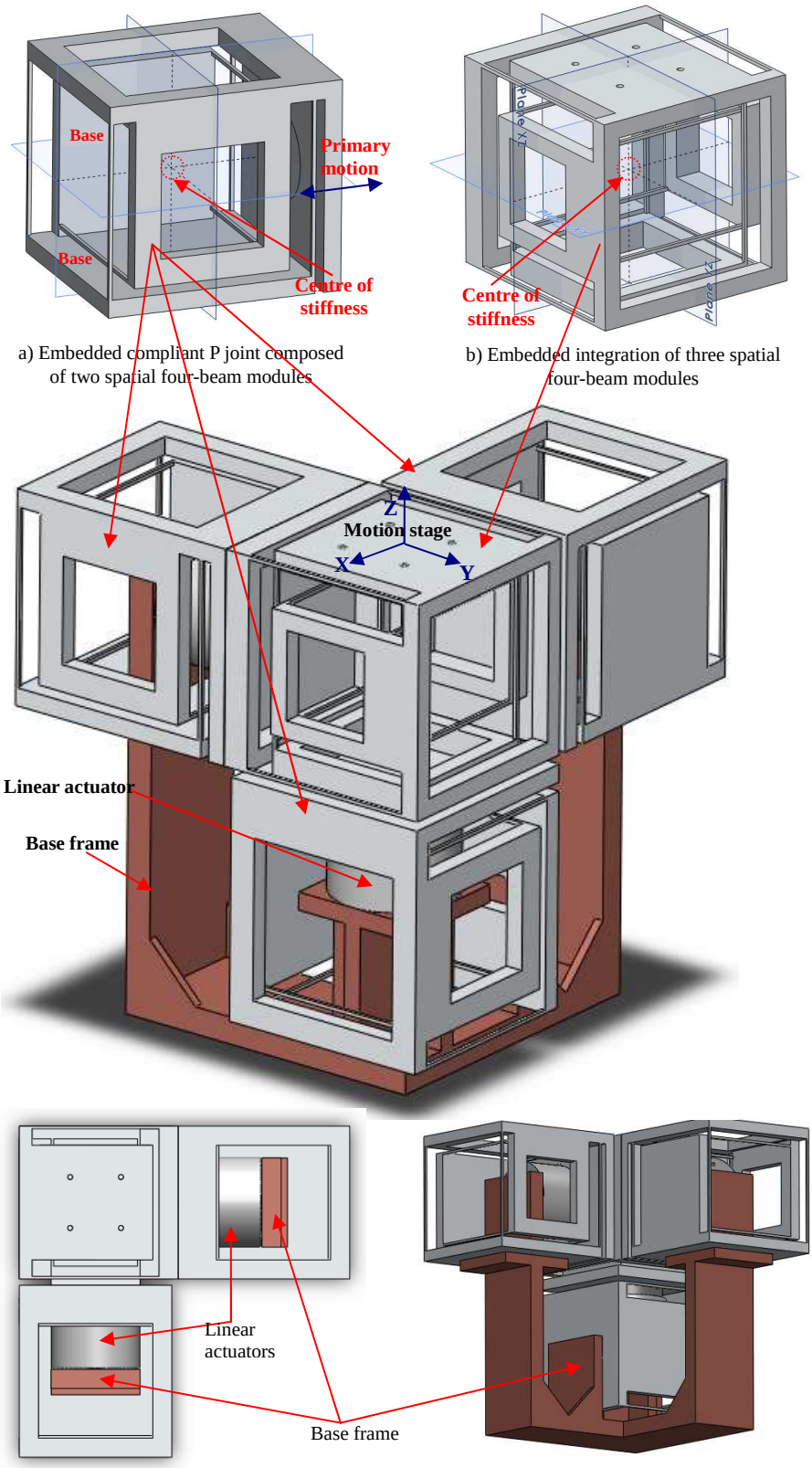

Figure 5.11 An embedded XYZ CPM with three legs and well-constrained parasitic rotational displacements

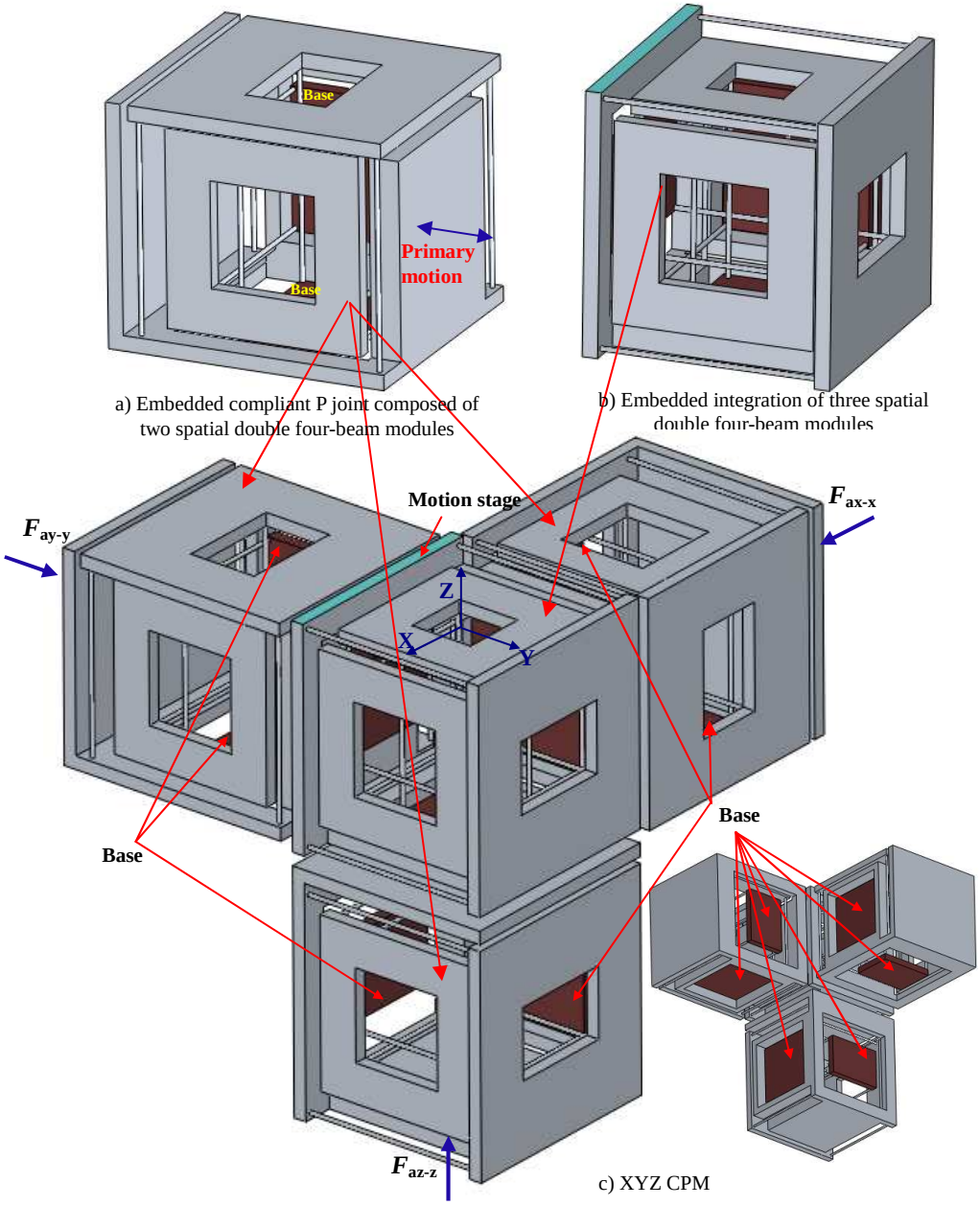

Figure 5.12 An improved embedded XYZ CPM with three legs and well-constrained parasitic rotational displacements

(4) XYZ CPMs with five legs

Another approach to approximately eliminate the parasitic rotational displacements for the design in Figure 5.10 is to use both symmetry and centre-of-stiffness-based strategy.

An XYZ CPM (Figure 5.13b) with well-constrained parasitic rotational displacements can also be obtained by 1) replacing the active P joint and the passive PPR chain in each leg of the 3-PPPR TPM (Figure 5.2b) with a large-range compliant P joint (Figure 5.5b)

and a spatial double four-beam in Figure 5.13a, respectively, 2) adding two same auxiliary compliant legs (no auxiliary leg is added in the Z direction in order to save space for the motion stage and operation space) in such a way that two legs in the X/Y-direction are symmetric, and 3) making the leg in the Z-direction in an embedded arrangement in a way that the acting line of the applied input force along the X/Y-axis passes through the centre of stiffness of the spatial double four-beam module in this leg. Here, the reason for using the large-range compliant P joint (Figure 5.5b) is to better guarantee the actuator isolation and to make the whole configuration compact.

More variations for the XYZ CPM with five legs can be found in *Appendix I*.

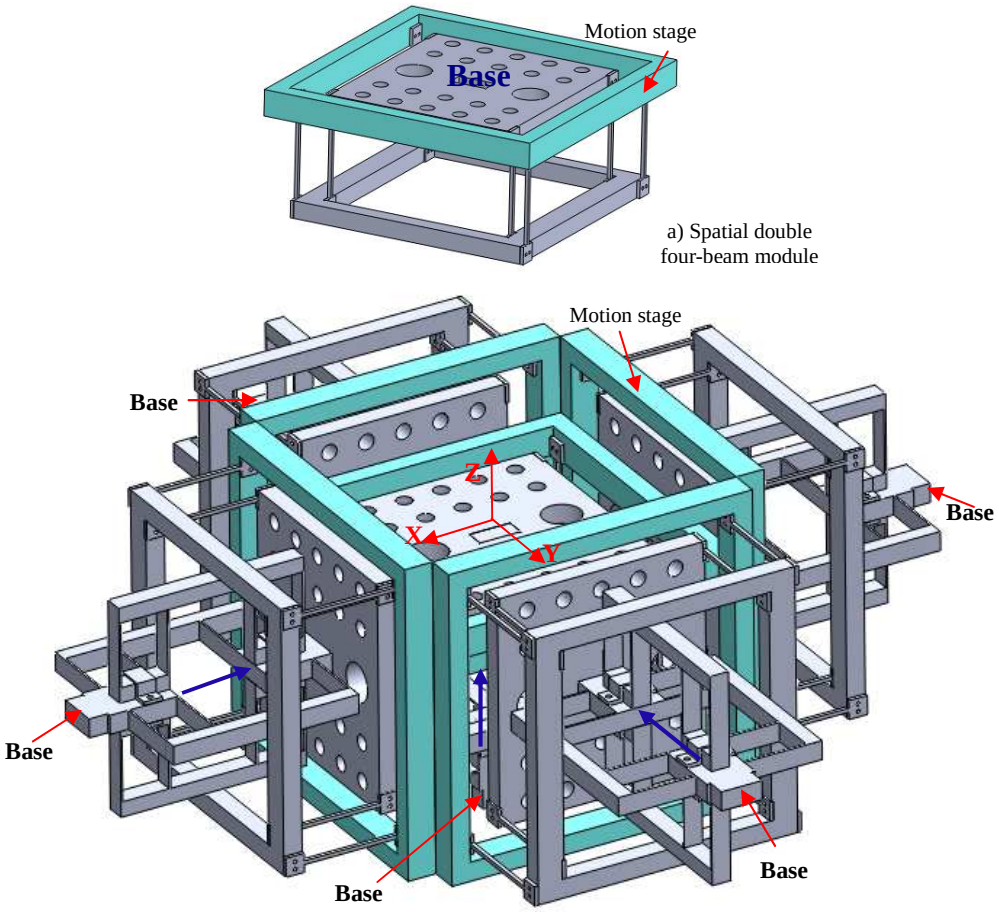

Figure 5.13 XYZ CPM with five legs and well-constrained parasitic rotational displacements

5.2.3 XYZ CPMs based on 3-PPPRR TPMs

Base on the configuration of 3-PPPRR TPM in Figure 5.2c, we can obtain an XYZ CPM, similar to Delta robot, by replacing the active P joint and the passive PPRR chain

in each leg with a large-range compliant P joint (Figure 5.5b) and a planar double two-beam module (each two-beam module is a spatial motion parallelogram having two rotational displacements and two translational displacements) in Figure 5.14a, respectively. Here, the double two-beam module in each leg should be arranged appropriately so that its two R joints are constrained by the other two adjacent legs, respectively. Therefore, the parasitic rotational displacements for the XYZ CPM (Figure 5.14) are not better-constrained compared with the designs in Figures 5.9-5.13.

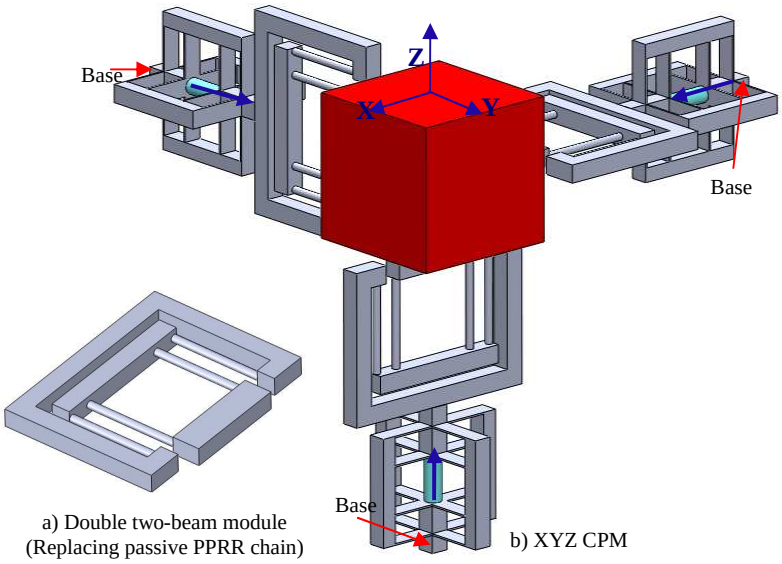

Figure 5.14 XYZ CPM using planar double two-beam modules

The XYZ CPMs proposed in this chapter and the typical existing kinematically decoupled designs are generally compared in Table 5.1.

Characteristics / *XYZ CPMs*	Large range of motion	Constrained parasitic angle	Minimal cross-axis coupling	Maximal actuator isolation	Compactness	Minimal number of geometrical parameters
Li's design [5.7]	−	0	+	0	0	0
Yue's design [5.11]	−	0	0	0	0	0
Tang's design [5.12]	−	−	+	0	−	0
Design in Figure 5.3	0	−	0	+	0	+
Design in Figure 5.4	0	+	0	+	−	+
Design in Figure 5.5	0	−	0	0	−	0
Design in Figure 5.6	0	+	+	0	−	0
Design in Figure 5.9	0	0	−	0	0	+
Design in Figure 5.10	+	0	0	0	0	+
Design in Figure 5.11	0	+	0	0	+	+
Design in Figure 5.12	+	+	+	+	+	+
Design in Figure 5.13	+	+	+	+	0	0
Design in Figure 5.14	+	−	0	0	0	0

Table 5.1 Characteristic comparisons of XYZ CPMs (Good: +, Normal: 0, Poor: −)

Considering the comprehensive performance characteristic comparison from Table 5.1, we can conclude that the proposed designs in Figures 5.10–5.13 are desired designs.

5.3 Kinematostatic Modelling of the Improved Modular XYZ CPM

In the followings, we only concern the modelling of the improved modular XYZ CPM (Figure 5.10) using identical spatial double four-beam modules due to its better manufacturability than those in Figures 5.11–5.13 although this design has worse parasitic rotational displacements. The simplified modelling of the improved embedded XYZ CPM (Figure 5.12) can also be found in *Appendix J*.

Similar to Chapters 2 and 4, and *Appendix C*, we use the normalization-based strategy and convention to represent loads and displacements. Also, we will adopt linear analytical approaches for modelling the improved modular XYZ CPM.

5.3.1 Modelling of the spatial double four-beam module

For a single four-beam module in Figure 5.7a with loads and displacement defined at the centre of the bottom-plane of its motion stage, and with its pitch circle radius of r_4, we obtain its stiffness matrix based on the modelling method of spatial three-beam module in *Appendix C* as follows:

$$\mathbf{K}_{\mathrm{m}} = \sum_{i=0}^{4} \mathbf{D}_i^{\mathrm{T}} \mathbf{K} \mathbf{D}_i \tag{5.1}$$

where

$$\mathbf{D}_i = \begin{bmatrix} 1 & 0 & 0 & 0 & z_i' & -y_i' \\ 0 & 1 & 0 & -z_i' & 0 & x_i' \\ 0 & 0 & 1 & y_i' & -x_i' & 0 \\ 0 & 0 & 0 & 1 & 0 & 0 \\ 0 & 0 & 0 & 0 & 1 & 0 \\ 0 & 0 & 0 & 0 & 0 & 1 \end{bmatrix}, \text{ and } \mathbf{K} = \begin{bmatrix} d & 0 & 0 & 0 & 0 & 0 \\ 0 & 12 & 0 & 0 & 0 & -6 \\ 0 & 0 & 12 & 0 & 6 & 0 \\ 0 & 0 & 0 & \dfrac{1}{1+v} & 0 & 0 \\ 0 & 0 & 6 & 0 & 4 & 0 \\ 0 & -6 & 0 & 0 & 0 & 4 \end{bmatrix}.$$

$x_1'=0$, $y_1'=2^{0.5}r_4/2$, and $z_1'=2^{0.5}r_4/2$; $x_2'=0$, $y_2'=2^{0.5}r_4/2$, and $z_2'=-2^{0.5}r_4/2$; $x_3'=0$, $y_3'=-2^{0.5}r_4/2$, and $z_3'=2^{0.5}r_4/2$; $x_4'=0$, $y_4'=-2^{0.5}r_4/2$, and $z_4'=-2^{0.5}r_4/2$. $d=12/(t)^2$ for square cross-section with normalized thickness t, or $d=16/(d_0)^2$ for round cross-section with normalized diameter d_0. v is the Poisson's ratio of the material.

Using Equation (5.1) and the modelling approach of spatial double three-beam

module in *Appendix C*, we can obtain the compliance matrix for the spatial double four-beam module (Figure 5.8a), with loads and displacement defined at the centre of the bottom-plane of its motion stage, and with its inner pitch circle radius of r_4 and outer pitch circle radius of r_4', as shown below

$$\mathbf{C}_{\mathrm{dm}} = \mathbf{C}_{\mathrm{m1}} + \mathbf{J}_{\mathrm{m}}(\mathbf{R}_{\mathrm{m}}\mathbf{C}_{\mathrm{m2}}\mathbf{R}_{\mathrm{m}}^{-1})\mathbf{J}_{\mathrm{m}}^{\mathrm{T}} \tag{5.2}$$

where $\mathbf{C}_{\mathrm{m1}} = \mathbf{K}_{\mathrm{m}}^{-1}$ and $\mathbf{C}_{\mathrm{m2}} = \mathbf{K}_{\mathrm{m2}}^{-1}$. It is noted that $\mathbf{K}_{\mathrm{m2}}$ is obtained based on Equation (5.1) using the parameter r_4' instead of r_4.

$$\mathbf{J}_{\mathrm{m}} = \begin{bmatrix} 1 & 0 & 0 & 0 & 0 & 0 \\ 0 & 1 & 0 & 0 & 0 & 1 \\ 0 & 0 & 1 & 0 & -1 & 0 \\ 0 & 0 & 0 & 1 & 0 & 0 \\ 0 & 0 & 0 & 0 & 1 & 0 \\ 0 & 0 & 0 & 0 & 0 & 1 \end{bmatrix},$$

which is obtained based on $\mathbf{D}_i$ in Equation (5.1), and

$$\mathbf{R}_{\mathrm{m}} = \begin{bmatrix} \cos(-\pi) & 0 & \sin(-\pi) & 0 & 0 & 0 \\ 0 & 1 & 0 & 0 & 0 & 0 \\ -\sin(-\pi) & 0 & \cos(-\pi) & 0 & 0 & 0 \\ 0 & 0 & 0 & \cos(-\pi) & 0 & \sin(-\pi) \\ 0 & 0 & 0 & 0 & 1 & 0 \\ 0 & 0 & 0 & -\sin(-\pi) & 0 & \cos(-\pi) \end{bmatrix} \begin{bmatrix} 1 & 0 & 0 & 0 & 0 & 0 \\ 0 & \cos(\pi) & -\sin(\pi) & 0 & 0 & 0 \\ 0 & \sin(\pi) & \cos(\pi) & 0 & 0 & 0 \\ 0 & 0 & 0 & 1 & 0 & 0 \\ 0 & 0 & 0 & 0 & \cos(\pi) & -\sin(\pi) \\ 0 & 0 & 0 & 0 & \sin(\pi) & \cos(\pi) \end{bmatrix}.$$

5.3.2 Modelling of the compliant P joint

The stiffness matrix of the compliant P joint (Figure 5.8b) in the leg 2 of the improved modular XYZ CPM (Figure 5.10), for the loads and displacement defined at the centre of the stage 2 (the centre of the cube formed by the stage 2), can be obtained as

$$\mathbf{K}_{\mathrm{p}} = (\mathbf{J}_{\mathrm{dm1}}\mathbf{C}_{\mathrm{dm}}\mathbf{J}_{\mathrm{dm1}}^{\mathrm{T}})^{-1} + [\mathbf{J}_{\mathrm{dm2}}(\mathbf{R}_{\mathrm{dm}}\mathbf{C}_{\mathrm{dm}}\mathbf{R}_{\mathrm{dm}}^{-1})\mathbf{J}_{\mathrm{dm2}}^{\mathrm{T}}]^{-1} \tag{5.3a}$$

where $\mathbf{C}_{\mathrm{dm}}$ is directly obtained from Equation (5.2).

$$\mathbf{J}_{\mathrm{dm1}} = \begin{bmatrix} 1 & 0 & 0 & 0 & 0 & 0 \\ 0 & 1 & 0 & 0 & 0 & u+w/2 \\ 0 & 0 & 1 & 0 & -u-w/2 & 0 \\ 0 & 0 & 0 & 1 & 0 & 0 \\ 0 & 0 & 0 & 0 & 1 & 0 \\ 0 & 0 & 0 & 0 & 0 & 1 \end{bmatrix}, \quad \mathbf{J}_{\mathrm{dm2}} = \begin{bmatrix} 1 & 0 & 0 & 0 & u+w/2 & 0 \\ 0 & 1 & 0 & -u-w/2 & 0 & 0 \\ 0 & 0 & 1 & 0 & 0 & 0 \\ 0 & 0 & 0 & 1 & 0 & 0 \\ 0 & 0 & 0 & 0 & 1 & 0 \\ 0 & 0 & 0 & 0 & 0 & 1 \end{bmatrix},$$

which are both obtained on a basis of $\mathbf{D}_i$ in Equation (5.1), and

$$\mathbf{R}_{\mathrm{dm}}=\begin{bmatrix} \cos(\frac{\pi}{2}) & 0 & \sin(\frac{\pi}{2}) & 0 & 0 & 0 \\ 0 & 1 & 0 & 0 & 0 & 0 \\ -\sin(\frac{\pi}{2}) & 0 & \cos(\frac{\pi}{2}) & 0 & 0 & 0 \\ 0 & 0 & 0 & \cos(\frac{\pi}{2}) & 0 & \sin(\frac{\pi}{2}) \\ 0 & 0 & 0 & 0 & 1 & 0 \\ 0 & 0 & 0 & -\sin(\frac{\pi}{2}) & 0 & \cos(\frac{\pi}{2}) \end{bmatrix}\begin{bmatrix} \cos(\pi) & -\sin(\pi) & 0 & 0 & 0 & 0 \\ \sin(\pi) & \cos(\pi) & 0 & 0 & 0 & 0 \\ 0 & 0 & 1 & 0 & 0 & 0 \\ 0 & 0 & 0 & \cos(\pi) & -\sin(\pi) & 0 \\ 0 & 0 & 0 & \sin(\pi) & \cos(\pi) & 0 \\ 0 & 0 & 0 & 0 & 0 & 1 \end{bmatrix}.$$

Here, *u* and *w* are normalized geometrical parameters as shown in Figure 5.8.

Thus, the compliance matrix of the compliant P joint is

$$\mathbf{C}_{\mathrm{p}}=\mathbf{K}_{\mathrm{p}}^{-1}. \tag{5.3b}$$

5.3.3 Modelling of a leg

When the loads and displacements for the leg 2 are defined at the centre of the motion stage of the improved modular XYZ CPM (the centre of the cube formed by the motion stage), we can obtain the compliance matrix for the leg 2:

$$\mathbf{C}_{\mathrm{leg2}}=\mathbf{J}_{\mathrm{dm3}}(\mathbf{R}_{\mathrm{pp}}\mathbf{C}_{\mathrm{dm}}\mathbf{R}_{\mathrm{pp}}^{-1})\mathbf{J}_{\mathrm{dm3}}^{\mathrm{T}}+\mathbf{J}_{\mathrm{p}}\mathbf{C}_{\mathrm{p}}\mathbf{J}_{\mathrm{p}}^{\mathrm{T}} \tag{5.4a}$$

where

$$\mathbf{J}_{\mathrm{dm3}}=\begin{bmatrix} 1 & 0 & 0 & 0 & 0 & -u-w/2 \\ 0 & 1 & 0 & 0 & 0 & 0 \\ 0 & 0 & 1 & u+w/2 & 0 & 0 \\ 0 & 0 & 0 & 1 & 0 & 0 \\ 0 & 0 & 0 & 0 & 1 & 0 \\ 0 & 0 & 0 & 0 & 0 & 1 \end{bmatrix},\quad \mathbf{J}_{\mathrm{p}}=\begin{bmatrix} 1 & 0 & 0 & 0 & 0 & -(s+w) \\ 0 & 1 & 0 & 0 & 0 & 0 \\ 0 & 0 & 1 & s+w & 0 & 0 \\ 0 & 0 & 0 & 1 & 0 & 0 \\ 0 & 0 & 0 & 0 & 1 & 0 \\ 0 & 0 & 0 & 0 & 0 & 1 \end{bmatrix},$$

which are both obtained based on $\mathbf{D}_i$ in Equation (5.1), and

$$\mathbf{R}_{\mathrm{pp}}=\begin{bmatrix} \cos(\pi/2) & -\sin(\pi/2) & 0 & 0 & 0 & 0 \\ \sin(\pi/2) & \cos(\pi) & 0 & 0 & 0 & 0 \\ 0 & 0 & 1 & 0 & 0 & 0 \\ 0 & 0 & 0 & \cos(\pi/2) & -\sin(\pi/2) & 0 \\ 0 & 0 & 0 & \sin(\pi/2) & \cos(\pi/2) & 0 \\ 0 & 0 & 0 & 0 & 0 & 1 \end{bmatrix}.$$

$\mathbf{C}_{\mathrm{dm}}$ and $\mathbf{C}_{\mathrm{p}}$ can be directly obtained from Equations (5.2) and (5.3b). Here, *s* is normalized geometrical parameter as shown in Figure 5.8.

Thus, the stiffness matrix of leg 2 is

$$\mathbf{K}_{\mathrm{leg2}}=\mathbf{C}_{\mathrm{leg2}}^{-1}. \tag{5.4b}$$

5.3.4 Modelling of the improved modular XYZ CPM

In the modelling of the improved modular XYZ CPM, the loads and displacements are defined at the centre of its motion stage (i.e. the centre of the cube) and denoted, respectively, by $\mathbf{F} = [f_x, f_y, f_z, m_x, m_y, m_z]^{\mathrm{T}}$, and $\mathbf{X}_{\mathrm{s}} = [x_s, y_s, z_s, \theta_{sx}, \theta_{sy}, \theta_{sz}]^{\mathrm{T}}$.

Following the modelling of leg 2, the stiffness and compliance matrices for legs 1 and 3 can be obtained by appropriate coordinate transformation since the improved modular XYZ CPM is composed of three identical legs,

Based on Equation (5.4b), the stiffness matrix of the improved modular XYZ CPM is

$$\mathbf{K}_{\mathrm{cpm}} = \mathbf{R}_{\mathrm{leg1}}\mathbf{K}_{\mathrm{leg2}}\mathbf{R}_{\mathrm{leg1}}^{-1} + \mathbf{K}_{\mathrm{leg2}} + \mathbf{R}_{\mathrm{leg3}}\mathbf{K}_{\mathrm{leg2}}\mathbf{R}_{\mathrm{leg3}}^{-1} \tag{5.5a}$$

where

$$\mathbf{R}_{\mathrm{leg1}} = \begin{bmatrix} \cos(-\frac{\pi}{2}) & -\sin(-\frac{\pi}{2}) & 0 & 0 & 0 & 0 \\ \sin(-\frac{\pi}{2}) & \cos(-\frac{\pi}{2}) & 0 & 0 & 0 & 0 \\ 0 & 0 & 1 & 0 & 0 & 0 \\ 0 & 0 & 0 & \cos(-\frac{\pi}{2}) & -\sin(-\frac{\pi}{2}) & 0 \\ 0 & 0 & 0 & \sin(-\frac{\pi}{2}) & \cos(-\frac{\pi}{2}) & 0 \\ 0 & 0 & 0 & 0 & 0 & 1 \end{bmatrix} \begin{bmatrix} \cos(-\frac{\pi}{2}) & 0 & \sin(-\frac{\pi}{2}) & 0 & 0 & 0 \\ 0 & 1 & 0 & 0 & 0 & 0 \\ -\sin(-\frac{\pi}{2}) & 0 & \cos(-\frac{\pi}{2}) & 0 & 0 & 0 \\ 0 & 0 & 0 & \cos(-\frac{\pi}{2}) & 0 & \sin(-\frac{\pi}{2}) \\ 0 & 0 & 0 & 0 & 1 & 0 \\ 0 & 0 & 0 & -\sin(-\frac{\pi}{2}) & 0 & \cos(-\frac{\pi}{2}) \end{bmatrix},$$

and

$$\mathbf{R}_{\mathrm{leg3}} = \begin{bmatrix} \cos(\frac{\pi}{2}) & 0 & \sin(\frac{\pi}{2}) & 0 & 0 & 0 \\ 0 & 1 & 0 & 0 & 0 & 0 \\ -\sin(\frac{\pi}{2}) & 0 & \cos(\frac{\pi}{2}) & 0 & 0 & 0 \\ 0 & 0 & 0 & \cos(-\frac{\pi}{2}) & 0 & \sin(-\frac{\pi}{2}) \\ 0 & 0 & 0 & 0 & 1 & 0 \\ 0 & 0 & 0 & -\sin(-\frac{\pi}{2}) & 0 & \cos(-\frac{\pi}{2}) \end{bmatrix} \begin{bmatrix} \cos(\frac{\pi}{2}) & -\sin(\frac{\pi}{2}) & 0 & 0 & 0 & 0 \\ \sin(\frac{\pi}{2}) & \cos(\frac{\pi}{2}) & 0 & 0 & 0 & 0 \\ 0 & 0 & 1 & 0 & 0 & 0 \\ 0 & 0 & 0 & \cos(\frac{\pi}{2}) & -\sin(\frac{\pi}{2}) & 0 \\ 0 & 0 & 0 & \sin(\frac{\pi}{2}) & \cos(\frac{\pi}{2}) & 0 \\ 0 & 0 & 0 & 0 & 0 & 1 \end{bmatrix}.$$

Accordingly, the compliance matrix for the improved modular XYZ CPM is obtained as

$$\mathbf{C}_{\mathrm{cpm}} = \mathbf{K}_{\mathrm{cpm}}^{-1}. \tag{5.5b}$$

Then, we have the load-displacement equations

$$\mathbf{F} = \mathbf{K}_{\mathrm{cpm}}\mathbf{X}_{\mathrm{s}} \tag{5.6}$$

In order to capture the effects of loads acting at both the actuation points and the centre of the motion stage, we derive the following equation by generalizing Equation (5.6):

$$\begin{aligned} \mathbf{F} = \mathbf{K}_{\mathrm{cpm}}\mathbf{X}_{\mathrm{s}} &- \mathbf{K}_{\mathrm{leg1}}\mathbf{R}_{\mathrm{leg1}}(\mathbf{J}_{\mathrm{p}}\mathbf{C}_{\mathrm{p}}\mathbf{J}_{\mathrm{p}}^{\mathrm{T}})\mathbf{R}_{\mathrm{leg1}}^{-1}\mathbf{J}_{\mathrm{pa1}}^{\mathrm{T}}\mathbf{F}_{\mathrm{ax}} \\ &- \mathbf{K}_{\mathrm{leg2}}(\mathbf{J}_{\mathrm{p}}\mathbf{C}_{\mathrm{p}}\mathbf{J}_{\mathrm{p}}^{\mathrm{T}})\mathbf{J}_{\mathrm{pa2}}^{\mathrm{T}}\mathbf{F}_{\mathrm{ay}} - \mathbf{K}_{\mathrm{leg3}}\mathbf{R}_{\mathrm{leg3}}(\mathbf{J}_{\mathrm{p}}\mathbf{C}_{\mathrm{p}}\mathbf{J}_{\mathrm{p}}^{\mathrm{T}})\mathbf{R}_{\mathrm{leg3}}^{-1}\mathbf{J}_{\mathrm{pa3}}^{\mathrm{T}}\mathbf{F}_{\mathrm{az}} \end{aligned} \tag{5.7}$$

where

$\mathbf{F}_{\text{ax}} = [f_{ax-x}, f_{ax-y}, f_{ax-z}, m_{ax-x}, m_{ax-y}, m_{ax-z}]^{\text{T}}$, $\mathbf{F}_{\text{ay}} = [f_{ay-x}, f_{ay-y}, f_{ay-z}, m_{ay-x}, m_{ay-y}, m_{ay-z}]^{\text{T}}$, and $\mathbf{F}_{\text{az}} = [f_{az-x}, f_{az-y}, f_{az-z}, m_{az-x}, m_{az-y}, m_{az-z}]^{\text{T}}$, which denote the actuation load vectors at the X-, Y- and Z-actuation points, respectively. $f_{\text{ax-x}}$, $f_{\text{ax-y}}$ and $f_{\text{ax-z}}$ denote the forces acting at the X-actuation point along the X-, Y-, and Z-axes, respectively. $\mathbf{J}_{\text{pa}i}$ is the displacement transformation matrix for each leg, which can be shown below according to $\mathbf{D}_i$ in Equation (5.1):

$$\mathbf{J}_{\text{pa}i} = \begin{bmatrix} 1 & 0 & 0 & 0 & z_i' & -y_i' \\ 0 & 1 & 0 & -z_i' & 0 & x_i' \\ 0 & 0 & 1 & y_i' & -x_i' & 0 \\ 0 & 0 & 0 & 1 & 0 & 0 \\ 0 & 0 & 0 & 0 & 1 & 0 \\ 0 & 0 & 0 & 0 & 0 & 1 \end{bmatrix} (i=1, 2, 3).$$

Here, $x_1'=-(-w_1+s+1.5w)$, $y_1'=0$, and $z_1'=0$; $x_2'=0$, $y_2'=-(-w_1+s+1.5w)$, and $z_2'=0$; $x_3'=0$, $y_3'=0$, and $z_3'=-(-w_1+s+1.5w)$. w_1 is normalized geometrical parameter as shown in Figure 5.10.

It is noted that when $\mathbf{F}_{\text{ax}}$, $\mathbf{F}_{\text{ay}}$ and $\mathbf{F}_{\text{az}}$ are all zero vectors, Equation (5.7) can be reduced to Equation (5.6).

When $\mathbf{F}$ is equal to a zero vector, Equation (5.7) can be further simplified to obtain the displacement vector of the motion stage as

$$\begin{aligned} \mathbf{X}_{\text{s}} = \mathbf{C}_{\text{cpm}}[&\mathbf{K}_{\text{leg1}}\mathbf{R}_{\text{leg1}}(\mathbf{J}_{\text{p}}\mathbf{C}_{\text{p}}\mathbf{J}_{\text{p}}^{\text{T}})\mathbf{R}_{\text{leg1}}^{-1}\mathbf{J}_{\text{pa1}}^{\text{T}}\mathbf{F}_{\text{ax}} \\ &+\mathbf{K}_{\text{leg2}}(\mathbf{J}_{\text{p}}\mathbf{C}_{\text{p}}\mathbf{J}_{\text{p}}^{\text{T}})\mathbf{J}_{\text{pa2}}^{\text{T}}\mathbf{F}_{\text{ay}} + \mathbf{K}_{\text{leg3}}\mathbf{R}_{\text{leg3}}(\mathbf{J}_{\text{p}}\mathbf{C}_{\text{p}}\mathbf{J}_{\text{p}}^{\text{T}})\mathbf{R}_{\text{leg3}}^{-1}\mathbf{J}_{\text{pa3}}^{\text{T}}\mathbf{F}_{\text{az}}]. \end{aligned} \tag{5.8}$$

Using the result of Equation (5.8), we can further derive the displacements at the Y-actuation point (the connecting centre between the Y-actuator and the XYZ CPM) as

$$\mathbf{X}_{\text{ay}} = \mathbf{J}_{\text{pay}}\mathbf{C}_{\text{p}}\mathbf{J}_{\text{p}}^{\text{T}}[\mathbf{K}_{\text{leg2}}(\mathbf{X}_{\text{s}} - \mathbf{J}_{\text{p}}\mathbf{C}_{\text{p}}\mathbf{J}_{\text{p}}^{\text{T}}\mathbf{J}_{\text{pa2}}^{\text{T}}\mathbf{F}_{\text{ay}}) + \mathbf{J}_{\text{pa2}}^{\text{T}}\mathbf{F}_{\text{ay}}] \tag{5.9}$$

where $\mathbf{X}_{ay} = [x_{ay}, y_{ay}, z_{ay}, \theta_{ay-x}, \theta_{ay-y}, \theta_{ay-z}]^{\text{T}}$, which is the displacement vector at the Y-actuation point. x_{ay}, y_{ay}, and z_{ay} denote the translational displacements of the Y-actuation point along the X-, Y- and Z-axes, respectively. Based on $\mathbf{D}_i$ in Equation (5.1), we have

$$\mathbf{J}_{\text{pay}} = \begin{bmatrix} 1 & 0 & 0 & 0 & 0 & -(w_1 - w/2) \\ 0 & 1 & 0 & 0 & 0 & 0 \\ 0 & 0 & 1 & (w_1 - w/2) & 0 & 0 \\ 0 & 0 & 0 & 1 & 0 & 0 \\ 0 & 0 & 0 & 0 & 1 & 0 \\ 0 & 0 & 0 & 0 & 0 & 1 \end{bmatrix}.$$

5.4 Case Study of an Improved Modular XYZ CPM

In this section, an example improved modular XYZ CPM with a motion range of 10mm×10mm×10mm is presented in detail.

5.4.1 Material, actuator and geometrical parameter determination

The material for the improved modular XYZ CPM is also selected to be an aluminium alloy, AL6061-T651, for which Young's modulus, E, is 69,000 Nmm^{-2} and Poisson's ratio, v, is 0.33, due to the material's low internal stresses, good strength and phase stability suitable for precision engineering application [5.18].

The objective of 10mm×10mm×10mm's motion range also requires a large-range linear actuator. As mentioned in Chapter 4, one can choose the linear voice coil actuator from BEI Kimco Magnetics (LA28-22-000A), which provides a total stroke of 11.43mm and a relatively large peak force of 266.89N, with dimension: Φ 69.85 mm×55.88 mm, for the modular XYZ CPM. This actuator has merits such as large-range nanopositioning (the large range of motion and high nanometric resolution), linear model, and force-control along with hysteresis-free, frictionless and cog-free motion.

Based on Equation (F.6) in *Appendix F*, the actual (non-normalized) transverse motion range for a beam in the spatial double four-beam module (Figure 5.8) should meet

$$\Delta_a \le \frac{1}{3\eta}\frac{\sigma_s}{E}\frac{L^2}{T} \tag{5.10}$$

where Δ_a is the actual transverse motion range of a beam. σ_s =276Mpa is the material yield strength, T is the actual thickness of the beam with square cross-section, and η is the safety coefficient.

Since $2\Delta_a$=10mm, we have

$$\frac{2}{3\eta}\frac{\sigma_s}{E}\frac{L^2}{T} \ge 10\text{mm}. \tag{5.11}$$

According to Equation (5.11) and the actuator mounting size requirement, we select the dimension of a beam with square cross-section to be L=100mm, T=2.6mm (t=0.026). The other geometric parameters are: R_4=68.8722mm (r_4=0.6887), R_4'= 89.5197mm (r_4'=0.8952), U=20mm (u=0.20), S=140mm (s=1.40), W=163.20mm (w=1.632), and W_1=153.20mm (w_1=1.532). The overall dimension for the improved modular XYZ

CPM without the base frame is 466.40mm×466.40mm×466.40mm.

5.4.2 Input load-output displacement equations

Substituting the above geometrical dimensions into Equation (5.8), we derive the displacements for the motion stage of the improved modular XYZ CPM under the action of three actuation forces, $f_{\text{ax-x}}$, $f_{\text{ay-y}}$, and $f_{\text{az-z}}$:

$$\begin{bmatrix} x_{\text{s}} \\ y_{\text{s}} \\ z_{\text{s}} \\ \theta_{sx} \\ \theta_{sy} \\ \theta_{sz} \end{bmatrix} = \begin{bmatrix} 0.010547 f_{ax-x} - 0.000066976 f_{ay-y} - 0.000066976 f_{az-z} \\ -0.000066976 f_{ax-x} + 0.010547 f_{ay-y} - 0.000066976 f_{az-z} \\ -0.000066976 f_{ax-x} - 0.000066976 f_{ay-y} + 0.010547 f_{az-z} \\ -0.000070591 f_{ay-y} + 0.000070591 f_{az-z} \\ 0.000070591 f_{ax-x} - 0.000070591 f_{az-z} \\ -0.000070591 f_{ax-x} + 0.000070591 f_{ay-y} \end{bmatrix}. \quad (5.12)$$

Equation (5.12) shows that the cross-axis coupling, for example the effect of $f_{\text{ay-y}}$ upon x_{s}, is acceptable because the coefficient of $f_{\text{ay-y}}$ is 157 (=0.010547/0.000066976) times less than that of $f_{\text{ax-x}}$. In addition, the parasitic motion caused by an input actuation force is also 150 (=0.010547/0.000070591) times less than the corresponding primary motion caused by the same force, which can be tolerated.

5.4.3 Lost motion

Substituting the above geometrical dimensions into Equation (5.9), under the action of three actuation forces, $f_{\text{ax-x}}$, $f_{\text{ay-y}}$, and $f_{\text{az-z}}$, we have

$$\begin{bmatrix} x_{\text{ay}} \\ y_{\text{ay}} \\ z_{\text{ay}} \\ \theta_{ay-x} \\ \theta_{ay-y} \\ \theta_{ay-z} \end{bmatrix} = \begin{bmatrix} 4.4965\times10^{-5} f_{ax-x} - 3.7916\times10^{-5} f_{ay-y} - 4.5270\times10^{-8} f_{az-z} \\ -6.6940\times10^{-5} f_{ax-x} + 1.0561\times10^{-2} f_{ay-y} - 6.6940\times10^{-5} f_{az-z} \\ -4.5270\times10^{-8} f_{ax-x} - 3.7916\times10^{-5} f_{ay-y} + 4.4965\times10^{-5} f_{az-z} \\ -5.3069\times10^{-5} f_{ay-y} + 5.3033\times10^{-5} f_{az-z} \\ 6.4743\times10^{-8} f_{ax-x} - 6.4743\times10^{-8} f_{az-z} \\ -5.3033\times10^{-5} f_{ax-x} + 5.3069\times10^{-5} f_{ay-y} \end{bmatrix}. \quad (5.13)$$

Based on Equations (5.12) and (5.13), the linear lost motion percentage along the Y-axis can be obtained as

$$\frac{y_{\text{ay}} - y_s}{y_s} \times 100\% = \frac{(0.010561 - 0.010547) f_{ay-y} - (6.6940 - 6.6976)\times10^{-5}(f_{ax-x} + f_{az-z})}{0.010547 f_{ay-y} - 6.6976\times10^{-5}(f_{ax-x} + f_{az-z})} \times 100\%. \quad (5.14)$$

If only one actuation force $f_{\text{ay-y}}$ is applied, Equation (5.14) can be simplified as

$$\frac{y_{\text{ay}} - y_s}{y_s} \times 100\% = \frac{0.010561 - 0.010547}{0.010547} \times 100\% = 0.132\%.$$

Similarly, the lost motion long the X- or Z-axis can also be obtained as follows

$$\frac{x_{ax}-x_s}{x_s}\times 100\% = \frac{(0.010561-0.010547)\,f_{ax-x}-(6.6940-6.6976)\times 10^{-5}(f_{ay-y}+f_{az-z})}{0.010547\,f_{ax-x}-6.6976\times 10^{-5}(f_{ay-y}+f_{az-z})}\times 100\%,$$

$$\frac{z_{az}-z_s}{z_s}\times 100\% = \frac{(0.010561-0.010547)\,f_{az-z}-(6.6940-6.6976)\times 10^{-5}(f_{ax-x}+f_{ay-y})}{0.010547\,f_{az-z}-6.6976\times 10^{-5}(f_{ax-x}+f_{ay-y})}\times 100\%.$$

5.4.4 Actuation isolation performance

From Equation (5.13), we can obtain the input coupling for the Y-actuator, which is reflected by the transverse motion of the Y-actuation point, as

$$x_{ay}=4.4965\times 10^{-5}f_{ax\text{-}x}-3.7916\times 10^{-5}f_{ay\text{-}y}-4.5270\times 10^{-8}f_{az\text{-}z}, \quad (5.15a)$$

$$z_{ay}=-4.5270\times 10^{-8}f_{ax\text{-}x}-3.7916\times 10^{-5}f_{ay\text{-}y}+4.4965\times 10^{-5}f_{az\text{-}z}. \quad (5.15b)$$

Similarly, the input coupling for the X- or Z-actuator can be obtained as follows:

$$y_{ax}=4.4965\times 10^{-5}f_{ay\text{-}y}-3.7916\times 10^{-5}f_{ax\text{-}x}-4.5270\times 10^{-8}f_{az\text{-}z},$$

$$z_{ax}=-4.5270\times 10^{-8}f_{ay\text{-}y}-3.7916\times 10^{-5}f_{ax\text{-}x}+4.4965\times 10^{-5}f_{az\text{-}z},$$

$$x_{az}=4.4965\times 10^{-5}f_{ax\text{-}x}-3.7916\times 10^{-5}f_{az\text{-}z}-4.5270\times 10^{-8}f_{ay\text{-}y},$$

$$y_{az}=-4.5270\times 10^{-8}f_{ax\text{-}x}-3.7916\times 10^{-5}f_{az\text{-}z}+4.4965\times 10^{-5}f_{ay\text{-}y}.$$

5.4.5 Buckling checking

Since the passive double four-beam module in each leg undergoes larger axial force than the active double four-beam module if they have the same transverse translational displacements, we only consider the non-bulking condition for the passive module:

$$(1/c_{cpm22}-1/c_{leg222})\frac{10ET^4}{12L^3}=4.69\frac{ET^4}{12L^2}\le 40\frac{ET^4}{12L^2} \quad (5.16)$$

where c_{cpm22} and c_{leg222} denote the elements (entries) in the second row and second column of the matrices $\mathbf{C}_{cpm}$ and $\mathbf{C}_{leg2}$ [Equations (5.5b) and (5.4a)], respectively. The term on the left-hand side is actual axial force acting at the passive double four-beam module to produce required motion range. The term on the right-hand side, $40ET^4/(12L^2)$, denotes the actual buckling load for the spatial double four-beam module obtained based on Equation (2.82).

5.4.6 Actuation force checking

In order to ensure the voice coil actuator to work normally, the actuation force must not be larger than the peak force of the selected voice coil actuator. In the case studied

above, we have

$$10\times\frac{1}{0.010547}\times\frac{ET^4}{12L^3}=249.12\le 266.89 \tag{5.17}$$

where the term on the left-hand side, obtained using Equation (5.12), is the actual actuation force to produce the 10mm' primary motion, and the term on the right-hand side is the peak force of the selected voice coil actuator (*LA28-22-000A*).

5.4.7 Manufacture

Due to impossible fabricating monolithic XYZ CPMs using EDM as one part, a possible manufacturing option is to fabricate separately all the parts for the spatial double four-beam modules from an AL6061-T651 block with thickness 163.20 mm, width 163.20mm and length 140mm at first using EDM. Then, one may assemble all these parts by screws, clamps and self-constraint to form a spatial double four-beam module (Figure 5.15). Meanwhile, one fabricates the stages 1, 2 and 3 (intermediate stages), and motion stage separately as shown in Figure 5.16. Finally, one can obtain the improved modular XYZ CPM (Figure 5.17) by assembling all the parts (spatial modules, intermediate stages and motion stage).

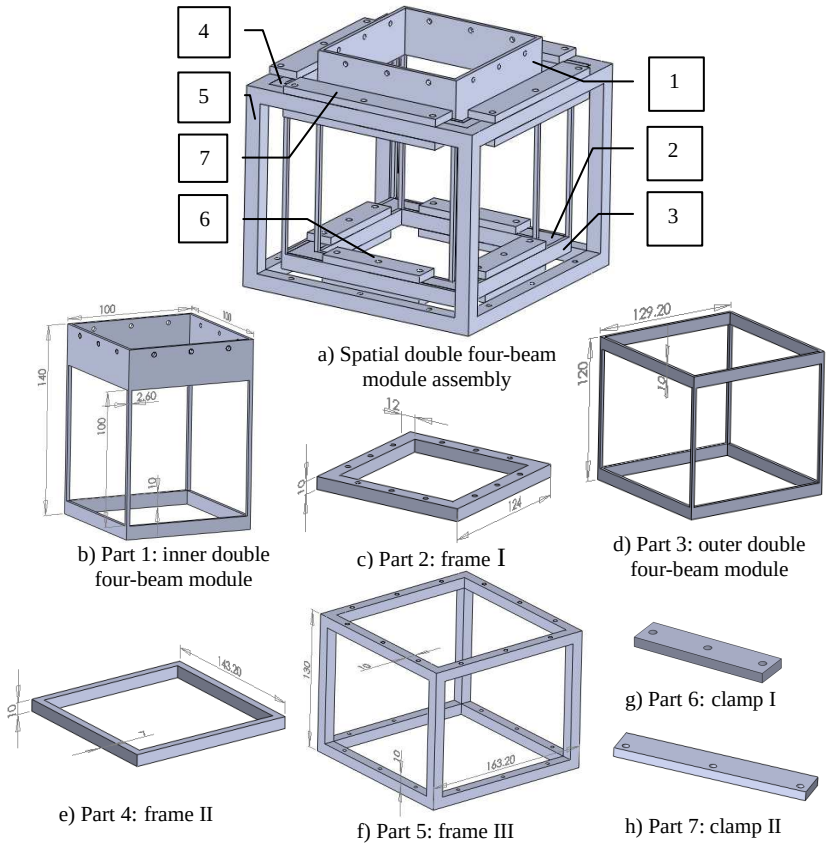

Figure 5.15 CAD models for the spatial module assembly and its compositional units

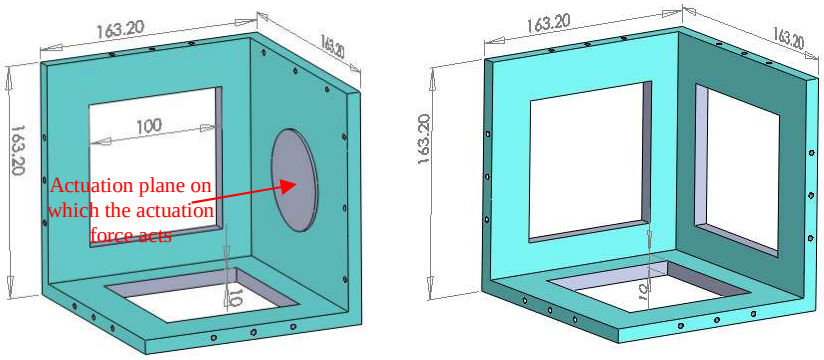

(a) Intermediate stage (b) Motion stage

Figure 5.16 CAD models for stages

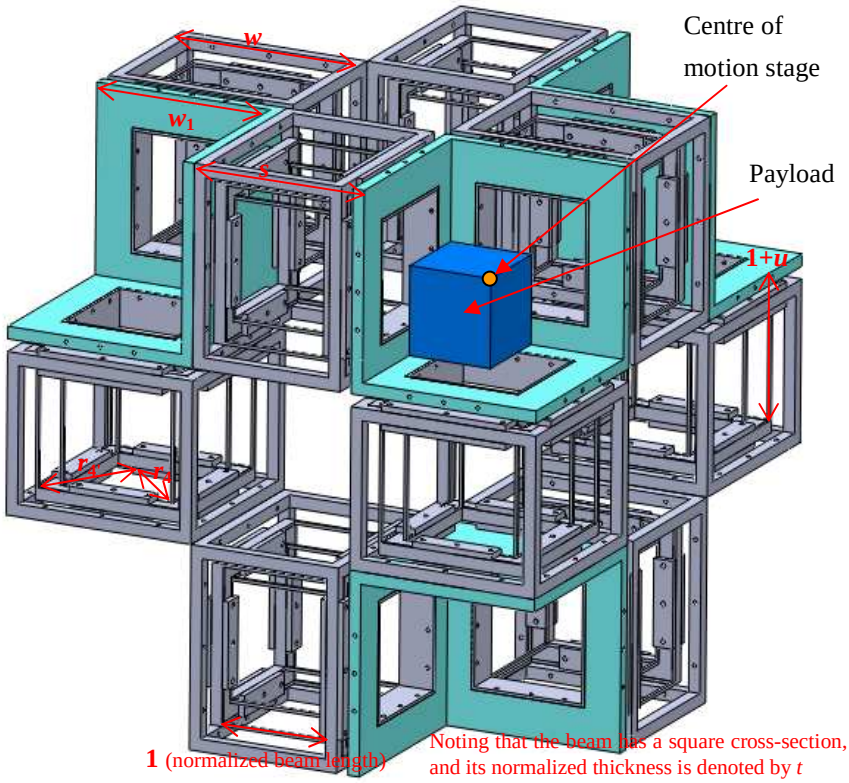

Figure 5.17 Virtual prototype model for the improved modular XYZ CPM

5.5 Modal Frequency

As discussed in Chapter 4, in order to improve the dynamic performance of CPMs, we can either further increase the number of beams in spatial multi-beam modules (see *Appendix K* for details) to raise the primary stiffness and hence first natural frequency, or use a high-order controller to achieve a high bandwidth greater than this first natural frequency. In the former case, a higher-performance linear voice coil actuator with large range of motion and a higher-peak force (therefore bulkier) is accordingly required. As a

result, a trade-off needs to be considered between the good dynamics and bulkier actuators.

Based on Equation (F.2), the normalized linear load-displacement equation for any x location on a beam, in the improved modular XYZ CPM, deformed in the XOY plane is approximately expressed as

$$\begin{bmatrix} y(x) \\ \theta_z(x) \end{bmatrix} = \begin{bmatrix} x^3/3 & x^2/2 \\ x^2/2 & x \end{bmatrix} \begin{bmatrix} f_y \\ f_y(1-x)-0.5f_y \end{bmatrix} \tag{5.18}$$

where $y(x)$ is the transverse displacement of any x location on the beam along the Y-axis. When x=1, the transverse displacement of the tip is $y_e=y(1)=f_y/12$. f_y is the transverse force acting at the tip.

Using Equation (5.18), the normalized transverse displacement at the x location can be further obtained as

$$y(x) = y_e x^2(3-2x). \tag{5.19}$$

According to Equation (5.19), we have the kinetic energy of the XYZ CPM (Figure 5.10) along the Y-direction:

$$\begin{aligned} &8\int_0^1 0.5\rho T^2 L(\dot{Y}_s x^2(3-2x)/2)^2 dx + 8\int_0^1 0.5\rho T^2 L(\dot{Y}_s x^2(3-2x)/2 + \dot{Y}_s/2)^2 dx \\ &+ 2\times 0.5[M_{m1} + M_{m2}/2]\dot{Y}_s^2 + 0.5[M_{s2} + M_s + M_{m1} + M_{m2} + M_{m3} + 8\rho T^2 L]\dot{Y}_s^2 \\ &= 0.5M_e\dot{Y}_s^2 \end{aligned} \tag{5.20}$$

where the first two terms on the left-hand capture the kinetic energy from the compliant beams in the Y-direction. M_{m1}, M_{m2} and M_{m3} are the actual mass of the motion stage, secondary motion stage and base of the double four-beam module (Figure 5.8a). M_{s2} is the actual mass of the stage 2, M_s is the actual mass of the motion stage of the XYZ CPM. ρ is the density of the material. M_e is the actual *equivalent mass* along each axis. Y_s is the actual primary motion along the Y-axis.

Equation (5.20) can be further simplified as

$$M_e = \frac{1088}{35}\rho T^2 L + 5M_{m1} + 3M_{m2} + M_{m3} + M_s + M_{s2}. \tag{5.21}$$

Therefore, we can obtain the following dynamic motion equation:

$$M_e\ddot{Y}_s + (k'EI/L^3)Y_s = F_{ay-y} \tag{5.22}$$

where k' is the nominal Y-axis stiffness (for zero X- and Z-actuation), which can be obtained from Equation (5.8).

Then, the first natural frequency along each axis is approximately estimated using

$$f_{n1} = \frac{\sqrt{(k'EI/L^3)/M_e}}{2\pi}. \tag{5.23}$$

5.6 FEA Comparisons

FEA (Figures 5.18–5.26) is conducted to analyse the performance characteristics, primary motion, cross-axis coupling, lost motion, actuation isolation, and parasitic rotational displacements, for the improved modular XYZ CPM (Figure 5.10), and is compared with the above proposed analytical model. Here, we choose COSMOSWorks for FEA using solid mesh (tetrahedral element) with the global element size of 4.6 mm, opened automatic looping for solid and other set-up of default. The reference point is the centre of the motion stage of the improved modular XYZ CPM for translational displacements.

Figure 5.18 illustrates the deformations for two cases obtained using FEA under static elastic domain.

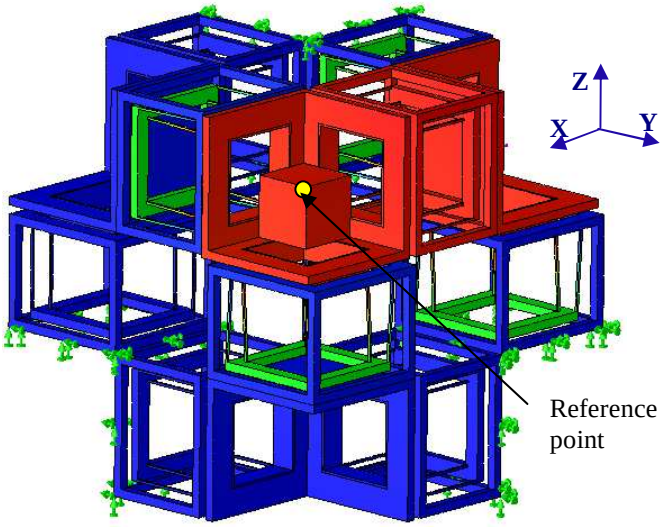

a) 10mm's translational displacement along the X-axis

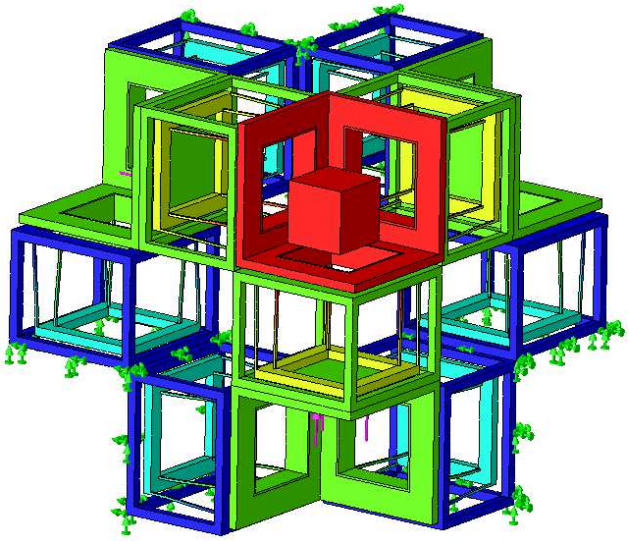

b) 10mm's translational displacements along the X-, Y- and Z-axes

Figure 5.18 Displacement illustrations in FEA (For showing the clear colour difference in figures, the reader is referred to the electronic version)

a) Performance characteristics analysis

Figure 5.19 shows that the nominal primary compliance obtained using the linear analytical model [Equation (5.12)] is slightly lower than that obtained using FEA, with an acceptable difference of 3.64%.

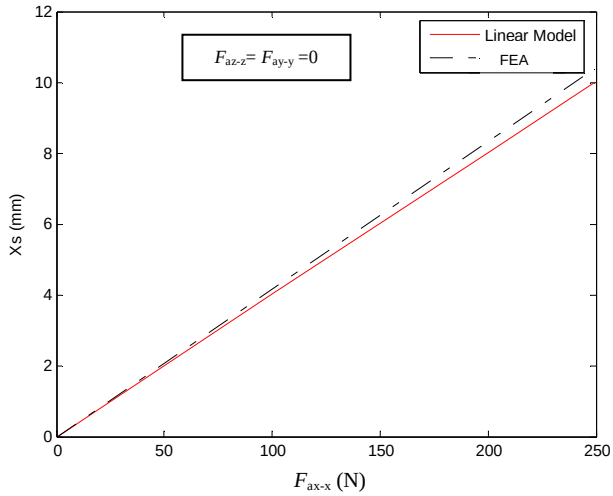

Figure 5.19 Primary motion along the X-axis

Figures 5.20 and 5.21 show the cross-axis coupling comparisons between FEA and linear analytical models, with an acceptable difference. FEA results illustrate that the cross-axis coupling, Y_s or Z_s, caused by $F_{ax\text{-}x}$ is less than 1% of the primary motion along the direction of $F_{ax\text{-}x}$. Both FEA and linear models show with the increase of the actuation force $F_{ax\text{-}x}$, the cross-axis displacements, Y_s and Z_s, decrease linearly.

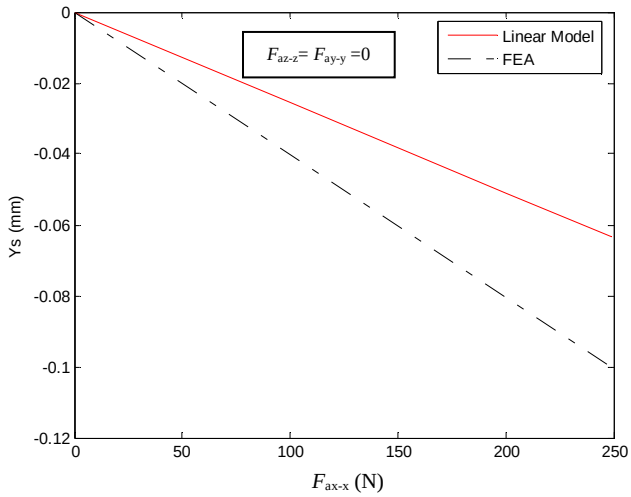

Figure 5.20 Cross-axis coupling: Y-displacement affected by $F_{ax\text{-}x}$

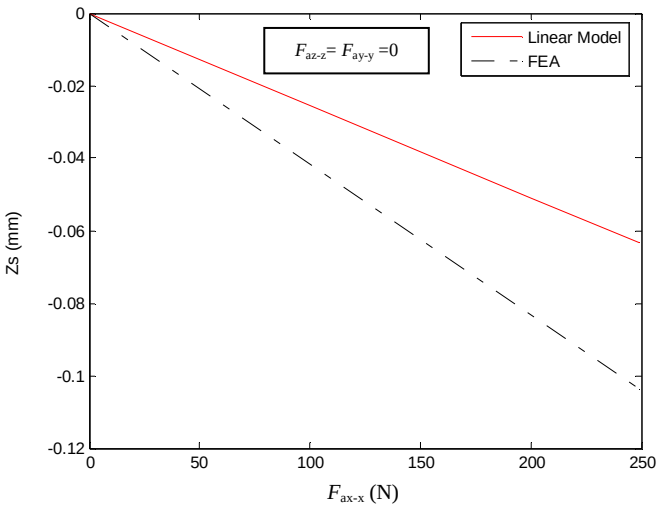

Figure 5.21 Cross-axis coupling: Z-displacement affected by $F_{ax\text{-}x}$

Figure 5.22 shows the lost motion in the X-direction. It can be observed that the ratio of the lost motion to the primary motion obtained using FEA model is negligible 0.3%, but much larger than 0.132% obtained the linear analytical model [Equation (5.14)].

Figure 5.23 shows that the input coupling obtained using the linear analytical model [Equation (5.15)] is smaller than that obtained using FEA. However, it reveals that the maximal FEA result X_{ay} (X_{az}) is approximately 0.65% of the corresponding primary motion, X_s, which can still be acceptable for most applications.

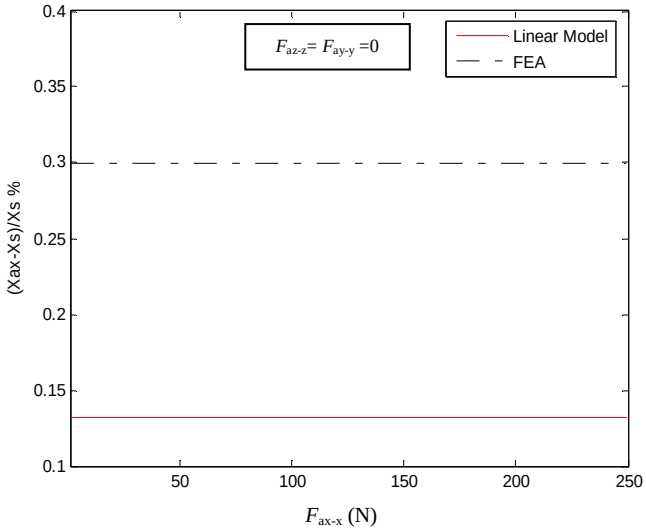

Figure 5.22 Lost motion percentage along the X-axis

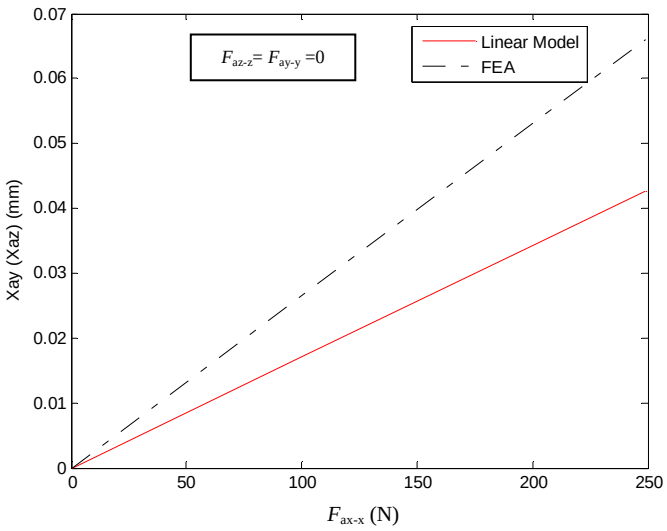

Figure 5.23 Input-coupling of the Y- or Z-actuator caused by $F_{ax\text{-}x}$

Figure 5.24 illustrates that parasitic rotation about the X-axis, obtained using FEA under only the acting of $F_{ax\text{-}x}$, is in the order of 1.4×10^{-6}, which is very close to zero obtained using linear model [Equation 5.12)]. This verifies that an actuation force cannot produce the parasitic rotation about the axis along the force direction.

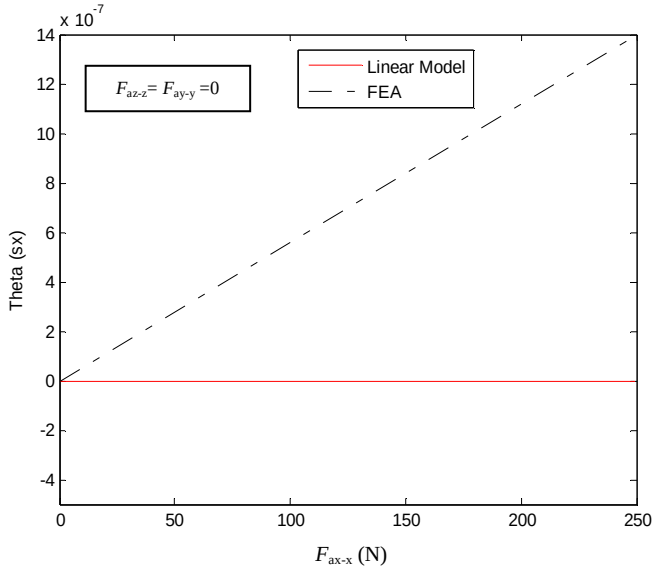

Figure 5.24 Parasitic rotation about the X-axis caused by $F_{ax\text{-}x}$

Figures 5.25 and 5.26 show the parasitic angles about the Y- and Z-axes. The maximal parasitic angles obtained using FEA model is in the order of 1.2×10^{-3}, larger than that obtained using the linear analytical model. In addition, both FEA and the linear analytical models show that θ_{sz} linearly decreases, while θ_{sy} linearly increases as the actuation force $F_{ax\text{-}x}$ increases.

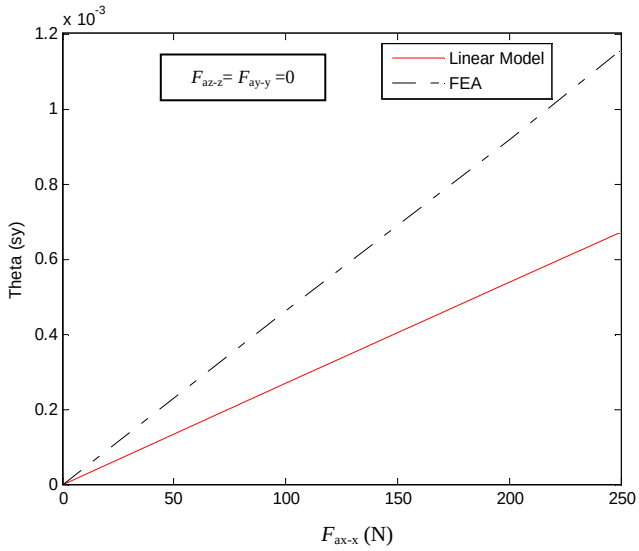

Figure 5.25 Parasitic rotation about the Y-axis caused by $F_{ax\text{-}x}$

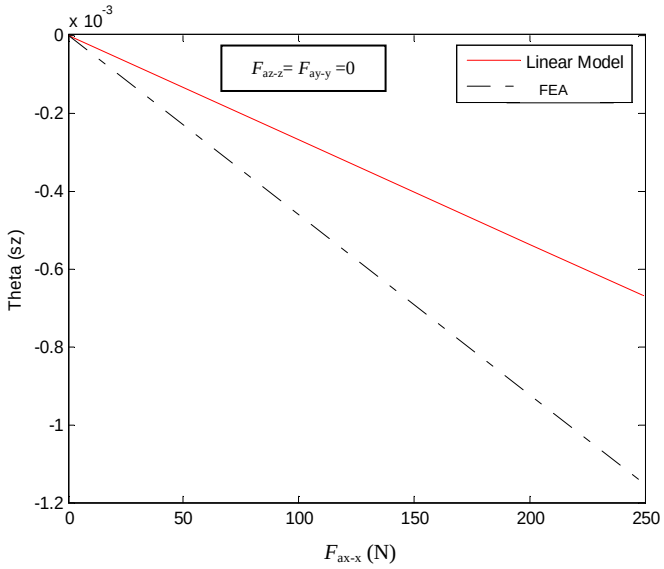

Figure 5.26 Parasitic rotation about the Z-axis caused by $F_{ax\text{-}x}$

The comparisons in Figures 5.19–5.26 only take into account the case of single-axis loading. For the more complicated multi-axis loading case, comparisons can be found in Table 5.1.

Displacements / *Models*	X_s (mm)	Y_s (mm)	Z_s (mm)	$(X_{ax}-X_s)/X_s$	$(Y_{ay}-Y_s)/Y_s$	$(Z_{az}-Z_s)/Z_s$	θ_{sx}	θ_{sx}	θ_{sx}
Linear model	3.963	3.963	3.963	0.135%	0.135%	0.135%	0	0	0
FEA	4.077	4.077	4.075	0.30%	0.31%	0.32%	0	0	0
Comparisons	2.88%	2.88%	2.83%	122%	130%	137%	0	0	0

Table 5.1 Comparisons between the linear model and FEA under multi-axis loading: $F_{ax\text{-}x}$=$F_{ay\text{-}y}$=$F_{az\text{-}z}$=100N

Table 5.1 shows that that the primary motion along each axis and the parasitic rotation about each axis obtained using the linear model comply with those obtained using FEA well, and the differences in the lost motion percentage are relatively large. Also, FEA results verify that two equal actuation forces cannot contribute to the parasitic rotation about the direction parallel to the normal of the plane associate with the two equal actuation forces, which is reflected in Equation (5.12).

In addition, the first natural frequency result obtained using FEA is 11.03 Hz, a little bit bigger than that, 10.99Hz, obtained using Equation (5.23).

b) Remarks

From the above comparisons, it is observed that there are certain difference between the FEA and the analytical results, which are due to inaccuracy of either linear analytical model or FEA. In addition, the results obtained from FEA are larger than that obtained from the analytical model since all parts are considered as elastic bodies in FEA. It is noted that the cross-axis coupling, lost motion, input coupling and parasitic motion differ much. This is probably because these characteristics are relatively small and FEA has relatively large inaccuracy in dealing with very small deformation/displacements.

As compared with the FEA approach, the proposed linear analytical models may enable rapid analysis and quick design synthesis.

5.7 Summary

A design methodology has been proposed for translational CPMs. Type synthesis has been conducted to generate several large-range XYZ CPMs using the proposed design approach. The improved modular XYZ CPM using identical spatial double four-beam modules has been selected for normalization modelling and analysing. It has been shown that, in the example case, the improved modular XYZ CPM has the following unique merits compared with existing designs: (1) large range of motion up to 10mm×10mm×10mm, and (2) reduced number of design parameters due to the use of identical spatial multi-beam modules.

It is noted that there are several open issues, such as manufacture and dynamics of CPMs composed of spatial multi-beam modules.

5.8 References

[5.1] Weckenmann, A., and Hoffmann, J., 2007, "Long Range 3D Scanning Tunnelling Microscopy", *CIRP Annals - Manufacturing Technology*, Vol. **56**(1):525–528.

[5.2] Xu, Q., Li, Y., 2008, "Design of a Partially Decoupled High Precision XYZ Compliant Parallel Micromanipulator", *Proceedings of the 3rd IEEE International Conference on Nano/Micro Engineered and Molecular Systems*, January 6–9, 2008, Sanya, China, pp. 13–18.

[5.3] Shinno, H., Yoshioka, H., 2010, "A Newly Developed Three-Dimensional Profile Scanner with Nanometer Spatial Resolution", *CIRP Annals - Manufacturing Technology*, Vol. **59**(1):525–528.

[5.4] Martock Design Limited, 1987, *Adjustable Mountings*, United States Patent, No.:4635887.

[5.5] Wang, Y., and Gosselin, C. M., 2004, "On the Design of a 3-PRRR Spatial Parallel Compliant Mechanism", *Proceeding of the ASME 28th Biennial Mechanisms and Robotics Conference*, Sep. 28–Oct. 2, 2004, Salt Lake City, Utah, USA.

[5.6] Pham, H.-H., Yeh, H. C., Chen, I.-M., 2006, "Micromanipulation System Design Based on Selective Actuation Mechanisms", *The International Journal of Robotics Research*, Vol. **25**(2):171–185.

[5.7] Li, Y., Xu, Q., 2011, "A Totally Decoupled Piezo-Driven XYZ Flexure Parallel Micropositioning Stage for Micro/Nanomanipulation", *IEEE Transactions on Automation Science and Engineerin*g, Vol. **8**(2):265–279.

[5.8] Koseki, Y., Tanikawa, T., and et al, 2002, Kinematic Analysis of a Translational 3-d.o.f. Micro-Parallel Mechanism Using Matrix Method, *Advanced Robotics*, Vol. **16**(3):251–264.

[5.9] Li, Y., Xu, Q., 2009, "Design and Optimization of an XYZ Parallel Micromanipulator with Flexure Hinges", *Journal of Intelligent and Robotic Systems*, Vol. **55**:377–402.

[5.10] Xu, Q., Li, Y., 2006, "Stiffness Modeling for an Orthogonal 3-PUU Compliant parallel Micromanipulator", *Proceedings of the 2006 IEEE International Conference on Mechatronic and Automations*, June 25–28, 2006, Luoyang, China, pp. 124–129.

[5.11] Yue, Y., Gao, F., Zhao, X., and Ge, Q., 2010, "Relationship among Input-Force, Payload, Stiffness and Displacement of a 3-DOF Perpendicular Parallel

Micro-Manipulator", *Mechanism and Machine Theory*, Vol. **45**(5):756–771.

[5.12] Tang, X., Chen, I.-M., Li, Q., 2006, "Design and Nonlinear Modeling of a Large-Displacement XYZ Flexure Parallel Mechanism with Decoupled Kinematics Structure", *Review of Scientific Instruments*, Vol. **77**:115101.

[5.13] Yun, Y., Li, Y., 2011, "Optimal Design of a 3PUPU Parallel Robot with Compliant Hinges for Micromanipulation in a Cubic Workspace", *Robotics and Computer-Integrated Manufacturing*, Vol. **27**(6):977–985.

[5.14] Quyang, P.R., 2011, "A Spatial Hybrid Motion Compliant Mechanism: Design and Optimization", *Mechatronics*, Vol. **21**(3):479–489.

[5.15] Kong X. and Gosselin, C.M, 2002, "Type Synthesis of Linear Translational Parallel Manipulators", *Advances in Robot Kinematics – Theory and Applications*, Lenarcic J. and Thomas F. (Eds.), Kluwer Academic Publishers, pp. 411–420..

[5.16] Gogu G., 2004, "Structural Synthesis of Fully-Isotropic Translational Parallel Robots via Theory of Linear Transformations", *European Journal of Mechanics A/Solids*, Vol. **23**(6):1021–1039.

[5.17] Carricato, M., Parenti-Castelli, V., 2002, "Singularity Free Fully-Isotropic Translational Parallel Mechanisms", *The International Journal of Robotics Research*, Vol. **21**(2):167–174.

[5.18] Awtar, S., 2004, "*Analysis and Synthesis of Planar Kinematic XY Mechanisms*", Sc.D. thesis, Massachusetts Institute of Technology, Cambridge, MA.

[5.19] Trease, B. P., Moon, Y.-M., Kota, S., 2005, "Design of Large-Displacement Compliant Joints", *Journal of Mechanical Design*, Vol. **127**(7): 788–798.

[5.20] Hale L.C., 1999, "*Principles and Techniques for Designing Precision Machines*", PhD thesis, University of California, Livermore, California.

Chapter 6 – Conclusions

6.1 General Conclusions

The large range of motion is one of the critical challenges for the design of CPMs since CPMs transmit motion/load only by the deformation of their compliant members. Nevertheless, there is an increasing need for large-range translational CPMs due to their merits such as eliminated backlash and friction, no need for lubrication, reduced wear and noise, and monolithic configuration.

In order to meet the need of the large-range translation, this thesis has proposed a design methodology for translational CPMs at first, and then presented and modelled large-range translational CPMs. Distributed-compliance modules have been proposed and then employed to construct CPMs from 1-DOF translation up to 3-DOF translation using the proposed design methodology. Especially, the spatial multi-beam modules have been nonlinearly modelled and creatively used to construct spatial translational CPMs with good performance characteristics. In addition, kinematostatic modelling of the proposed large-range translational CPMs has been implemented to analyse the performance characteristics.

Considering the analytical and FEA results, the large-range translational CPMs proposed in Chapters 3, 4, and 5 have good performance characteristics as follows.

1) The auto-adaptive CPG possesses some advantages including auto-adaptive grasping function driven by only one linear actuator, large-stroke, no stress-concentration, well-constrained parasitic rotation, actuator isolation, and a simple and compact configuration.

2) The stiffness-enhanced XY CPM with the overall dimension of 540mm×540mm×75mm in the example case has

(a) a large range of motion up to 10mm×10mm,

(b) well-constrained parasitic motion with the parasitic translation along the Z-axis less than 2×10^{-4} mm, the parasitic rotation about the X-/Y-axis better than 2×10^{-6}, and the parasitic rotation about the Z-axis below 1×10^{-6},

(c) approximate actuator-isolation with input-coupling of the actuator smaller than 1.52% of the primary motion along the same direction,

(d) approximate cross-axis decoupling with cross-axis coupling error less than 1.56% of the primary motion along the same direction,

(e) acceptable lost motion below 4.45% of the primary motion along the same

direction, and

(f) enhanced out-of-plane stiffness approximately same as that of the planar XY CPM having 2.2 times higher beams.

3) The improved modular XYZ CPM with the overall dimension of 466.40mm×466.40mm×466.40mm in the example case has

(a) a large range of motion up to 10mm×10mm×10mm,

(b) well-constrained parasitic motion with all the parasitic rotations below 1.2×10^{-3},

(c) approximate actuator-isolation with input-coupling of the actuator smaller than 0.65% of the primary motion along the same direction,

(d) approximate cross-axis decoupling with cross-axis coupling less than 1% of the primary motion along the direction of the actuation force that causes the cross-axis coupling,

(e) acceptable lost motion below 0.3% of the primary motion along the same direction, and

(f) reduced number of design parameters by using *identical spatial* multi-beam modules.

6.2 Contributions

The major contributions for the thesis are shown as follows.

1) A design methodology for translational CPMs has been proposed. The proposed design approach to synthesize translational CPMs is an extension of the traditional PRBM approach. Unlike the traditional PRBM approach in which the traditional joints are replaced with lumped compliance joints, the proposed approach involves both replacing kinematic chains with appropriate multi-DOF compliant parallel modules and replacing traditional joints with lumped compliance joints.

2) The normalized, nonlinear and analytical load-displacement equations for the spatial three-beam module have been solved using three methods: approximate analytical method, improved approximate analytical method and numerical method. In addition, a class of multi-beam modules with four or more beams has been proposed, and their general nonlinear load-displacement equations have been obtained based on the approximate analytical load-displacement equations of the spatial three-beam module.

3) A novel auto-adaptive compliant parallel gripper (CPG) for 1-D large-range translation has been proposed using a cymbal-type amplifier and two parallelogram

modules. The analytical model for the auto-adaptive CPG has also been derived.

4) A large-range stiffness-enhanced XY CPM has been proposed by combining a planar XY CPM and a spatial double four-beam module in an appropriate parallel arrangement. Normalized analytical models for the stiffness-enhanced XY CPM have been further presented to analyse performance characteristics.

5) Several large-range XYZ CPMs have been proposed based on the proposed design methodology through the use of: (a) identical double parallelogram flexure modules, (b) inverted planar XY CPMs, (c) identical spatial modules, (d) embedded spatial modules, (e) five legs composed of spatial modules, and (f) planar double two-beam modules. The improved modular XYZ CPM using identical spatial double four-beam modules has been modelled and analysed using a normalization approach.

6) The normalization-based mobility analysis for spatial multi-beam modules has been studied to deal with the inconsistence of dimension for displacements and loads, and the determination of the magnitude of loads. DOF of spatial multi-beam modules can be identified from their normalized compliance matrices by direct observation and screw representation.

6.3 Suggestions of Future Works

The research on CPMs is still a challenging issue. Several future works under investigation are identified as follows.

a) Experimental verification

Experiment is very costly considering the manufacture or experimental measurement (relate to sensors etc) accuracy required. Due to the current experiment conditions and available finance limitations, we only employ Comsol/Cosmosworks commercial software to carry out the comparison between the analytical model and FEA instead of experiment.

However, experiment should be carried out in the near future in order to verify the proposed analytical models or FEA models for the translational CPMs. In this way, various issues related to manufacturing, assembly, tolerances, testing, etc can be addressed.

b) Accurate nonlinear modelling

Although linear modelling has been presented for the proposed translational CPMs, it

ignores some nonlinear constraint characteristics, such as cross-axis coupling. Therefore, a more accurate nonlinear model should be developed in order to capture all nonlinear characteristics for the proposed designs.

c) Dynamics modelling

Lagrange equation can be used to deal with the dynamics to accurately capture high-order natural frequencies in order to determine various vibration modes and facilitate the control.

d) High-performance control system

In order to achieve large range of motion, distributed-compliance modules have been used to construct translational CPMs in this thesis. However, such CPMs suffer from relatively low primary stiffness, which leads to relatively low first natural frequency. Thus a high-order controller should be used to achieve a high bandwidth greater than the first natural frequency by averting the resonance domain along with large range of motion.

e) Optimization

In order to obtain more reasonable and reliable translational CPMs, optimizations should be implemented. Such optimizations may focus on fatigue consideration, layouts and layer amount of multi-beam modules, beam length, thickness and pitch circle radii under given design indices such as motion range and dynamic performance.

f) Rapid design synthesis

The proposed analytical models throughout this thesis may be further used to enable rapid design synthesis. This means that one can use these models to analyse the effect of parameters upon the performance characteristics of proposed designs, and then choose appropriate parameters according the desired performance characteristics.

g) Manufacturing and material

For planar compliant mechanisms/manipulators, EDM has been proved to be a good manufacturing approach to obtain monolithic configuration. Whereas for spatial modules/mechanisms/manipulators, it is very hard to obtain monolithic configuration using EDM. Over recent years, 3-D printing technology has been developed rapidly. Various base materials can be used such as engineering plastics, ceramics and metal.

But 3-D printing technology may lead to limited or undesired performance of material because of no traditional heat treatment. This has been proved by testing our prototype, made of engineering plastic, obtained using a 3-D printer. Therefore, better manufacturing approaches for spatial mechanism fabrication are eagerly needed.

Another shortcoming for large-range CPMs using distributed-compliance is the relatively large lost motion compared with CPMs using lumped-compliance. If we can find a good anisotropic material (like timber) suitable for precision motion stages, such issue can be solved accordingly.

h) Novel sensor design

The proposed XY/XYZ CPMs can also be used as accelerometers and force sensors and in other applications. In the former case, no linear actuators are used to generate the motion of the motion stage. By measuring the translation of the motion stage along each axis, one can calculate the inertial force, and then work out the acceleration along each axis. In the latter case, the external forces applied on the motion stage need to be measured. One can measure the primary translation at each input port to work out the external force along each axis.

Appendix A – Nonlinear Analysis of a Beam for Bending in a Plane

Figure A.1 shows a deformed beam for the bending only in the XY plane.

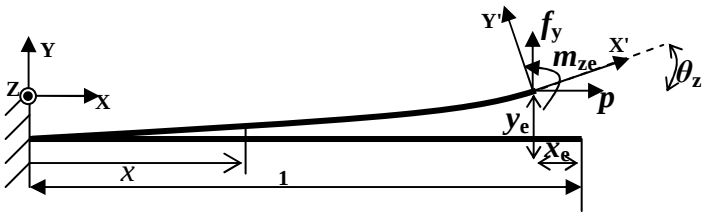

Figure A.1 Deformation of a beam.

Based on the Euler's formula and load equilibrium condition after deformation, we can obtain the differential equation of a beam under and normalization strategy and small deflection as

$$y''(x) = m_{ze} + f_y(1 + x_e - x) - p[y_e - y(x)]$$

where $y(x)$ is the transverse displacement of any x location on the beam along the Y-axis. $y''(x)$ is the secondary-order derivative of the transverse displacement. $m_{ze} + f_y(1 + x_e - x) - p[y_e - y(x)]$ is the bending moment acting at any x location of the beam about the Z-axis; m_{ze}, f_y and p are, respectively, the bending moment about the Z-axis, the transverse force along the Y-axis and the axial force along the X-axis acting at the free-end of the beam; y_e and x_e are, respectively, the transverse displacement along the Y-axis and axial displacement along the X-axis of the free-end of the beam; In the case shown in Figure A.1, x_e is negative. The subscript e denotes the free-end.

The above equation can be rewritten as

$$y''(x) - py(x) = m_{ze} + f_y(1 + x_e - x) - py_e . \tag{A.1}$$

The boundary conditions for Equation (A. 1) are

$$y=0 \text{ when } x=0,$$
$$y' = 0 \text{ when } x=0 \tag{A.2}$$

where $y'(x)$ is the first-order derivative of the transverse displacement of any x location on the beam.

Awtar [2.2] used a homogeneous 4th-order differential equation, obtained by differentiating Equation (A.1) with respect to x twice, to solve load-displacement equations.

This appendix presents an alternative solution to Equation (A.1) (non-homogeneous 2nd-order differential equation) directly by combining the general solution to the corresponding homogeneous differential equation and the particular solution to the

non-homogeneous differential equation.

The general solution to the corresponding homogeneous differential equation ($y'' - py = 0$) is

$$y = Ae^{kx} + B^{-kx} \tag{A.3}$$

where $k^2=p$.

The particular solution to the non-homogeneous differential equation is assumed as

$$y=Cx+D. \tag{A.4}$$

Substituting Equation (A.4) into Equation (A.1), we can obtain

$$-k^2(Cx+D) = m_{ze} + f_y(1+x_e) - k^2 y_e - f_y x .$$

Then we have

$$\begin{cases} -k^2 C = -f_y \\ -k^2 D = m_{ze} + f(1+x_e) - k^2 y_e \end{cases},$$

i.e.

$$\begin{cases} C = f_y / k^2 \\ D = -\dfrac{m_{ze} + f_y(1+x_e) - k^2 y_e}{k^2} \end{cases}. \tag{A.5}$$

Combining Equations (A.3), (A.4) and (A.5), we can obtain the general solution to the non-homogeneous 2-order differential equation as

$$y = Ae^{kx} + B^{-kx} + \frac{f_y}{k^2}x - \frac{m_{ze} + f_y(1+x_e) - k^2 y_e}{k^2}. \tag{A.6}$$

Substituting the boundary condition, Equation (A.2), into Equation (A.6), we can obtain

$$A + B - \frac{m_{ze} + f_y(1+x_e) - k^2 y_e}{k^2} = 0,$$

$$Ak - Bk + \frac{f_y}{k^2} = 0 .$$

Solving the above equations, we then obtain

$$\begin{cases} A = \dfrac{1}{2}\left(\dfrac{m_{ze} + f_y(1+x_e) - k^2 y_e}{k^2} - \dfrac{f_y}{k^3}\right) \\ B = \dfrac{1}{2}\left(\dfrac{m_{ze} + f_y(1+x_e) - k^2 y_e}{k^2} + \dfrac{f_y}{k^3}\right) \end{cases}. \tag{A.7}$$

Substituting Equations (A.5) and (A.7) into Equation (A.6), the general solution to Equation (A.1) is obtained as

$$y(x)=\frac{m_{ze}+f_y(1+x_e)-k^2y_e}{k^2}(\frac{e^{kx}+e^{-kx}}{2})-\frac{f_y}{k^3}(\frac{e^{kx}-e^{-kx}}{2})+\frac{f_y}{k^2}x-\frac{m_{ze}+f_y(1+x_e)-k^2y_e}{k^2}$$
$$=\frac{m_{ze}+f_y(1+x_e)-k^2y_e}{k^2}\cosh kx-\frac{f_y}{k^3}\sinh kx+\frac{f_y}{k^2}x-\frac{m_{ze}+f_y(1+x_e)-k^2y_e}{k^2} \quad \text{. (A.8)}$$

An analogous solution can also be obtained in terms of trigonometric functions rather than the above hyperbolic functions for negative values of *p*.

When *x*=1, the transverse displacement y_e and the rotational angle θ_z about the Z-axis of the free-end can be obtained using Equation (A. 8) as

$$y_e=y(1)\approx\frac{m_{ze}+f_y-k^2y_e}{k^2}\cosh k-\frac{f_y}{k^3}\sinh k+\frac{f_y}{k^2}-\frac{m_{ze}+f_y-k^2y_e}{k^2},$$

i.e.

$$y_e=\frac{f_y(k-\tanh k)}{k^3}+\frac{m_{ze}(\cosh k-1)}{k^2\cosh k}. \quad \text{(A.9)}$$

$$\theta_z=y'(1)\approx\frac{m_{ze}+f_y-k^2y_e}{k}\sinh k-\frac{f_y}{k^2}\cosh k,$$

i.e.

$$\theta_z=\frac{f_y(\cosh k-1)}{k^2\cosh k}+\frac{m_{ze}\tanh k}{k}. \quad \text{(A.10)}$$

Equations (A.9) and (A.10) are the same as the results derived in [2.2, 2.6].

As in [2.2], the axial displacement can be divided in two parts: a purely elastic component and a kinematic component as

$$x_e=x_e^e+x_e^k \quad \text{(A.11a)}$$

where x_e^e and x_e^k are the purely elastic component and the kinematic component of the free-end's axial displacement, respectively. And $x_e^e=p/d$.

The kinematic component can be further obtained as follows:

$$\mathrm{d}s=\mathrm{d}x/\cos\theta=(1+\tan^2\theta)^{1/2}\,\mathrm{d}x=(1+y'^2)^{1/2}\,\mathrm{d}x\approx(1+\frac{1}{2}y'^2)\,\mathrm{d}x, \quad \text{(A.11b)}$$

where *s* is the length of arc elements on the beam.

Then we obtain

$$\int_0^{1+x_e^e}\mathrm{d}s=\int_0^{1+x_e}(1+\frac{1}{2}y'^2)\,\mathrm{d}x, \quad \text{(A.11c)}$$

i.e.

$$1+x_e^e\approx1+(x_e^e+x_e^k)+\frac{1}{2}\int_0^1y'^2\,\mathrm{d}x.$$

Then Equation (A.11c) can be rewritten as

$$x_e^k = -\frac{1}{2}\int_0^1 y'^2 \, \mathrm{d}x \,. \tag{A.11d}$$

Substituting Equation (A.8) into Equation (A.11d) and combining with the purely elastic component, we can obtain the axial displacement [2.2].

$$x_e = \frac{p}{d} - [y_e, \theta_z]\begin{bmatrix} r_{11} & r_{12} \\ r_{21} & r_{22} \end{bmatrix}\begin{bmatrix} y_e \\ \theta_z \end{bmatrix} \tag{A.11e}$$

where

$$r_{11} = \frac{k^2(\cosh^2 k + \cosh k - 2) - 3k\sinh k(\cosh k - 1)}{2(k\sinh k - 2\cosh k + 2)^2},$$

$$r_{12}=r_{21}=\frac{k^2(\cosh k - 1) + k\sinh k(\cosh k - 1) - 4(\cosh k - 1)^2}{4(k\sinh k - 2\cosh k + 2)^2}, \text{ and}$$

$$r_{22}=\frac{-k^3 + k^2\sinh k(\cosh k + 2) - 2k(2\cosh^2 k - \cosh k - 1) + 2k\sinh k(\cosh k - 1)}{4k(k\sinh k - 2\cosh k + 2)^2}.$$

Then making approximations for all load-displacement equations of the free-end of the beam based on the Taylor series expansion, we obtain from Awtar's work [2.2]

$$\begin{bmatrix} f_y \\ m_{ze} \end{bmatrix} = \begin{bmatrix} a & c \\ c & b \end{bmatrix}\begin{bmatrix} y_e \\ \theta_z \end{bmatrix} + p\begin{bmatrix} e & h \\ h & g \end{bmatrix}\begin{bmatrix} y_e \\ \theta_z \end{bmatrix} + p^2\begin{bmatrix} -1/700 & 1/1400 \\ 1/1400 & -11/6300 \end{bmatrix}\begin{bmatrix} y_e \\ \theta_z \end{bmatrix} + \cdots, \tag{A.12a}$$

$$x_e = \frac{1}{d}p + [y_e, \theta_z]\begin{bmatrix} i & k \\ k & j \end{bmatrix}\begin{bmatrix} y_e \\ \theta_z \end{bmatrix} + p[y_e, \theta_z]\begin{bmatrix} r & q \\ q & s \end{bmatrix}\begin{bmatrix} y_e \\ \theta_z \end{bmatrix} + p^2[y_e, \theta_z]\begin{bmatrix} 1/42000 & -1/84000 \\ -1/84000 & 1/18000 \end{bmatrix}\begin{bmatrix} y_e \\ \theta_z \end{bmatrix} + \cdots. \tag{A.12b}$$

Similarly, the load-displacement equations of the free-end of a beam for the bending only in the XZ plane can be obtained as

$$\begin{bmatrix} f_z \\ -m_{ye} \end{bmatrix} = \begin{bmatrix} a & c \\ c & b \end{bmatrix}\begin{bmatrix} z_e \\ -\theta_y \end{bmatrix} + p\begin{bmatrix} e & h \\ h & g \end{bmatrix}\begin{bmatrix} z_e \\ -\theta_y \end{bmatrix} + p^2\begin{bmatrix} -1/700 & 1/1400 \\ 1/1400 & -11/6300 \end{bmatrix}\begin{bmatrix} z_e \\ -\theta_y \end{bmatrix} + \cdots, \tag{A.13a}$$

$$x_e = \frac{1}{d}p + [z_e, -\theta_y]\begin{bmatrix} i & k \\ k & j \end{bmatrix}\begin{bmatrix} z_e \\ -\theta_y \end{bmatrix} + p[z_e, -\theta_y]\begin{bmatrix} r & q \\ q & s \end{bmatrix}\begin{bmatrix} z_e \\ -\theta_y \end{bmatrix} + p^2[z_e, -\theta_y]\begin{bmatrix} 1/42000 & -1/84000 \\ -1/84000 & 1/18000 \end{bmatrix}\begin{bmatrix} z_e \\ -\theta_y \end{bmatrix} + \cdots \tag{A.13b}$$

where m_{ye}, f_z and p are, respectively, the bending moment about the Y-axis, the transverse force along the Z-axis and the axial force along the X-axis acting at the free-end of the beam; z_e, x_e and θ_y are, respectively, the transverse displacement along the Z-axis, the axial displacement along the X-axis and the rotational angle about the Y-axis of the free-end of the beam.

Appendix B – Torsion of a Deformed Beam about the X-Axis

Following the discussion in Chapter 2, we will derive the torsional angle formula for a beam under spatial combined deformation. Due to the small deflection hypothesis, we can assume

$$\mathrm{d}\theta_x = m_x(x)\mathrm{d}x \tag{B.1a}$$

where $m_x(x) = m_{xe} + f_z[y_e - y(x)]/\delta - f_y[z_e - z(x)]/\delta$, which is the torque acting at any x location on the beam about the X-axis in deformed configuration; δ=2G/E; m_{xe}, f_{z}, and f_{y} are, respectively, the torque about the X-axis, the transverse force along the Z-axis and the transverse force along the Y-axis acting at the free-end of the beam; y_{e} and z_{e} are the transverse displacements of the free-end of the beam along the Y- and Z-axes, respectively; $y(x)$ and $z(x)$ are the transverse displacements of any x location on the beam along the Y- and Z-axes, respectively.

Equation (B.1a) can be rewritten as

$$\mathrm{d}\theta_x = \{m_{xe} + f_z[y_e - y(x)]/\delta - f_y[z_e - z(x)]/\delta\}\mathrm{d}x\,. \tag{B.1b}$$

Based on Equation (A.8), $y(x)$ and $z(x)$ can be expressed respectively as

$$y(x) = \frac{m_{ze} + f_y - k^2 y_e}{k^2}\cosh kx - \frac{f_y}{k^3}\sinh kx + \frac{f_y}{k^2}x - \frac{m_{ze} + f_y - k^2 y_e}{k^2},$$

$$z(x) = \frac{-m_{ye} + f_z - k^2 z_e}{k^2}\cosh kx - \frac{f_z}{k^3}\sinh kx + \frac{f_z}{k^2}x - \frac{-m_{ye} + f_z - k^2 z_e}{k^2} \tag{B.2}$$

where k^2=p. p, m_{ye} and m_{ze} are, respectively, the axial force along the X-axis, the bending moment about the Y-axis and the bending moment about the Z-axis acting at the free-end of the beam.

The torsional angle of the free-end can be obtained by integrating Equation (B.1b) as

$$\begin{aligned}\theta_x &= \int_0^1 \{m_{xe} + f_z[y_e - y(x)]/\delta - f_y[z_e - z(x)]/\delta\}\mathrm{d}x \\ &= m_{xe} + (f_z y_e - f_y z_e)/\delta - \int_0^1 [f_z y(x)/\delta - f_y z(x)/\delta]\mathrm{d}x\end{aligned}.$$

Substituting Equation (B.2) into the earlier equation, we obtain

$$\begin{aligned}\theta_x = m_{xe} + (f_z y_e - f_y z_e)/\delta - \int_0^1 \{ f_z[&\frac{m_{ze} + f_y - k^2 y_e}{k^2}\cosh kx - \frac{f_y}{k^3}\sinh kx + \frac{f_y}{k^2}x - \frac{m_{ze} + f_y - k^2 y_e}{k^2}]/\delta \\ - f_y[&\frac{-m_{ye} + f_z - k^2 z_e}{k^2}\cosh kx - \frac{f_z}{k^3}\sinh kx + \frac{f_z}{k^2}x - \frac{-m_{ye} + f_z - k^2 z_e}{k^2}]/\delta\}\mathrm{d}x\end{aligned}. \tag{B.3}$$

We take the third term in Equation (B.3) for further simplification as follows:

$$\int_0^1 \{ f_z [\frac{m_{ze} + f_y - k^2 y_e}{k^2} \cosh kx - \frac{f_y}{k^3} \sinh kx + \frac{f_y}{k^2} x - \frac{m_{ze} + f_y - k^2 y_e}{k^2}] / \delta$$
$$- f_y [\frac{-m_{ye} + f_z - k^2 z_e}{k^2} \cosh kx - \frac{f_z}{k^3} \sinh kx + \frac{f_z}{k^2} x - \frac{-m_{ye} + f_z - k^2 z_e}{k^2}] / \delta \} \mathrm{d}x$$
$$= (f_z y_e - f_y z_e) / \delta + \int_0^1 \{ [\frac{f_z m_{ze} - f_z k^2 y_e}{k^2} \cosh kx - \frac{f_z m_{ze}}{k^2}] / \delta - [\frac{-f_y m_{ye} - f_y k^2 z_e}{k^2} \cosh kx - \frac{-f_y m_{ye}}{k^2}] / \delta \} \mathrm{d}x$$
$$= (f_z y_e - f_y z_e) / \delta + \int_0^1 \{ [\frac{f_z m_{ze} - f_z k^2 y_e}{k^2} - \frac{-f_y m_{ye} - f_y k^2 z_e}{k^2}] \cosh kx / \delta + [\frac{-f_y m_{ye}}{k^2} - \frac{f_z m_{ze}}{k^2}] / \delta \} \mathrm{d}x$$
$$= (f_z y_e - f_y z_e) / \delta + [(\frac{f_z m_{ze} + f_y m_{ye}}{k^2} + f_y z_e - f_z y_e) / \delta] \sinh k / k + (\frac{-f_y m_{ye} - f_z m_{ze}}{k^2}) / \delta$$

(B.4)

According to the Taylor series expansion, we have

$$e^k = 1 + k + k^2 / 2 + \cdots + k^n / n! + \cdots .$$

Thus, we have

$$\sinh k / k = \frac{e^k - e^{-k}}{2k} = \frac{(1 + k + k^2 / 2 + \cdots) - (1 - k + k^2 / 2 + \cdots)}{2k} \approx 1 . \qquad \text{(B.5)}$$

Substituting Equation (B.5) into Equation (B.4), and substituting the result into Equation (B.3), we obtain

$$\theta_x = m_{xe} + (f_z y_e - f_y z_e) / \delta - \{ (f_z y_e - f_y z_e) / \delta + [(\frac{f_z m_{ze} + f_y m_{ye}}{k^2} + f_y z_e - f_z y_e) / \delta] + (\frac{-f_y m_{ye} - f_z m_{ze}}{k^2}) / \delta \} .$$
$$= m_{xe} + (f_z y_e - f_y z_e) / \delta + 0$$

(B.6)

Equation (B.6) can also be explained qualitatively as follows. When we calculate the torsional angle θ_x, the beam can be assumed as a straight beam without bending deformation (Figure B.1).

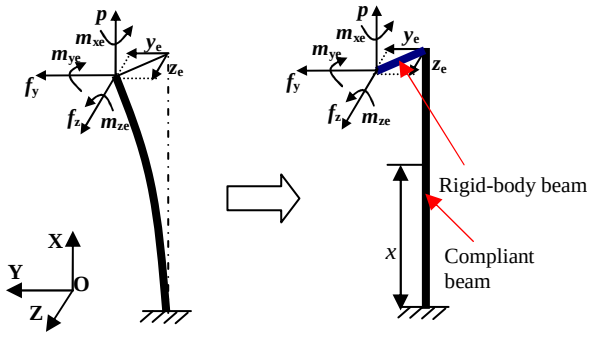

(a) Real configuration in deformation (b) Equivalent configuration

Figure B.1 Equivalent transformation for the torsional-angle calculation.

Therefore, the torsional moment $m_x(x)$, with respect to central axis of the undeformed beam, at any x location on the beam may be regarded as

$$m_{xe} + (f_z y_e - f_y z_e) / \delta$$

and therefore the torsional angle can be also obtained as

$$\theta_x = \int_0^1 [m_{xe} + (f_z y_e - f_y z_e)/\delta]\mathrm{d}\,x = m_{xe} + (f_z y_e - f_y z_e)/\delta\,.$$

Based on the mentioned principle of superposition in Section 2.1, we can substitute Equations (A.12a) and (A.13a) into Equation (B.6) to obtain

$$\begin{aligned}\theta_x &= m_{xe} + (f_z y_e - f_y z_e)/\delta \\ &= m_{xe} + (az_e + pez_e)y_e/\delta - (ay_e + pey_e)z_e/\delta - c(\theta_z z_e + \theta_y y_e)/\delta - ph(\theta_z z_e + \theta_y y_e)/\delta\,. \\ &= m_{xe} - c(\theta_z z_e + \theta_y y_e)/\delta - ph(\theta_z z_e + \theta_y y_e)/\delta\end{aligned} \tag{B.7}$$

Appendix C – Mobility Analysis of Spatial Multi-Beam Modules

Mobility analysis of spatial multi-beam modules is a basic issue in the analysis and design. This appendix will analyse the mobility of different types of spatial multi-beam modules using the approximate linear analytical approach. Except the class of spatial non-tilted multi-beam modules discussed in Chapter 2, nonlinear and analytical modelling of the spatial tilted multi-beam modules is still an open issue.

The DOF of traditional rigid-body mechanisms can be identified and calculated using formulas proposed in the literatures. But for the compliant mechanisms, there is no apparent boundary to identify the DOF or the DOC. Reference [C.1] determined the DOF of compliant mechanisms especially the planar compliant mechanisms using the PRBM concept. References [C.2, C.3] proposed an eigenscrew-based method to determine the DOF or compliance of compliant mechanisms. In addition, as discussed in the Chapter 1, the CBDA, the STBA and the FCTA have been proposed to analyse the DOF or DOC of compliant mechanisms.

However, all the above proposed approaches for the DOF analysis of compliant mechanisms do not take into account the effect of dimension, loads or motion range in detail.

When analysing the DOF of a compliant mechanism quantitatively, we need to compare output displacements to identify the DOF or DOC. If a displacement is much larger than another displacement under the same dimension, then larger one can be regarded as the DOF. If two displacements, such as one translational displacement and one rotational angle, are not under the same dimension, then the DOF identification becomes very difficult. In order to make translational displacements and rotational angles (or the forces and the moments) comparable, a normalization strategy (non-dimensional/homogeneous measures) is necessary to unify dimension for compliant mechanisms. Normalization technique has been employed in the modelling and design of compliant/flexural mechanisms [C.4–C.8, C.20]. It has been shown that this strategy can also simplify equations and derivation in compliant mechanisms. In rigid-body manipulators/mechanisms, such strategy has also been employed. For example, Ref. [C.9] proposed a characteristic length for normalizing the rigid-body displacements.

In addition, the DOF of some compliant mechanisms, such as the linear motion flexure [C.10, C.11] composed of two parallelogram modules in mirror-symmetry, can

also degenerate into the DOC when they achieve large range of motion. This is caused by the load-stiffening effect [C.10, C.11]. Under the small deflection assumption, this issue can be neglected. It should also be noted that the location and magnitude of applied loads may affect the identification of the DOF and DOC. For example, for a cantilever beam, it is well known that the axial displacement of the tip is usually thought of as the DOC, and the transverse displacement of the tip is usually regarded as the DOF. However, if the axial force acting at the tip of the beam is much larger than the exerted transverse force, the resulting axial displacement will be able to be much larger than the transverse displacement. Thus, in the analysis of compliant mechanisms, we may assume all loads to be in the same order of magnitude and comparable under the same dimension.

In this appendix, we focus on a normalization-based approach to the mobility analysis of spatial multi-beam modules. The multi-beam modules are composed of identical and uniform beams with symmetrical cross-sections, which can be used in many applications either independently or as a compositional unit of a compliant manipulator. This appendix is organized as follows. Section C.1 introduces the normalization strategy by normalizing the force-displacement equations for a cantilever beam. Section C.2 analyses spatial non-tilted multi-beam modules including a three-beam module and a double three-beam module. Section C.3 discusses spatial tilted multi-beam modules including a three-beam module and a double three-beam module, which also introduces a screw theory to reflect the DOF straightforwardly using the compliance matrix. Section C.4 discusses the mobility of multi-sheet modules using the normalization-strategy. Finally, a summary are implemented.

C.1 Normalization Strategy

As in Chapter 2, normalizing the beam-based modules is recalled briefly as follows (see Chapter 2 and [C.4] for details).

All translational displacements and length parameters are divided by the beam length L, forces by EI/L^2, and moments by EI/L to get their non-dimensional values. Here, E and I ($\pi D_0^4/64$) denote, respectively, the Young's modulus and the second moment of the area of a round cross-section with a diameter of D_0 for the beam. The normalized beam is equivalent to a beam with unit length, unit Young's modulus and unit cross-sectional moment. Throughout this appendix, non-dimensional quantities are represented by the corresponding lower-case letters.

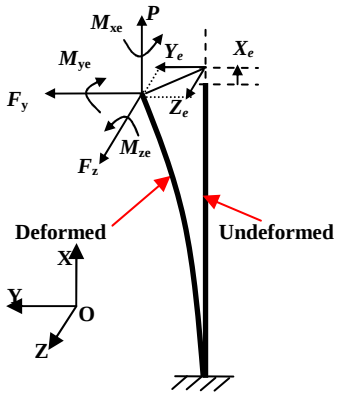

Figure C.1 Spatial deformation of a basic cantilever beam

For the basic cantilever beam (Figure C.1), P, F_y, F_z, M_{xe}, M_{ye} and M_{ze} denote the actual loads acting at the centre of the free-end. P, F_y and F_z are the forces along the X-, Y- and Z-axes, respectively, and M_{xe}, M_{ye} and M_{ze} are the actual moments about the X-, Y- and Z-axes, respectively. X_e, Y_e and Z_e are the translational displacements of the centre of the free-end along X-, Y- and Z-axes, respectively; θ_x, θ_y and θ_z are the rotational displacements of the free-end about the X-, Y- and Z-axes, respectively.

The linear load-displacement equations of the free-end centre without normalization, similar to the ones used in [C.12, C.18], are

$$\begin{bmatrix} P \\ F_y \\ F_z \\ M_{xe} \\ M_{ye} \\ M_{ze} \end{bmatrix} = \begin{bmatrix} \frac{E\pi D_0^2}{4L} & 0 & 0 & 0 & 0 & 0 \\ 0 & \frac{12EI}{L^3} & 0 & 0 & 0 & \frac{-6EI}{L^2} \\ 0 & 0 & \frac{12EI}{L^3} & 0 & \frac{6EI}{L^2} & 0 \\ 0 & 0 & 0 & \frac{2GI}{L} & 0 & 0 \\ 0 & 0 & \frac{6EI}{L^2} & 0 & \frac{4EI}{L} & 0 \\ 0 & \frac{-6EI}{L^2} & 0 & 0 & 0 & \frac{4EI}{L} \end{bmatrix} \begin{bmatrix} X_e \\ Y_e \\ Z_e \\ \theta_x \\ \theta_y \\ \theta_z \end{bmatrix} \quad \text{(C.1)}$$

where G denotes the shear modulus of material.

Using the above normalization procedure, Equation (C.1) can be re-written in a normalized form as:

$$\begin{bmatrix} p \\ f_y \\ f_z \\ m_{xe} \\ m_{ye} \\ m_{ze} \end{bmatrix} = \mathbf{K} \begin{bmatrix} x_e \\ y_e \\ z_e \\ \theta_x \\ \theta_y \\ \theta_z \end{bmatrix} = \begin{bmatrix} d & 0 & 0 & 0 & 0 & 0 \\ 0 & a & 0 & 0 & 0 & c \\ 0 & 0 & a & 0 & -c & 0 \\ 0 & 0 & 0 & \delta & 0 & 0 \\ 0 & 0 & -c & 0 & b & 0 \\ 0 & c & 0 & 0 & 0 & b \end{bmatrix} \begin{bmatrix} x_e \\ y_e \\ z_e \\ \theta_x \\ \theta_y \\ \theta_z \end{bmatrix} \tag{C.2}$$

where all the loads and displacements are the normalized quantities (scalar), which are corresponding to the non-normalized loads and displacements in Equation (C.1):

$$p = \frac{P}{EI/L^2}, f_y = \frac{F_y}{EI/L^2}, f_z = \frac{F_z}{EI/L^2},$$

$$m_{xe} = \frac{M_{xe}}{EI/L}, m_{ye} = \frac{M_{ye}}{EI/L}, m_{ze} = \frac{M_{ze}}{EI/L},$$

$$x_e = X_e/L, y_e = Y_e/L, z_e = Z_e/L.$$

All the non-dimensional numbers, a=12, c=−6, d=16/$(D_0/L)^2$, b=4, and δ=2G/E=1/(1+v) (v is the Possion ratio of the material), are the characteristics of the uniform round cross-section beam.

It is shown that Equation (C.2) obtained from Equation (C.1) is the exactly same as the one obtained using the approximate linear load-displacement equations as indicated in Section 2.2.4 in Chapter 2. Equation (C.2) is accurate enough under small deflection condition for the purpose of mobility analysis.

C.2 Spatial Non-Tilted Multi-Beam Modules

In this section, we will investigate the modelling of compliance matrices of a spatial three-beam module and a spatial double three-beam module, and also analyse their DOF using these obtained compliance matrices.

C.2.1 Analysis of a spatial three-beam module

A spatial three-beam module is shown in Figure 2.1. Its detailed quantitative analysis will be explained in the subsequent sections.

a) Modelling of the spatial three-beam module

The modelling of a spatial three-beam module can refer to the stiffness modelling of flexure parallel structure [C.13]. The detailed derivations of the approximate linear

analysis for the spatial three-beam module are shown as follows.

The geometry compatibility conditions, between the mobile end, connected to the motion stage, of each beam and the motion stage, can be re-written in a matrix form based on Equation (2.8) as

$$\begin{bmatrix} x_i \\ y_i \\ z_i \\ \theta_{ix} \\ \theta_{iy} \\ \theta_{iz} \end{bmatrix} = \mathbf{D}_{\mathrm{p}i} \begin{bmatrix} x_s \\ y_s \\ z_s \\ \theta_{sx} \\ \theta_{sy} \\ \theta_{sz} \end{bmatrix} = \begin{bmatrix} 1 & 0 & 0 & 0 & z_i' & -y_i' \\ 0 & 1 & 0 & -z_i' & 0 & x_i' \\ 0 & 0 & 1 & y_i' & -x_i' & 0 \\ 0 & 0 & 0 & 1 & 0 & 0 \\ 0 & 0 & 0 & 0 & 1 & 0 \\ 0 & 0 & 0 & 0 & 0 & 1 \end{bmatrix} \begin{bmatrix} x_s \\ y_s \\ z_s \\ \theta_{sx} \\ \theta_{sy} \\ \theta_{sz} \end{bmatrix} \tag{C.3}$$

where $\mathbf{D}_{\mathrm{P}i}$ is the transformation matrix of the displacements of the motion stage centre. x_i, y_i and z_i (i=1, 2, 3) are the translational displacements of the centre (tip) of the mobile end of the i-th beam along the X-, Y- and Z-axes, respectively; $\theta_{i\mathrm{x}}$, $\theta_{i\mathrm{y}}$ and $\theta_{i\mathrm{z}}$ are the rotational displacements of the mobile end of the i-th beam about the X-, Y- and Z-axes, respectively. x_i', y_i' and z_i' (i=1, 2, 3) are the local coordinates of the tip of the i-th beam relative to mobile rigid body coordinate system ($x_1'=0$, $y_1'=r_3\sin(\pi/3)$, $z_1'=r_3\cos(\pi/3)$ for the tip 1, $x_2'=0$, $y_2'=0$, $z_2'=-r_3$ for the tip 2, $x_3'=0$, $y_3'=-r_3\sin(\pi/3)$, $z_3'=r_3\cos(\pi/3)$ for the tip 3).

Based on Equation (C.2), the load-displacements equations for the tip of the i-th beam in the spatial three-beam module can be further obtained as

$$\begin{bmatrix} p_i \\ f_{iy} \\ f_{iz} \\ m_{ix} \\ m_{iy} \\ m_{iz} \end{bmatrix} = \mathbf{K}_i \begin{bmatrix} x_i \\ y_i \\ z_i \\ \theta_{ix} \\ \theta_{iy} \\ \theta_{iz} \end{bmatrix} = \begin{bmatrix} d & 0 & 0 & 0 & 0 & 0 \\ 0 & a & 0 & 0 & 0 & c \\ 0 & 0 & a & 0 & -c & 0 \\ 0 & 0 & 0 & \delta & 0 & 0 \\ 0 & 0 & -c & 0 & b & 0 \\ 0 & c & 0 & 0 & 0 & b \end{bmatrix} \begin{bmatrix} x_i \\ y_i \\ z_i \\ \theta_{ix} \\ \theta_{iy} \\ \theta_{iz} \end{bmatrix} \tag{C.4}$$

where $\mathbf{K}_i$ is the stiffness matrix of the i-th beam. p_i, $f_{i\mathrm{y}}$, $f_{i\mathrm{z}}$, $m_{i\mathrm{x}}$, $m_{i\mathrm{y}}$ and $m_{i\mathrm{z}}$ (i=1, 2, 3), denote the internal loads acting at the tip of the i-th beam, of which p_i, $f_{i\mathrm{y}}$ and $f_{i\mathrm{z}}$ are the forces along the X-, Y- and Z-axes, respectively, and $m_{i\mathrm{x}}$, $m_{i\mathrm{y}}$ and $m_{i\mathrm{z}}$ are the moments about the X-, Y- and Z-axes, respectively.

Using the transformation matrix $\mathbf{D}_{\mathrm{P}i}$ in Equation (C.3), the load-equilibrium conditions for the motion stage are shown as follows.

$$\begin{bmatrix} p \\ f_y \\ f_z \\ m_x \\ m_y \\ m_z \end{bmatrix} = \sum_{i=1}^{n=3} \mathbf{D}_{\mathrm{p}i}^{\mathrm{T}} \begin{bmatrix} p_i \\ f_{iy} \\ f_{iz} \\ m_{ix} \\ m_{iy} \\ m_{iz} \end{bmatrix} = \sum_{i=1}^{n=3} \begin{bmatrix} 1 & 0 & 0 & 0 & 0 & 0 \\ 0 & 1 & 0 & 0 & 0 & 0 \\ 0 & 0 & 1 & 0 & 0 & 0 \\ 0 & -z_i' & y_i' & 1 & 0 & 0 \\ z_i' & 0 & 0 & 0 & 1 & 0 \\ -y_i' & 0 & 0 & 0 & 0 & 1 \end{bmatrix} \begin{bmatrix} p_i \\ f_{iy} \\ f_{iz} \\ m_{ix} \\ m_{iy} \\ m_{iz} \end{bmatrix} \tag{C.5}$$

where $\mathbf{D}_{\mathrm{p}i}^{\mathrm{T}}$ is the transformation matrix of the loads acting at the centre of the end of the i-th beam.

Substituting Equation (C.4) into Equation (C.5), and then substituting Equation (C.3) into the result, we have

$$\mathbf{F} = \mathbf{K}_{\mathrm{p}} \mathbf{X}_{\mathrm{s}} \tag{C.6}$$

where $\mathbf{X}_{\mathrm{s}} = [x_s, y_s, z_s, \theta_{sx}, \theta_{sy}, \theta_{sz}]^{\mathrm{T}}$, and $\mathbf{F} = [p,\ f_y,\ f_z, m_x, m_y, m_z]^{\mathrm{T}}$, and $\mathbf{K}_{\mathrm{p}} = \mathbf{D}_{\mathrm{p1}}^{\mathrm{T}} \mathbf{K}_1 \mathbf{D}_{\mathrm{p1}} + \mathbf{D}_{\mathrm{p2}}^{\mathrm{T}} \mathbf{K}_2 \mathbf{D}_{\mathrm{p2}} + \mathbf{D}_{\mathrm{p3}}^{\mathrm{T}} \mathbf{K}_3 \mathbf{D}_{\mathrm{p3}}$. The latter is the stiffness matrix of the spatial three-beam module.

The load-displacement relationships for the motion stage can also be expressed as

$$\mathbf{X}_{\mathrm{s}} = \mathbf{C}_{\mathrm{p}} \mathbf{F} \tag{C.7}$$

where $\mathbf{C}_{\mathrm{p}} = \mathbf{K}_{\mathrm{p}}^{-1}$, which is the compliance matrix of the spatial three-beam module.

Equations (C.7) and (C.6) are the forward load-displacement equations and inverse load-displacement equations of the motion stage of the spatial three-beam module, respectively.

Substituting all the values of the non-dimensional numbers and local coordinates into the compliance matrix in Equation (C.7), and letting the CPM be made from aluminium alloy for which Young's modulus, E, is 69,000 Nmm^{-2} and Poisson's ratio, v, is 0.33, we have

$$\mathbf{C}_{\mathrm{p}} = \begin{bmatrix} 1/3d & 0 & 0 & 0 & 0 & 0 \\ 0 & \dfrac{(r_3^2 d + 8)}{36(r_3^2 d + 2)} & 0 & 0 & 0 & \dfrac{1}{3(r_3^2 d + 2)} \\ 0 & 0 & \dfrac{(r_3^2 d + 8)}{36(r_3^2 d + 2)} & 0 & \dfrac{-1}{3(r_3^2 d + 2)} & 0 \\ 0 & 0 & 0 & \dfrac{625}{9(2500 r_3^2 + 157)} & 0 & 0 \\ 0 & 0 & \dfrac{-1}{3(r_3^2 d + 2)} & 0 & \dfrac{2}{3(r_3^2 d + 2)} & 0 \\ 0 & \dfrac{1}{3(r_3^2 d + 2)} & 0 & 0 & 0 & \dfrac{2}{3(r_3^2 d + 2)} \end{bmatrix} \tag{C.8}$$

where $d \geq 10000$ for $L/D_0 \geq 25$, and r_3 should usually be comparable with the beam length L, which may be larger than 0.5. This compliance matrix is a symmetrical matrix.

Equation (C.8) shows that $\theta_{sz}=0$ if $m_z=-f_y/2$, and $\theta_{sy}=0$ if $m_y=f_z/2$. This reveals that we can exert two transverse forces on the motion stage and at the symmetric centre of all beams to eliminate the parasitic bending angles. The new action position refers to the *centre of stiffness* [C.5].

b) DOF analysis of the spatial three-beam module

When multiplying the compliance matrix [Equation (C.8)] by a load vector [1, 1, 1, 1, 1, 1]^T to generate the displacements, each compliance entry in the compliance matrix can be thought of as the product of the compliance entry times a relevant unit load. In Equation (C.8), the highlighted diagonal compliance entries associated with the two transverse displacements and the torsional angle are much larger than those compliance entries associated with the axial displacement and the two bending angles under large d. Therefore, both the two transverse displacements and the torsional angle are DOF, whereas both the two bending angles and the axial displacement are DOC. Equation (C.8) also shows how the size parameters r_3 and d influence the compliance matrix. When d or r_3 increases, the three rotational angles all decrease.

We assume that the parameters are: D_0=2mm (d=10000), R_3=30mm (r_3=0.6) and L=50mm. From Equation (C.8), we obtain

$$\mathbf{C}_p = 1\times10^{-3}\begin{bmatrix} 0.0333 & 0 & 0 & 0 & 0 & 0 \\ 0 & 27.824 & 0 & 0 & 0 & 0.0925 \\ 0 & 0 & 27.824 & 0 & -0.0925 & 0 \\ 0 & 0 & 0 & 65.700 & 0 & 0 \\ 0 & 0 & -0.0925 & 0 & 0.1851 & 0 \\ 0 & 0.0925 & 0 & 0 & 0 & 0.1851 \end{bmatrix}. \quad \text{(C.9)}$$

If some entries in Equation (C.9), which are very small (approximately in the order of 0.01 of the dominant (diagonal) compliance entry), are assumed to be zero, Equation (C.9) is further simplified as

$$\mathbf{C}_p = 1\times10^{-3}\begin{bmatrix} 0 & 0 & 0 & 0 & 0 & 0 \\ 0 & 27.824 & 0 & 0 & 0 & 0 \\ 0 & 0 & 27.824 & 0 & 0 & 0 \\ 0 & 0 & 0 & 65.700 & 0 & 0 \\ 0 & 0 & 0 & 0 & 0 & 0 \\ 0 & 0 & 0 & 0 & 0 & 0 \end{bmatrix}. \quad \text{(C.10)}$$

The above simplified matrix shows that only the two transverse displacements and the torsional angle about the X-axis are the DOF.

If there is no normalization applied in the above stiffness modelling [Equations

(C.3)–(C.8)], the compliance matrix of the spatial three-beam module can be re-expressed as

$$\mathbf{C}_{\mathrm{p}} = 1\times10^{-3}\begin{bmatrix} 0.0769 & 0 & 0 & 0 & 0 & 0 \\ 0 & 64.1788 & 0 & 0 & 0 & 0.0043 \\ 0 & 0 & 64.1788 & 0 & -0.0043 & 0 \\ 0 & 0 & 0 & 0.0606 & 0 & 0 \\ 0 & 0 & -0.0043 & 0 & 0.0002 & 0 \\ 0 & 0.0043 & 0 & 0 & 0 & 0.0002 \end{bmatrix}. \quad \text{(C.11)}$$

Different from Equation (C.9), the compliance entry associated with the torsional angle in Equation (C.11) is as small as that associated with the axial displacement so that it may mislead us into that the torsional angle is the DOC rather than the DOF. This shows that one may to identify the DOF using the normalization method straightforwardly.

C.2.2 Analysis of a spatial double three-beam module

A spatial double three-beam module, connecting two spatial three-beam modules as two building blocks in series, is shown in Figure C.2.

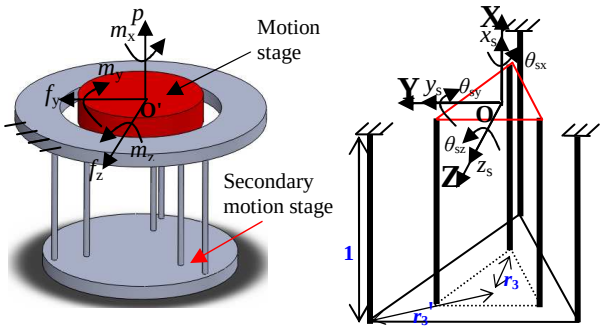

(a) CAD model (b) Schematic model

Figure C.2 A spatial double three-beam module

The modelling of the spatial double three-beam module (Figure C.2) can be derived as the stiffness modelling of flexure serial chains [C.13].

Since the displacements of the motion stage in the spatial double three-beam module are caused by both the inner spatial three-beam module deformation and outer spatial three-beam module deformation, we have

$$\mathbf{X}_{\mathrm{s}} = \mathbf{\Delta X}_{\mathrm{s1}} + \mathbf{\Delta X}_{\mathrm{s2}} \quad \text{(C.12)}$$

where $\mathbf{X}_{\mathrm{s}} = [x_s, y_s, z_s, \theta_{sx}, \theta_{sy}, \theta_{sz}]^{\mathrm{T}}$ is the displacement vector of the motion stage, $\mathbf{\Delta X}_{\mathrm{s1}}$ is the displacement vector component of the motion stage resulting from the inner spatial

three-beam module deformation alone, $\mathbf{\Delta X}_{s2}$ is the displacement vector component of the motion stage resulting from the outer spatial three-beam module deformation alone.

From Equation (C.7), we obtain

$$\mathbf{\Delta X}_{s1} = \mathbf{C}_p\mathbf{F} \tag{C.13}$$

where $\mathbf{C}_p$, shown in Equation (C.8), is the local compliance matrix of the inner spatial three-beam module. $\mathbf{F} = [p,\ f_y,\ f_z, m_x, m_y, m_z]^T$, which is the load vector acting at the motion stage.

Similar to Equation (C.3), we further have

$$\mathbf{\Delta X}_{s2} = \mathbf{J}\Delta\mathbf{X}'_{s2} \tag{C.14}$$

where $\Delta\mathbf{X}'_{s2}$ is the displacement vector of the secondary motion stage, and $\mathbf{J}$ is the transformation matrix of the center displacements of the secondary motion stage. The latter is obtained based on $\mathbf{D}_{pi}$ in Equation (C.3) using the relative location (1, 0, 0) of the centre of the motion stage with respect to that of the secondary motion stage.

Based on Equation (C.7), we obtain

$$\Delta\mathbf{X}'_{s2} = \mathbf{C}_{p2}\mathbf{F}_2 \tag{C.15}$$

where $\mathbf{C_{p2}}$, obtained using Equation (C.8), is the local compliance matrix of the outer spatial three-beam module with a pitch circle radius of r_3'. $\mathbf{F_2=J^TF,}$ obtained using Equation (C.5), is the load vector acting at the secondary motion stage.

Combining Equations (C.12)–(C.15), the load-displacement equations for the motion stage can be obtained as

$$\mathbf{X}_s = \mathbf{C}_p\mathbf{F} + \mathbf{J}\mathbf{C}_{p2}\mathbf{J}^T\mathbf{F} = (\mathbf{C}_p + \mathbf{J}\mathbf{C}_{p2}\mathbf{J}^T)\mathbf{F}\ . \tag{C.16}$$

Thus, the compliance matrix for the spatial double three-beam module can be expressed as

$$\mathbf{C}_s = \mathbf{C}_p + \mathbf{J}\mathbf{C}_{p2}\mathbf{J}^T = \begin{bmatrix} c_{s11} & 0 & 0 & 0 & 0 & 0 \\ 0 & c_{s22} & 0 & 0 & 0 & c_{s26} \\ 0 & 0 & c_{s33} & 0 & c_{s35} & 0 \\ 0 & 0 & 0 & c_{s44} & 0 & 0 \\ 0 & 0 & c_{s53} & 0 & c_{s55} & 0 \\ 0 & c_{s62} & 0 & 0 & 0 & c_{s66} \end{bmatrix} \tag{C.17}$$

where $\mathbf{C}_{p2}$ and $\mathbf{J}$ are shown in detail as follows:

$$\mathbf{C}_{p2}=\begin{bmatrix}-1&0&0&0&0&0\\0&-1&0&0&0&0\\0&0&1&0&0&0\\0&0&0&-1&0&0\\0&0&0&0&-1&0\\0&0&0&0&0&1\end{bmatrix}\mathbf{C}_{p}\begin{bmatrix}-1&0&0&0&0&0\\0&-1&0&0&0&0\\0&0&1&0&0&0\\0&0&0&-1&0&0\\0&0&0&0&-1&0\\0&0&0&0&0&1\end{bmatrix}^{-1}$$

$$=\begin{bmatrix}1/3d&0&0&0&0&0\\0&\dfrac{(r_3'^2d+8)}{36(r_3'^2d+2)}&0&0&0&\dfrac{-1}{3(r_3'^2d+2)}\\0&0&\dfrac{(r_3'^2d+8)}{36(r_3'^2d+2)}&0&\dfrac{1}{3(r_3'^2d+2)}&0\\0&0&0&\dfrac{625}{9(2500r_3'^2+157)}&0&0\\0&0&\dfrac{1}{3(r_3'^2d+2)}&0&\dfrac{2}{3(r_3'^2d+2)}&0\\0&\dfrac{-1}{3(r_3'^2d+2)}&0&0&0&\dfrac{2}{3(r_3'^2d+2)}\end{bmatrix},$$

$$\mathbf{J}=\begin{bmatrix}1&0&0&0&0&0\\0&1&0&0&0&1\\0&0&1&0&-1&0\\0&0&0&1&0&0\\0&0&0&0&1&0\\0&0&0&0&0&1\end{bmatrix}.$$

The entries in $\mathbf{C}_s$ are

$$c_{s11}=\frac{2}{3d},\ c_{s22}=\frac{(r_3^2d+8)}{36(r_3^2d+2)}+\frac{(r_3'^2d+8)}{36(r_3'^2d+2)},\ c_{s26}=\frac{1}{3(r_3^2d+2)}+\frac{1}{3(r_3'^2d+2)},\ c_{s33}=\frac{(r_3^2d+8)}{36(r_3^2d+2)}+\frac{(r_3'^2d+8)}{36(r_3'^2d+2)},$$

$$c_{s35}=\frac{-1}{3(r_3^2d+2)}-\frac{1}{3(r_3'^2d+2)},\ c_{s44}=\frac{625}{9(2500r_3^2+157)}+\frac{625}{9(2500r_3'^2+157)},\ c_{s53}=\frac{-1}{3(r_3^2d+2)}-\frac{1}{3(r_3'^2d+2)},$$

$$c_{s55}=\frac{2}{3(r_3^2d+2)}+\frac{2}{3(r_3'^2d+2)},\ c_{s26}=\frac{1}{3(r_3^2d+2)}+\frac{1}{3(r_3'^2d+2)},\ c_{s66}=\frac{2}{3(r_3^2d+2)}+\frac{2}{3(r_3'^2d+2)}.$$

Equation (C.17) shows that, under large d (for example ≥10000), the spatial double three-beam module is still a 3-DOF CPM, but it has half primary stiffness of a spatial three-beam module. Under the conditions of large enough r_3 and r_3', the spatial double three-beam module can also be regarded as a 2-DOF compliant module without torsion.

C.3 Spatial Tilted Multi-Beam Modules

In this section, we will investigate the modelling of compliance matrices of a spatial tilted three-beam module and a double tilted three-beam module, and also analyse their DOF.

C.3.1 Analysis of a spatial tilted three-beam module

A spatial tilted three-beam module is shown in Figure C.3, which has been presented elsewhere [C.14, C.19]. It is composed of three parts: a base, three tilted beams and a

thin motion stage. The base and motion stage are connected by the tilted three beams. Here, the three beams are uniformly spaced around two circles of radius r_3 and r_3' ($r_3 < r_3'$) on the motion stage and base, respectively, and three central axes of the three beams intersect at one point (named theoretical virtual rotational centre: C). β is the angle between the tilted beam and the X-axis.

Based on the type synthesis of CPMs in [C.15, C.16, C.19], the mechanism in Figure C.3 is a 3-DOF rotational CPM, and all the three rotational displacements are with respect to the theoretical virtual rotational centre C. The external applied loads, displacements of the motion stage and global fixed coordinate system are defined in the same way as before. We further establish three local coordinate systems (O_1-$X_1Y_1Z_1$, O_2-$X_2Y_2Z_2$, and O_3-$X_3Y_3Z_3$) at the tips of the three beams (Figures. C.3b and C.3c).

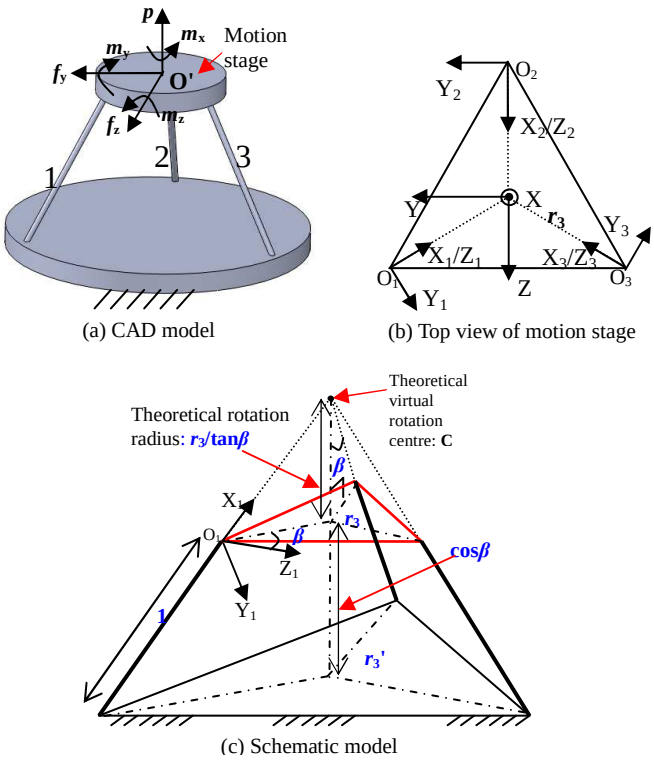

(a) CAD model

(b) Top view of motion stage

(c) Schematic model

Figure C.3 A spatial tilted three-beam module

a) Modelling of the spatial tilted three-beam module

Similar to the modelling in Section C.2.1, the geometric compatibility relationships between the centre displacements of the motion stage and *i*-th tip displacements, with respect to the O_i-$X_iY_iZ_i$ (i=1, 2, 3), can be obtained as

$$\begin{bmatrix} x_i \\ y_i \\ z_i \\ \theta_{ix} \\ \theta_{iy} \\ \theta_{iz} \end{bmatrix} = \mathbf{R}_{\mathrm{Y}_i}(\beta)\mathbf{R}_{\mathrm{X}}(-\alpha_i)\mathbf{D}_i \begin{bmatrix} x_s \\ y_s \\ z_s \\ \theta_{sx} \\ \theta_{sy} \\ \theta_{sz} \end{bmatrix} = \begin{bmatrix} \cos\beta & 0 & \sin\beta & 0 & 0 & 0 \\ 0 & 1 & 0 & 0 & 0 & 0 \\ -\sin\beta & 0 & \cos\beta & 0 & 0 & 0 \\ 0 & 0 & 0 & \cos\beta & 0 & \sin\beta \\ 0 & 0 & 0 & 0 & 1 & 0 \\ 0 & 0 & 0 & -\sin\beta & 0 & \cos\beta \end{bmatrix}$$

$$\times \begin{bmatrix} 1 & 0 & 0 & 0 & 0 & 0 \\ 0 & \cos\alpha_i & \sin\alpha_i & 0 & 0 & 0 \\ 0 & -\sin\alpha_i & \cos\alpha_i & 0 & 0 & 0 \\ 0 & 0 & 0 & 1 & 0 & 0 \\ 0 & 0 & 0 & 0 & \cos\alpha_i & \sin\alpha_i \\ 0 & 0 & 0 & 0 & -\sin\alpha_i & \cos\alpha_i \end{bmatrix} \begin{bmatrix} 1 & 0 & 0 & 0 & z_i' & -y_i' \\ 0 & 1 & 0 & -z_i' & 0 & x_i' \\ 0 & 0 & 1 & y_i' & -x_i' & 0 \\ 0 & 0 & 0 & 1 & 0 & 0 \\ 0 & 0 & 0 & 0 & 1 & 0 \\ 0 & 0 & 0 & 0 & 0 & 1 \end{bmatrix} \begin{bmatrix} x_s \\ y_s \\ z_s \\ \theta_{sx} \\ \theta_{sy} \\ \theta_{sz} \end{bmatrix} \tag{C.18}$$

where x_i, y_i, z_i, θ_{ix}, θ_{iy} and θ_{iz} (i=1, 2, 3) are the displacements of the i-th tip with respect to O_i-$X_iY_iZ_i$. x_i', y_i' and z_i' are the relative location parameters of the i-th tip with respect to the centre, **O',** of the motion stage. $\alpha_1=2\pi/3$, $\alpha_2=0$, $\alpha_3=-2\pi/3$.

Then, the load-displacement equations for the i-th tip with respect to O_i-$X_iY_iZ_i$ is

$$\begin{bmatrix} p_i \\ f_{iy} \\ f_{iz} \\ m_{ix} \\ m_{iy} \\ m_{iz} \end{bmatrix} = \mathbf{K}_i \begin{bmatrix} x_i \\ y_i \\ z_i \\ \theta_{ix} \\ \theta_{iy} \\ \theta_{iz} \end{bmatrix} = \begin{bmatrix} d & 0 & 0 & 0 & 0 & 0 \\ 0 & a & 0 & 0 & 0 & c \\ 0 & 0 & a & 0 & -c & 0 \\ 0 & 0 & 0 & \delta & 0 & 0 \\ 0 & 0 & -c & 0 & b & 0 \\ 0 & c & 0 & 0 & 0 & b \end{bmatrix} \begin{bmatrix} x_i \\ y_i \\ z_i \\ \theta_{ix} \\ \theta_{iy} \\ \theta_{iz} \end{bmatrix} \tag{C.19}$$

where p_i, f_{iy}, f_{iz}, m_{ix}, m_{iy} and m_{iz} (i=1, 2, 3), denote the loads acting at the tip of the i-th beam with respect to O_i-$X_iY_iZ_i$.

Further, the load-equilibrium conditions for the motion stage can be obtained as

$$\begin{bmatrix} p \\ f_y \\ f_z \\ m_x \\ m_y \\ m_z \end{bmatrix} = \sum_{i=1}^{n=3} \mathbf{D}_i{}^{\mathrm{T}} \mathbf{R}_{\mathrm{X}}{}^{\mathrm{T}}(-\alpha_i)\mathbf{R}_{\mathrm{Y}_i}{}^{\mathrm{T}}(\beta) \begin{bmatrix} p_i \\ f_{iy} \\ f_{iz} \\ m_{ix} \\ m_{iy} \\ m_{iz} \end{bmatrix} \tag{C.20}$$

where $\mathbf{D}_i$, $\mathbf{R}_{\mathrm{x}}(-\alpha_i)$ and $\mathbf{R}_{\mathrm{X}_i}(\beta)$ (i=1, 2, 3) are those matrices shown in Equation (C.18).

Combining Equations (C.18)–(C.20), we have the load-displacement equations for the motion stage:

$$\mathbf{X}_{\mathrm{s}} = \mathbf{K}_{\mathrm{p1}}^{-1}\mathbf{F} = \mathbf{C}_{\mathrm{p1}}\mathbf{F} \tag{C.21}$$

where $\mathbf{X}_{\mathrm{s}} = [x_s, y_s, z_s, \theta_{sx}, \theta_{sy}, \theta_{sz}]^{\mathrm{T}}$, and $\mathbf{F} = [p, f_y, f_z, m_x, m_y, m_z]^{\mathrm{T}}$.

$\mathbf{K}_{\mathrm{p1}} = \sum_{i=1}^{3} \mathbf{D}_i{}^{\mathrm{T}} \mathbf{R}_{\mathrm{X}}{}^{\mathrm{T}}(-\alpha_i) \mathbf{R}_{\mathrm{Y}_i}{}^{\mathrm{T}}(\beta) \mathbf{K}_i \mathbf{R}_{\mathrm{Y}_i}(\beta) \mathbf{R}_{\mathrm{X}}(-\alpha_i) \mathbf{D}_i$, which is the stiffness matrix of the spatial tilted three-beam module. $\mathbf{C}_{\mathrm{p1}} = \mathbf{K}_{\mathrm{p1}}^{-1}$, which is its compliance matrix, symmetrical matrix, accordingly.

b) DOF analysis of the spatial tilted three-beam module

Let $\beta=\pi/4$, L=50 (mm), r_3=0.6 and d=10000, (x_1'=0, $y_1'=r_3\sin(\pi/3)$, $z_1'=r_3\cos(\pi/3)$ for tip 1, x_2'=0, y_2'=0, $z_2'=-r_3$ for tip 2, x_3'=0, $y_3'=-r_3\sin(\pi/3)$, $z_3'=r_3\cos(\pi/3)$ for tip 3). The material of the module is detailed in Section C.2.1. From Equations (C.18)–(C.21), we obtain the compliance matrix

$$\mathbf{C}_{\mathrm{p1}} = 1\times10^{-3}\begin{bmatrix} 0.0666 & 0 & 0 & 0 & 0 & 0 \\ 0 & 6.983 & 0 & 0 & 0 & -11.504 \\ 0 & 0 & 6.983 & 0 & 11.504 & 0 \\ 0 & 0 & 0 & 28.277 & 0 & 0 \\ 0 & 0 & 11.504 & 0 & 19.320 & 0 \\ 0 & -11.504 & 0 & 0 & 0 & 19.320 \end{bmatrix}. \qquad \text{(C.22)}$$

If ignoring some insignificant entries in $\mathbf{C}_{\mathrm{p1}}$, Equation (C.22) can be re-expressed as

$$\mathbf{C}_{\mathrm{p1}} = 1\times10^{-3}\begin{bmatrix} 0 & 0 & 0 & 0 & 0 & 0 \\ 0 & 6.983 & 0 & 0 & 0 & -11.504 \\ 0 & 0 & 6.983 & 0 & 11.504 & 0 \\ 0 & 0 & 0 & 28.277 & 0 & 0 \\ 0 & 0 & 11.504 & 0 & 19.320 & 0 \\ 0 & -11.504 & 0 & 0 & 0 & 19.320 \end{bmatrix}. \qquad \text{(C.23)}$$

From Equation (C.23), it is observed that

$$y_{\mathrm{s}} \approx -(6.893/11.504)\theta_{\mathrm{sz}} \approx -(11.504/19.320)\theta_{\mathrm{sz}} \approx -[0.6/\tan(\beta)]\theta_{\mathrm{sz}},$$

$$z_{\mathrm{s}} \approx (6.893/11.504)\theta_{\mathrm{sy}} \approx (11.504/19.320)\theta_{\mathrm{sy}} \approx [0.6/\tan(\beta)]\theta_{\mathrm{sy}}.$$

i.e. two transverse displacements are not independent of the rotations. Therefore, the tilted three-beam module has three DOF, which can be represented by three rotational angles as discussed below. Here, the difference such as |6.983/11.504−0.6|=0.007 or |11.504/19.320−0.6|=0.0046 is the well-known *centre-drift* [C.17]. Equations (C.22) or (C.23) also shows that $y_{\mathrm{s}}=\theta_{\mathrm{sz}}\approx0$ if $m_{\mathrm{z}}=0.6f_{\mathrm{y}}$, and $z_{\mathrm{s}}=\theta_{\mathrm{sy}}\approx0$ if $m_{\mathrm{y}}=-0.6f_{\mathrm{z}}$. From the above analysis, one can further learn that two transverse forces, exerted on the motion stage, at the theoretical virtual rotational centre can not cause any motion.

Alternatively, we can also treat the compliance matrix $\mathbf{C}_{\mathrm{p1}}$ as a matrix composed of six screws [C.3], which can reflect motion characteristics more straightforwardly than the above observation method.

Equation (22) can be expressed in a screw form as

$$\mathbf{C}_{\mathrm{p1}} = [\mathbf{s}_1, \mathbf{s}_2, \mathbf{s}_3, \mathbf{s}_4, \mathbf{s}_5, \mathbf{s}_6] \approx \begin{bmatrix} \mathbf{0} & \mathbf{v}_2 & \mathbf{v}_3 & \mathbf{v}_4 & \mathbf{v}_5 & \mathbf{v}_6 \\ \mathbf{0} & \mathbf{w}_2 & \mathbf{w}_3 & \mathbf{w}_4 & \mathbf{w}_5 & \mathbf{w}_6 \end{bmatrix} \tag{C.24}$$

where

$\mathbf{s}_i$ (i=1, 2,…, 6) is the screw, and $\mathbf{s}_1 \approx \mathbf{0}$, which means no motion.

$\mathbf{w}_2$ is the rotation vector along the −Z-axis.

$\mathbf{w}_3$ is the rotation vector along the Y-axis.

$\mathbf{w}_4$ is the rotation vector along the X-axis.

$\mathbf{w}_5$ is the rotation vector along the Y-axis .

$\mathbf{w}_6$ is the rotation vector along the Z-axis.

$\boldsymbol{v}_i$ (i=1, 2,…, 6) is the translational displacement vector, which can be expressed as

$$\mathbf{v}_2 = \mathbf{r}_2 \times \mathbf{w}_2 + p_2 \mathbf{w}_2,$$

$$\mathbf{v}_3 = \mathbf{r}_3 \times \mathbf{w}_3 + p_3 \mathbf{w}_3,$$

$$\mathbf{v}_4 = \mathbf{r}_4 \times \mathbf{w}_4 + p_4 \mathbf{w}_4,$$

$$\mathbf{v}_5 = \mathbf{r}_5 \times \mathbf{w}_5 + p_5 \mathbf{w}_5 \ ,$$

$$\mathbf{v}_6 = \mathbf{r}_6 \times \mathbf{w}_6 + p_6 \mathbf{w}_6 .$$

p_i (i=1, 2,…, 6) is the pitch of the screw.

$\mathbf{r}_i$ (i=1, 2,…, 6) is the position vector of any point on the corresponding screw axis with respect to the fixed coordinate system.

All the pitches can be obtained as

$$p_2 = \frac{\mathbf{v}_2 \cdot \mathbf{w}_2}{\mathbf{w}_2 \cdot \mathbf{w}_2} = 0,\ p_3 = \frac{\mathbf{v}_3 \cdot \mathbf{w}_3}{\mathbf{w}_3 \cdot \mathbf{w}_3} = 0,\ p_4 = \frac{\mathbf{v}_4 \cdot \mathbf{w}_4}{\mathbf{w}_4 \cdot \mathbf{w}_4} = 0,$$

$$p_5 = \frac{\mathbf{v}_5 \cdot \mathbf{w}_5}{\mathbf{w}_5 \cdot \mathbf{w}_5} = 0,\ p_6 = \frac{\mathbf{v}_6 \cdot \mathbf{w}_6}{\mathbf{w}_6 \cdot \mathbf{w}_6} = 0. \tag{C.25}$$

Each rotation radius (the magnitude of the minimal position vector) of the center of the motion stage with respect to the relevant real screw axis (Figure C.4) can be further obtained as

$$\underline{r}_2 = \frac{|\mathbf{v}_2|}{|\mathbf{w}_2|} = 0.607 \approx 0.6, \underline{r}_3 = \frac{|\mathbf{v}_3|}{|\mathbf{w}_3|} = 0.607 \approx 0.6, \underline{r}_4 = \frac{|\mathbf{v}_4|}{|\mathbf{w}_4|} = 0,$$

$$\underline{r}_5 = \frac{|\mathbf{v}_5|}{|\mathbf{w}_5|} = 0.5954 \approx 0.6, \underline{r}_6 = \frac{|\mathbf{v}_6|}{|\mathbf{w}_6|} = 0.5954 \approx 0.6. \tag{C.26}$$

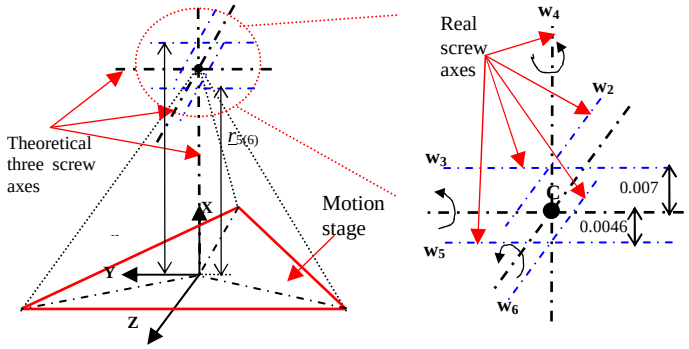

Figure C.4 Illustration for real screw axes and theoretical screw axes

Figure C.4 shows that the real screw axis $\mathbf{w}_3$ ($\mathbf{w}_5$) is very close to the corresponding theoretical screw axis which goes through the point C and is parallel to the Y-axis. The distance between the two axes is 0.007(or 0.0046), negligible compared with the theoretical rotation radius of 0.6. Therefore, the real screw axis $\mathbf{w}_3$ ($\mathbf{w}_5$) can be thought of as overlapping with the theoretical axis parallel to the Y-axis. Similarly, the real screw axis $\mathbf{w}_2$ ($\mathbf{w}_6$) can be thought of as overlapping with the theoretical axis parallel to the Z-axis. These approximations reveal that the spatial tilted three-beam module is a 3-DOF rotational CPM.

The above analysis shows that only the independent *pure rotational displacements* about the X-, Y- and Z-axes are the DOF.

If there is no normalization applied in the above stiffness modelling [Equations (C.18)–(C.21)], the compliance matrix of the spatial tilted three-beam module can be re-expressed as follows:

$$\mathbf{C}_{\mathrm{p1}} = 1\times10^{-3}\begin{bmatrix} 0.1536 & 0 & 0 & 0 & 0 & 0 \\ 0 & 16.107 & 0 & 0 & 0 & -0.531 \\ 0 & 0 & 16.107 & 0 & 0.531 & 0 \\ 0 & 0 & 0 & 0.0261 & 0 & 0 \\ 0 & 0 & 0.531 & 0 & 0.0178 & 0 \\ 0 & -0.531 & 0 & 0 & 0 & 0.0178 \end{bmatrix}. \qquad \text{(C.27)}$$

In the compliance matrix of Equation (C.27), without normalization, the compliance entry associated with the translational displacement along the X-axis (x_{s}) is larger than that associated with the rotation about the X-axis (θ_{sx}), which may mislead us into that x_{s} is the DOF, and θ_{sx} is the DOC.

An inverted spatial tilted three-beam module is shown in Figure C.5. The coordinate system, loads and displacements are all defined in the same way.

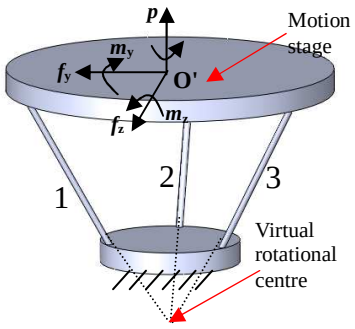

Figure C.5 An inverted spatial tilted three-beam module

Similar to the derivation of Equation (C.21), the compliance matrix for the inverted spatial tilted three-beam module is given as

$$\mathbf{C}_{\mathrm{p2}} = [\sum_{i=1}^{3} \mathbf{D}_i^{\mathrm{T}} \mathbf{R}_{\mathrm{X}}{}^{\mathrm{T}}(-\alpha_i) \mathbf{R}_{\mathrm{Y}_i}{}^{\mathrm{T}}(-\beta) \mathbf{K}_i \mathbf{R}_{\mathrm{Y}_i}(-\beta) \mathbf{R}_{\mathrm{X}}(-\alpha_i) \mathbf{D}_i]^{-1}. \tag{C.28}$$

Let L=50 (mm), d=10000, $\beta=\pi/4$, r_3=0.6 and $r_3'=r_3+\sin\beta$=1.307 (x_1'=0, $y_1'=r_3'\sin(\pi/3)$, $z_1'=r_3'\cos(\pi/3)$ for the tip 1, x_2'=0, y_2'=0, $z_2'=-r_3$ 'for the tip 2, x_3'=0, $y_3'=-r_3'\sin(\pi/3)$, $z_3'=r_3'\cos(\pi/3)$ for the tip 3). We have

$$\mathbf{C}_{\mathrm{p2}} = 1\times10^{-3}\begin{bmatrix} 0.0666 & 0 & 0 & 0 & 0 & 0 \\ 0 & 32.912 & 0 & 0 & 0 & 25.166 \\ 0 & 0 & 32.912 & 0 & -25.166 & 0 \\ 0 & 0 & 0 & 28.277 & 0 & 0 \\ 0 & 0 & -25.166 & 0 & 19.320 & 0 \\ 0 & 25.166 & 0 & 0 & 0 & 19.320 \end{bmatrix}. \tag{C.29}$$

From Equation (C.29), it is observed that

$$y_s \approx [0.6/\tan(\beta)+\cos(\beta)]\ \theta_{sz} = 1.307\theta_{sz},$$

$$z_s \approx -[0.6/\tan(\beta)+\cos(\beta)]\ \theta_{sy} = -1.307\theta_{sy}.$$

This reveals that the motion stage of this inverted spatial tilted three-beam module can produce large-range translation than the original one under same rotation since the theoretical rotational radius, 1.307 of the inverted module is larger than that, 0.6, of the original module.

C.3.2 Analysis of a spatial double tilted three-beam module

Similar to the generation of the spatial double non-tilted three-beam module (Figure C.2), we can combine two spatial tilted three-beam modules as two basic building blocks in series to obtain a spatial double tilted three-beam module shown in Figure C.6. This module has approximately double range of motion and half stiffness of a single

spatial tilted three-beam module.

Based on Equations (C.17), (C.21) and (C.28), we obtain the compliance matrix for the spatial double tilted three-beam module:

$$\mathbf{C}_s = \mathbf{C}_{p1} + \mathbf{J}\mathbf{C}_{p2}\mathbf{J}^T \tag{C.30}$$

where

$$\mathbf{J} = \begin{bmatrix} 1 & 0 & 0 & 0 & 0 & 0 \\ 0 & 1 & 0 & 0 & 0 & -2r_3/\tan\beta - \cos\beta \\ 0 & 0 & 1 & 0 & 2r_3/\tan\beta + \cos\beta & 0 \\ 0 & 0 & 0 & 1 & 0 & 0 \\ 0 & 0 & 0 & 0 & 1 & 0 \\ 0 & 0 & 0 & 0 & 0 & 1 \end{bmatrix}.$$

Substituting all the geometric parameters into Equation (C.30), we obtain

$$\mathbf{C}_s = 1\times10^{-3}\begin{bmatrix} 0.1332 & 0 & 0 & 0 & 0 & 0 \\ 0 & 14.1744 & 0 & 0 & 0 & -23.1833 \\ 0 & 0 & 14.1744 & 0 & 23.1833 & 0 \\ 0 & 0 & 0 & 56.5540 & 0 & 0 \\ 0 & 0 & 23.1833 & 0 & 38.6400 & 0 \\ 0 & -23.1833 & 0 & 0 & 0 & 38.6400 \end{bmatrix}. \tag{C.31}$$

Compared with Equation (C.22), Equation (C.31) shows that the spatial double tilted three-beam module is also a 3-DOF rotational CPM, but has approximately half rotational stiffness of a spatial tilted three-beam module [for example, the compliance entry in the sixth-row and second-column of $\mathbf{C}_{p1}$, Equation (C.22), is approximately half that of $\mathbf{C}_s$, Equation (C.31)].

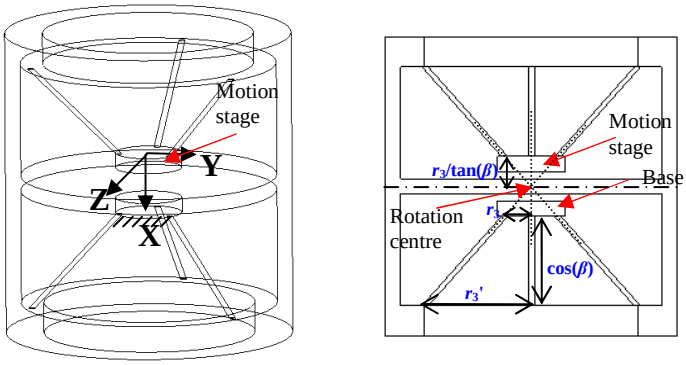

(a) 3-D view of CAD model

(b) Front view of CAD model

Figure C.6 A spatial double tilted three-beam module

The normalization–based strategy can be also used to deal with the DOF identification of other multi-beam modules (see the four-beam module shown in Figure

C.7 for example).

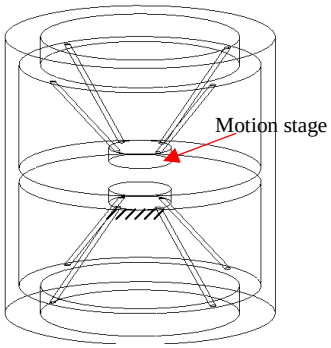

Figure C.7 A double tilted four-beam module

C.4 Other Multi-Sheet Modules

Following the mobility analysis of the spatial multi-beam modules in the previous sections of this appendix, we will discuss the normalization method for compliant modules composed of identical and uniform sheets (usually long-side length/ short-side length of a rectangular cross-section>10). Here, all the definition for the global coordinate system, loads and displacements is in the same way. All translational displacements and length parameters are divided by the sheet length L, forces by $E'I/L^2$, and moments by $E'I/L$. Here, $E'=E/(1-\nu^2)$ and I denotes, respectively, the plate modulus and the second moment of the area of a rectangular cross-section of the sheet about the axis parallel to its long side.

C.4.1 Analysis of a parallelogram module with two sheets

We first analyse the parallelogram module (Figure C.8) in common use. Similar to the formulation of Equation (C.2), the stiffness matrix for each sheet with respect to the coordinate system O-XYZ can be derived as

$$\mathbf{K}_{1(2)}=\begin{bmatrix} 12(1-\nu^2)/t^2 & 0 & 0 & 0 & 0 & 0 \\ 0 & 12 & 0 & 0 & 0 & -6 \\ 0 & 0 & 12(u/t)^2(1-\nu^2) & 0 & 6(u/t)^2(1-\nu^2) & 0 \\ 0 & 0 & 0 & 2/(1-\nu) & 0 & 0 \\ 0 & 0 & 6(u/t)^2(1-\nu^2) & 0 & 4(u/t)^2(1-\nu^2) & 0 \\ 0 & -6 & 0 & 0 & 0 & 4 \end{bmatrix} \quad \text{(C.32)}$$

where u and t are the normalized spacing parameters of a sheet as shown in Figure C.8.

It should be pointed out that there is *plane stress in the XZ plane*, and there is *plane strain in the XY plane.*

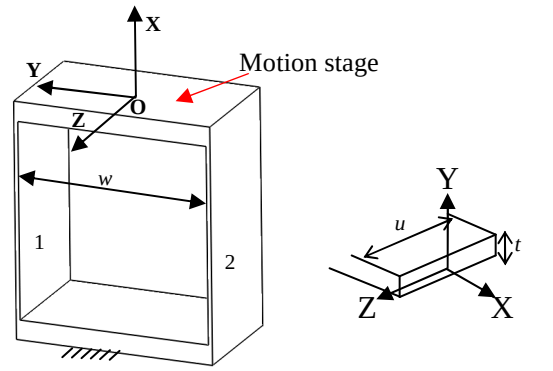

(a) 3-D view of CAD model (b) Dimension the a sheet

Figure C.8 Parallelogram module with two sheets

Then, the transformation matrices of the centre displacements of the motion stage are represented as

$$\mathbf{D}_{p1}=\begin{bmatrix}1&0&0&0&0&-w/2\\0&1&0&0&0&0\\0&0&1&w/2&0&0\\0&0&0&1&0&0\\0&0&0&0&1&0\\0&0&0&0&0&1\end{bmatrix},\quad \mathbf{D}_{p2}=\begin{bmatrix}1&0&0&0&0&w/2\\0&1&0&0&0&0\\0&0&1&-w/2&0&0\\0&0&0&1&0&0\\0&0&0&0&1&0\\0&0&0&0&0&1\end{bmatrix} \tag{C.33}$$

where w is the normalized geometrical parameter as shown in Figure C.8.

Therefore, the compliance matrix for the motion stage centre is obtained using Equations (C.32) and (C.33) as follows.

$$\mathbf{C}_p=(\mathbf{D}_{p1}^{\mathrm{T}}\mathbf{K}_1\mathbf{D}_{p1}+\mathbf{D}_{p2}^{\mathrm{T}}\mathbf{K}_2\mathbf{D}_{p2})^{-1}. \tag{C.34}$$

As an example, let L=50 (mm), W=50 (mm), T=1 (mm), U=20 (mm) and v=0.3. The substitution of all these normalized values into Equation (C.34) yields

$$\mathbf{C}_p=1\times10^{-3}\begin{bmatrix}0.0167&0&0&0&0&0\\0&41.6833&0&0&0&0.0333\\0&0&0.4579&0&-0.6868&0\\0&0&0&0.4567&0&0\\0&0&-0.6868&0&1.3736&0\\0&0.0333&0&0&0&0.0667\end{bmatrix}. \tag{C.35}$$

Equation (C.35) shows that the translation along the Y-axis is the only DOF since the highlighted element associated with the transverse displacement along the Y-axis is much larger than the other elements, which complies with the qualitative analysis.

C.4.2 Analysis of a four-sheet rotational module

The four-sheet module is shown in Figure C.9.

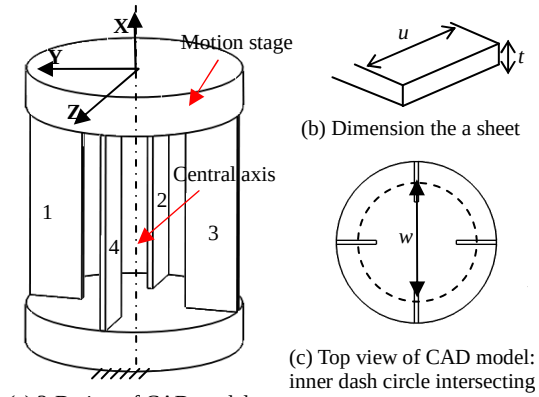

(a) 3-D view of CAD model

(b) Dimension the a sheet

(c) Top view of CAD model: inner dash circle intersecting with the centres of the

Figure C.9 Four-sheet rotational module

This module proposed as a rotational joint [1.45] is composed of four non-tilted sheets in parallel. Here, the neutral surface of each sheet, associated with the bending about the long side of its cross-section, contains the central axis of the module.

Similar to the derivation of Equation (C.2), the stiffness matrices for the sheets with respect to the coordinate system O-XYZ can be derived as

$$\mathbf{K}_{1(3)} = \begin{bmatrix} 12(1-v^2)/t^2 & 0 & 0 & 0 & 0 & 0 \\ 0 & 12(u/t)^2(1-v^2) & 0 & 0 & 0 & -6(u/t)^2(1-v^2) \\ 0 & 0 & 12 & 0 & 6 & 0 \\ 0 & 0 & 0 & 2/(1-v) & 0 & 0 \\ 0 & 0 & 6 & 0 & 4 & 0 \\ 0 & -6(u/t)^2(1-v^2) & 0 & 0 & 0 & 4(u/t)^2(1-v^2) \end{bmatrix},$$

$$\mathbf{K}_{2(4)} = \begin{bmatrix} 12(1-v^2)/t^2 & 0 & 0 & 0 & 0 & 0 \\ 0 & 12 & 0 & 0 & 0 & -6 \\ 0 & 0 & 12(u/t)^2(1-v^2) & 0 & 6(u/t)^2(1-v^2) & 0 \\ 0 & 0 & 0 & 2/(1-v) & 0 & 0 \\ 0 & 0 & 6(u/t)^2(1-v^2) & 0 & 4(u/t)^2(1-v^2) & 0 \\ 0 & -6 & 0 & 0 & 0 & 4 \end{bmatrix} \quad \text{(C.36)}$$

where u and t are the normalized parameters of a sheet as shown in Figure C.9.

Then, the transformation matrices of the centre displacements of the motion stage are represented as

$$\mathbf{D}_{p1}=\begin{bmatrix}1&0&0&0&0&-w/2\\0&1&0&0&0&0\\0&0&1&w/2&0&0\\0&0&0&1&0&0\\0&0&0&0&1&0\\0&0&0&0&0&1\end{bmatrix},\mathbf{D}_{p2}=\begin{bmatrix}1&0&0&0&-w/2&0\\0&1&0&w/2&0&0\\0&0&1&0&0&0\\0&0&0&1&0&0\\0&0&0&0&1&0\\0&0&0&0&0&1\end{bmatrix},$$

$$\mathbf{D}_{p3}=\begin{bmatrix}1&0&0&0&0&-w/2\\0&1&0&0&0&0\\0&0&1&w/2&0&0\\0&0&0&1&0&0\\0&0&0&0&1&0\\0&0&0&0&0&1\end{bmatrix},\mathbf{D}_{p4}=\begin{bmatrix}1&0&0&0&w/2&0\\0&1&0&-w/2&0&0\\0&0&1&0&0&0\\0&0&0&1&0&0\\0&0&0&0&1&0\\0&0&0&0&0&1\end{bmatrix} \quad \text{(C.37)}$$

where w is the normalized spacing parameter as shown in Figure C.9.

Therefore, the compliance matrix for the motion stage centre is obtained using Equations (C.36) and (C.37) as follows.

$$\mathbf{C}_p=(\mathbf{D}_{p1}^T\mathbf{K}_1\mathbf{D}_{p1}+\mathbf{D}_{p2}^T\mathbf{K}_2\mathbf{D}_{p2}+\mathbf{D}_{p3}^T\mathbf{K}_3\mathbf{D}_{p3}+\mathbf{D}_{p4}^T\mathbf{K}_4\mathbf{D}_{p4})^{-1}. \quad \text{(C.38)}$$

As an example, let L=50 (mm), W=50 (mm), T=1 (mm), U=20 (mm) and v=0.3. Substituting all these normalized values into Equation (C.38), we have

$$\mathbf{C}_p=1\times10^{-3}\begin{bmatrix}0.0083&0&0&0&0&0\\0&0.1300&0&0&0&0.0318\\0&0&0.1300&0&-0.0318&0\\0&0&0&42.6829&0&0\\0&0&-0.0318&0&0.0636&0\\0&0.0318&0&0&0&0.0636\end{bmatrix}. \quad \text{(C.39)}$$

Equation (C.39) shows that the rotation about the X-axis is the only DOF since the highlighted element associated with the rotation about the X-axis is much larger than the other elements, which complies with the qualitative analysis.

Similar to the design in Section C.3.2, we can also obtain a better rotational joint: double four-sheet rotational joint as shown in Figure C.10. It doubles the rotation range without rotation centre-drift, and alleviates the axial translational displacement along the X-axis.

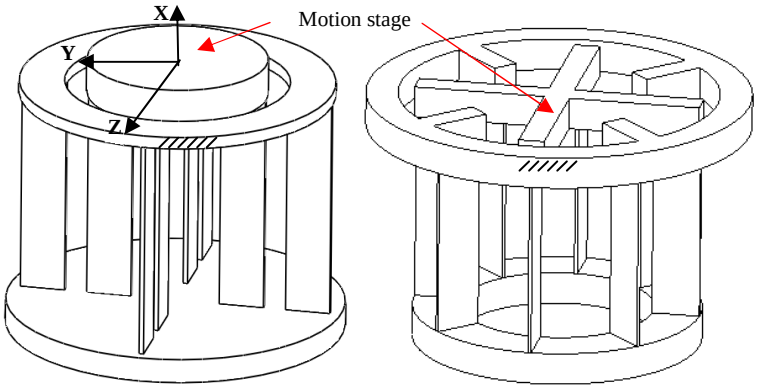

a) Type 1 b) Type 2

Figure C.10 Double four-sheet rotational module

C.5 Summary

This appendix has analysed the mobility of spatial multi-beam modules. By using a normalization strategy, rotational angles and the translational displacements (or the forces and moments) can be compared reasonably. Therefore the derived compliance matrices for the spatial multi-beam modules can reflect the DOF straightforwardly.

It should be noted that the normalization conditions for complicated compliant mechanisms, such as compliant modules composed of beams with different length, are still an open issue.

C.6 References

[C.1] Howell, L. L., and Midha, A., 1995, "Determination of the Degrees of Freedom of Compliant Mechanisms Using the Pseudo-Rigid-Body Model Concept", *Proceedings of the Ninth World Congress on the Theory of Machines and Mechanisms*, Aug. 30–Sep. 2, 1995, Milan, Italy, Vol. **2**:1537–1541.

[C.2] Yu, J.J., Bi S.S., Zong, G.H., Dai, J.S., and Liu X.J., 2006, "Mobility Characteristics of a Flexure-based Compliant Manipulator with Three Legs", *Proceedings of the 2006 IEEE/RSJ International Conference on Intelligent Robots and Systems*, Oct. 9–15, 2006, Beijing, 1076–1081.

[C.3] Dai, J. S., and Ding, X. L., 2006, "Compliance Analysis of a Three-Legged Rigidly-Connected Platform Device", *Journal of Mechanical Design*, Vol. **128**(6): 755–764.

[C.4] Awtar, S., 2004, "*Analysis and Synthesis of Planar Kinematic XY Mechanisms*",

Sc.D. thesis, Massachusetts Institute of Technology, Cambridge, MA.

[C.5] Awtar, S., and Slocum, A. H., 2007, "Constraint-Based Design of Parallel Kinematic XY Flexure Mechanisms", *Journal of Mechanical Design*, Vol. **129**(8):816–830.

[C.6] Awtar, S., and Slocum, A. H., 2007, "Characteristics of Beam-Based Flexure Modules", *Journal of Mechanical Design*, Vol. **129** (6): 624–639.

[C.7] Awtar, S., and Sen, S., 2010, "A Generalized Constraint Model for Two-Dimensional Beam Flexures: Nonlinear Load-Displacement Formulation", *Journal of Mechanical Design,* Vol. **132**(8): 081008.

[C.8] Zelenika, S., and De Bona, F., 2002, "Analytical and Experimental Characterization of High-Precision Flexural Pivots Subjected to Lateral Loads", *Precision Engineering*, Vol. **26**(4): 381–388.

[C.9] Angeles J., 2006, "Is There a Characteristic Length of a Rigid-Body Displacement?", *Mechanism and Machine Theory*, Vol. **41** (8): 884–896.

[C.10] Lobontiu, N., 2002, *Compliant Mechanisms: Design of Flexure Hinges*, CRC PRESS.

[C.11] Howell, L. L., Dibiasio, C. M, and et al, 2010, "A Pseudo-Rigid-Body Model for Large Deflections of Fixed–Clamped Carbon Nanotubes", *Journal of Mechanisms and Robotics*, Vol. **2**(3): 034501.

[C.12] Hopkins, J.B., 2010, "*Design of Flexure-Based Motion Stages for Mechatronic Systems via Freedom, Actuation and Constraint Topologies (FACT)*", Ph.D. thesis. Massachusetts Institute of Technology.

[C.13] Pham, H.-H., and Chen, I.-M., 2005, "Stiffness Modeling of Flexure Parallel Mechanism", *Precision Engineering*, Vol. **29**(4): 467–478.

[C.14] Samuel, H. D., and Sergio, N. S., 1979, *Compliant Assembly System*, United States patent, No.: 4155169.

[C.15] Su, H.-J., and Tari, H., 2010, "Realizing Orthogonal Motions with Wire Flexures Connected in Parallel", *Proceedings of 2010 ASME International Design Engineering Technical Conferences& Computers and Information in Engineering Conference*, Aug. 15–18, 2010, Montréal, Québec, Canada. DETC2010-28517

[C.16] Hopkins, J. B., and Culpepper, M. L., 2010, "Synthesis of Multi-Degree of Freedom, Parallel Flexure System Concepts via Freedom and Constraint Topology (FACT). Part I: Principles", *Precision Engineering*, Vol. **34**(1): 259–270.

[C.17] Zhao, H., and Bi, S., 2010, "Accuracy Characteristics of the Generalized

Cross-Spring Pivot", *Mechanism and Machine Theory*, Vol. **45**(10): 1434–1448.

[C.18] Koseki, Y., Tanikawa, T., and et al, 2002, "Kinematic Analysis of a Translational 3-d.o.f. Micro-Parallel Mechanism Using Matrix Method", *Advanced Robotics*. **16**(3):251–264.

[C.19] Hale L.C., 1999, "*Principles and Techniques for Designing Precision Machines*", PhD thesis, University of California, Livermore, California.

[C.20] Odhner, L., and Dollar, A., 2010, "The Smooth Curvature Flexure Model: an Accurate, Low-Dimensional Approach for Robot Analysis", *Proceedings of the 2010 Robotics: Science and Systems*, June 27–June 30, 2010, Zaragoza, Spain

Appendix D – Prototypes of Spatial Multi-Beam Modules

A prototyped spatial three-beam module under the action of f_z and m_x is shown in Figure D.1. It is made of engineering plastics, and fabricated using a 3-D printer. Under the action of the above payloads, the spatial three-beam module has two primary motion displacements: z_s and θ_{sx} [Figure D.1a]. In addition, the parasitic rotational angle of the motion stage about the Z-axis is dominated by $1.2z_s\theta_{sx}$ [see Equation (2.29) for details], which can be roughly verified by the experiment as shown in Figure D.1b.

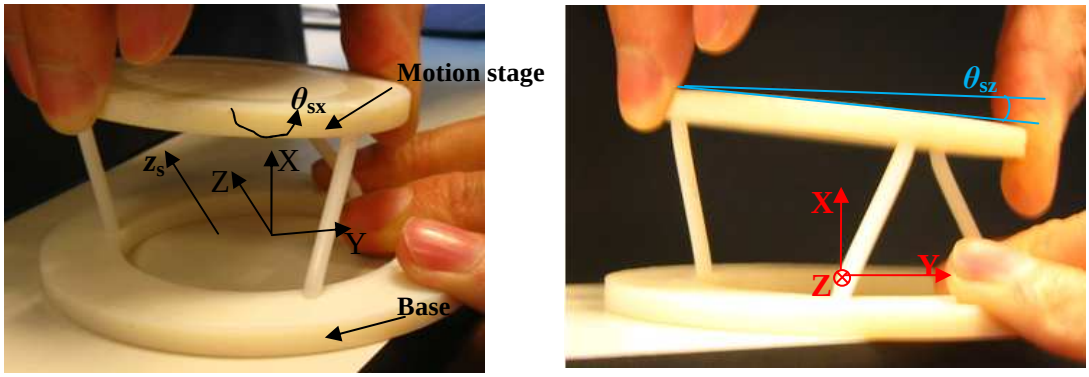

(a) (b)

Figure D.1 Prototype of a spatial three-beam module in deformation

In addition, a spatial double three-beam module (Figure D.2) is prototyped for motion demonstration purpose.

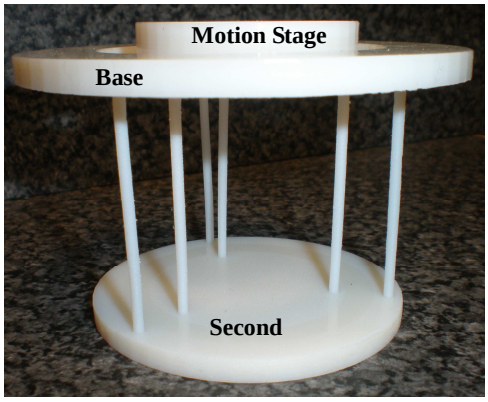

Figure D.2 Prototype of a spatial double three-beam module

Appendix E – Analysis of Spatial Multi-Beam Modules with Different Layouts

Following the approximate nonlinear-analytical modelling of the spatial three-beam module in Chapter 2, we can obtain the load-displacement equations for the spatial six-beam module on the left-hand in Figure 2.14d as follows.

$$\begin{cases} \theta_{sx} \approx \dfrac{m_x + (m_z z_s + m_y y_s)e}{6[\delta + \dfrac{a}{2}(r_3^2 + r_3'^2) + \dfrac{pe(r_3^2 + r_3'^2)}{12} - \dfrac{3d(r_3^2 - r_3'^2)^2 \theta_{sx}^2 ie}{12}]} \\ y_s \approx \dfrac{f_y + m_y \theta_{sx} e}{6a + pe} \\ z_s \approx \dfrac{f_z + m_z \theta_{sx} e}{6a + pe} \\ \theta_{sy} \approx \dfrac{2}{3(r_3^2 + r_3'^2)}(\dfrac{1}{d} + y_s^2 r + z_s^2 r)[m_y + (6c + ph) z_s] - 2\theta_{sx} y_s i \\ \theta_{sz} \approx \dfrac{2}{3(r_3^2 + r_3'^2)}(\dfrac{1}{d} + y_s^2 r + z_s^2 r)[m_z - (6c + ph) y_s] - 2\theta_{sx} z_s i \\ x_s \approx \dfrac{p}{6d} + (y_s^2 + z_s^2) i + \dfrac{p}{6}(y_s^2 + z_s^2) r + \dfrac{(r_3^2 + r_3'^2)}{2} \theta_{sx}^2 i + \dfrac{p}{6} \dfrac{(r_3^2 + r_3'^2)}{2} \theta_{sx}^2 r \\ \quad + 2(y_s \theta_{sz} - z_s \theta_{sy}) k - \dfrac{1}{3}(m_y y_s + m_z z_s) \theta_{sx} r \end{cases} \tag{E.1}$$

where all moments are normalized by EI/L. r_3 and r_3' are the radii of the pitch circles around which the inner three-beams and the outer three beams are uniformly spaced , respectively. It is noted that this equation is also suitable for the spatial six-beam module on the right-hand in Figure 2.14d.

From the torque equation in Equation (E.1), we can learn that the torsional stiffness increases with the increaseof the torsional angle due to the introduction of the added term: $-3d(r_3^2 - r_3'^2)^2 \theta_{sx}^2 ie/12$ in comparison with Equation (2.81). Furthermore, if r_3 approaches r_3', Equation (E.1) is equivalent to Equation (2.81) approximately.

Then, we can analyse a module of eight beams distributed around two regular squares as shown in Figure E.1. Here, two layouts have same outer and inner pitch circle radii.

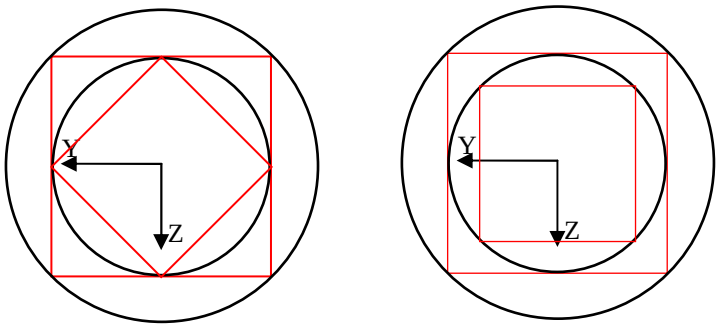

a) Layout 1 b) Layout 2

Figure E.1 Top view for spatial eight-beam module with beams distributed around two regular squares

Similarly, the load-displacement equations of the eight-beam module for both two layouts are

$$\begin{cases} \theta_{sx} \approx \dfrac{m_x + (m_z z_s + m_y y_s)e}{8[\delta + \dfrac{a}{2}(r_4^2 + r_4'^2) + \dfrac{pe(r_4^2 + r_4'^2)}{16} - \dfrac{4d(r_4^2 - r_4'^2)^2 \theta_{sx}^2 ie}{16}]} \\ y_s \approx \dfrac{f_y + m_y \theta_{sx} e}{8a + pe} \\ z_s \approx \dfrac{f_z + m_z \theta_{sx} e}{8a + pe} \\ \theta_{sy} \approx \dfrac{1}{2(r_4^2 + r_4'^2)}(\dfrac{1}{d} + y_s^2 r + z_s^2 r)[m_y + (8c + ph)z_s] - 2\theta_{sx} y_s i \\ \theta_{sz} \approx \dfrac{1}{2(r_4^2 + r_4'^2)}(\dfrac{1}{d} + y_s^2 r + z_s^2 r)[m_z - (8c + ph)y_s] - 2\theta_{sx} z_s i \\ x_s \approx \dfrac{p}{8d} + (y_s^2 + z_s^2)i + \dfrac{p}{8}(y_s^2 + z_s^2)r + \dfrac{(r_4^2 + r_4'^2)}{2}\theta_{sx}^2 i + \dfrac{p}{8}\dfrac{(r_4^2 + r_4'^2)}{2}\theta_{sx}^2 r \\ \quad + 2(y_s \theta_{sz} - z_s \theta_{sy})k - \dfrac{1}{4}(m_y y_s + m_z z_s)\theta_{sx} r \end{cases} \tag{E.2}$$

where all moments are normalized by EI/L, and r_4' (or r_4) is the radius of the pitch circle around which the outer (inner) four beams are uniformly spaced. .

We can further analyse a spatial four-beam module with the layouts that four beams distributed around a regular triangle with one beam connecting to centre (Figure E.2).

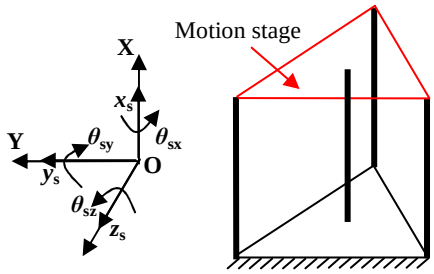

Figure E.2 Spatial four-beam module with beams distributed around a regular triangle with one beam connecting to centre

Similarly, its load-displacement equations can be derived as

$$\begin{cases} \theta_{sx} \approx \dfrac{m_x + (m_z f_z + m_y f_y)e/(4a+pe)}{4(\delta + \dfrac{3}{4}ar_3^2 + \dfrac{3per_3^2 - 3dr_3^4\theta_{sx}^2 ie}{16})} \\ y_s \approx \dfrac{f_y + m_y\theta_{sx}e}{4a+pe} \\ z_s \approx \dfrac{f_z + m_z\theta_{sx}e}{4a+pe} \\ \theta_{sy} \approx \dfrac{2}{3r_3^2}(\dfrac{1}{d} + y_s^2 r + z_s^2 r)[m_y + (4c+ph)z_s] - 2\theta_{sx}y_s i \\ \theta_{sz} \approx \dfrac{2}{3r_3^2}(\dfrac{1}{d} + y_s^2 r + z_s^2 r)[m_z - (4c+ph)y_s] - 2\theta_{sx}z_s i \\ x_s \approx \dfrac{(3p - 3dr_3^2\theta_{sx}^2 i)/4}{3d} + (y_s^2 + z_s^2)i + \dfrac{(3p - 3dr_3^2\theta_{sx}^2 i)/4}{3}(y_s^2 + z_s^2)r + r_3^2\theta_{sx}^2 i + \dfrac{(3p - 3dr_3^2\theta_{sx}^2 i)/4}{3} r_3^2\theta_{sx}^2 r \\ \quad + 2(y_s\theta_{sz} - z_s\theta_{sy})k - \dfrac{2}{3}(m_y y_s + m_z z_s)\theta_{sx} r \end{cases} \tag{E.3}$$

where all moments are normalized by EI/L, and r_3 is the radius of the pitch circle around which the outer three beams are uniformly spaced .

From the torque equation in Equation (E.3), we can also learn that the torsional stiffness increases with the increase of the torsional angle due to the introduction of the term, $-3dr_3^4\theta_{sx}^2 ie/16$, that Equation (2.80) has not.

Appendix F – Maximal Transverse Displacement of the Free-End of a Beam without Free-End Rotation

For a deformed beam for the bending only in the XY plane as shown in Figure A.1, Equation (A.12a), load-displacement equation for the free-end, can be simplified to the linear load-displacement relationships as

$$\begin{bmatrix} f_y \\ m_{ze} \end{bmatrix} = \begin{bmatrix} a & c \\ c & b \end{bmatrix} \begin{bmatrix} y_e \\ \theta_z \end{bmatrix}. \tag{F.1}$$

If the free-end rotation is constrained to be zero, we have

$$m_{ze} = -0.5 f_y, \tag{F.2a}$$

$$f_y = 12 y_e. \tag{F.2b}$$

Then we can obtain the maximal bending moment acting at the beam, which occurs at the fixed end:

$$m_{zmax} = f_y - 0.5 f_y. \tag{F.3}$$

Therefore, the maximal shear stress theory gives

$$\sigma_{max} = \frac{m_{z\,max} E I_z / L}{I_z / (D_0 / 2)} \le \sigma_s. \tag{F.4}$$

where σ_{max} is the maximal stress at the fixed end, σ_s is the yield stress of material, I_z denotes the second moment of the area of the beam's cross-section about the Z-axis, L denotes the length of the beam, and D_0 denotes the diameter of a round cross-section of the beam.

Substituting Equation (F.2b) into Equation (F.3) and then substituting the result in to Equation (F.4), we obtain

$$y_e \le \frac{1}{3} \frac{\sigma_s}{E} \frac{L}{D_0}. \tag{F.5}$$

If a beam has a rectangle cross-section with thickness T (Figure F.1), we have the following relationship similar to Equation (F.5)

$$y_e \le \frac{1}{3} \frac{\sigma_s}{E} \frac{L}{T}. \tag{F.6}$$

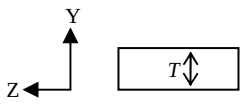

Figure F.1 Rectangle cross-section with thickness T (non-normalization)

Appendix G – Demonstration of Different Actuation Arrangements for an Elastic System

For an elastic system shown in Figure G.1 below, we will demonstrate that different actuation arrangements may have different load-displacement equations under static balance.

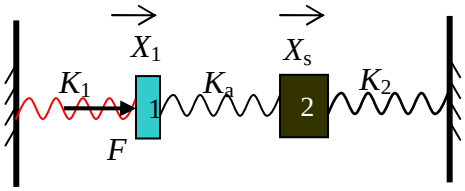

a) Force exerted on stage 1

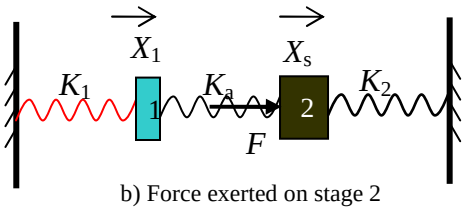

b) Force exerted on stage 2

Figure G.1 Two actuation arrangements for an elastic system

For the actuation arrangement in Figure G.1a, we have

$$\begin{cases} F = K_1 X_1 + K_2 X_s \\ K_2 X_s = K_a (X_1 - X_s) \end{cases}. \tag{G.1}$$

From Equation (G.1), we can solve

$$F = (K_1 \frac{K_a + K_2}{K_a} + K_2) X_s > (K_1 + K_2) X_s . \tag{G.2}$$

For the actuation arrangement in Figure G.1b, we have

$$\begin{cases} F = K_1 X_1 + K_2 X_s \\ K_1 X_1 = K_a (X_s - X_1) \end{cases}. \tag{G.3}$$

From Equation (G.1), we can solve

$$F = (K_1 \frac{K_a}{K_a + K_1} + K_2) X_s < (K_1 + K_2) X_s . \tag{G.4}$$

The difference between Equation (G.2) and Equation (G.3) shows the distinction of

two actuation arrangements. If K_a approaches to infinity, the two actuation arrangement are same.

Appendix H – XY CPM Composed of Identical Spatial Modules

An XY CPM, composed of identical spatial double four-beam modules, originating from the improved modular XYZ CPM (Figure 5.10) is shown in Figure H.1. It is obtained by removing the compliant P joint in the Z-direction of the improved modular XYZ CPM.

In addition, a varied XY CPM (Figure H.2) can be obtained. It is composed of four PPPR legs and an E leg. Each compliant P joint connected to the base consists of three spatial double four-beam modules.

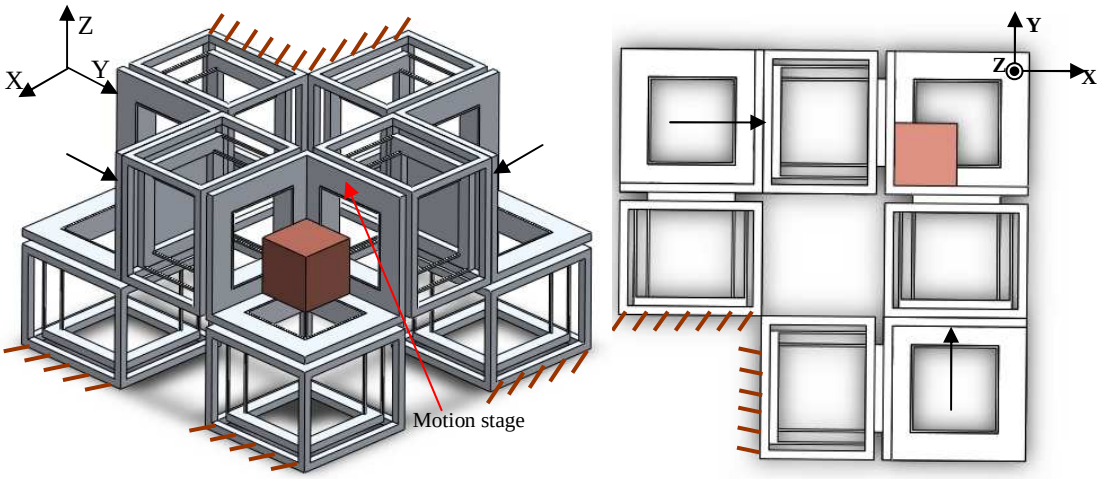

a) 3D view b) Top view

Figure H.1 An XY CPM composed of identical spatial double four-beam modules

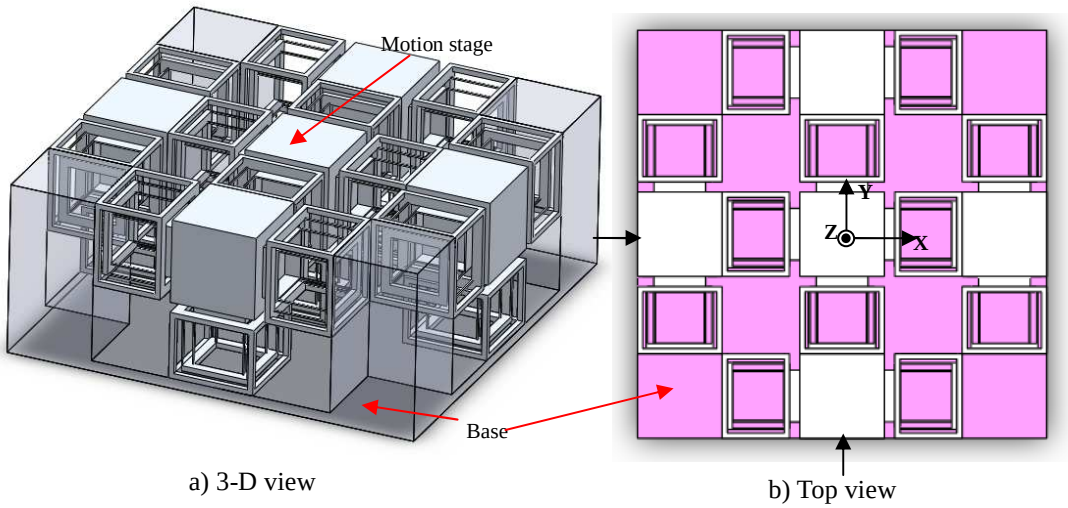

a) 3-D view b) Top view

Figure H.2 Variation for the XY CPM composed of identical spatial double four-beam modules

Appendix I – Variations for the XYZ CPM with Five Legs

Figures I.1 and I.2 show two variations for the XYZ with five legs (Figure 5.13). The first one uses the double three-beam modules as building blocks, and has no embedded arrangement for the leg in the Z-direction. The other one also use the *quadruple* three-beam modules, and make the embedded arrangement for the leg in the Z-direction to approximately eliminate the parasitic rotational displacements based on the stiffness centre strategy.

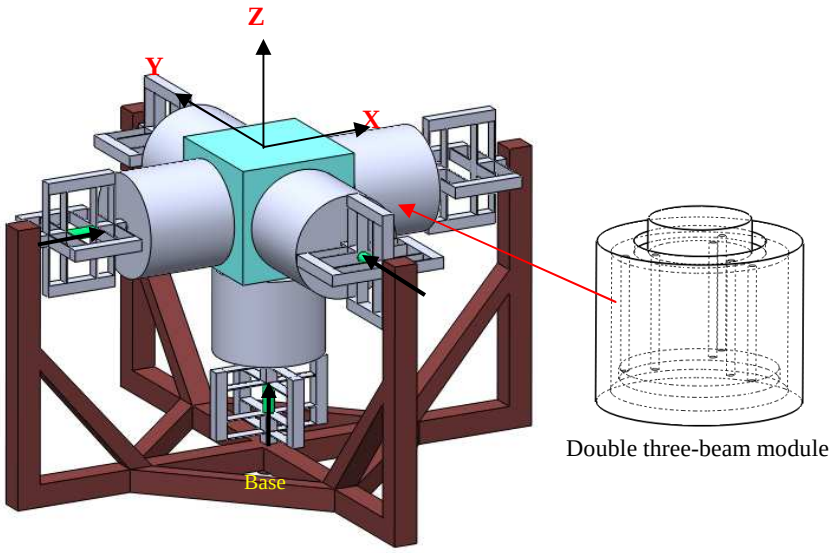

(a) XYZ CPM without embedded
arrangement for the leg in the Z-direction

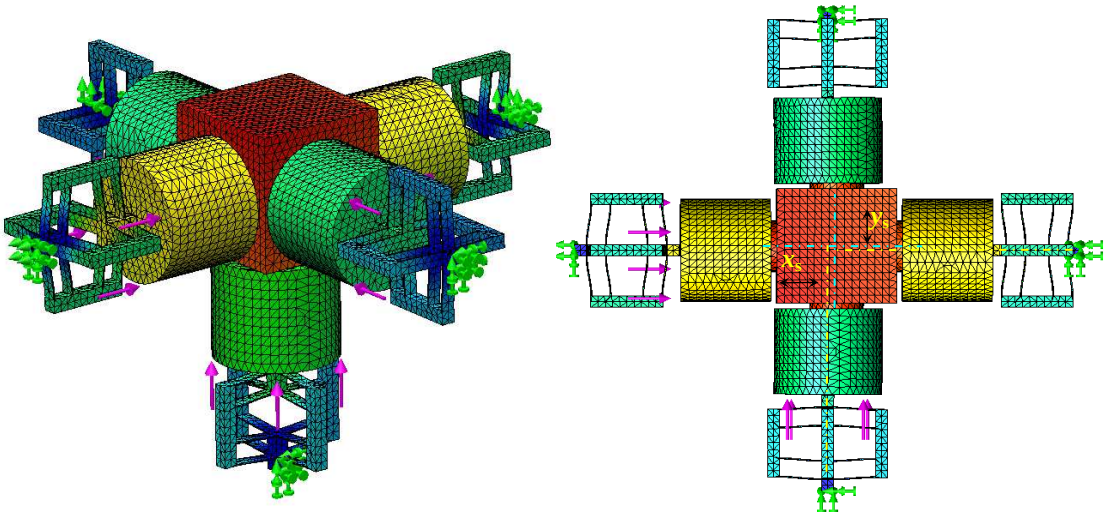

(b) Configuration in deformation

Figure I.1 Variation I of 5-legged XYZ CPM

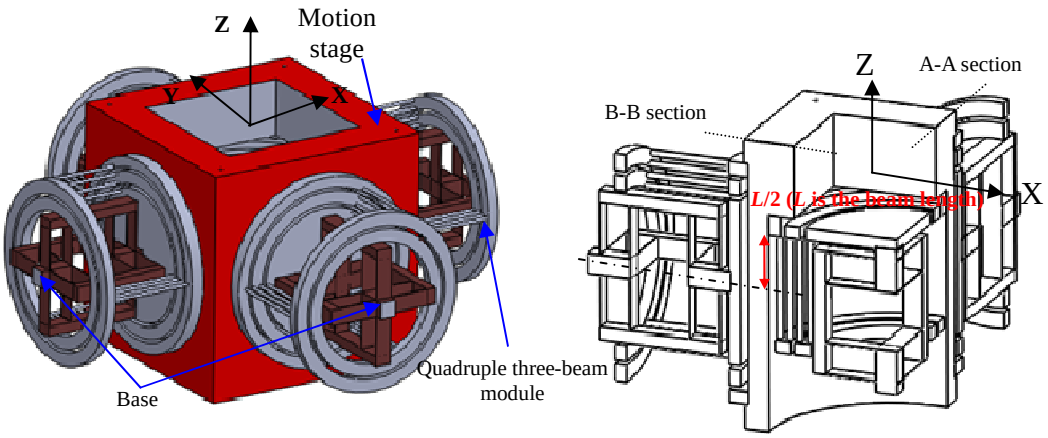

(b) XYZ CPM using quadruple three-beam modules

(b) Sectional view

Figure I.2 Variation II of 5-legged XYZ CPM

Appendix J – Nonlinear Modelling of the Improved Embedded XYZ CPM

For the improved embedded XYZ CPM (Figure 5.12), we can derive its approximate nonlinear model in order to capture the nonlinear cross-axis coupling effect – primary stiffness changes in presence of other actuation force(s) based on Equations (2.86a), (2.86b), (2.86c) and Equation (G.2):

$$x_s = \frac{f_{ax-x}}{(k_{ay}+k_{az})\dfrac{k_x+(k_{py}+k_{pz})}{k_x}+(k_{py}+k_{pz})} \approx \frac{f_{ax-x}}{8a-\dfrac{3}{256a}(f_{ay-y}^2+f_{az-z}^2)}, \tag{J.1a}$$

$$y_s = \frac{f_{ay-y}}{(k_{ax}+k_{az})\dfrac{k_y+(k_{px}+k_{pz})}{k_y}+(k_{px}+k_{pz})} \approx \frac{f_{ay-y}}{8a-\dfrac{3}{256a}(f_{ax-x}^2+f_{az-z}^2)}, \tag{J.1b}$$

$$z_s = \frac{f_{az-z}}{(k_{ax}+k_{ay})\dfrac{k_z+(k_{px}+k_{py})}{k_z}+(k_{px}+k_{py})} \approx \frac{f_{az-z}}{8a-\dfrac{3}{256a}(f_{ax-x}^2+f_{ay-y}^2)} \tag{J.1c}$$

where

$k_{ax} = \dfrac{(4a)^2-(\dfrac{\bar{x}_s 2a2d}{2a+2d})^2 e^2}{8a}$, $k_{ay} = \dfrac{(4a)^2-(\dfrac{\bar{y}_s 2a2d}{2a+2d})^2 e^2}{8a}$, and $k_{az} = \dfrac{(4a)^2-(\dfrac{\bar{z}_s 2a2d}{2a+2d})^2 e^2}{8a}$,

which are the transverse stiffness of the active spatial double four-beam modules.

$k_{px} = \dfrac{(4a)^2-(\bar{x}_s 4a)^2 e^2}{8a}$, $k_{py} = \dfrac{(4a)^2-(\bar{y}_s 4a)^2 e^2}{8a}$, and $k_{pz} = \dfrac{(4a)^2-(\bar{z}_s 4a)^2 e^2}{8a}$,

which are the transverse stiffness of the passive spatial double four-beam modules.

$k_x = 1/[\dfrac{1}{2d}-\dfrac{1}{4a}(\bar{y}_s^2+\bar{z}_s^2)ei+\dfrac{1}{8}(\bar{y}_s^2+\bar{z}_s^2)r]$, $k_y = 1/[\dfrac{1}{2d}-\dfrac{1}{4a}(\bar{x}_s^2+\bar{z}_s^2)ei+\dfrac{1}{8}(\bar{x}_s^2+\bar{z}_s^2)r]$, and

$k_z = 1/[\dfrac{1}{2d}-\dfrac{1}{4a}(\bar{x}_s^2+\bar{y}_s^2)ei+\dfrac{1}{8}(\bar{x}_s^2+\bar{y}_s^2)r]$, which are the axial stiffness of the passive spatial double four-beam modules. $\bar{x}_s = \dfrac{f_{ax-x}}{8a}, \bar{y}_s = \dfrac{f_{ay-y}}{8a}, \bar{z}_s = \dfrac{f_{az-z}}{8a}$, which are the initial estimations for the output displacements of the motion stage centre. x_s, y_s and z_s are the translational displacements of motion stage along the X-, Y- and Z-axes, respectively, $f_{ax\text{-}x}$, $f_{ay\text{-}y}$ and $f_{az\text{-}z}$ are the input actuation forces from the actuators along X-, Y- and Z-axes, respectively.

Equations (J.1), (J.2) and (J.3) show that the cross-axis actuation forces can reduce

the primary stiffness.

Based on Equation (G.1) and the above results, we can obtain the lost motion percentage along each axis:

$$\frac{x_{ax} - x_s}{x_s} \times 100\% = \frac{(k_{py} + k_{pz})}{k_x} \times 100\%, \tag{J.2a}$$

$$\frac{y_{ay} - y_s}{y_s} \times 100\% = \frac{(k_{px} + k_{pz})}{k_y} \times 100\%, \tag{J.2b}$$

$$\frac{z_{az} - z_s}{z_s} \times 100\% = \frac{(k_{px} + k_{py})}{k_z} \times 100\%. \tag{J.2c}$$

Appendix K – Stiffness and Motion-Range Adjustable Spatial Multi-Beam Modules

In order to improve the dynamic performance of spatial multi-beam modules, we can increase the number of the beams to raise the primary stiffness without affecting the maximal allowable motion stage. Figure K.1 shows a stiffness adjustable spatial multi-beam module. Its primary stiffness is changeable by simply adding/removing the beams.

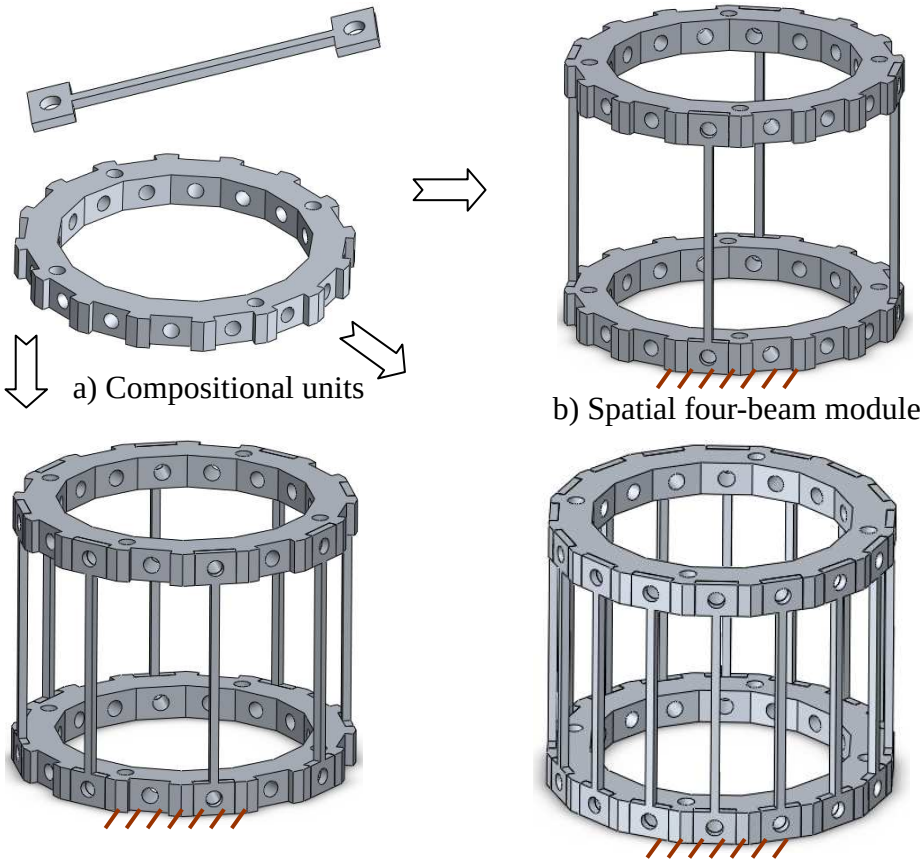

a) Compositional units

b) Spatial four-beam module

c) Spatial eight-beam module

d) Spatial sixteen-beam module

Figure K.1 A stiffness adjustable spatial multi-beam module

In order to raise the motion range of spatial multi-beam modules, a more-layer strategy can be employed. Figure K.2 shows a motion-range adjustable spatial multi-beam module. Its motion range is changeable by increasing/decreasing the layer number.

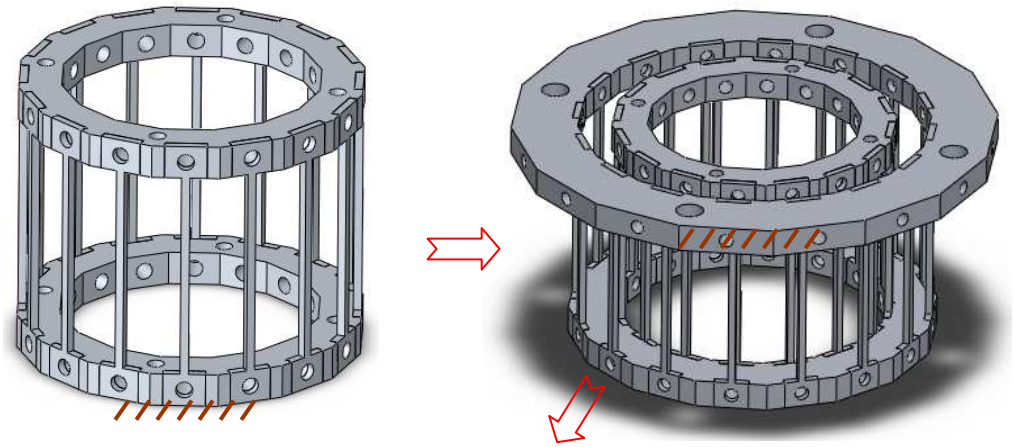

a) Spatial single sixteen-beam module b) Spatial double sixteen-beam module

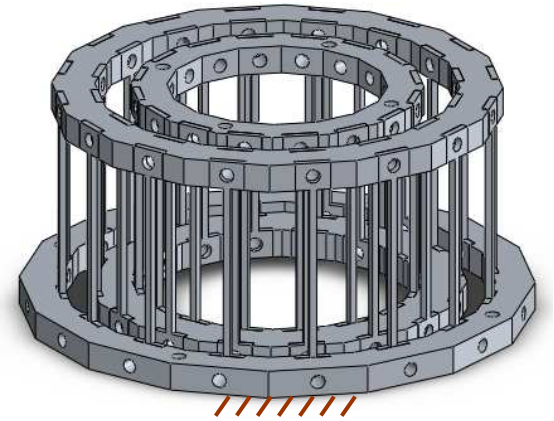

c) Spatial triple sixteen-beam module

Figure K.2 A motion-range adjustable spatial multi-beam module

Appendix L – A 3-Legged XY CPM with Well-Constrained Parasitic Rotation

Figure L.1 shows a 3-legged XY CPM with well-constrained parasitic rotation about the Z-axis based on the partial-symmetry and stiffness centre strategy. It is composed of two types of parallelogram flexure modules with identical beams to produce approximate equal primary motion stiffness along each axis. Note that the applied force along the Y-axis passes through the centre of stiffness of the passive parallelogram module having primary translation along the Y-axis.

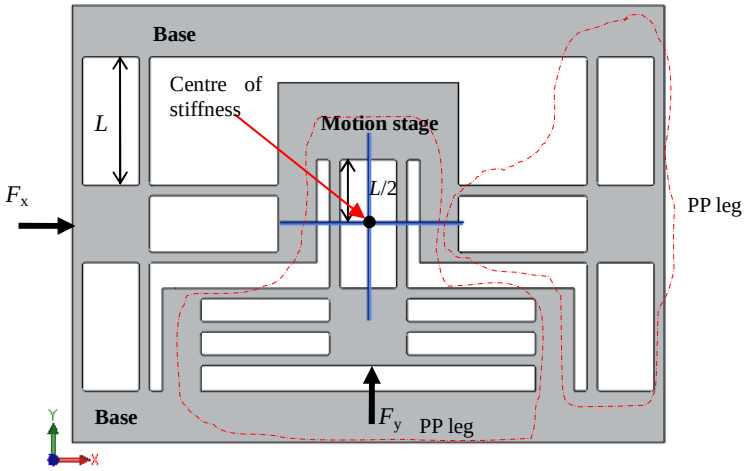

(a) CAD model

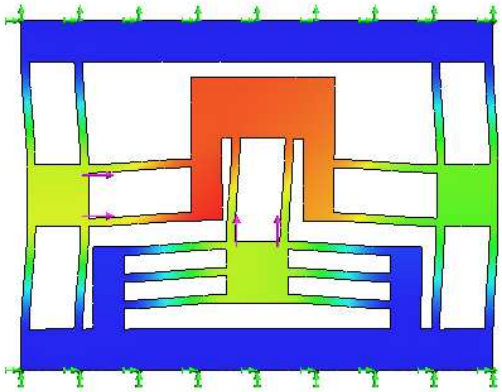

(b) Deformed configuration in FEA

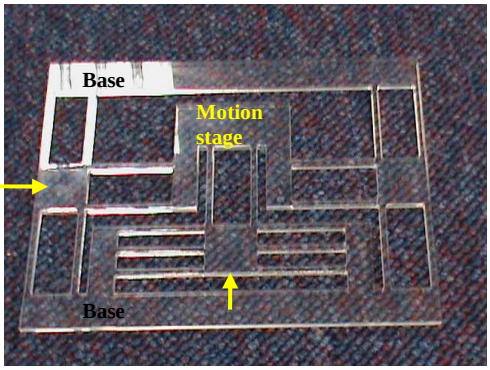

(c) Prototype made of engineering plastic and fabricated using laser cutting

Figure L.1 A 3-legged XY CPM with well-constrained parasitic rotation